Eduardo Costa Girão

Propriedades eletrônicas e de transporte de nanoestruturas de carbono

–

Electronic and transport properties of carbon nanostructures

Fortaleza - CE

Dezembro / 2011

Eduardo Costa Girão

Propriedades eletrônicas e de transporte de nanoestruturas de carbono / Electronic and transport properties of carbon nanostructures

Tese apresentada ao Curso de Pós-Graduação em Física da Universidade Federal do Ceará como parte dos requisitos para a obtenção do título de Doutor em Física.

Prof. Antônio Gomes Souza Filho / Prof. Vincent Meunier

DOUTORADO EM FÍSICA
DEPARTAMENTO DE FÍSICA
CENTRO DE CIÊNCIAS
UNIVERSIDADE FEDERAL DO CEARÁ

Fortaleza - CE

Dezembro / 2011

Tese de Doutorado sob o título *Propriedades eletrônicas e de transporte de nanoestruturas de carbono / Electronic and transport properties of carbon nanostructures*, defendida por *Eduardo Costa Girão* e aprovada no dia 20 de Dezembro de 2011 em Fortaleza, Ceará, pela banca examinadora:

Prof. Antônio Gomes Souza Filho
Departamento de Física - Universidade Federal do Ceará
Advisor

Prof. Vincent Meunier
Department of Physics, Applied Physics, and Astronomy -
Rensselaer Polytechnic Institute
Advisor

Prof. Antônio José Roque da Silva
Laboratório Nacional de Luz Síncrotron and
Instituto de Física - Universidade de São Paulo

Prof. Douglas Soares Galvão
Instituto de Física 'Gleb Wataghin' - Universidade
Estadual de Campinas

Prof. François M. Peeters
Department of Physics - University of Antwerp

Prof. Humberto Terrones
Department of Physics - The Pennsylvania State University
and Departamento de Física - Universidade Federal do
Ceará

To my parents,
Emília and Airton
and to my wife
Adriana

Acknowledgements

Well, I have to thank a lot of people.

First of all, I thank God for everything. Each person knows his/her life experiences better than anyone else and, in my case, I know the importance He has in my life. I thank Him for showing me where to go and for giving me all the tools I needed to construct everything I have.

I thank my wife, Adriana, for being by my side for the last 11 years. I can not imagine my life without her. I thank her for the good moments, because they made us happy, and also for the bad ones, because they made us stronger. Along these years together, we made right and wrong choices, but the best choice I made was you. Thank you for letting me be your choice.

I thank my family for being my first support, my first school. Despite my defects, I am very happy with who I am and a great part of it was constructed with what I learned from my parents. Thanks for being strong when distant, thanks for being lovely when close.

I thank Professor Antônio Gomes Souza Filho for being my advisor since I was an undergraduate student. It has been hard to work with completely different tools, but you have always tried to direct me to the right path. I thank you for being sincere in all the stages of my academic trajectory. In special, I thank you for not letting me to take the wrong choice. Your calm was fundamental to show me the best decision to make and it has conducted me to a position from where I can see good things ahead.

I thank Professor Josué Mendes Filho for the motivation. I had some tough moments during my the academic path, but the few words I heard from him during these times were enough to make me confident that I could get over the problems and make a good job at the end.

I thank Professor Solange Binotto Fagan for introducing me to the field of theoretical calculations. Today I'm very happy with the area I chose to work and you have great influence on this decision. Thanks for your advising when I was a undergraduate, during the master's and in part of my PhD.

When I went to Oak Ridge, I had help from people that behaved like old friends of mine, but without even knowing me. Their attitudes made a huge difference for me. So thank you guys, Lalo, Alejandro and Daniela! You were (and are) real friends. Just know that, wherever

I'll be, you'll have a friend there.

I also thanks the other guys from Oak Ridge, Viviane, Álvaro, Miguel, Paschoale, Bobby, and Deb Holder. Staying far from home in a place you do not know is usually hard, specially in the beginning, but you guys made it all easier for me and make me fell a little more like home.

I also thank Professor Humberto Terrones who I meet in Oak Ridge. It has been very good changing ideas with you. I hope we have more opportunities for coffee time. I thank you for you support in Oak Ridge and here in Fortaleza.

I have had a great time in Troy. Work made me happy there, but I also made good friends. My days always got better after a ride in the "Red Hawk Shuttle". Karen, James, Sean and all the other drivers made my everyday easier after the ride and nicer after the chat. I want you to know that your work and friendship were very important to me. Thanks a lot.

While being in US, I could still fell a little like in Brazil. This is because Adriana and I had our friends "Don" Fernando and Sônia and their kids Mariel, Nicolas and Gabriela. We have had very good moments in Troy and I really want this friendship to last forever. Fernando, I will never forget that crazy journey to New York city, that was a lot of fun. Thank you guys for the help and friendship.

Leo is another good friend I made in Troy. Together with Adriana, we had a lot of fun hanging out. It was very nice working with you everyday and I wish you all the best in your PhD. Thanks for the friendship.

Even though I have already cited Dr. Eduardo Cruz-Silva, I need to dedicate some more lines to him. Lalo helped me like a brother. His help with the arrangements for my arrival in Oak Ridge were enough to make me grateful. But once I got to Oak Ridge, I had the opportunity to know him better. More than I expect, Lalo revealed to be a great friend. But there is more. Lalo is great researcher and I am also happy for having the chance of changing ideas and making science with him. Lalo and his lovely wife Marcia are friends that will always be in my heart. Thanks you guys for everything.

I also thank my friends from the Physics Department in UFC. Well, I know these guys for almost 10 years and I thank God for giving me such good friends. Time goes by and we are naturally getting far from each other, but the friendship is the same and I thank you guys for all the support and the good moments. I really wish all the best for you.

In special, I thank my closer friends Acrísio, Aldi and Abraão. Acrísio and I worked together for years. Facing the challenges of science with a good friend was very good and I thank him for all his support. The same applies to Aldi, such a source of joy during days of hard work.

Abraão stayed away from physics for some time, but even in that time, he was a close friend and his support was very important to me. We are now geographically far from each other, but there is no distance for friendship. I wish success for your guys in the new challenges you are about to face.

I have another special thank to my friends Antônio Márcio and Lavor for their attention when hosting me and Adriana in Recife.

I also thank all my other friends not related to the University. Each of you guys have, somehow, a special contribution for my achievements.

I thank Oak Ridge National Laboratory for all the support during my stay in Tennessee.

I thank Rensselaer Polytechnic Institute all the support and for providing me the best work environment I have ever had to develop my work.

I thank Universidade Federal do Ceará for all the support during my whole academic life.

I thank Brazilian agency CNPq for the precious financial support which made it possible for me to develop my academic work when I was as undergraduate student, as well as during my master's and PhD.

I thank Brazilian agency CAPES for the financial support during my stay in USA through the sandwich program fellowship.

I thank my colleagues from Universidade Federal do Piauí, specially Professors Bartolomeu Cruz Viana Neto and Cleânio da Luz Lima, for all the support during my initiation in the institution.

Finally, I have a special thanks to Professor Vincent Meunier. If I am happy with the final result of my PhD and if I am optimistic about the future of my professional life, Vincent is especially responsible for that. Working with him made a huge difference in my life. It gave me back the pleasure of working with science. Thanks for trusting me and for giving me good projects to work on, thanks for the motivation, thanks for showing me what I could do. Some people are lucky for having a good boss as a scientist, some are lucky for having a good boss as a person, I was lucky for having both. Thanks, Vincent, for being the best boss I could ever have.

"I'm a great believer in luck, and I find the harder I work the more I have of it."

Thomas Jefferson

Resumo

À medida que o limite de miniaturização da eletrônica baseada no silício aproxima-se do seu limite, alternativas em estado sólido devem ser investigadas na busca da diminuição da escala de tamanho de dispositivos operacionais, ao mesmo tempo em que se deve considerar problemas de crescente interessse como dissipação de calor e ruído associado com a baixa dimensionalidade. Nesta busca, já está claro que nanosistemas semicondutores de carbono são candidatos de primeiro pelotão para comporem os blocos básicos para dispositivos em escala atômica e molecular. Grafeno e nanotubos de carbono são os sistemas mais estudados desta classe de estruturas que se estende por uma vasta coleção de sistemas. Estas nanoestruturas de carbono apresentam uma riqueza de propriedades físicas e químicas que se reflete no enorme número de artigos científicos tendo esses sistemas como foco [1]. Apesar de a ciência das nanoestruturas de carbono ainda ter um longo caminho pela frente antes de alcançar as prateleiras das lojas depois de ter sido transformada em tecnologia, a comunidade científica tem caminhado rapidamente no sentido de entender e controlar tais sistemas de modo a diminuir esta distância.

Nesta tese nós realizamos um estudo teórico das propriedades eletrônicas e de transporte de um número de nanoestruturas de carbono, tais como nanosistemas toroidais e nanofitas de carbono de arranjo complexo. Nossos cálculos de estrutura eletrônica são baseados em um modelo tight-binding que inclui um Hamiltoniano de Hubbard para descrever a influência do spin sobre os estados eletrônicos. As propriedades de transporte eletrônico foram calculadas utilizando o formalismo de Landauer e o método de funções de Green para determinar a transmitância quântica em sistemas em nanoescala. Parte destes cálculos foram realizados com pacotes computacionais desenvolvidos especialmente para esta tese. Em particular, nós desenvolvemos uma extensão de um algorítmo eficiente para o cálculo de função de Green em uma infraestrutura computacional em paralelo.

Nanotoroides de carbono apresentam estrutura eletrônica específica se comparados aos nanotubos de carbono, já que sua geometria impõe um grau suplementar de confinamento espacial. Como consequência, condições adicionais devem ser impostas à sua geometria para que a estrutura seja metálica. Aqui nos analizamos nanotoroides de carbono a partir de duas perspectivas diferentes: sistemas de dois terminais com um ângulo variável entre os eletrodos e estruturas de múltiplos terminais. Esses sistemas possuem potencial para serem aplicados em nanoeletrônica graças à sua geometria particular que permite que a corrente flua através do sistema por diferentes caminhos eletrônicos. Isso resulta em propriedades de transporte interessantes, as quais são ditadas por efeitos de interferência eletrônica que variam com o ângulo entre os eletrodos e com os detalhes da estrutura atômica da junção nanotoroide-terminal. Nós mostramos que a presença de múltiplos terminais acrescenta novos aspectos ao transporte eletrônico destes toroides já que o número de possibilidades para o fluxo eletrônico cresce rapidamente com o número de eletrodos. Observa-se que a condutância é caracterizada por um conjunto de picos resonantes que são relacionados com caminhos eletrônicos específicos. Estes resultados são racionalizados em termos de uma série de regras para se determinar o caminho para a corrente elétrica como uma função da energia do elétron incidente.

Na segunda parte da tese, nós estudamos as propriedades físicas de uma classe de fitas de carbono as quais nós chamamos de fitas sinuosas (ou simplesmente *wiggles*, em inglês). A estrutura atômica destas *wiggles* pode ser descrita por um conjunto reduzido de fatores já que elas podem ser construídas utilizando-se fitas de carbono de borda reta como blocos básicos. Nós mostramos que essas *wiggles* de carbono apresentam um conjunto de propriedades eletrônicas e magnéticas ainda mais amplo quando comparadas com os seus constituintes básicos (fitas de carbono de borda reta). Isso é especialmente devido à formação de domínios nas bordas, resultantes da sucessiva repetição de setores de fitas retas paralelas e obliquas ao longo da direção periódica da *wiggle*. Nós demonstramos que as *wiggles* de carbono apresentam múltiplos estados magnéticos que podem ser explorados para se manipular as propriedades físicas desses sistemas. Estes diferentes estados magnéticos resultam em propriedades eletrônicas e de transporte distintas, de modo que a corrente eletrônica pode ser controlada pela escolha de valores específicos da energia do elétron incidente no sistema, assim do spin eletrônico e do estado magnético da *wiggle*. Essas propriedades tornam as *nanowiggles* potenciais candidatas para novas aplicações em nanodispositivos.

Finalmente, nos esperamos que o trabalho apresentado nesta tese constitua uma importante contribuição para a investigação das propriedades físicas de nanoestruturas de carbono. Nós mostramos que nanotoroides e *nanowiggles* de carbono apresentam uma série de novas propriedades que podem tornar possível o seu uso em nanoeletrônica. À medida que estudos experimentais em nanomateriais de carbono têm sido desenvolvidos a passos largos, nós projetamos que os resultados apresentados nesta tese se tornarão uma ótima oportunidade para se confrontar teoria e experimento na proposta de novos dispositivos em nanoescala com propriedades eletrônicas e de transporte específicas.

Abstract

As the miniaturization limit of the physical size of Si-based electronics is projected to be reached in a near future, solid-state alternatives must be investigated in the pursuit of further scaling down the effective operational device structures, while considering growingly important problems such as heat dissipation and noise associated with reduced dimensionality. In this quest, it is clear that semiconducting carbon nanosystems are solid front-runner candidates to compose the building blocks for devices at molecular and atomic scales. Graphene and carbon nanotubes are the most studied members of this class of structures which extends over a broad collection of systems. These carbon nanostructures present a wealth of promising physical and chemical properties which is reflected in the number of scientific works having these systems as focus [1]. Even though the science of carbon nanostructures has a long path ahead before reaching the shelves of stores after being transformed into technology, the scientific community has been walking fast towards the understanding and the control of such systems in order to shorten this gap.

In this thesis we theoretically studied the electronic structure and transport properties of a number of carbon nanostructures, such as toroidal carbon nanosystems and complex assembled graphitic nanoribbons. Our electronic structure calculations are based on a tight-binding model including a Hubbard Hamiltonian to describe the influence of spin on the electronic states. The electronic transport properties were computed using the Landauer formalism and a Green's function approach to determine the quantum transmission in nanoscaled systems. Part of these calculations were performed with computational packages developed specifically for this thesis. In particular, we developed an extension of an efficient algorithm to calculate the Green's function on a parallel computational infrastructure.

Carbon nanotori display specific electronic structure compared to carbon nanotubes, since this geometry imposes a supplemental degree of spatial confinement. As a consequence, additional conditions on the structure geometry have to be obeyed for a given torus to be metallic. Here we analyzed carbon nanotori from two different perspectives: two-terminal systems with a variable angle between the terminals and multi-terminal structures. These rings are potential systems for nanoelectronic application as their particular geometry allows the current to flow through the system along different electronic paths. This results in interesting transport properties dictated by electron interference effects which vary with the angle between the electrodes and the atomic details of the nanotorus-electrode junction. We showed that the presence of multi-terminals adds new features to the electronic transport on these tori as the number of possibilities for the electronic flow increases quickly with the number of electrodes. It turns out that the conductance is characterized by a set of resonant peaks which are related to specific electronic paths. These results are rationalized into a set of rules to determine the path for the electrical current as a function of the impinging electron energy.

In the second part of the thesis we studied the physical properties of a class of complex graphitic nanoribbons that we called *wiggles*. The atomic structure of these wiggles can be

described by a reduced set of factors since they can be built using straight carbon nanoribons as basic building blocks. We show that carbon nanowiggles present a broader set of electronic and magnetic properties in comparison to those of their constituents (graphene nanoribbons). This is mainly due to the formation of edge domains resulting from the successive repetition of parallel and oblique graphene nanoribbon sectors along the wiggle's periodic direction. We demonstrate that carbon wiggles present multiple magnetic states which can be exploited to tune the physical properties of these systems. These different magnetic states lead to dissimilar electronic structure and transport properties for the wiggles so that the electronic current on these systems can be tuned by selecting specific values for the impinging electron energy as well as its spin and the wiggle's magnetic state. These properties make carbon nanowiggles potential candidates as new nanodevices.

Finally, we expect that the work reported in this thesis will constitute an important contribution to the investigation of the physical properties of carbon nanostructures. We show that carbon nanotori and nanowiggles present a series of new properties that can enable their use in nanoelectronics. As experimental studies on carbon nanomaterials have been developed at a fast pace, we project the findings presented in this thesis to be a great opportunity to confront theory and experiment in the proposal of new nanoscaled devices with specific electronic and transport properties.

Contents

List of Figures

List of Tables

Prologue

Two Nobel prizes (1996 and 2010); the topic of about 13000 papers and 2500 patent applications only in the last year (2010) [1]; a front runner candidate to conduct the next generation of nanotechnology [1]; a growing media interest in such a way that it starts to be known by all the sectors of society. Any of these statements would suffice to make us ask: "Who or what is this phenomenon?". What a surprise it would be if all these affirmations referred to the same answer? Yes, it is true and the answer is ***nano carbon***.

Carbon has been known for a long time. It is not only the spinal cord of organic chemistry, but it also is capable to form interesting inorganic structures. Graphite and diamond are "old forms" of carbon which contrast in their properties and abundance. Carbon fibers led to a revolution in resistant materials research, going from the laboratory test-beds, in the 50's, to the industry, in the 70's and 80's. Today they are present in our daily routine as building parts in planes, cars, helmets and most anything which needs to be mechanically resistant. In 1985, the scientific interest in carbon underwent an important turning point with the discovery of the fullerenes [10]. Even though, to date, fullerenes have not spurred a corresponding turning point in consumer technology, they have paved the way to the rising of a new research field and confirmed past predictions.

In 1959 Richard P. Feynmam pointed out the possibility of manipulating matter with atomic precision [11]. Even though it was impossible with the technology of his time, he envisioned that in some decades we would be able to explore the matter characteristics in their most intrinsic properties. This is why Feynmam is commonly called the "father" of nanoscience (the science of systems with nanometer sizes: 1 nm$= 10^{-9}$ m). In this context, fullerenes represent the real starting point of this research field as they attracted special attention due to their nanoscopic size and highly self-organized structure. New properties, such as their high surface curvature, led to a set of new phenomena exploited in chemistry, physics and other fields. It is not surprising that its discovery gave to Kroto, Curl and Smalley the Nobel Prize in Chemistry in 1996.

Following the discovery of fullerenes, researchers have speculated about the possibility of carbon forming tubular structures [12]. It did not take long for this new form of carbon to

be discovered, placing carbon in the spotlight of nanoscience. In 1991, Iijima reported the observation of multiple concentric one-atom-thick tubes made of carbon [13]. Two years later, Iijima and Bethune simultaneously reported the synthesis of single-wall carbon nanotubes [14, 15]. Compared to C_{60}, carbon nanotubes brought an even larger net of possible applications due to their extreme mechanical resistance, high aspect ratio and unusual relation between their atomic structure and their physical and chemical properties. Even though they still have not met all the projected expectations, they remain potential candidates for a series of technological breakthrough applications and their production reaches the amount of 100 tons per year.

However, history does not end with the hollow carbon structure. Even though graphite (the stacking of inumerous carbon honeycomb sheets) is a common and well known material, the isolation of single sheets (graphene) was not accomplished until 2004 when Novoselov and Geim isolated a graphene sheet using a scotch tape [16]. Due to graphene's simplicity, its properties were already the subject of previous theoretical studies (Wallace's paper in 1947 is the pioneer [17]), but the experimental isolation of single sheets produced a strong transition in the attention dispensed to graphene and graphene related structures. Advantages such as an easier experimental control make them even more promising for applications than carbon nanotubes. As a sign of this, it took only six years for Novoselov and Geim to be awarded with the Physics Nobel Prize in 2010.

The family of carbon nanostructures is not limited to fullerenes (0D), nanotubes (1D) and graphene (2D), but also extends to a huge set of related structures having those three "stars" as building blocks. While experimentalists accelerate the pace to develop control on synthesizing, modifying and manipulating carbon nanostructures, theoretical studies are essential to understand the underlying physics and chemistry in these systems, as well as to provide the indispensable tools to help guide and interpret experiments.

In this thesis we employ theoretical calculations to study the electronic structure and transport of two classes of nanostructures: toroidal systems and complex assembled graphene nanoribbons. The thesis is divided in three parts. In Part I we present a general introduction and the methods employed in the computational calculations. The results on toroidal nanostructures are discussed in Part II and Part III is dedicated to graphene nanowiggles. We finish the thesis with the conclusions.

Part I

Generalities

1 Introduction to nano carbon

This chapter is dedicated to explain why carbon is so scientifically and technologically rich as well as to give a small overview on the carbon science. After discussing basic properties of carbon as a chemical element, we describe the main components of the huge family of carbon nanomaterials and some of their striking properties. As we present the different carbon nanostructures, we highlight the particular systems we studied in this thesis, namely carbon nanowiggles and toroidal structures. As our studies are based on computational calculations, we describe the corresponding methods in the subsequent 3 chapters.

1.1 Atomic electronic structure

We will now present the general framework to classify the electronic states in single atoms. Let us first consider the problem of an hydrogen-like atom. This is an atom with only one electron orbiting its nucleus. If we consider that the atomic nucleus is static and positioned at the origin of the coordinate system, the potential energy can be written as a spherically symmetric function of the electron coordinate:

$$V(\mathbf{r}) = V(r) = -\frac{cZ}{r} \tag{1.1}$$

where r is the distance to the origin and c a constant depending on the system of units. Under this condition, one expects that the angular momentum $\hat{L}$ will present stationary values. Equivalently, the commutation relation

$$[\hat{H}, \hat{L}^2] = 0 \tag{1.2}$$

must be obeyed between the Hamiltonian operator ($\hat{H}$) and the square of the angular momentum operator ($\hat{L}$). This allows us to write eigenstates that are simultaneously eigenfunctions of both $\hat{H}$ and $\hat{L}^2$. The eigenvalues of $\hat{L}^2$ are given by:

$$L^2 = l(l+1)\hbar^2 \tag{1.3}$$

where l is a natural number. Furthermore, we can also write the following expressions for one of the components of the $\hat{L}$ operator (z for example):

$$[\hat{H},\hat{L}_z]=0 \qquad [\hat{L}^2,\hat{L}_z]=0. \tag{1.4}$$

As a consequence, the (E,L^2) eigenstates can also have a well defined value for L_z, given by:

$$L_z=m\hbar; \qquad m=0,\pm1,\pm2,...,\pm l. \tag{1.5}$$

It follows that for each energy eigenvalue, we have $2l+1$ degenerate eigenstates corresponding to the pairs $(l,-l)$, $(l,-l+1)$, ..., $(l,l-1)$, (l,l), where the first and second numbers in each pair refer to the eigenvalues for $\hat{L}^2$ and $\hat{L}_z$, respectively. We observe that the energy levels in the hydrogen atom do not depend on either l or m. This is in fact expected since the problem is spherically symmetric so that the energy does not depend on the orientation of the angular momentum. However, for a specific (l,m) pair, we have a number of different eigenstates. Those are labeled by a third number n (called principal quantum number) in such a way that n can assume integer values greater than l. It can be shown that the energy eigenvalues for hydrogen-like atoms are given by:

$$E_n=-\frac{Z^2}{n^2}13.6\ eV \tag{1.6}$$

where Z is the atomic number. The eigenfunction for a (n,l,m) state in the position representation (or any electron wavefunction in an atom or molecule or representing a bond) will be hereafter called an orbital (in analogy with the fixed energy and angular momentum classical orbit for the electron). It is common to use the following terminology for the orbitals with small angular momentum:

- $l=0\rightarrow s$ state;
- $l=1\rightarrow p$ state;
- $l=2\rightarrow d$ state;
- $l=3\rightarrow f$ state.

Each atomic orbital can be written as a product between a radial function (depending on n and l) and a spherical harmonic:

$$\psi_{n,l,m}=R_{nl}(r)Y_{lm}(\theta,\phi) \tag{1.7}$$

where the radial part is written as:

$$R_{nl} = \left[\left(\frac{\alpha}{n} \right)^3 \frac{(n-l-1)!}{2n(n+l)!} \right]^{1/2} e^{-\alpha r/2n} (\alpha r/n)^l L_{n-l-1}^{2l+1}(\alpha r/n); \quad \alpha = \frac{2Z}{a_0} \tag{1.8}$$

where $a_0 = 0.53$ Å is the Bohr radius and L_j^i are the associated Laguerre polynomials. In Fig 1.1 we plot the radial functions for the first 3 states for the s and p angular momenta.

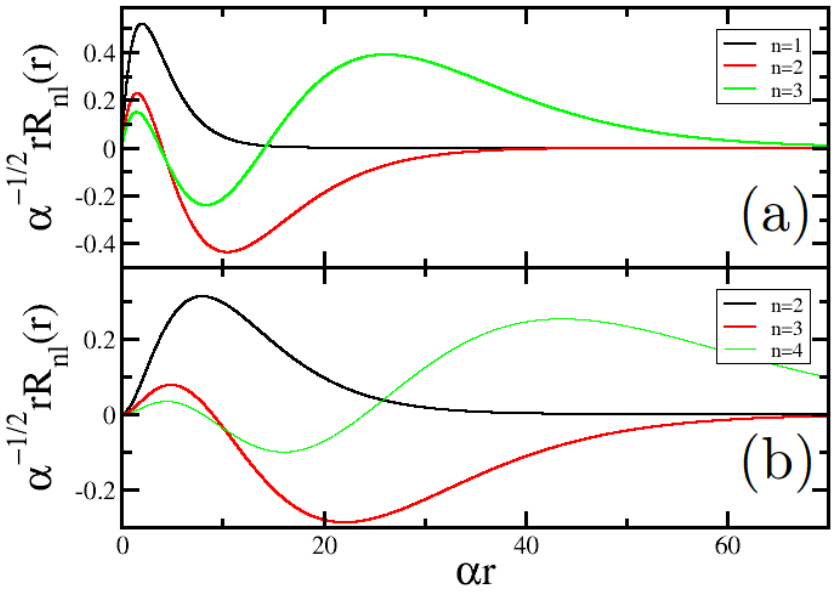

Figure 1.1: Radial functions for the first three s (a) and p (b) orbitals.

Different representations can be used to illustrate the $Y_{l,m}$ dependence with both θ and ϕ. Here we will represent those spherical harmonics as surfaces where the distance from the surface to the origin represents the modulus of $Y_{l,m}$ for the corresponding (θ, ϕ) coordinate pair. Regarding the sign of $Y_{l,m}$, positive values will be represented by blue, while red will refer to negative values of $Y_{l,m}$. The s states have spherical symmetry and are represented by a sphere. The three p orbitals have real and imaginary parts forming two spheres tangent to each other and oriented along the coordinate axis. A unitary transformation can be applied in such a way to construct real orbitals along x, y and z. These four orbitals are represented in Fig. 1.2.

The last quantity describing the electronic levels is the electron's intrinsic angular momentum (spin). For an electron, the eigenvalue for the square of the intrinsic angular momentum operator $\hat{S}^2$ is $s(s+1)\hbar^2$ with $s = 1/2$ and the corresponding eigenvalue s_z for the z component $\hat{S}_z$ can assume either $+1/2$ or $-1/2$ values. In analogy to electric dipoles, these spin values are usually labeled by "up" or "down". Pauli's exclusion principle and Hund's rule are two fundamental concepts regarding spin and the filling of the electronic states in multi-electron systems. Pauli's principle states that any single orbital can be filled by no more than two electrons and these particles must have opposite spins. So, in order to obtain the ground state for the elec-

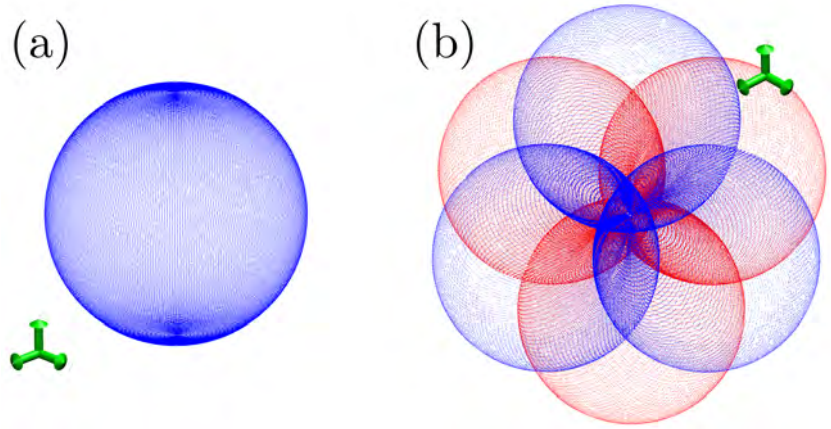

Figure 1.2: Spherical harmonics for the s (a) and p (b) orbitals.

tronic configuration, one starts filling the levels from the lowest ones in such a way that we only fill a given energy level when all the states below are occupied by two electrons with opposite spins. However, the rules state that when filling a degenerate set of states, one has to fill them so as to maximize the total spin. In other words, one only adds the second electron for a given state when all the degenerate levels contain at least one electron. This is known as Hund's rule and its origin lies in the electron-electron interaction. If we have a double degenerate level and two electrons, for example, it is preferable to fill each state with one electron since filling one level with two electrons would increase the electronic repulsion as they would occupy the same region in space. These two rules are intrinsically related to the exchange energy which will be discussed in more details in Section 2.2.2.

While the potential form $V(\mathbf{r}) = V(r)$ holds only for mono-electronic atoms, the (n,l,m) nomenclature is still very useful for multi-electron atoms, even though the eigenvalues will no longer depend only on n. One way to understand how the orbital energies vary for a varying atomic number is presented in [2]. As one raises Z starting from hydrogen, an additional electron has to be included every time the nuclear charge increases by an $|e|$ unit. When adding each extra electron, all the levels get lower in energy. For the multi-electronic case we observe that, in general, s states are always lower in energy than p states due to symmetry. As the previously filled states (inner or core electrons) get lower and lower, they are less influenced by different chemical environments where the atoms are placed. So, the changes in the electronic structure of the atom due to external atoms usually affect mostly the highest energy (valence) electrons.

1.2 Hybridization

When orbitals corresponding to different angular momenta have a small energy difference (compared to the binding energies with other atoms), they can be combined so that the electrons will be described by hybrid orbitals obtained by linear combinations of the original orbital wavefunctions. This phenomenon is called hybridization. When such hybridization involves only s and p orbitals, we have three main hybridization schemes which involve one $2s$ orbital and one (sp), two (sp^2) or three (sp^3) $2p$ orbitals.

1.2.1 sp hybridization

First, we can have a mixing between the s and one of the p orbitals (p_x, for example). This hybridization occurs when the atoms form linear chains, like in poliines chains. The sp combination reads:

$$|sp_a\rangle = a_s|s\rangle + a_p|p_x\rangle \tag{1.9}$$

$$|sp_b\rangle = b_s|s\rangle + b_p|p_x\rangle \tag{1.10}$$

and the hybrid orbitals have to obey the orthonormality conditions:

$$\langle sp_a|sp_b\rangle = \langle sp_b|sp_a\rangle = 0 \tag{1.11}$$

$$\langle sp_a|sp_a\rangle = \langle sp_b|sp_b\rangle = 1 \tag{1.12}$$

which results in:

$$|sp_a\rangle = \frac{1}{\sqrt{2}}|s\rangle + \frac{1}{\sqrt{2}}|p_x\rangle \tag{1.13}$$

$$|sp_b\rangle = \frac{1}{\sqrt{2}}|s\rangle - \frac{1}{\sqrt{2}}|p_x\rangle. \tag{1.14}$$

Schematic representations of these hybrid orbitals are shown in Fig. 1.3a. In this case, strong chemical bonds (σ bonds) are formed involving the sp_a (sp_b) state from on atom and the sp_b (sp_a) state of its right (left) neighbor. The other two p orbitals (perpendicular to the chain) form weaker bonds with the corresponding orbitals from the neighbor atoms (π bonds).

1.2.2 sp^2 hybridization

In the sp^2 hybridization, one s-orbital mixes with two p orbitals (p_x and p_y, for example). The mixing is defined so as to create three hybrid orbitals directed along three in-plane axis

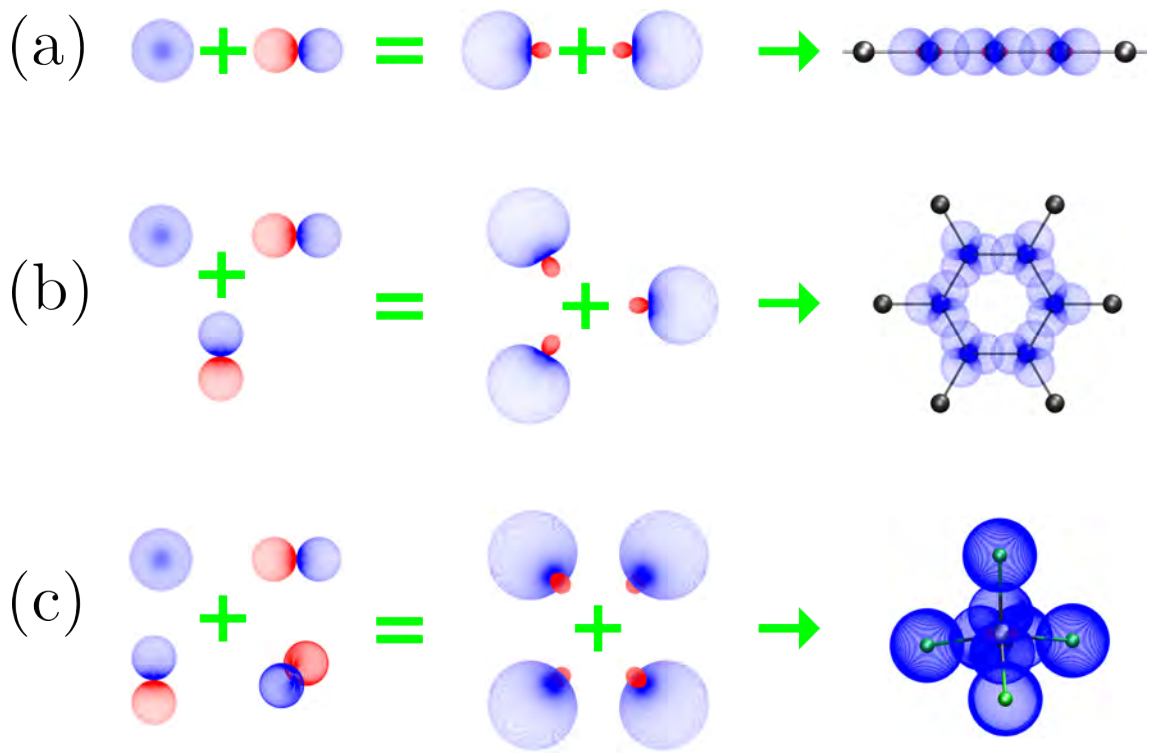

Figure 1.3: (a) sp,(b) sp^2 and (c) sp^3 hybridization schemes and corresponding examples.

making a 120° angle with each other. By using this symmetry argument together with the orthonormality conditions (analogously to the sp case) we can show that the three mixed orbitals will be written as:

$$|sp_a^2\rangle = \frac{1}{\sqrt{3}}|s\rangle + \frac{\sqrt{2}}{\sqrt{3}}|p_x\rangle \tag{1.15}$$

$$|sp_b^2\rangle = \frac{1}{\sqrt{3}}|s\rangle + \frac{\sqrt{2}}{\sqrt{3}}\Big(-\frac{1}{2}|p_x\rangle + \frac{\sqrt{3}}{2}|p_y\rangle\Big) \tag{1.16}$$

$$|sp_c^2\rangle = \frac{1}{\sqrt{3}}|s\rangle + \frac{\sqrt{2}}{\sqrt{3}}\Big(-\frac{1}{2}|p_x\rangle - \frac{\sqrt{3}}{2}|p_y\rangle\Big). \tag{1.17}$$

A suggestive example is the graphene sheet, where the hybrid orbitals from neighbor carbon atoms form σ bonds and the remaining out-of-plane p orbital forms a weaker itinerant π bond with the corresponding orbitals from its neighbors. The hybrid sp^2 orbitals are shown in Fig. 1.3b.

1.2.3 sp^3 hybridization

The last highly symmetric hybridization scheme for only s and p orbitals is the one involving the s orbital and all three p orbitals. In this sp^3 mixing, the hybrid wavefunctions are positioned along four different directions making a $109°28'$ angle between each pair. If we want

to construct orbitals along the $(1,1,1)$, $(1,-1,-1)$, $(-1,1,-1)$ and $(-1,-1,1)$ directions we will have the following hybrid orbitals:

$$|sp^3_a\rangle = \frac{1}{2}\Big(|s\rangle + |p_x\rangle + |p_y\rangle + |p_z\rangle\Big) \tag{1.18}$$

$$|sp^3_b\rangle = \frac{1}{2}\Big(|s\rangle + |p_x\rangle - |p_y\rangle - |p_z\rangle\Big) \tag{1.19}$$

$$|sp^3_c\rangle = \frac{1}{2}\Big(|s\rangle - |p_x\rangle + |p_y\rangle - |p_z\rangle\Big) \tag{1.20}$$

$$|sp^3_d\rangle = \frac{1}{2}\Big(|s\rangle - |p_x\rangle - |p_y\rangle + |p_z\rangle\Big). \tag{1.21}$$

This hybridization occurs in methane (CH_4, see Fig. 1.3c) and in diamond, for instance. This particular sp^3 hybridization tends to form longer bonds in comparison with the previous sp and sp^2 cases. The length of a carbon-carbon bond, for instance, is 1.20 Å, 1.42 Åand 1.54 Åfor sp, sp^2 and sp^3, respectively [18, 19].

1.2.4 sp^δ hybridization

It is important to note that the atoms do not always form perfectly symmetric structures with bonds making angles of 180°, 120° or 109°29′. As discussed above, out of these particular cases, we still have the formation of hybrid orbitals, but the details of the linear combinations will be determined by the geometry of the specific system so as to form a special sp^δ hybridization (with $\delta \neq 1,2,3$). However, it is customary, for simplicity, to associate a sp^δ mixing with the closest of the sp^n ($n = 1,2,3$) schemes. In this context we simply say, for example, that the hybridization of carbon in a nanotube is sp^2 (even though rigorously it is sp^δ with δ close to 2), noticing that it gets further from sp^2 as the nanotube radius gets smaller and smaller. For illustration purposes, let us consider the case of a $(n,0)$ nanotube (to be discussed in Section 1.3). We chose a coordinate system having one carbon as origin, the x axis parallel to the nanotube axis and the z axis orthogonal to the tube surface, as shown in Fig. 1.4. The unit vectors along the bonds between this atom and its first neighbors can be written as:

$$\mathbf{u}_1 = \mathbf{i} \tag{1.22}$$

$$\mathbf{u}_2 = -\sin\theta\cos\phi\,\mathbf{i} + \sin\theta\sin\phi\,\mathbf{j} + \cos\theta\,\mathbf{k} \tag{1.23}$$

$$\mathbf{u}_3 = -\sin\theta\cos\phi\,\mathbf{i} - \sin\theta\sin\phi\,\mathbf{j} + \cos\theta\,\mathbf{k} \tag{1.24}$$

where $\mathbf{i}$, $\mathbf{j}$ and $\mathbf{k}$ are the canonical unit vectors along the x, y and z axis, respectively.

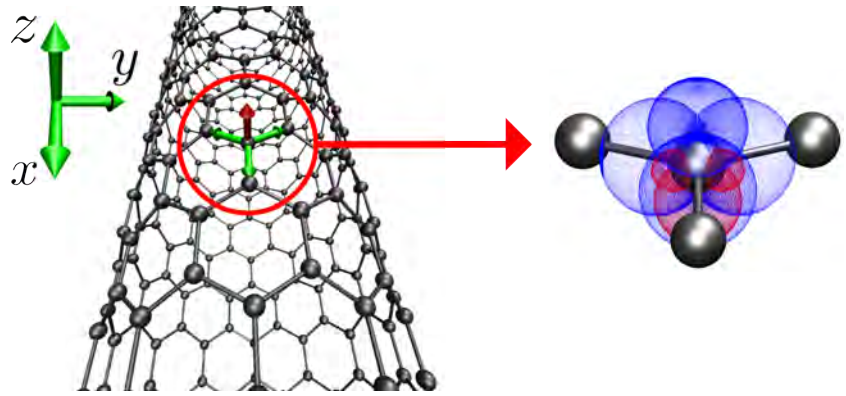

Figure 1.4: Bonds for a carbon atom in a $(12,0)$ nanotube and the corresponding sp^δ hybrid orbitals.

The hybrid orbitals are written as:

$$|sp_a^\delta\rangle = C_1|s\rangle + C_2|p_x\rangle + C_3|p_z\rangle \tag{1.25}$$

$$|sp_b^\delta\rangle = C_4|s\rangle + \sqrt{1-C_4^2}|p_x\rangle \tag{1.26}$$

$$|sp_c^\delta\rangle = C_5|s\rangle + \sqrt{1-C_5^2}\Big(-\sin\theta\cos\phi|p_x\rangle + \sin\theta\sin\phi|p_y\rangle + \cos\theta|p_z\rangle\Big) \tag{1.27}$$

$$|sp_d^\delta\rangle = C_5|s\rangle + \sqrt{1-C_5^2}\Big(-\sin\theta\cos\phi|p_x\rangle - \sin\theta\sin\phi|p_y\rangle + \cos\theta|p_z\rangle\Big), \tag{1.28}$$

with

$$C_1^2 = \frac{\cos^2\theta}{2\sin^2\theta\sin^2\phi} \tag{1.29}$$

$$C_2^2 = \frac{\cos^2\theta}{2\sin^2\theta\sin^2\phi} \tag{1.30}$$

$$C_3^2 = 1 - \frac{\cos^2\theta}{\sin^2\theta\sin^2\phi} \tag{1.31}$$

$$C_4^2 = \frac{\cos^2\phi}{\sin^2\phi} \tag{1.32}$$

$$C_5^2 = \frac{2\sin^2\theta\sin^2\phi - 1}{2\sin^2\theta\sin^2\phi}. \tag{1.33}$$

We plot these orbitals for the $(12,0)$ nanotube in Fig. 1.4 (corresponding to $\theta \approx 96.486°$ and $\phi \approx 59.715°$). Here we have $C_1 = C_2 \approx 0.093$, $C_3 \approx 0.991$, $C_4 \approx 0.584$, $C_5 \approx 0.566$. Note that the sp_a^δ orbital has a strong p character.

While there is no simple way to plot δ as a function of the bonds geometry (and conse-

quently as a function of the nanotube radius R), we can have an idea of how δ varies with R by plotting the coefficient of $|s\rangle$ in the sp^δ orbitals. In Fig. 1.5a we plot C_1, C_4 and C_5 for a $(n,0)$ nanotube as a function of n.

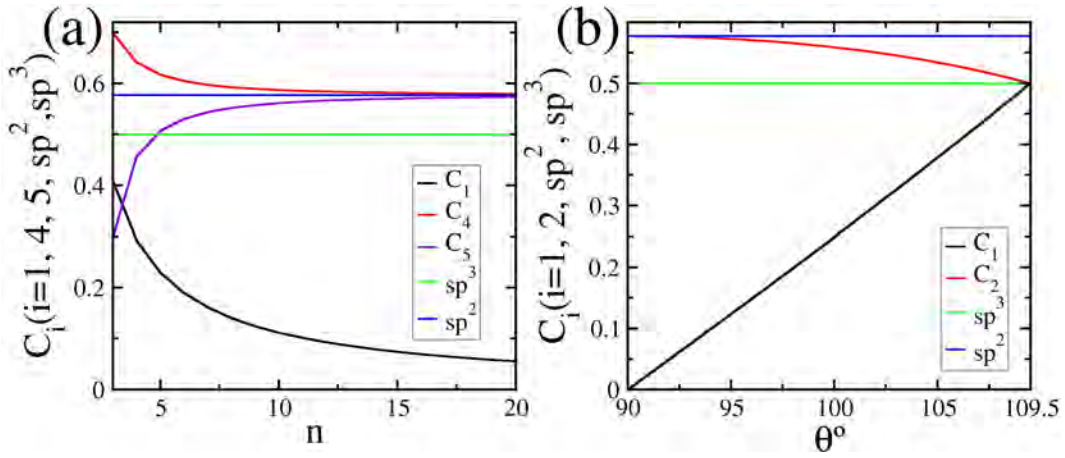

Figure 1.5: Coefficients for the s orbital in the sp^2 and sp^3 hybridization schemes and for the sp^δ case for a $(n,0)$ nanotube (a) as a function of n and for a $CHCl_3$ like molecule (b) as a function of θ.

Note that as n increases, C_1 tends to zero, while both C_4 and C_5 go to $1/\sqrt{3}$, which is the value corresponding to sp^2 hybridization. On the other hand, for small n, the hybridization clearly goes far away from sp^2, but the result also does not resemble a sp^3 scheme (with s coefficient $1/4$) since the bond angles do not go to $109°29'$.

A similar picture occurs in fullerenes (Fig. 1.6a). While carbon makes three bonds (a sp^2

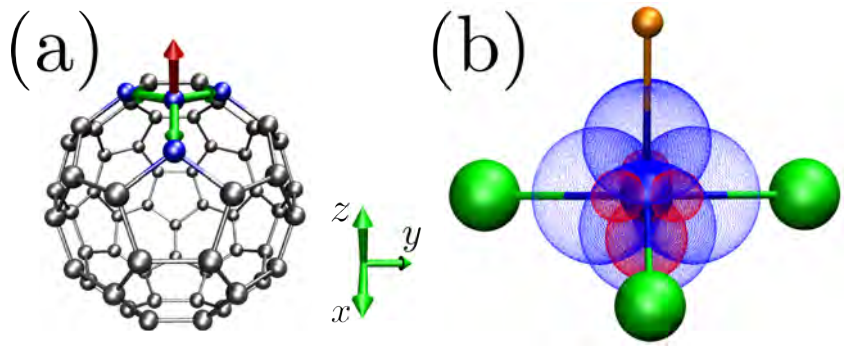

Figure 1.6: Bonds for a carbon atom in a C_{60} fullerene (a) and the sp^δ hybridization for a $CHCl_3$-like molecule (b).

characteristic), they are not contained in a single plane (sp^3 characteristic). If we choose the coordinates system such that the origin is centered on one carbon atom so that the z-axis is orthogonal to the spherical surface, we can write the unit vectors along the bonds between this

atom and its first neighbors as:

$$\mathbf{u}_1 = \sin\theta_1\mathbf{i} + \cos\theta_1\mathbf{k} \qquad \theta_1 \approx 101.4^\circ \tag{1.34}$$

$$\mathbf{u}_2 = \sin\theta_2\cos\phi_2\mathbf{i} + \sin\theta_2\sin\phi_2\mathbf{j} + \cos\theta_2\mathbf{k} \qquad \theta_2 \approx 101.8^\circ; \phi_2 \approx 124.3^\circ \tag{1.35}$$

$$\mathbf{u}_3 = \sin\theta_3\cos\phi_3\mathbf{i} + \sin\theta_3\sin\phi_3\mathbf{j} + \cos\theta_3\mathbf{k} \qquad \theta_3 \approx 101.8^\circ; \phi_3 \approx 235.7^\circ. \tag{1.36}$$

If we make the simplification $\theta_1 = \theta_2 = \theta_3 = \theta$ and $\phi_3 = 2\phi_2 = 240^\circ$ (suitable for certain molecules such as $CHCl_3$), we can use symmetry arguments to mix the orbitals by means of:

$$|sp_a^\delta\rangle = C_1|s\rangle + \sqrt{1-C_1^2}|p_z\rangle \tag{1.37}$$

$$|sp_b^\delta\rangle = C_2|s\rangle + \sqrt{1-C_2^2}\Big(\sin\theta|p_x\rangle + \cos\theta|p_z\rangle\Big) \tag{1.38}$$

$$|sp_c^\delta\rangle = C_2|s\rangle + \sqrt{1-C_2^2}\Big(-\frac{1}{2}\sin\theta|p_x\rangle + \frac{\sqrt{3}}{2}\sin\theta|p_y\rangle + \cos\theta|p_z\rangle \tag{1.39}$$

$$|sp_d^\delta\rangle = C_2|s\rangle + \sqrt{1-C_2^2}\Big(-\frac{1}{2}\sin\theta|p_x\rangle + \frac{\sqrt{3}}{2}\sin\theta|p_y\rangle + \cos\theta|p_z\rangle \tag{1.40}$$

with

$$C_1 = \frac{\sqrt{2}}{\tan\theta} \qquad C_2 = \sqrt{\frac{1-3\cos^2\theta}{3\sin^2\theta}}. \tag{1.41}$$

Note that as θ approaches $\pi/2$ or $109^\circ 29'$ we recover the sp^2 or sp^3 hybridization, respectively (Fig. 1.5b). For illustrative purposes, if we make $\theta = 102^\circ$ we have $C_1 = 0.301$ ($\sqrt{1-C_1^2} = 0.954$) and $C_2 = 0.551$ ($\sqrt{1-C_2^2} = 0.835$), so that the $|sp_a^\delta\rangle$ orbital has a stronger $|p\rangle$ character than the other $|sp_i^\delta\rangle$, $i = b,c,d$ (Fig. 1.6b).

1.2.5 What is so special about carbon?

What makes carbon so chemically versatile and able to form a large variety of different structures is a convenient combination of different factors in its electronic structure. Carbon has 6 electrons in its neutral condition. Its electronic distribution is given by $1s^2 2s^2 2p^2$, where the $1s^2$ electrons are strongly bonded to the nucleus, leaving the interaction with the external world to the four $2s^2 2p^2$ valence electrons. This allows carbon (in principle) to present any of the sp^n ($n = 1,2,3$) hybridization schemes.

In Fig. 1.7 we show how the $2s$ and $2p$ orbital energies vary as a function of the atomic number Z for the atoms in the second row of the periodic table. We observe that the $s-p$ energy splitting increases with increasing Z. Therefore we expect that, for atoms with smaller Z, the $2s$ and $2p$ can be easily combined to form hybrid orbitals suitable to induce covalent

bonds, while such hybridization states becomes less favored as Z increases due to the larger $s-p$ energy difference. As the number of different hybridization states an element can form depends on this $s-p$ splitting, it is directly related to how chemically rich the element is.

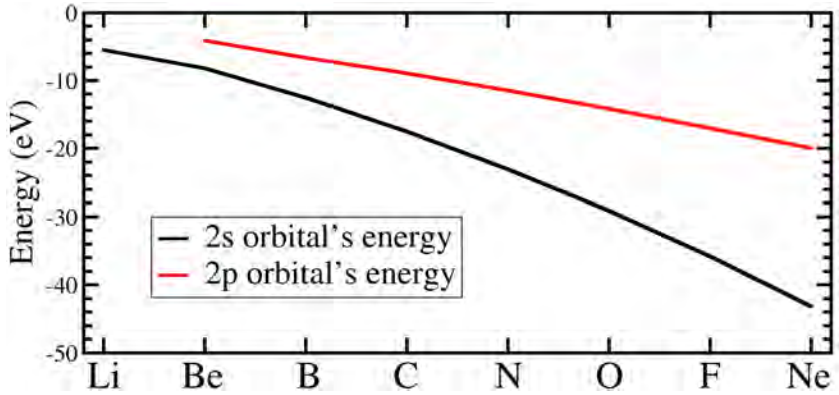

Figure 1.7: Energies for the $2s$ and $2p$ orbitals as a function of the atomic number for the atoms in the second row of the periodic table [2].

Turning to the case of boron, for example, we have a small $s-p$ splitting (lower than in carbon), which favors boron to present hybrid orbitals. However, boron's electronic distribution is given by $1s^2 2s^2 2p^1$, so that we have only three electrons eligible to form bonds and the only available hybridization states are sp and sp^2.

Now moving to nitrogen, we can see that it has 5 valence electrons ($1s^2 2s^2 2p^3$). Even though it can present sp, sp^2 or sp^3 hybridizations, it has an excessive number of valence electrons that usually end up occupying one of the hybrid orbitals, lowering the number of possible bonds to other atoms. An additional issue with nitrogen is that it has a higher $s-p$ splitting compared to boron and carbon.

While boron (nitrogen) has low (high) $s-p$ splitting and few (many) valence electrons, nature shows that carbon is intermediate between these two properties, and in the right point so as to make carbon's chemistry so rich. In other words, while carbon has $2s$ and $2p$ orbitals close in energy (allowing for multiple hybridization schemes), it has the right number of electrons so as to take advantage of it. These are some of the reasons that make carbon so special.

Another important point in the electronic structure of carbon is the absence of p electrons in the core, rendering carbon a small atomic radius. This is another important factor that allows carbon atoms to pack together in order to form linear (sp) and planar (sp^2) structures as carbon *pi*-bonds are stronger than those in elements with larger radius. Following this discussion, it is suggestive to move vertically along the periodic table in order to compare carbon with silicon (whose electronic distribution is $1s^2 2s^2 2p^6 3s^2 3p^2$) as this element has the same number of valence electrons as carbon. We observe that silicon has a larger atomic radius in comparison

with carbon and eventual *pi*-bonds are not strong enough to produce stable linear and planar geometries in silicon based structures. In other words, silicon preferably forms longer bonds, favoring sp^3 hybridization. A good illustration of this aspect is the silicon doping in carbon nanotubes, where the silicon doping produces an outward local structural distortion along the radial direction [20].

In the following sections we discuss the most important carbon nanostructures and some of their related structures.

1.3 Carbon nanotubes

The post 80's discovery of carbon nanotubes was a natural consequence of both intense research on developing highly crystaline carbon fibers [18] and the discovery of fullerenes [10]. Even though discussions over possible carbon tubular forms took place in the early 90's [12], the true starting point of carbon nanotubes' science is usually considered to be the work of Iijima in 1991 where the observation and resolved structure of multi-wall carbon nanotubes (MWNTs) was reported [13]. It did not take long for Iijima and Bethune to observe simultaneously (the two papers are printed back–to–back in the same issue of *Nature*) the existence of single-walled carbon nanotubes (SWNTs) [14, 15]. Nanotubes excited the scientific community due to a series of new interesting properties like their singular geometry–electronic structure–optical spectra relation, high mechanical resistance, chemical selectivity to chemical and physical adsorption of molecules on its surface, among others. This section is dedicated to describe some basic properties of this interesting structure.

1.3.1 Nanotube's structure

Even though graphene is the subject of another section, we dedicate a few words to it before talking about carbon nanotubes because they are closely related to each other. Graphene is a 2D system composed by carbon atoms organized in hexagons, as a honeycomb, where the atoms present a perfect sp^2 hybridization, leaving a p_z (or π) orbital free to form itinerant π bonds (see Section 2.7). Its structure is a hexagonal 2D Bravais lattice (primitive vectors $\mathbf{a}_1$ and $\mathbf{a}_2$) with a 2 atom basis whose structure is depicted in Fig. 1.8a.

The nanotube structure can be viewed as a graphene sheet rolled up into a tube as depicted in Fig. 1.8b. There are several different ways to roll the sheet to form the tube. This is uniquely determined by the chiral vector $\mathbf{C}_h$ which is a linear combination of graphene's lattice vectors.

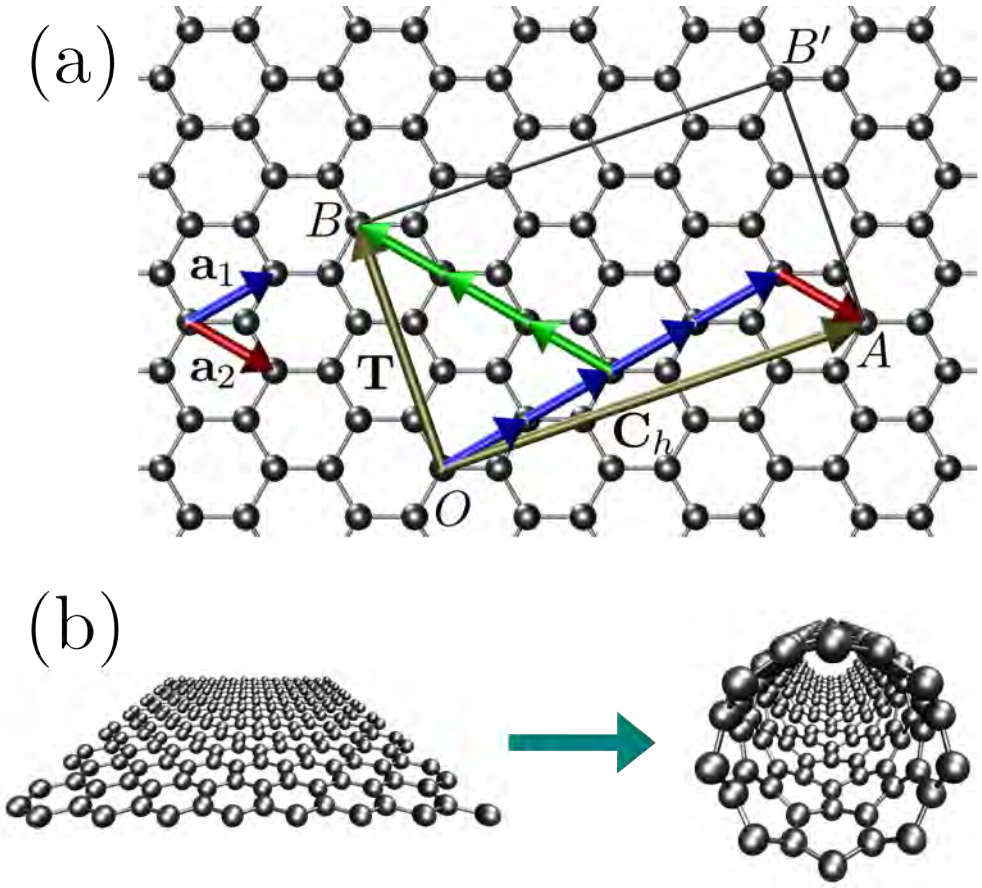

Figure 1.8: (a) Graphene honeycomb lattice and the vectors defining a nanotube unit cell; (b) A graphene sheet piece being rolled up to form a nanotube.

The smallest vector which is orthogonal to $\mathbf{C}_h$ and that joins two carbon atoms is called the translational vector $\mathbf{T}$. These vectors are given by:

$$\mathbf{C}_h = n\mathbf{a}_1 + m\mathbf{a}_2 \equiv (n,m) \tag{1.42}$$

$$\mathbf{T} = t_1\mathbf{a}_1 + t_2\mathbf{a}_2 = \frac{n+2m}{d_r}\mathbf{a}_1 - \frac{2n+m}{d_r}\mathbf{a}_2 \tag{1.43}$$

where n and m are integers and d_r is the greatest common divisor (gcd) of $2n+m$ and $n+2m$. In Fig. 1.8a we show these vectors for the case of a $(4,1)$ nanotube. If we extract the rectangle defined by $\mathbf{C}_h$ and $\mathbf{T}$ and roll it up (by joining O to A and B to B') we will have the nanotube's unit cell.

Not only the translational vector, but the whole nanotube's geometry is determined by the (n,m) pair. In fact, the nanotube radius R is simply determined by:

$$R = |\mathbf{C}_h|/2\pi = a\sqrt{n^2+nm+m^2} \tag{1.44}$$

where $a = |\mathbf{a}_1| = |\mathbf{a}_2| = a_{CC}\sqrt{3}$ and a_{CC} is the carbon-carbon distance. The number N of

hexagons within a nanotube unit cell (and consequently, half the number of atoms) is obtained by dividing the area of the rectangle defined by $\mathbf{C}_h$ and $\mathbf{T}$ by the area of an hexagon ($\mathbf{a}_1 \cdot \mathbf{a}_2$) [18]:

$$N = \frac{\mathbf{C}_h \cdot \mathbf{T}}{\mathbf{a}_1 \cdot \mathbf{a}_2} = \frac{2(n^2 + nm + m^2)}{d_r}. \tag{1.45}$$

Finally, the chirality θ (defined as the angle between $\mathbf{a}_1$ and $\mathbf{C}_h$) is given by:

$$\theta = \arccos\left(\frac{\mathbf{C}_h \cdot \mathbf{a}_1}{|\mathbf{C}_h||\mathbf{a}_1|}\right) = \arccos\left(\frac{2n+m}{2\sqrt{n^2+nm+m^2}}\right). \tag{1.46}$$

Due to the C_6 symmetry of the graphene sheet, we should restrict θ to the $[0, \pi/6]$ range, or equivalently m to $[0, n]$.

Two types of nanotubes are special due to their particular symmetry. Nanotubes $(n,0)$ and (n,n) are usually called zigzag and armchair nanotubes, respectively, due to the particular arrangement of their atoms along a section perpendicular to their axis (as shown for the $(n,0)$ and (n,n) in Fig. 1.9a-b). All the other nanotubes are collectively called chiral nanotubes (as the $(8,2)$ case in Fig. 1.9c).

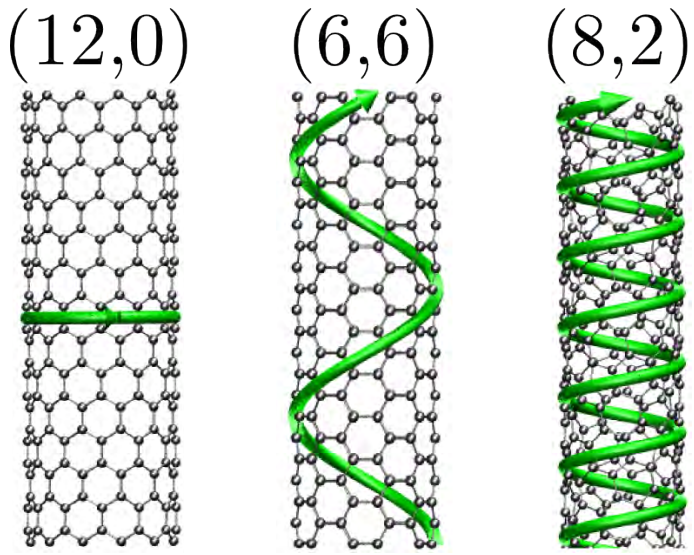

Figure 1.9: Examples of zigzag, armchair and chiral nanotubes.

1.3.2 Electronic structure

When rolling up the graphene sheet to form the nanotube, carbon's orbitals undergo a re-hybridization so as to form sp^δ states. As discussed earlier, this mixing scheme is very close to sp^2 for nanotubes with a large radius. For this reason, when the nanotube's radius is large, its electronic structure can be understood by means of a simple model based on graphene's electronic structure. We will show (see Section 2.7) that, within a tight-biding model, the graphene

energy levels for π electrons are given by

$$E(\mathbf{k}) = \frac{\varepsilon \pm \gamma |f(\mathbf{k})|}{1 \pm s|f(\mathbf{k})|} \tag{1.47}$$

with

$$f(\mathbf{k}) = 1 + e^{-i\mathbf{k}\cdot\mathbf{a}_1} + e^{-i\mathbf{k}\cdot\mathbf{a}_2}, \qquad \varepsilon = \langle \psi_A^i | \hat{H} | \psi_A^i \rangle, \qquad \gamma = \langle \psi_A^i | \hat{H} | \psi_B^j \rangle, \qquad s = \langle \psi_A^i | \psi_B^j \rangle \tag{1.48}$$

where $\mathbf{k}$ is a vector in the graphene's first Brillouin zone (BZ), ψ_A^i is the basis function corresponding to the A-atom labeled by i, ψ_B^j is the basis function corresponding to the B-atom labeled by j which is a neighbor of i, ε is the on site energy, γ is the first-neighbor hopping integral (between i and any of its neighbors j) and s the first-neighbor overlap integral. For an infinite sheet, the *2D*-$\mathbf{k}$ vector varies continuously along the reciprocal space (whose primitive vectors are $\mathbf{b}_1$ and $\mathbf{b}_2$ so that $\mathbf{b}_i \cdot \mathbf{a}_j = 2\pi\delta_{ij}$). We can write the reciprocal lattice vectors $\mathbf{K}_1$ and $\mathbf{K}_2$ along the chiral and translational vectors, respectively, as:

$$\mathbf{K}_1 = \frac{1}{N}(-t_2\mathbf{b}_1 + t_1\mathbf{b}_2) \tag{1.49}$$

$$\mathbf{K}_2 = \frac{1}{N}(m\mathbf{b}_1 - n\mathbf{b}_2) \tag{1.50}$$

and the vector $\mathbf{k}$ is written as:

$$\mathbf{k} = k_c \frac{\mathbf{K}_1}{|\mathbf{K}_1|} + k_a \frac{\mathbf{K}_2}{|\mathbf{K}_2|}, \tag{1.51}$$

where k_c and k_a are the vector components along the circumferential and axial directions of the BZ, respectively. As the electronic density is confined along the nanotube circumference, the electron's wavelength λ_q is restricted to:

$$\lambda_q = |\mathbf{C}_h|/q, \quad q = 0,1,2,3,...,N-1, \tag{1.52}$$

so that the vector $\mathbf{k}$ is quantized along the nanotube's circumference according to:

$$k_c = 2\pi/\lambda = 2\pi q/|\mathbf{C}_h| \tag{1.53}$$

resulting in

$$\mathbf{k} = q\mathbf{K}_1 + k_a \frac{\mathbf{K}_2}{|\mathbf{K}_2|} \tag{1.54}$$

with k_a varying continuously along $]-\pi/|\mathbf{T}|, \pi/|\mathbf{T}|]$ for an infinite tube. In summary, the boundary conditions imposed by the electronic confinement along the nanotube's circumferential direction determine lines of allowed k vectors, given by Eq. 1.54, over graphene's BZ (as illustrated in Fig. 1.10).

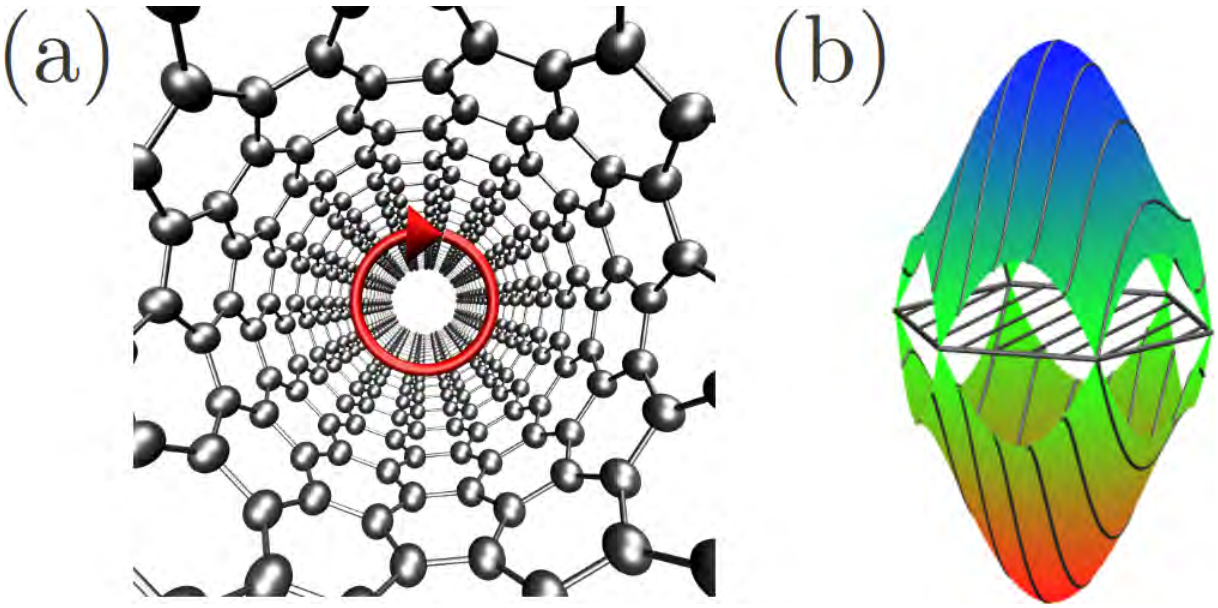

Figure 1.10: Illustration of the quantum confinement along the circumferential direction in a carbon nanotube and the corresponding cutting lines over graphene's Brillouin zone.

Since the $\mathbf{C}_h$–$\mathbf{T}$ unit cell is larger than the $\mathbf{a}_1$–$\mathbf{a}_2$ cell, the $\mathbf{K}_1$–$\mathbf{K}_2$ cell is smaller than the $\mathbf{b}_1$–$\mathbf{b}_2$ cell. In fact, the present approach is equivalent to taking graphene's electronic structure over its BZ and fold it into the smaller nanotube BZ, obtaining the nanotube's electronic band structure by the cutting lines where the zone is folded. For this reason, this model is usually referred to as zone-folding. The quantization of the reciprocal vector along the circumferential direction determines the cutting lines over graphene's BZ so that a nanotube is metallic when a cutting line crosses a K point (reciprocal space point where the graphene's valence and conduction bands touch each other). One can show that this condition is satisfied when we have:

$$n - m = 3i, \quad \text{where } i \text{ is an integer.} \tag{1.55}$$

Furthermore we can differentiate two kinds of metallic nanotubes. If $d = gcd(n,m)$, then:

- Metal 1 (M1): when $n-m$ is a multiple of 3, but not of $3d$;
- Metal 2 (M2): when $n-m$ is a multiple of $3d$.

These cutting lines are shown in Fig. 1.11 for the nanotubes $(12,0)$, $(6,6)$, $(8,2)$ and $(10,0)$. Note that a K point is cut for the first three, while no vertice is cut in the semiconducting $(10,0)$ case.

For the first group, the bands cross the Fermi energy at the Γ point ($k_a = 0$) as in the case of the nanotube $(12,0)$ (Fig. 1.12a). On the other hand, the second group has such crossing at

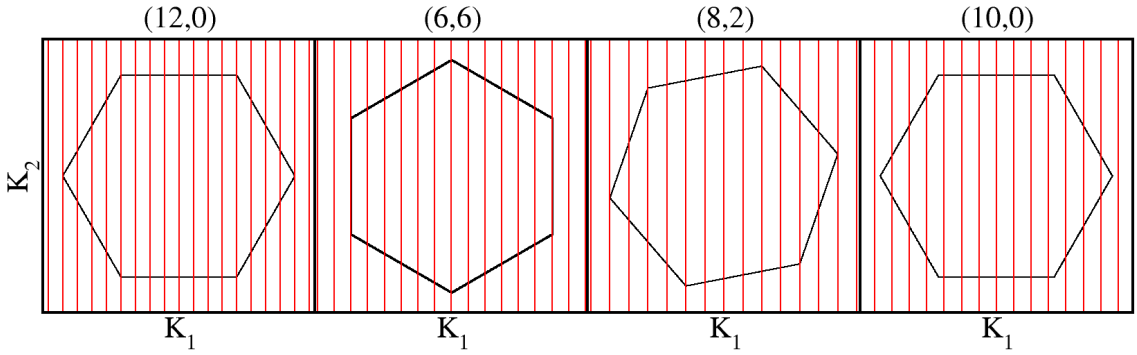

Figure 1.11: Cutting lines over graphene's Brillouin zone for the nanotubes $(12,0)$, $(6,6)$, $(8,2)$ and $(10,0)$.

$k_a = 2\pi/3T$, like in the $(6,6)$ and $(8,2)$ nanotubes (Fig. 1.12b-c). In Fig. 1.12d we show the electronic bands for the nanotube $(10,0)$ as an example of a semiconducting tube.

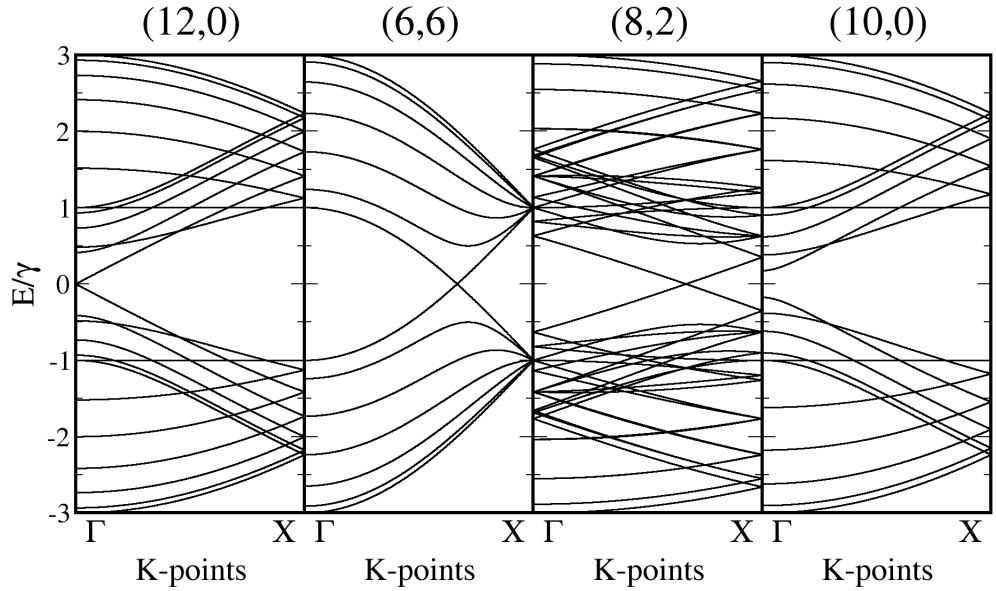

Figure 1.12: Electronic band structure for the $(12,0)$ (a), $(6,6)$ (b), $(8,2)$ (c) and $(10,0)$ (d) nanotubes obtained with the zone-folding-tight-binding method. Here we used $\varepsilon = s = 0$. The Fermi level is at 0 eV.

It should be noticed, however, that for nanotubes with a large curvature (small radii), their hybridization deviates significantly from sp^2 (as explained in Section 1.2.4) and this simple model does not give good results. As an example the $(5,0)$ nanotube (which should be semiconducting within the zone-folding picture) is metallic according to first-principles calculations [21].

1.4 Graphene and graphitic ribbons

Even though graphite is an abundant and well-known material, the isolation and measurements of individual graphene sheets was only accomplished in 2004 [16]. This result marked the starting point of a boom in the scientific publications based on both experimental and theoretical investigation of this structure, making graphene a pop star in materials science. As stated in the last section, graphene's structure is composed of a bidimensional arrangement of hexagons formed by the carbon atoms.

Graphene's electronic structure can be satisfactorily described within the tight-binding model (see Section 2.7). If we set $E_F = s = 0$ we can write:

$$E(\mathbf{k}) = \pm\gamma\sqrt{3 + 2\cos\mathbf{k}\cdot\mathbf{a}_1 + 2\cos\mathbf{k}\cdot\mathbf{a}_2 + 2\cos\mathbf{k}\cdot(\mathbf{a}_1 - \mathbf{a}_2)}. \tag{1.56}$$

In Fig. 1.13 we plot this relation over the graphene's hexagonal BZ by different methods.

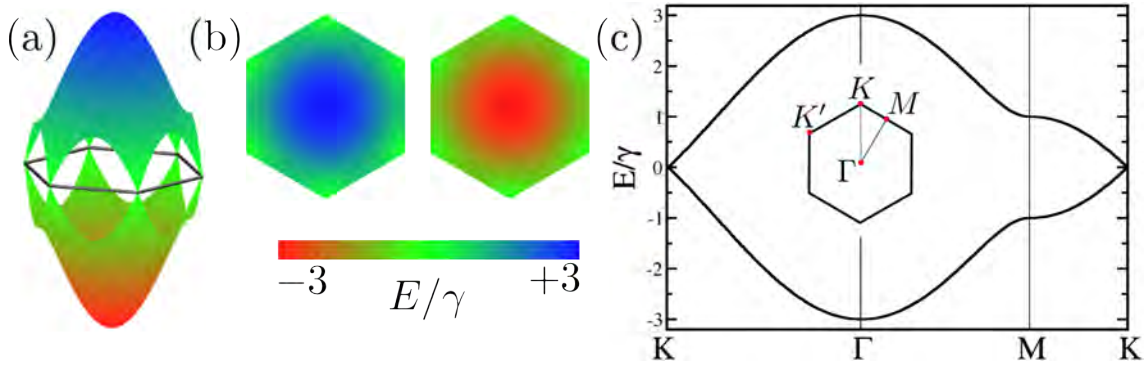

Figure 1.13: Electronic band structure for the graphene over the Brillouin zone in a 3D (a) and 2D (b) representations and along the high symmetry lines (c). The Fermi level is at $E = 0$.

A special characteristic of the $E - \mathbf{k}$ relation is its conic form near the K and K' points (vertices of the BZ where the valence and conduction bands meet). Due to this local linear relation for low-energy levels, the electrons behave as massless Dirac fermions and we have the onset of Klein tunneling (where an electron can enter a potential barrier with unity transmission probability) [22]. This effect was predicted by theory for a graphene $p-n$ junction [23] and further confirmed by experiments [24].

1.4.1 Graphene nanoribbons

Graphene is regarded as a potential candidate to replace silicon technology as silicon approaches its miniaturization limit [25]. Among the reasons for such prediction is graphene's high electronic mobility and low contact resistance [26, 27]. Even though graphene itself has a

rich physics, it can be further modified both chemically or physically in order to tune its properties further [28]. While ideal infinite graphene is not a semiconducting system, the presence of an energy gap is fundamental for some applications in nanoelectronics. To this end, it is possible to modify graphene's structure in order to create an opening of the energy bands around the Fermi energy. One widely studied approach is to induce quantum confinement along one in-plane direction, thus creating structures called graphene nanoribbons (GNRs). It is known that these ribbons present electronic properties strongly dependent on their width and edge structure. For the most symmetric cases of armchair (n-A-GNR, Fig. 1.14a) and zigzag (n-Z-GNR, Fig. 1.14b) edged ribbons, their width is trivially obtained from the number n of $C-C$ dimer lines or zigzag strips, respectively.

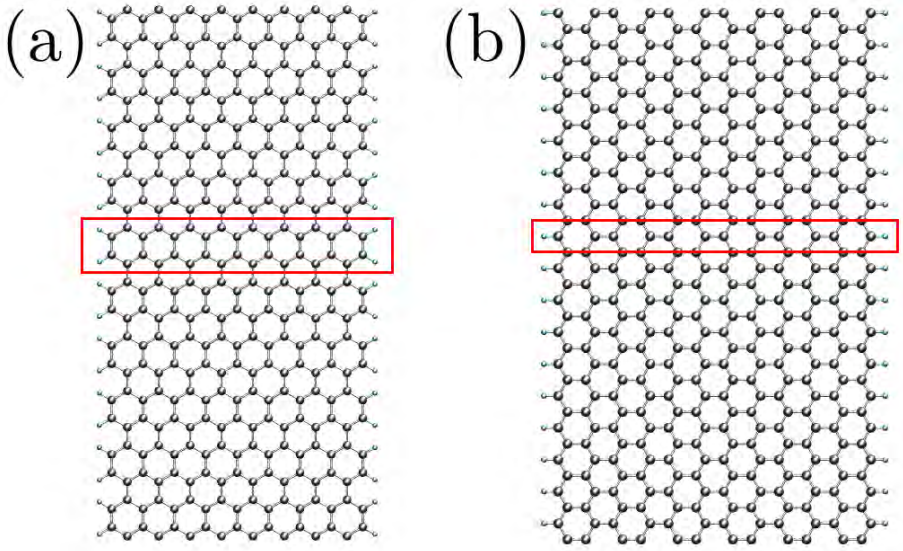

Figure 1.14: Basic structures for A-GNRs (a) and Z-GNRs (b). The red boxes indicate the GNRs unit cells.

A-GNRs present a semiconductor character with band gap Δ_n strongly dependent on the number n of $C-C$ lines along its width. While the gap of an n-A-GNR with $n \to \infty$ tends to zero (so as to recover the graphene result), the Δ_n *versus* n curve has three different branches so that $\Delta_{3i+1} \geq \Delta_{3i} \geq \Delta_{3i+2}$ [29]. In Fig. 1.15 we show the calculated band gaps for varying A-GNR width as a function of n using the method described in Chapter 2.

The other Z-GNRs present a richer set of properties. While spin polarization is absent in A-GNRs, Z-GNRs possess ferromagnetically polarized edges with two possibilities for the edge-to-edge polarization. These two possibilities correspond to parallel (FM) and anti-parallel (AFM) alignments, where the latter one is the ground state. The spin polarization for these two states together with the non-polarized paramagnetic (PM) case are illustrated in Fig. 1.16 with their corresponding band structures calculated using the TBU method described in Chapter 2.

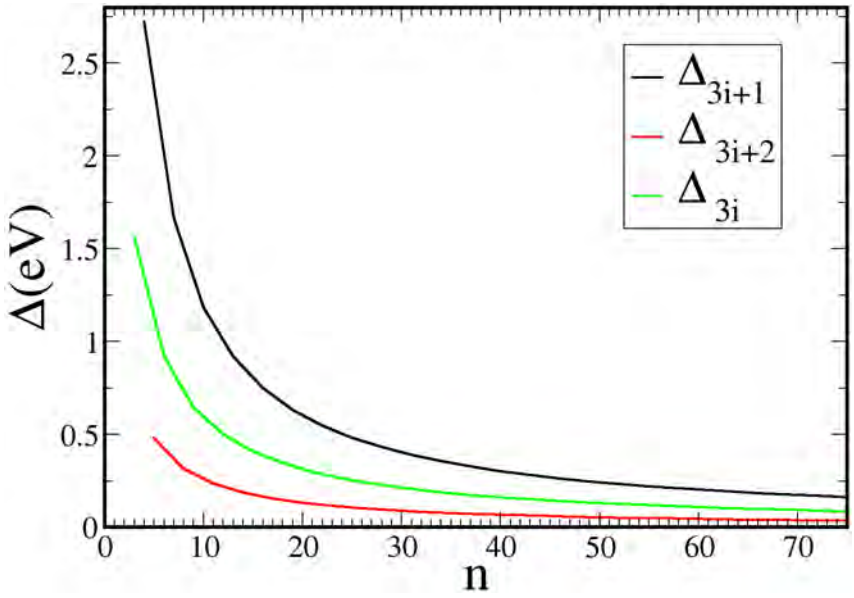

Figure 1.15: Electronic band gap Δ for an A-GNR as a function of the number n of $C-C$ lines. The three families correspond to $n = 3i + j$ with $j = 0, 1, 2$.

One observes that the PM state has two 2-fold degenerated bands around the Fermi energy which meet and become a flat 4-fold degenerated band which extends along one third of the BZ and whose energy value approaches $E_F = 0$ as the ribbon width increases [30]. These states are strongly localized along the edges (therefore the 4-fold degeneracy: 2 due to the spin and 2 due to the two symmetric edges), producing a high concentration of low energy electrons as a consequence [31]. Such edge states are predicted to be responsible for a paramagnetic behavior of Z-GNRs at low temperatures [32] (while a diamagnetic behavior is expected for high-temperature regimes). This high density indeed produces a instability (paramagnetic instability) which gives rise to the two lower energy magnetic states. One observes that the spin up and down polarizations along the opposite edges are located on different graphene-sub-lattices for the AFM case which turns to be the ground state [31]. In the FM case, edge atoms belonging to both sub-lattices present the same spin orientation and this ends up raising slightly the FM energy in comparison with the previous case. While AFM is lower in energy, a remarkably interesting fact about these AFM and FM states is the small energy difference between them. In the upper panel of Fig. 1.17 we show the band-energy difference (calculated with the method described in Chapter 2) between the AFM and FM states for one Z-GNR cell as a function of n. We can see that this difference tends to zero as the ribbon's width increases, reflecting a lowering in the edge-to-edge interaction as they are farther away from each other. A possible switching property due to this low energy difference is an interesting aspect that motivates the proposal of a Z-GNR based magnetic sensor [33]. These states are considerably more stable than the PM states [31]. As shown in the lower panel Fig. 1.17, this paramagnetic instability

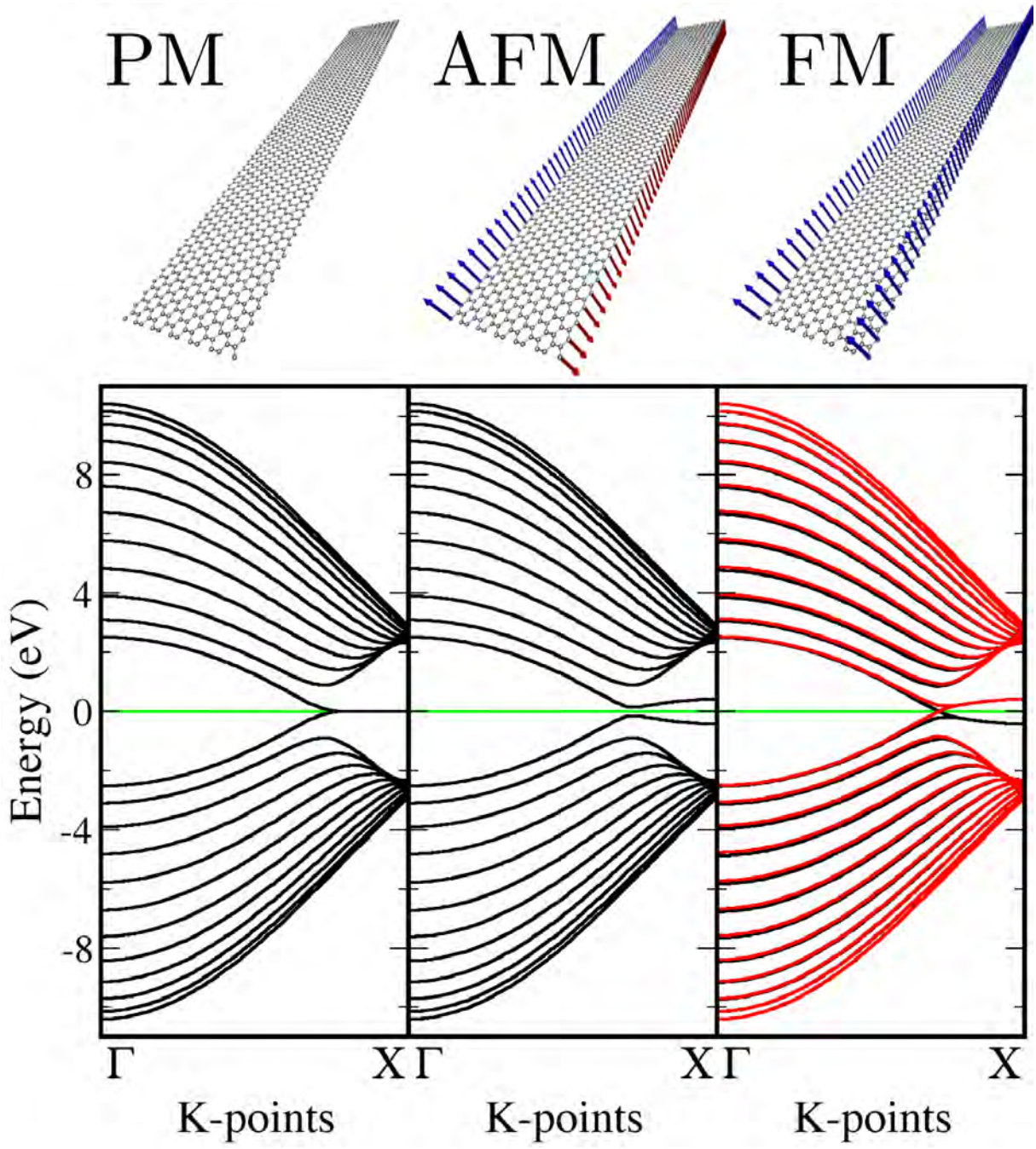

Figure 1.16: Paramagnetic (PM), anti-ferromagnetic (AFM) and ferromagnetic (FM) states in a Z-GNR and their corresponding band structures (green line is the Fermi energy, and black and red lines stand for spin up and down levels).

approach its upper limit as we increase the ribbon's width.

These magnetic properties open up a series of possibilities for the use of finite pieces of graphene in nanoelectronics and spintronics. In fact, it has been shown that Z-GNRs present a half-metallicity behavior (where the electronic structure has a metallic character for spin up levels and is semiconducting for spin down levels, or vice-versa) which can be tuned by means of a gate voltage [34]. Other proposals exploit the interplay between armchair and zigzag edges

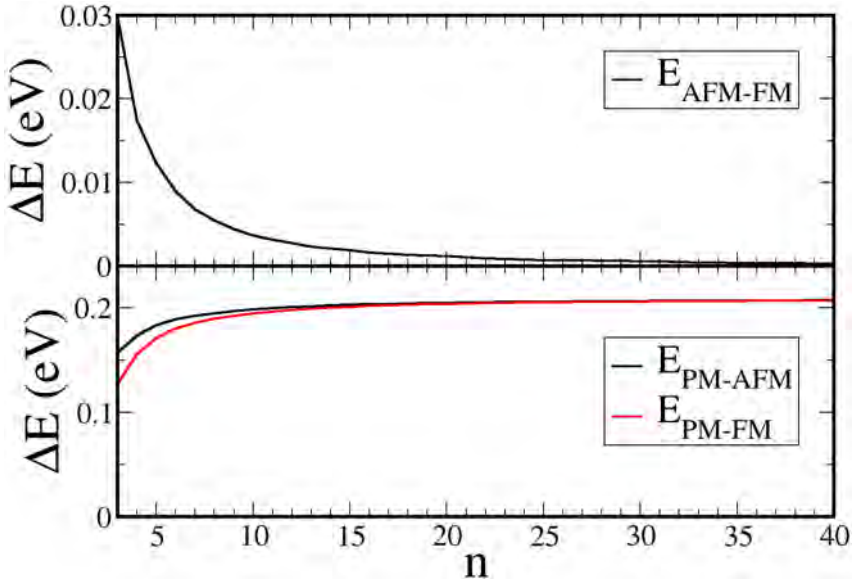

Figure 1.17: Energy difference between any pair of different states in a Z-GNR with $n = 3, ..., 40$.

in more complex ribbon geometries to show spin-filter devices and geometry-dependent controlling approaches for the localization of magnetic edge-states [35, 36, 37, 38, 39]. Extended lines of defects (ELDs - see Fig. 1.18) and grain boundaries (GBs) are natural extended defects in some synthesized graphene samples that can assume a highly crystalline organization. These structures do not necessarily represent a problem on the goal for producing high crystalline structures, but instead open a set of new possibilities to modify and tune graphene's properties to suit new applications [3, 40, 41, 42, 43, 44].

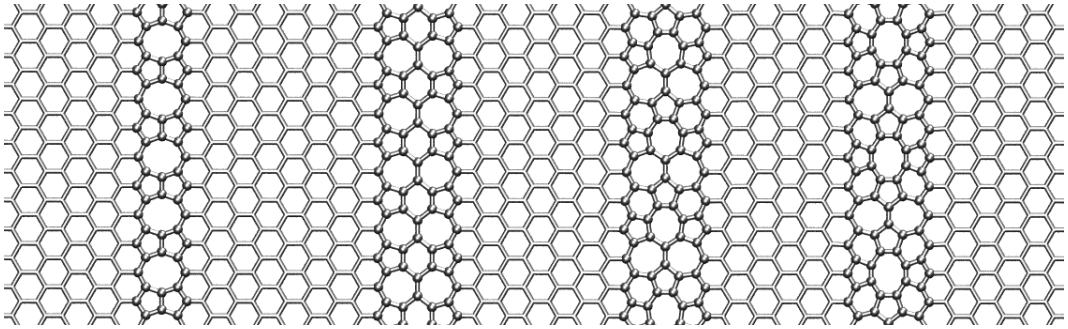

Figure 1.18: Different proposed ELD geometries in graphene [3].

1.4.2 Graphene nanoribbons synthesis

While graphene's isolation is a recent experimental achievement, the knowledge about the synthesis of narrow nanoribbons has been significantly developed. Different approaches have been proposed to obtain GNRs. Among them we can cite CVD [45], etching of 2D graphene [46, 47, 48] and carbon nanotubes unzipping [49, 50]. It has been shown that the

intriguing electronic and magnetic properties of GNRs are strongly related to clean edges, so that from some points of view, edge defects can suppress some GNR-applications [51]. In some synthesis approaches, the controlled formation of clean edges can be difficult and this issue is among the central challenges on the experimental research on GNRs. In this quest for a high quality synthesis approach, Cai and co-workers have recently proposed a truly bottom-up approach to obtain narrow and crystalline ribbons [4]. In this procedure they heated a gas of halogenated polyaromatic molecules over a metallic template. During this surface assisted process, the molecules lose their halogens and start to create a polyaromatic polymer which goes further through a de-hydrogenation process which results in perfect small-width ribbons (as illustrated in Fig. 1.19a). An exciting point in this study is the control we can have over the final product by using different polyaromatic precursors (Fig. 1.19b-c). In fact, other complex wiggle-like (Fig. 1.19c) ribbons and symmetric junctions have been obtained with different initial aromatic molecules [4]. This is a remarkable result which enables us to put theory and experiment side-by-side so as to employ, develop, test and improve new theoretical methodologies. This is a fundamental problem in science since calculations are a powerful and indispensable tool to produce knowledge on nanoscience and nanotechnology. They can act not only as a predicting tool, but also as an auxiliary for interpreting experimental outcomes (and consequently consolidating conclusions) and as a road map guide for the conduction of experiments.

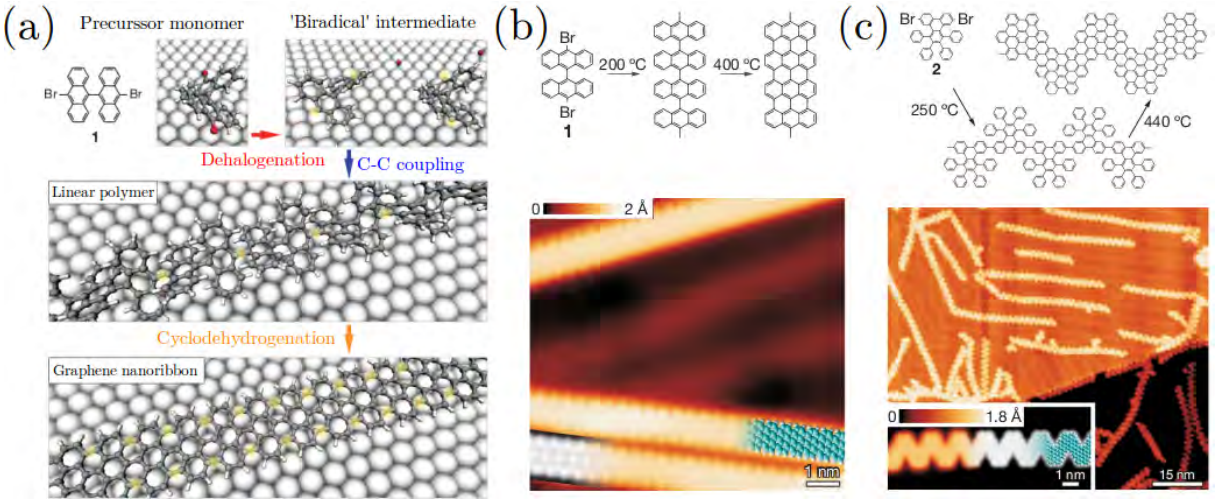

Figure 1.19: (a) Illustration of the bottom-up approach developed by Cai et al. to obtain graphene nanoribbons with clean armchair edges. (b-c) Different molecular precursors for the procedure illustrated in (a) and their corresponding final products. Adapted from [4].

This experimental work of Cai et al. on the synthesis of perfect and complex graphitic ribbons motivated us to study the electronic structure and transport properties of these wiggle-like structures. In fact, this particular system constitutes one of the main focus of this thesis. In Chapter 7 we present a detailed description of their geometry, while the results on the electronic

structure and transport are presented and discussed in Chapters 8 [9] and 9, respectively.

1.5 Combining pieces

The rich family of carbon nanostructures in not limited to fullerenes, carbon nanotubes, graphene and GNRs. These structures can be further combined and/or modified to give rise to a huge set of systems. Carbon nanotubes are ideal candidates as basic building blocks for a bottom-up design of a number of nanostructures and novel devices. For instance, complex 1D, 2D, and 3D networks based on carbon nanotubes have been proposed in recent years. Properties such as their porosity renders them good candidates for potential applications as catalysts, sensors, filters and molecular storage materials. These complex structures are also prototype models for complex circuits in nanoscale. The study of their geometrical, mechanical, chemical, and transport properties has been the topic of intense theoretical and numerical researches [52, 53, 54, 55, 56]. Even though highly ordered covalent structures have not been synthesized yet, current advances in materials synthesis and processing clearly point to the possibility of assembling individual nanotubes covalently into functional structures [54, 57, 58].

Graphene and GNRs have also been assembled in several new structures. Graphene antidot lattices have been demonstrated to allow a controlled manipulation of graphene's electronic properties [59] and the experimentally obtained perfect lines of defects in graphene is predicted theoretically to posses interesting electronic and transport properties [3]. Junctions composed of A- and Z-GNRs [60] and 1D GNR-superlattices [38, 39] are also new structures suitable to be embedded in new electronic nanodevices.

Defects play an important role in the science of sp^2 carbon materials by offering an additional degree of freedom to tune their properties. Vacancies are a common defect that changes locally the structure properties [61], enhancing the system's reactivity and opening a set of new possibilities for the physics and chemistry of these structures [62, 63, 64]. Other pentagon-heptagon defects (produced by a 90° rotation of a $C-C$ bond in the hexagonal lattice) bring a set of interesting properties in carbon nanosystems. The strategic distribution of these Stone-Wales defects on a supergraphene lattice, for example, allows for a controlled conduction path for the electrons [55]. An even more radical example of the impact of defects in carbon nanostructures are the haeckelite lattices (Fig. 1.20). In these systems we have an extended distribution of Stone-Wales defects over the graphene sheet so that the final result does not resemble at all the perfect graphene honeycomb structure in both geometry and electronic properties [5]. Even with no experimental realization, these structures present a set of new properties that can

be further expanded since those haeckelite planar structures may have counterpart versions for nanotubes [5] and ribbons, what is a sufficient reason to motivate future experimental studies aiming their synthesis.

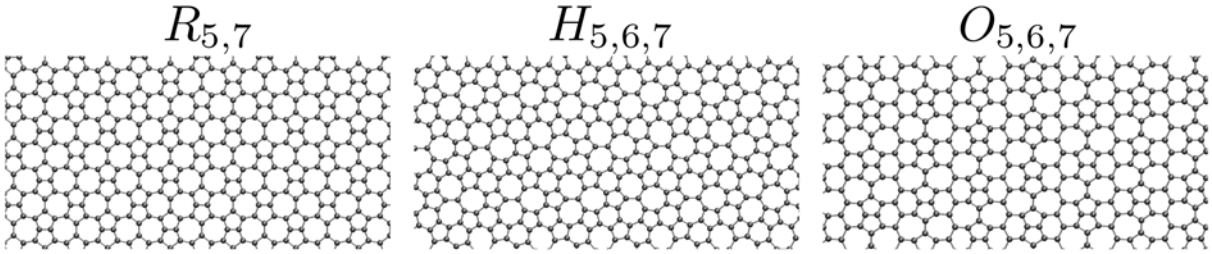

Figure 1.20: $R_{5,7}$, $H_{5,6,7}$ and $O_{5,6,7}$ planar haeckelites structures [5].

A number of other complex structures based on nanotubes as elementary building blocks have already been observed. For example, carbon nanotubes can be seen as the basic components of helically coiled and cage-like structures such as nanotoroids [65]. For small radii of curvature, these structures require the presence of pentagons and heptagons in the otherwise hexagonal lattice in order to accommodate sharp variations in surface curvature [66]. In contrast, smoothly curved tori can be obtained from the purely elastic bending of a long straight nanotube into a ring [67]. These structures present a series of interesting electronic, magnetic and mechanical properties and have been the subject of a number of theoretical and experimental studies in the literature [7, 8, 66, 67, 68, 69, 70, 71, 72, 73, 74, 75, 76, 77]. Another focus of this thesis is the study of the electronic and transport properties of these carbon nanotube rings seamlessly attached to a number of terminals. In Chapter 5 we present the results published in reference [7] where we study toroidal systems with two terminals. In Chapter 6 we extend the study for a multi-terminal system as well as we consider a ring structure made of GNRs instead of nanotubes (results published in reference [8]).

1.6 Engineering carbon nanostructures: experimental advances and practical aspects

At the same time that theoretical studies provide deep understanding on the new science of carbon nanostructures, the experimental realization of a number of devices at the nanoscale brings the potential applications of these systems into the real world [78, 79]. However, these accomplishments need to carry an additional characteristic to become technology: their reproduction needs to be practical. In order to be technologically applicable, one has to be able to pack billions of such devices together into a centimeter wide chip wafer. This demands a high level of control on the synthesis and manipulation of nanostructures and constitutes one of the

main challenges on the science of carbon.

Let us take the example of graphene and related structures. Technological applications demand graphene pieces with well defined size and edge structure [80]. In addition, one has to have enough control over these structures to stitch them together in specific and highly ordered conformations. To this end, a series of top-down and bottom-up approaches have been developed [26]. The former route is mainly concentrated on etching pre-synthesized graphene and lithography methods. Different strategies on graphene cutting have demonstrated successive improvement on graphene patterning. Chemical etching using a gas mixture of ammonia and oxygen has been shown a 1 nm per minute control in graphene cutting, resulting in 5 nm wide nanoribbons [46]. On the other hand, H_2 plasma-etching allows cutting the honeycomb lattice in a atom-by-atom basis, resulting in a ≈ 2.7 Å per minute control and ≈ 8 nm wide ribbons [47, 48]. However, randomnesses due to topological irregularities in graphene prevent exact reproducibility in the crafting process [26, 47].

The other bottom-up approaches are based on assembling complex structures by fusing small molecular building blocks. They have been successful as reported in the late literature. The general strategy is to heat a gaseous solution of molecular precursors over a given surface. These approaches take advantage of surface assisted reactions which reduce the degrees of freedom of the molecular building blocks and can result in narrow highly crystalline systems. During the conduction of this engineering process, a number of aspects have to be carefully taken into account as they can prevent the success of the synthesis protocol or act as convenient tools to obtain the desired product. The interplay between diffusion energies and surface coupling is one of these aspects [26, 81]. As one intends to grow a large crystalline structure, high diffusion barriers (related to a strong adsorption over the assistant surface) prevent the molecular building blocks to group over a large extent, so that a weak precursors-substrate coupling is needed [82]. On the other hand, if the desired product is a small structure, a high adsorption to the surface is necessary to avoid the formation of extended systems [83]. Another important ingredient in this engineering process is the choice of the precursors used in the synthesis procedure. We have a number of examples in the literature that make clear the importance of this choice. A non-planar geometry for the precursors, for instance, can be used to reduce the molecule-surface coupling, allowing the growth of extended structures [84]. On the other hand, the type of monomers ends up being determinant in the final product geometry. In the experiment conducted by Cai and co-workers [4], for instance, the simple choice of a 10,10'-dibromo-9,9'-bianthryl molecule as the precursor leads to a straight crystalline carbon nanoribbon with an armchair edge geometry. However, if a 6,11-dibromo-1,2,3,4-tetraphenyltriphenylene molecule is chosen, the final result is a more complex chevron-like ribbon [4]. In summary, while conducting these bottom-up

synthesis approaches, all the factors discussed above can be used as programming tools to tune the experiment to give the desired product.

As can be seen, both top-down and bottom-up synthesis techniques on carbon nanostructures have been developed at a fast pace. In the latter case, an intense experimental and theoretical effort is needed to develop a wide and precise library for the synthesis and properties of these nanosystems. Such library is fundamental to pave the way to the practical applications of these new materials. Furthermore, additional challenges remain for turning knowledge in technology such as control on transferring and assembling of these structures into nanocircuits after their synthesis. So, as the current scenario is better for synthesis, manipulating nanostructures constitutes the main barrier to further developing of carbon-based technology.

1.7 Economic and societal considerations

An obvious question that comes from people outside the research field is:

"What is the impact of these things in the world outside the lab?"

Or in other words (more suitable in some cases):

"What about money?"

As discussed earlier in this chapter, fullerenes, nanotubes and graphene have induced a lot of scientific excitement regarding their technological potentialities on the occasion of their discoveries. However, fullerenes and nanotubes were discovered 26 and 20 years ago, respectively. Even though their existence is becoming known by more and more layman people, their direct impact on everyday life is still behind the possibilities pointed out early on. While carbon nanotubes fare better than fullerenes, their applications were most successful in their use in composite materials for planes and cars. Other applications like nanotube-based conducting films for energy storage and touch screens are closer to the market. Despite the remarkable advances already shown at the experimental level for nanotubes (like the realization of a transistor made of a single nanotube [1]), their high cost and hard control are still obstacles to their use at an industrial level. Graphene has some advantages in comparison to carbon nanotubes regarding their control. While carbon nanotubes' excessive variety is still a big problem in their synthesis, graphene sheets variety is usually less uncontrollable and their sheets easier to handle. On the other hand, nanotubes have advantages like the fact that they can form very long structures (allowing applications as substitutes for copper wires, for example). It is clear that graphene science tends to develop faster that nanotube's science since graphene can take

advantage of years in studies on carbon nanotubes due to a more mature scientific community.

In addition, there is a natural latency between the discovery of a new material and its industrialization. Carbon fibers are a clear example of that since they started to be studied in the 50's, their first military applications occurred in the 60's and their commercial advent happened on the 70's. It is therefore natural to see a new material to take 20 or more years to be turned into technology. This is why a lot of respected scientists believe that carbon nanostructures will in the future give many times back the money invested in their investigation [1]

1.8 This thesis

In this thesis we present theoretical investigations of the electronic structure and transport properties of toroidal carbon nanostructures and complex assembled carbon nanoribbons.

In the next chapter we describe the tight-binding+Hubbard model we employed to calculate the electronic structure. In Chapter 3 we present the Green's function formalism used to calculate the quantum conductance in our nanoscaled systems. Chapter 4 presents the algorithms we used to compute the Green's function.

Chapters 5 and 6 are dedicated to a discussion of the properties of toroidal structures. In the first one we present the results for nanotube-based two-terminals systems with a variable angle α between the leads [7]. In the second one we explore the physical properties of multi-terminal toroidal systems composed by nanotubes or GNRs [8].

The properties of complex assembled carbon nanoribbons are presented in Chapters 7, 8 and 9. The first one explains the geometrical construction of the systems while the second explores their electronic structure and multi magnetic states [9]. Finally, transport properties of these ribbons are discussed in Chapter 9. The thesis is then concluded with a chapter where we present the conclusions.

2 *Methods to calculate the electronic band structure of solids*

In this chapter we will discuss some methods employed to perform electronic structure calculations. We start by presenting a general quantum mechanical framework to describe a molecule or a solid. We then introduce the Born-Oppenheimer approximation (also called adiabatic approximation) which allows us to reduce the problem to its corresponding electronic part. In the following we introduce the independent-electrons approximation and the main methods to solve the electronic problem. We then focus on the tight-binding method and finally describe the TBFOR package we have developed to perform part of the calculations presented in this thesis.

2.1 Hamiltonian

The starting point for calculating the electronic structure of molecules and solids is the system Hamiltonian, written as:

$$\hat{H} = -\frac{\hbar^2}{2m_e}\sum_i \nabla_i^2 - \frac{1}{4\pi\varepsilon_0}\sum_i\sum_I \frac{Z_I e^2}{|\mathbf{r}_i - \mathbf{R}_I|} + \frac{1}{8\pi\varepsilon_0}\sum_i\sum_{j\neq i}\frac{e^2}{|\mathbf{r}_i - \mathbf{r}_j|} - \sum_I \frac{\hbar^2}{2M_I}\nabla_I^2 + \frac{1}{8\pi\varepsilon_0}\sum_I\sum_{J\neq I}\frac{Z_I Z_J e^2}{|\mathbf{R}_I - \mathbf{R}_J|} \tag{2.1}$$

where i, j label the electrons and I, J the atomic nuclei. The quantities M_I, Z_I and $\mathbf{R}_I$ are, respectively, the mass, the atomic number, and the position of nucleus I, while $-e$ and m_e are the electron charge and mass and $\mathbf{r}_i$ is the position of electron i.

An interesting aspect of this problem is the fact that the nuclei are much more massive than the electrons. This makes the kinetic energy of the nuclei to be small compared to the other Hamiltonian contributions. In fact, a perturbation series with general validity can be written in terms of $1/M_I$ and its limit for $M_I \to \infty$ leads to static nuclei. This allows us to decou-

ple the nuclear and electronic problems and to work on them separately. This constitutes a practical and useful simplification which makes both the structural optimization and electronic structure calculations easier to perform, but still with a good accuracy. This is the so-called Born-Oppenheimer (BO) or adiabatic approximation [85, 86], which is a useful approximation for many purposes such as the calculation of vibrational modes in solids. A widely used approach is to consider the energy from the remaining electronic problem as an extra term added to the ion-ion interaction and perform a subsequent geometry optimization based on this effective interatomic potential. Therefore, within the BO approximation, our problem is reduced to the electronic Hamiltonian given by:

$$\hat{H}_e = -\frac{\hbar^2}{2m_e}\sum_i \nabla_i^2 - \frac{1}{4\pi\varepsilon_0}\sum_i\sum_I \frac{Z_I e^2}{|\mathbf{r}_i - \mathbf{R}_I|} + \frac{1}{8\pi\varepsilon_0}\sum_i\sum_{j\neq i} \frac{e^2}{|\mathbf{r}_i - \mathbf{r}_j|} \tag{2.2}$$

where the atomic positions enter as parameters.

2.2 Electronic problem

Within the BO approximation, the electronic problem is reduced compared to the initial problem. However, it is still very complicated and its solution is not easy to get. A set of widely used strategies employs the independent-electron approximation. This mean-field approximation consists in defining one-electron wavefunctions that can be obtained from an one-electron Schrödinger-like equation. This is a significant simplification but gives extremely satisfactory results and is used in most theoretical calculations on the electronic structure of molecules and solids.

2.2.1 Hartree method

The first quantitative calculations on multi-electronic systems were performed by Hartree [87]. In his approach, a one electron equation is defined as:

$$\hat{H}_{Hartree}\psi_i^\sigma(\mathbf{r}) = -\frac{\hbar^2}{2m_e}\nabla^2\psi_i^\sigma(\mathbf{r}) + V_{Hartree}\psi_i^\sigma(\mathbf{r}) = \varepsilon_i^\sigma\psi_i^\sigma(\mathbf{r}) \tag{2.3}$$

where σ represents the spin and $V_{Hartree}$ is an effective potential for each electron in the presence of the others. In his original work, Hartree defined a different potential for each electron in order to avoid self-interaction of the electron with itself. In order to obtain the system's ground state, one fills the states starting from the lowest levels to obey the Pauli's exclusion principle.

2.2.2 Hartree-Fock (HF) method

In 1930, Fock expanded Hartree's approach by using an anti-symmetric wavefunction in terms of a Slater determinant written from one-electron wavefunctions [88, 89]. The one-electron equations are then obtained by finding the corresponding wavefunctions that minimize the total energy obtained as the expected value for the full Hamiltonian. This process yields the following equations:

$$\begin{aligned} \hat{H}_{HF}\psi_i^{\sigma}(\mathbf{r}) &= \Big[-\frac{\hbar^2}{2m_e}\nabla^2 + V_{ext}(\mathbf{r}) + V_{Hartree}(\mathbf{r}) + V_{echange}(\mathbf{r})\Big]\psi_i^{\sigma}(\mathbf{r}) \\ &= \varepsilon_i^{\sigma}\psi_i^{\sigma}(\mathbf{r}) \end{aligned} \tag{2.4}$$

with

$$V_{Hartree}(\mathbf{r}) = \frac{e^2}{4\pi\varepsilon_0}\sum_{j,\sigma_j}\int d\mathbf{r}'\frac{\psi_j^{\sigma_j *}(\mathbf{r}')\psi_j^{\sigma_j}(\mathbf{r}')}{|\mathbf{r}-\mathbf{r}'|} \tag{2.5}$$

$$V_{exchange}(\mathbf{r}) = -\frac{e^2}{4\pi\varepsilon_0}\sum_{j}\int d\mathbf{r}'\frac{\psi_j^{\sigma *}(\mathbf{r}')\psi_i^{\sigma}(\mathbf{r}')}{|\mathbf{r}-\mathbf{r}'|}\frac{\psi_j^{\sigma}(\mathbf{r})}{\psi_i^{\sigma}(\mathbf{r})}. \tag{2.6}$$

Note that, unlike the original Hartree's approach, the mean Coulomb interaction includes a self-interaction contribution. On the other hand, the additional exchange term (without a classical analogous) has also such self-interaction energy, but with opposite sign so that the final result is self-interaction free. The presence of this exchange potential is a clear difference of the HF approach in comparison with Hartree's early work.

As the exchange does not have a classical analogous (like the mean Coulomb potential given by the Hartree potential), it is initially hard to understand its meaning. In order to understand what physics it represents, one has to look at the foundations of the independent electron approximation. Without considering any approximation, the solution for the electronic problem consists of a wavefunction Ψ which is a function of the coordinates of all the electrons $\mathbf{r}_i$, $i = 1,2,3,...,N$. As the electrons are fermions, they should obey Pauli's exclusion principle which is reflected by the fact that the electronic wavefunction has to be anti-symmetric with respect to any permutation involving the positions of two electrons. In mathematical terms, we have:

$$\Psi(\mathbf{r}_1,\mathbf{r}_2,...,\mathbf{r}_i,...,\mathbf{r}_j,...,\mathbf{r}_{N-1},\mathbf{r}_N) = -\Psi(\mathbf{r}_1,\mathbf{r}_2,...,\mathbf{r}_j,...,\mathbf{r}_i,...,\mathbf{r}_{N-1},\mathbf{r}_N). \tag{2.7}$$

In addition, we expect the Ψ dependence on the different $\mathbf{r}_i$ to be correlated in a more general way, so that the behavior of Ψ relative to a given $\mathbf{r}_i$ depends on the values of the $\mathbf{r}_j$ with $j \neq i$. However, when we use the independent electrons approximation, we are restricting Ψ to have

the form given by a Slater determinant. By doing that, we are intrinsically loosing information which can be directly associated with the electronic correlation. While the Hartree potential, in both Hartree and HF approaches, represents the interaction of any electron with the system's electronic cloud, the correlation is related to the specific interaction of a given electron with any single electron in the system. This is not a simple problem to solve and accounting for this correlation is a central problem in the electronic structure research field. The HF method, however, is a first step in this direction as the exchange potential represents two correlation related aspects:

- It removes self-interaction contributions;
- It accounts for short range interactions related to the Pauli's exclusion principle.

As can be seen from Equation 2.6, $V_{exchange}$ lowers the energy and can be interpreted as the interaction of the electron with an agent usually referred to as an "exchange hole". According to the expression for the exchange potential, this positive "exchange charge density" is determined by the electronic density (sum over the j states) surrounding the electron i and favors a ferromagnetic ordering of the electronic spins as this interaction involves only electrons with the same spin. This is a consequence of Hund's rule: as a number of electrons start to fill a set of degenerate states, they will fill evenly the available states so as to maximize the total spin as much as possible, starting to occupy orbitals with opposite spin only when there is no empty levels. Note also that there is no energy lowering associated with two electrons with the same spin occupying the same orbital as the $j = i$ contribution in the sum in Eq. 2.6 cancels with the corresponding self-interacting term in the sum from Eq. 2.5, constituting a clear manifestation of Pauli's principle.

2.2.3 Density Functional Theory

Not all the correlation effects are accounted for by the exchange energy term. In that regard, Density Functional Theory (DFT) [90, 91] is an important advance in the field. As we will see, DFT allows to recast the many-electron problem into a set of one-electron Schrödinger-like equations. However, in contrast to Hartree and HF, DFT is an exact theory (even though its practical implementation demands other approximations) [86]. The central role within DFT is played by the electronic density $n(\mathbf{r})$. This is better understood with the two theorems which constitute the basis of DFT [90]:

1^{st} *Theorem*: If a system of interacting electrons is immersed in a external potential V_{ext},

this potential is uniquely determined (except by a constant) by the electronic density n_0 of the ground-state (GS).

2^{st} *Theorem*: Let $E[n]$ be the functional for the energy relative to the electronic density n for a given V_{ext}. Then this functional has its global minimum (GS energy) for the exact density n_0 corresponding to the ground-state.

Those theorems are commonly known as the Hohenberg-Kohn theorems. Note that, based on the first theorem, we can affirm that all the system properties are determined by the electronic density for the GS since n_0 determines V_{ext}, which determines the Hamiltonian, which in turn defines the GS and all the excited states. Also, we can use the energy functional $E[n]$ to determine the exact GS energy and density. It is important to note, however, that DFT is not only a GS theory, but instead gives the system's Hamiltonian which is, in principle, all we need to obtain the ground state and all the excited states. However, the GS can be obtained in a systematic way, while there is no clear strategy to obtain excited states. The energy functional is written as:

$$E_{HK}[n] = T[n] + E_{electronic}[n] + \int d\mathbf{r} V_{ext}(\mathbf{r}) n(\mathbf{r}) \tag{2.8}$$

where T is the kinetic energy functional, V_{ext} is the external potential felt by the electrons (including the nuclei contribution) and $E_{electronic}$ accounts for all the electron-electron interactions.

Despite having the correct tool to obtain the electronic GS (i. e. the minimization of $E[n]$ relative to n), it is still not clear how to proceed on using this tool. The necessary recipe is given by the Kohn-Sham ansatz [91]. According to it, the GS density of our system can be written as the GS of an auxiliary system of non-interacting electrons. The one-electron wavefunctions for this auxiliary system are determined by Schrödinger-like equations in the form:

$$\hat{H}^{\sigma}_{aux} \psi^{\sigma}_i(\mathbf{r}) = -\frac{\hbar^2}{2m_e} \nabla^2 \psi^{\sigma}_i(\mathbf{r}) + V^{\sigma} \psi^{\sigma}_i(\mathbf{r}) = \varepsilon^{\sigma}_i \psi^{\sigma}_i(\mathbf{r}) \tag{2.9}$$

where σ labels the electron spin. The electronic density is written as:

$$n(\mathbf{r}) = \sum_{\sigma} \sum_{i=1}^{N_\sigma} |\psi^{\sigma}_i(\mathbf{r})|^2 \tag{2.10}$$

and the corresponding kinetic energy is:

$$T_{aux} = -\frac{\hbar^2}{2m_e} \sum_{\sigma} \sum_{i=1}^{N^\sigma} \langle \psi^{\sigma}_i | \nabla^2 | \psi^{\sigma}_i \rangle = \frac{\hbar^2}{2m_e} \sum_{\sigma} \sum_{i=1}^{N^\sigma} \int d\mathbf{r} |\nabla \psi^{\sigma}_i(\mathbf{r})|^2. \tag{2.11}$$

The classical Coulomb interaction is:

$$E_{Hartree}[n] = \frac{1}{8\pi\varepsilon_0}\int\int d\mathbf{r}d\mathbf{r}'\frac{n(\mathbf{r})n(\mathbf{r}')}{|\mathbf{r}-\mathbf{r}'|} \tag{2.12}$$

and the expression for the energy functional reads:

$$E_{KS}[n] = T_{aux}[n] + \int d\mathbf{r}V_{ext}(\mathbf{r})n(\mathbf{r}) + E_{Hartree}[n] + E_{xc}[n] \tag{2.13}$$

where V_{ext} is the external potential (including the contribution due to the nuclei) and E_{xc} is the functional which accounts for the exchange and all the correlation effects. If we consider $E_{HK} = E_{KS}$ we have:

$$E_{xc}[n] = T[n] - T_{aux}[n] + E_{electronic}[n] - E_{Hartree}[n] \tag{2.14}$$

which indicates that E_{xc} contains the exchange contribution and all the other correlation effects related to kinetic energy and electron-electron interactions. Here lies the main problem of DFT: we do not know the exact form of E_{xc}. Even though DFT yields the exact solution for the electronic problem, its practical implementation requires an approximation as to the form of the exchange and correlation energy term. The usual approach is to write this energy as:

$$E_{xc}[n] = \int d\mathbf{r}n(\mathbf{r})\varepsilon_{xc}([n],\mathbf{r}) \tag{2.15}$$

where $\varepsilon_{xc}([n],\mathbf{r})$ is the exchange-correlation energy per electron at position $\mathbf{r}$ for the given density $n(\mathbf{r})$. One then proceeds with the minimization of the energy functional relative to the density n. We end up with the following variational equations for $E_{KS}[n]$:

$$\frac{\delta}{\delta\psi_i^{\sigma*}}\Big(E_{KS}[n] - \sum_{\sigma}\sum_{j=1}^{N_\sigma}\varepsilon_j^{\sigma}(\int d\mathbf{r}\psi_j^{\sigma*}\psi_j^{\sigma} - 1)\Big) = 0 \tag{2.16}$$

where we used the Lagrange multipliers ε_i^{σ} corresponding to the normalization constraint $\langle\psi_i^{\sigma}|\psi_i^{\sigma}\rangle = 1$. As $E_{ext}[n]$, $E_{Hartree}[n]$ and $E_{xc}[n]$ are functionals of the density, we use the chain rule for these terms so that:

$$\begin{aligned}
&\frac{\delta T_{aux}[n]}{\delta\psi_i^{\sigma*}} + \frac{\delta E_{ext}[n]}{\delta\psi_i^{\sigma*}} + \frac{\delta E_{Hartree}[n]}{\delta\psi_i^{\sigma*}} + \frac{\delta E_{xc}[n]}{\delta\psi_i^{\sigma*}} - \varepsilon_i^{\sigma}\psi_i^{\sigma} \\
= \;& -\frac{\hbar^2}{2m_e}\nabla^2\psi_i^{\sigma}(\mathbf{r}) + \left(\frac{\delta E_{ext}[n]}{\delta n(\mathbf{r})} + \frac{\delta E_{Hartree}[n]}{\delta n(\mathbf{r})} + \frac{\delta E_{xc}[n]}{\delta n(\mathbf{r})}\right)\frac{\delta n(\mathbf{r})}{\delta\psi_i^{\sigma*}} - \varepsilon_i^{\sigma}\psi_i^{\sigma} = 0
\end{aligned} \tag{2.17}$$

resulting in:

$$\boxed{-\frac{\hbar^2}{2m_e}\nabla^2\psi_i^\sigma(\mathbf{r}) + \left(V_{ext}(\mathbf{r}) + V_{Hartree}(\mathbf{r}) + \varepsilon_{xc}(\mathbf{r})\right)\psi_i^\sigma = \varepsilon_i^\sigma\psi_i^\sigma}. \tag{2.18}$$

Here the Hartree potential (representing the interaction of any electron with the electronic cloud) is given by:

$$V_{Hartree}[n] = \frac{1}{8\pi\varepsilon_0}\int d\mathbf{r}'\frac{n(\mathbf{r})}{|\mathbf{r}-\mathbf{r}'|} \tag{2.19}$$

and V_{ext} and ε_{ext} are early defined. These are the well-known Kohn-Sham equations for the auxiliary problem. They are the basis for a great amount of theoretical calculations on the electronic structure of molecules and solids.

In this thesis we employed DFT to perform part of the electronic structure calculations in Chapter 8. Such calculations allow us to asses the suitability of a simpler model (see the TBU model in Section 2.8) to study the electronic structure of a broader set of carbon nanostructures.

2.3 Localized Basis

In order to solve Schrödinger equation for a molecule or a solid, one first has to choose a basis-set to expand the electronic wavefunctions. The first property we expect from a basis set in order to obtain precise results is completeness:

$$\sum_i |\phi_i\rangle\langle\phi_i| = 1. \tag{2.20}$$

It turns out that, in practice, it is never possible to use such a complete set. Plane waves, for instance, constitute a basis set which is naturally complete, as long as an infinite number of them are included. However, one always has to use a finite discretized version from the plane wave set in a numerical implementation. In this case, the systematic way to improve the accuracy of the calculation is to increase the number of functions in the basis set. Such improvement is not boundless since computational resources have a finite processing capability [86]. A plane waves basis approach is used in the DFT calculations [92, 93] we present in Chapter 8.

One alternative to plane waves is to use the Linear Combination of Atomic Orbitals (LCAO) method [86]. Here, the basis consists of functions corresponding to the electronic states from the isolated atoms. Despite its simplicity this method yields very accurate results and it constitutes the foundation of several computational packages and studies in the literature. The main advantages of this method are the reduced computational cost and the easy association of the

molecular levels with the atomic orbitals. One major drawback is the difficulty in assessing validity, given the impossibility to systematically improve the basis set. This approach is the basis for all the electronic transport and most electronic structure calculations we present in this thesis (see Parts II and III).

Let us examine the use of LCAO by expanding the electronic wavefunctions from a crystal in terms of a local orbital basis. In such a basis, each orbital basis function is associated with an atom in the structure. One appropriate choice for these orbitals are functions centered on the atomic sites. These functions can be written as:

$$\phi_j(\mathbf{r}-\mathbf{R}) = \phi_\alpha(\mathbf{r}-\mathbf{r}_P-\mathbf{R}) = \phi^{\mathbf{R}}_{n_j l_j m_j}(\vec{\rho}) = \phi^{\mathbf{R}}_{n_j l_j}(\rho) Y_{l_j m_j}(\hat{\rho}) \tag{2.21}$$

$$\vec{\rho} = \mathbf{r}-\mathbf{r}_P-\mathbf{R} \tag{2.22}$$

where $\mathbf{r}_P$ is the position of the P-th atom in the crystal unit cell (relative to the cell origin), α enumerates the atomic orbitals centered on P and $\mathbf{R}$ is a vector from the Bravais lattice (which localizes the origin of its corresponding cell). In this terminology, we define j to represent the (P,α) pair. The (l_j, m_j) pair represents the angular momentum and its projection on a given axis and n_j enumerates different functions with the same angular momentum. Also, $Y_{l_j m_j}(\hat{\rho})$ are the ubiquitous spherical harmonics. We present the spherical harmonics for $l_j = 0,1,2$ below:

$$Y_{0,0}(\theta,\phi) = \frac{1}{2}\sqrt{\frac{1}{\pi}} \tag{2.23}$$

$$Y_{1,0}(\theta,\phi) = \frac{1}{2}\sqrt{\frac{3}{2\pi}}\cos\theta \tag{2.24}$$

$$Y_{1,\pm1}(\theta,\phi) = \mp\frac{1}{2}\sqrt{\frac{3}{2\pi}}e^{\pm i\phi}\sin\theta \tag{2.25}$$

$$Y_{2,0}(\theta,\phi) = \frac{1}{4}\sqrt{\frac{5}{\pi}}(3\cos^2\theta - 1) \tag{2.26}$$

$$Y_{2,\pm1}(\theta,\phi) = \mp\frac{1}{2}\sqrt{\frac{15}{2\pi}}e^{\pm i\phi}\sin\theta\cos\theta \tag{2.27}$$

$$Y_{2,\pm2}(\theta,\phi) = \frac{1}{4}\sqrt{\frac{15}{2\pi}}e^{\pm 2i\phi}\sin^2\theta. \tag{2.28}$$

As discussed earlier, orbitals with $m = 0$ are real, while real orbitals can be obtained for the $m \neq 0$ cases by the following transformation:

$$Y^{\pm}_{l,|m|} = \frac{1}{2}(Y_{l,m} \pm Y_{l,-m}). \tag{2.29}$$

Plots for the individual $Y^{\pm}_{l,|m|}$ are shown in Fig. 2.1 (considering the method described in Sec-

tion 1.1).

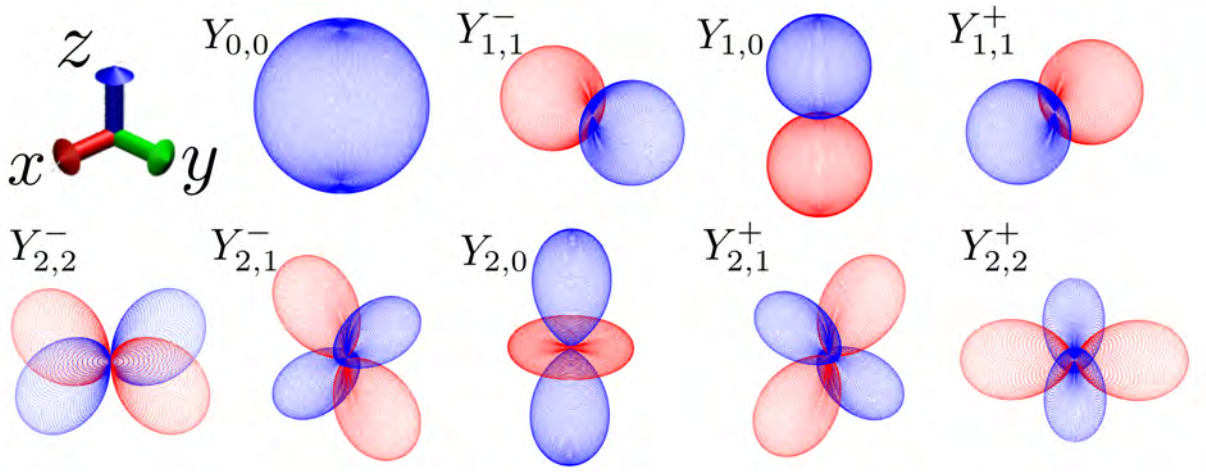

Figure 2.1: Spherical harmonics in the $Y^{\pm}_{l,|m|}$ form.

It is often more convenient to use the imaginary expressions in actual calculations since this will allow us to simplify the calculation of two-center integrals contributions for the Hamiltonian elements.

2.4 Hamiltonian elements

The Hamiltonian elements written in terms of the localized basis presented in Section 2.3 are written as:

$$H_{j,l}(\mathbf{R}',\mathbf{R}'') = \int dr^3 \phi^*_j(\mathbf{r}-\mathbf{R}')\hat{H}\phi_l(\mathbf{r}-\mathbf{R}''). \tag{2.30}$$

In addition, the translational crystal symmetry allows us to write:

$$H_{j,l}(\mathbf{R}'-\mathbf{R}''',\mathbf{R}''-\mathbf{R}''') = H_{j,i}(\mathbf{R}',\mathbf{R}'') \tag{2.31}$$

so that the $\mathbf{R}'$ and $\mathbf{R}''$ dependence of $H_{j,l}(\mathbf{R}',\mathbf{R}'')$ is determined exclusively by the difference $\mathbf{R} = \mathbf{R}'' - \mathbf{R}'$. Using this fact, we can write:

$$H_{j,l}(\mathbf{R}',\mathbf{R}'') = H_{j,l}(\mathbf{0},\mathbf{R}''-\mathbf{R}') = H_{j,l}(\mathbf{R}) = \int dr^3 \phi^*_j(\mathbf{r})\hat{H}\phi_l(\mathbf{r}-\mathbf{R}). \tag{2.32}$$

Similarly, the overlap terms are given by:

$$S_{j,l}(\mathbf{R}) = \int dr^3 \phi^*_j(\mathbf{r})\phi_l(\mathbf{r}-\mathbf{R}). \tag{2.33}$$

The one particle Hamiltonian operator has the form:

$$\hat{H} = \hat{T} + \sum_{p\mathbf{R}} V(|\mathbf{r} - \mathbf{r}_p - \mathbf{R}|) \tag{2.34}$$

where $\hat{T}$ is the one-electron kinetic energy operator and $V(|\mathbf{r} - \mathbf{r}_p - \mathbf{R}|)$ is the potential energy decomposed as a sum of spherically symmetric terms centered on the atoms located at positions $\mathbf{r}_p$ relative to the unit cell located at $\mathbf{R}$. The kinetic energy contribution to the Hamiltonian elements can be composed of one- or two-center integrals depending on whether the orbitals i and j are centered on the same atom or not. As the potential can be viewed as a sum of spherically symmetric terms, its contributions to the Hamiltonian elements can also have three-center integrals as well as one- and two-center integrals. We can readily notice four different types of potential energy contributions:

- **One-center:** when both orbitals and potential are centered on the same atom;
- **Two-center 1:** when the orbitals are centered on different atoms and the potential on one of these atoms;
- **Two-center 2:** when both orbitals are centered on the same atom and the potential on another one;
- **Three-center:** when both orbitals and potential are centered on different atoms.

Overlap terms are always composed of one- or two-center integrals.

Important aspects can be easily addressed for the two-center integrals. Let $M_{lm,l'm'}$ be a two-center integral, between two orbitals from different atoms, corresponding to the kinetic or potential energy contribution to a Hamiltonian element or an overlap element. For simplicity, let us suppose the line joining the two centers corresponds to the z-axis. We can then write:

$$M_{lm,l'm'} = \int f_1(\rho_1) f_2(\rho_2) Y^*_{l,m}(\hat{\rho}_1) Y_{l',m'}(\hat{\rho}_2) d^3\mathbf{r} \tag{2.35}$$

with

$$\hat{\rho}_i = \frac{\mathbf{r} - \mathbf{r}_i}{|\mathbf{r} - \mathbf{r}_i|} \quad i = 1, 2. \tag{2.36}$$

The ϕ dependence from this integral can be isolated so that:

$$M_{lm,l'm'} = \frac{M_{ll'm}}{2\pi} \int_0^{2\pi} e^{-im\phi} e^{im'\phi} d\phi = M_{ll'm} \delta_{mm'}. \tag{2.37}$$

Equation 2.37 is a significant simplification for the calculation of these terms. The usual nomenclature for such quantities is to denote $l = 0,1,2,3,...$ by $s,p,d,f,...$ and $m = 0,\pm1,\pm2,...$ by $\sigma,\pi,\delta,....$ Below we illustrate the different two-center integral schemes for $l = 0,1,2$.

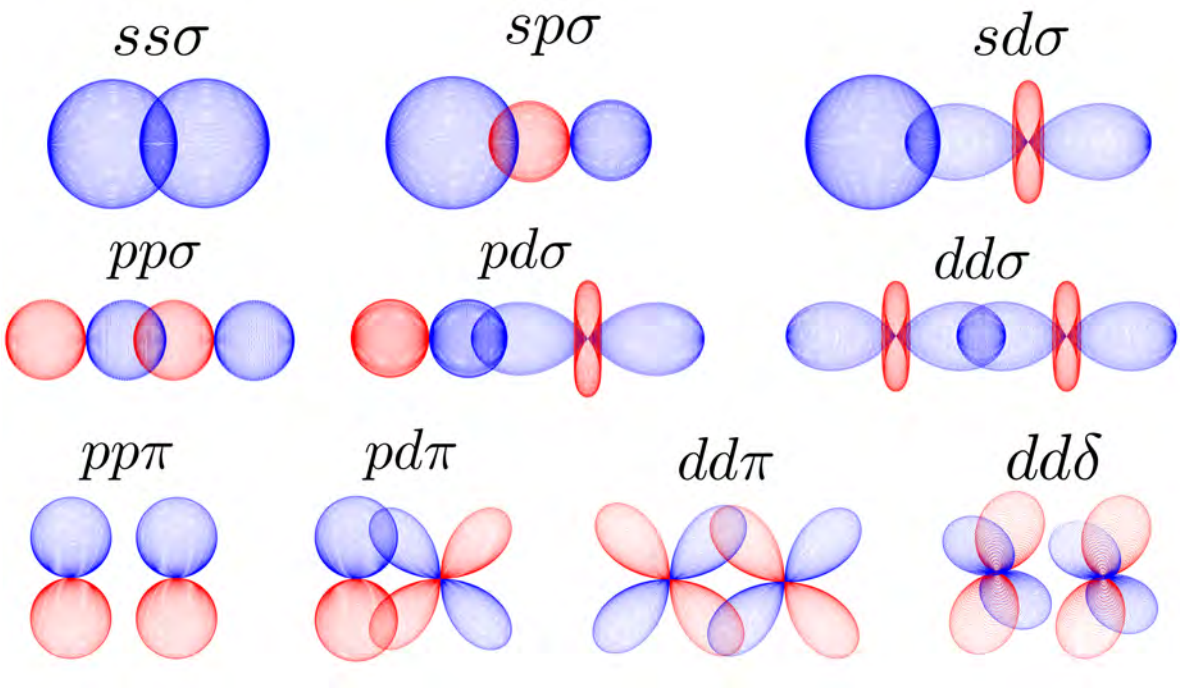

Figure 2.2: Different two-center integrals schemes for the Hamiltonian elements on a localized basis.

2.5 Bloch functions

Even with the simplifications introduced in the last section, it is impractical to work with the Hamiltonian in the simple atomic orbitals representation for a periodic solid. Even though we have a band matrix (whose matrix elements $M_{i,i+j}$ are zero for j larger than a given value), it is still infinite and there is no systematic way to solve it. On the other hand, Bloch's theorem [94, 95] indicates that we can write the eigenfunctions in a single unit cell as:

$$\phi_{j\mathbf{k}}(\mathbf{r}) = N_{j\mathbf{k}} \sum_{\mathbf{R}} e^{i\mathbf{k}\cdot\mathbf{R}} \phi_j(\mathbf{r}-\mathbf{R}) \tag{2.38}$$

where $N_{j\mathbf{k}}$ is a normalization constant. In the case of an infinite crystal, $\mathbf{k}$ is a vector which can assume any value within the first Brillouin Zone (BZ). Within this approach we redirect our attention from a set of vectors $\mathbf{R}$ which extend along the infinite real space to a set of vectors $\mathbf{k}$ which are contained within a finite portion (determined by the BZ) of the reciprocal space. In

this new basis, the Hamiltonian elements can be written as:

$$\begin{aligned}
H_{j,l}(\mathbf{k},\mathbf{k}') &= \int dr^3 \phi^*_{j\mathbf{k}}(\mathbf{r})\hat{H}\phi_{l\mathbf{k}'}(\mathbf{r}) \\
&= \int dr^3 \left(N^*_{j\mathbf{k}} \sum_{\mathbf{R}'} e^{-i\mathbf{k}\cdot\mathbf{R}'} \phi^*_j(\mathbf{r}-\mathbf{R}')\right) \hat{H} \left(N_{l\mathbf{k}'} \sum_{\mathbf{R}''} e^{i\mathbf{k}'\cdot\mathbf{R}''} \phi_l(\mathbf{r}-\mathbf{R}'')\right) \\
&= N^*_{j\mathbf{k}} N_{l\mathbf{k}'} \sum_{\mathbf{R}'} e^{-i\mathbf{k}\cdot\mathbf{R}'} \sum_{\mathbf{R}''} e^{i\mathbf{k}'\cdot\mathbf{R}''} \int dr^3 \phi^*_j(\mathbf{r}-\mathbf{R}')\hat{H}\phi_l(\mathbf{r}-\mathbf{R}'') \\
&= N^*_{j\mathbf{k}} N_{l\mathbf{k}'} \sum_{\mathbf{R}'} e^{-i\mathbf{k}\cdot\mathbf{R}'} \sum_{\mathbf{R}''} e^{i\mathbf{k}'\cdot\mathbf{R}''} H_{j,l}(\mathbf{R}''-\mathbf{R}') \\
&= N^*_{j\mathbf{k}} N_{l\mathbf{k}'} \sum_{\mathbf{R}'} e^{-i\mathbf{k}\cdot\mathbf{R}'} e^{i\mathbf{k}'\cdot\mathbf{R}'} \left(\sum_{\mathbf{R}''} e^{i\mathbf{k}'\cdot(\mathbf{R}''-\mathbf{R}')} H_{j,l}(\mathbf{R}''-\mathbf{R}') \right)
\end{aligned}$$

but the quantity between parenthesis corresponds to the $H_{j,l}(\mathbf{k}') = H_{j,l}(\mathbf{k}',\mathbf{k}')$. So we can write:

$$\begin{aligned}
H_{j,l}(\mathbf{k},\mathbf{k}') &= N^*_{j\mathbf{k}} N_{l\mathbf{k}'} \sum_{\mathbf{R}'} e^{-i\mathbf{k}\cdot\mathbf{R}'} e^{i\mathbf{k}'\cdot\mathbf{R}'} H_{j,l}(\mathbf{k}') \\
&= N^*_{j\mathbf{k}} N_{l\mathbf{k}'} H_{j,l}(\mathbf{k}') \sum_{\mathbf{R}'} e^{-i\mathbf{k}\cdot\mathbf{R}'} e^{i\mathbf{k}'\cdot\mathbf{R}'} \\
&= N^*_{j\mathbf{k}} N_{l\mathbf{k}'} H_{j,l}(\mathbf{k}') \delta_{\mathbf{k}\mathbf{k}'}
\end{aligned}$$

and finally

$$\boxed{H_{j,l}(\mathbf{k},\mathbf{k}) = H_{j,l}(\mathbf{k}) = \sum_{\mathbf{R}} e^{i\mathbf{k}\cdot\mathbf{R}} H_{j,l}(\mathbf{R})}. \tag{2.39}$$

Analogously, for the overlap matrix elements, we have:

$$\boxed{S_{j,l}(\mathbf{k},\mathbf{k}) = S_{j,l}(\mathbf{k}) = \sum_{\mathbf{R}} e^{i\mathbf{k}\cdot\mathbf{R}} S_{j,l}(\mathbf{R})}. \tag{2.40}$$

We can then expand the electronic eigenfunctions as:

$$\Psi_\alpha(\mathbf{r}) = \sum_j c_{j\alpha}\phi_{j\mathbf{k}}(\mathbf{r}). \tag{2.41}$$

Hence, the Schrödinger equation reads:

$$\hat{H}\Psi_\alpha(\mathbf{r}) = E_\alpha \Psi_\alpha(\mathbf{r}) \tag{2.42}$$

or, in the LCAO basis:

$$\sum_j c_{j\alpha}\hat{H}\phi_{j\mathbf{k}}(\mathbf{r}) = E_\alpha \sum_j c_{j\alpha}\phi_{j\mathbf{k}}(\mathbf{r}). \tag{2.43}$$

If we multiply on the left by $\phi^*_{l\mathbf{k}}(\mathbf{r})$ and integrate over the whole space we end up with:

$$\sum_j c_{j\alpha} \int \phi^*_{l\mathbf{k}}(\mathbf{r}) \hat{H} \phi_{j\mathbf{k}}(\mathbf{r}) d^3r = E_\alpha \sum_j c_{j\alpha} \int \phi^*_{l\mathbf{k}}(\mathbf{r}) \phi_{j\mathbf{k}}(\mathbf{r}) d^3r \tag{2.44}$$

$$\sum_j c_{j\alpha} H_{l,j}(\mathbf{k}) = \sum_j c_{j\alpha} E_\alpha S_{l,j}(\mathbf{k}) \tag{2.45}$$

$$\boxed{\mathbf{H}\mathbf{c}_\alpha = E_\alpha \mathbf{S}\mathbf{c}_\alpha}, \tag{2.46}$$

where $\mathbf{H}$ and $\mathbf{S}$ are square matrices with elements $H_{l,j}(\mathbf{k})$ and $S_{l,j}(\mathbf{k})$, respectively, and $\mathbf{c}_\alpha$ the column vector with elements $c_{j\alpha}$. The eigenvalues are then obtained by the secular equation:

$$\boxed{|\mathbf{H} - E_\alpha \mathbf{S}| = 0} \tag{2.47}$$

where $|\quad|$ denotes the determinant.

Within a computational procedure to calculate the electronic structure, one has to use a discrete set $\mathbf{k}_i$, $i = 1,2,3,...,N$ of $\mathbf{k}$ vectors to represent how the electronic states behave as functions of $\mathbf{k}$. Since the Hamiltonian elements from different $\mathbf{k}$ vectors are zero, we can write the secular equation 2.47 as:

$$\begin{vmatrix} \mathbf{H}(\mathbf{k}_1) - E_\alpha \mathbf{S}(\mathbf{k}_1) & 0 & 0 & \dots & 0 \\ 0 & \mathbf{H}(\mathbf{k}_2) - E_\alpha \mathbf{S}(\mathbf{k}_2) & 0 & \dots & 0 \\ 0 & 0 & \mathbf{H}(\mathbf{k}_3) - E_\alpha \mathbf{S}(\mathbf{k}_3) & \dots & 0 \\ \vdots & \vdots & \vdots & \ddots & \vdots \\ 0 & 0 & 0 & \dots & \mathbf{H}(\mathbf{k}_N) - E_\alpha \mathbf{S}(\mathbf{k}_N) \end{vmatrix} = 0 \tag{2.48}$$

and such matrix diagonalization can be broken into smaller problems:

$$\boxed{|\mathbf{H}(\mathbf{k}_i) - E_\alpha \mathbf{S}(\mathbf{k}_i)| = 0, \qquad i = 1,2,3,...,N} \tag{2.49}$$

for each $\mathbf{k}$-point $\mathbf{k}_i$.

2.6 The Slater-Koster approach

Bloch was the pioneer in the calculation of electronic levels in a crystal. He introduced the concept of electronic bands and his famous "Bloch's Theorem" [94]. Later on, Jones and co-workers were the first to expand the original s-symmetry-only approach to take into account a

basis of different orbitals [96]. However, the Tight-Binding (TB) model in the form it is widely used today was presented by Slater and Koster [97]. This is the simplest model to solve the electronic problem of periodic systems and despite its simplicity, it gives excellent results and deep insight into solid state and surface problems. In this TB approach, one uses a basis of highly localized atomic orbitals and consider the Hamiltonian elements of the studied system as empirical parameters [2, 86].

The TB parameters are further simplified by discarding three-center-integral contributions for the Hamiltonian elements [2, 86, 97]. We are then restricted to the one-center and two-center contributions. The two-center integrals are then simplified using Eq. 2.37. However when applying Equation 2.37 one can argue that the choice for the axis will in general not coincide with the line joining the atoms. However it is always possible to write the spherical harmonics relative to the bond line as linear combinations of the spherical harmonics relative to the z-axis. Using these transformations we can write the two-center-integral contributions to the Hamiltonian elements as linear combinations of the $M_{ll'm}$ terms from Equation 2.37. Slater and Koster came up with expressions for the elements involving s, p and d orbitals [97]. Below we reproduce these relations for the case of orbitals s and p.

$$M_{s,s} = M_{s,s,\sigma} \tag{2.50}$$

$$M_{s,p_z} = z^2 M_{s,p,\sigma} \tag{2.51}$$

$$M_{p_x,p_x} = x^2 M_{p,p,\sigma} + (1-x^2) M_{p,p,\pi} \tag{2.52}$$

$$M_{p_x,p_y} = xy(M_{p,p,\sigma} - M_{p,p,\pi}). \tag{2.53}$$

The TB parameters are fitted to reproduce crystal properties (such as electronic bands or lattice parameters) of a given model system. In addition, one has also to define a cutoff radius for the distance between the atoms so that Hamiltonian elements, for orbitals from atoms separated by a distance larger than the cutoff, are zero.

In this process, we call the ability of a given parametrization to give accurate results (for systems other than the one used to obtain the parametrization) as its transferability. This is an important concept that has to be taken into account carefully by the computational physicist. The inclusion of multiple-center-integrals effects is an example. Even though the influence of these integrals can be included in the two-center terms to give an accurate description for the electronic structure of some systems, such accuracy is usually not completely transferable to other structures when using the same parameters [86].

In this thesis we used graphene and GNRs as model systems to determine the TB parameters used in our calculations. Since the series of sp^2-like carbon nanostructures we studied

in this thesis are very similar to the model systems (as they are constructed from the same basic structural units), we believe we are within an acceptable transferability margin. Note that a number of TB calculations were compared to DFT with remarkable agreement (see, e. g. Chapter 8).

In the next section we apply the TB approach to describe the electronic structure of graphene.

2.7 Graphene

The carbon atoms in the graphene sheet form hexagons which fill completely the plane. The carbon positions by themselves do not form a Bravais lattice: they are organized in an hexagonal 2D lattice with a two atoms basis as shown in Fig. 2.3.

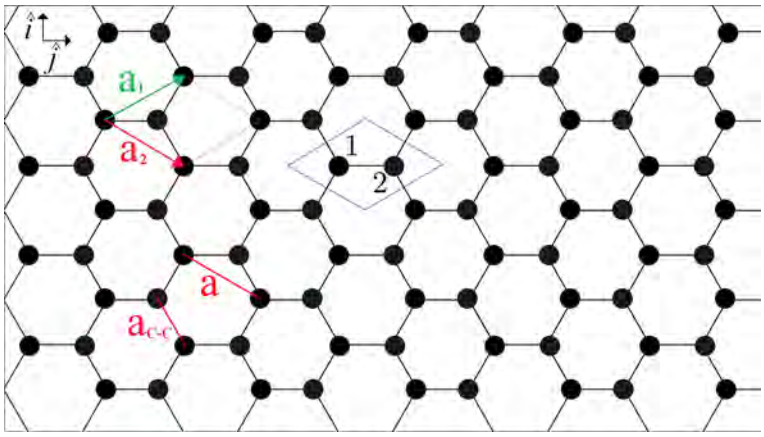

Figure 2.3: Graphene and lattice vectors definition.

The lattice vectors can be written as:

$$\mathbf{a}_1 = a(\frac{\sqrt{3}}{2}, \frac{1}{2}) \qquad \mathbf{a}_2 = a(\frac{\sqrt{3}}{2}, -\frac{1}{2}) \qquad a = a_{C-C}\sqrt{3}. \tag{2.54}$$

By definition, the lattice vectors have the same length and make a 60° angle between them. By using an $sp_xp_yp_z$ basis and by considering only integrals between first neighbors atoms we can write:

$$\mathbf{H} = \begin{bmatrix} H_1 & H_{12} \\ H_{21} & H_2 \end{bmatrix} \tag{2.55}$$

where H_1 and H_2 represent the Hamiltonians for the atoms 1 and 2, respectively, and H_{12} and H_{21} represent the interaction between them. If the sub-set of basis functions associated with a

given atom are orthonormal, we do not expect cross terms among them. So it is natural to write:

$$H_1 = H_2 = \begin{bmatrix} \varepsilon_s & 0 & 0 & 0 \\ 0 & \varepsilon_p & 0 & 0 \\ 0 & 0 & \varepsilon_p & 0 \\ 0 & 0 & 0 & \varepsilon_p \end{bmatrix}. \tag{2.56}$$

On the other hand, if we carefully take into account the interactions between first neighbors atoms, we can show that:

$$H_{12} = H_{21}^{\dagger} = \begin{bmatrix} f\gamma_{ss\sigma} & q\gamma_{sp\sigma} & w\gamma_{sp\sigma} & 0 \\ -q\gamma_{sp\sigma} & q(\gamma_{pp\sigma}) + w(\gamma_{pp\pi}) & g(\gamma_{pp\sigma} - \gamma_{pp\pi}) & 0 \\ -w\gamma_{sp\sigma} & g(\gamma_{pp\sigma} - \gamma_{pp\pi}) & q\gamma_{pp\pi} + w\gamma_{pp\sigma} & 0 \\ 0 & 0 & 0 & f\gamma_{pp\pi} \end{bmatrix} \tag{2.57}$$

where

$$f(\mathbf{k}) = 1 + e^{-i\mathbf{k}\cdot\mathbf{a}_1} + e^{-i\mathbf{k}\cdot\mathbf{a}_2} \tag{2.58}$$

$$g(\mathbf{k}) = \frac{\sqrt{3}}{4}(e^{-i\mathbf{k}\cdot\mathbf{a}_1} - e^{-i\mathbf{k}\cdot\mathbf{a}_2}) \tag{2.59}$$

$$q(\mathbf{k}) = \frac{1}{4}(1+3f) \tag{2.60}$$

$$w(\mathbf{k}) = \frac{1}{4}(f-1). \tag{2.61}$$

Since the Hamiltonian is an Hermitian operator we have $H_{12} = H_{21}^{\dagger}$. On the other hand, using symmetry arguments, we can write $H_1 = H_2$. When writing these matrices, we are considering the order $(s_1, p_{x1}, p_{y1}, p_{z1}, s_2, p_{x2}, p_{y2}, p_{z2})$ for the basis set to write the Hamiltonian $\mathbf{H}$. It is, however, suggestive to reorder the orbitals to $(p_{z1}, p_{z2}, s_1, p_{x1}, p_{y1}, s_2, p_{x2}, p_{y2})$. Doing so, the Hamiltonian is rewritten as

$$\begin{bmatrix} H_z & 0 & 0 \\ 0 & H_1' & H_{12}' \\ 0 & H_{21}' & H_2' \end{bmatrix} \tag{2.62}$$

with

$$H_z = \begin{bmatrix} \varepsilon_p & f\gamma_{pp\pi} \\ f^*\gamma_{pp\pi} & \varepsilon_p \end{bmatrix} \tag{2.63}$$

$$H_1' = H_2' = \begin{bmatrix} \varepsilon_s & 0 & 0 \\ 0 & \varepsilon_p & 0 \\ 0 & 0 & \varepsilon_p \end{bmatrix} \tag{2.64}$$

$$H'_{12} = H'^{\dagger}_{21} = \begin{bmatrix} f\gamma_{ss\sigma} & q\gamma_{sp\sigma} & w\gamma_{sp\sigma} \\ -q\gamma_{sp\sigma} & q(\gamma_{pp\sigma}) + w(\gamma_{pp\pi}) & g(\gamma_{pp\sigma} - \gamma_{pp\pi}) \\ -w\gamma_{sp\sigma} & g(\gamma_{pp\sigma} - \gamma_{pp\pi}) & q\gamma_{pp\pi} + w\gamma_{pp\sigma} \end{bmatrix} \tag{2.65}$$

with similar forms for the overlap matrix. This form is a direct consequence of symmetry properties. Since the π orbitals are odd relative to the graphene plane (they change sign upon a reflexion on the graphene plane), their cross-terms with the in-plane σ orbitals (which are even relative to the plane) will be zero. This property allows us to treat the π orbitals part of the problem separately from the remaining orbitals. Since the σ orbitals form strong bonds along the plane, the electronic properties around the Fermi Level are determined by the π orbitals part of the problem. We can then write the eigenvalue equation for the π bands as:

$$\begin{vmatrix} E - \varepsilon_p & Efs_{pp\pi} - f\gamma_{pp\pi} \\ Ef^* s_{pp\pi} - f^*\gamma_{pp\pi} & E - \varepsilon_p \end{vmatrix} = 0 \tag{2.66}$$

$$\boxed{E = \frac{\varepsilon_p \pm \gamma_{pp\pi} f}{1 \pm s_{pp\pi} f}}. \tag{2.67}$$

As the carbon atoms have a quasi-sp^2 hybridization in the nanostructures we studied, we expect these systems' electronic structure near the Fermi energy to be mostly determined by the π electrons, so the reason for us to use such a single-atomic-orbital basis for the TB-based calculation we present in this thesis.

2.8 The TBFOR project

In this section we present the TBFOR (*Tight-Binding Fortran Operational Resource*) project, which is the program we developed to carry out many of the electronic structure calculations presented in this thesis (as well as to obtain the inputs for the electronic transport calculations from Chapter 9). In addition, we also present the Hubbard-model Hamiltonian that we employed to include spin interactions and their effect on the electronic energy levels.

2.8.1 Hamiltonian

In its current version (that was the one used to obtain the results shown in this thesis), TBFOR treats only one orbital per atom, namely the π orbital for our sp^2 like systems. Examples of the input files needed by TBFOR are provided in Appendix A. Let us consider a Dirac notation so that $|\mathbf{R}, i, \sigma\rangle$ denotes the atomic orbital with spin σ centered on the atom i in the

real space cell located by $\mathbf{R}$. Our tight-binding Hamiltonian is then written as:

$$\hat{H}_0 = \sum_{\mathbf{R}}\sum_{i}\sum_{\sigma}|\mathbf{R},i,\sigma\rangle\varepsilon_i\langle\mathbf{R},i,\sigma| + \sum_{\mathbf{R}}\sum_{i}\sum_{\mathbf{R}'}\sum_{j}\sum_{\sigma}|\mathbf{R},i,\sigma\rangle V_{(\mathbf{R},i),(\mathbf{R}',j)}\langle\mathbf{R}',j,\sigma| \tag{2.68}$$

where $V_{(\mathbf{R},i),(\mathbf{R}',j)}$ are the hopping integrals representing the real-space Hamiltonian elements between the orbitals $|\mathbf{R},i,\sigma\rangle$ and $|\mathbf{R}',j,\sigma\rangle$ (with $V_{(\mathbf{R},i),(\mathbf{R},i)} = 0$) and ε_i is the on-site energy representing the real-space Hamiltonian element between the orbital $|\mathbf{R},i,\sigma\rangle$ and itself. Here we consider orthonormal orbitals:

$$\langle\mathbf{R},i,\sigma|\mathbf{R}',j,\sigma'\rangle = \delta_{(\mathbf{R},i,\sigma),(\mathbf{R}',j,\sigma')}. \tag{2.69}$$

In practical terms, we truncate the sums involving $V_{(\mathbf{R},i),(\mathbf{R}',j)}$ until n^{th}-nearest-neighbors with a given integer n. More specifically, we consider this term as non zero only when $|\mathbf{R},i\rangle$ and $|\mathbf{R}',j\rangle$ are no more than 3 neighbor away.

2.8.2 Eigenfunctions

The eigenfunctions in a periodic potential must obey Bloch's theorem:

$$\Psi(\mathbf{r}+\mathbf{R}) = e^{i\mathbf{k}\cdot\mathbf{R}}\Psi(\mathbf{r}). \tag{2.70}$$

Let $\phi_{(\mathbf{R},i,\sigma)}(\mathbf{r}) = \langle\mathbf{r}|\mathbf{R},i,\sigma\rangle$ be the real space representation of the orbital $|\mathbf{R},i,\sigma\rangle$. If we consider a lattice with a one-atom basis with no spin, we can show that the construction:

$$\Psi(\mathbf{r}) = \sum_{\mathbf{R}} e^{i\mathbf{k}\cdot\mathbf{R}}\phi_{(\mathbf{R},i)}(\mathbf{r}) \qquad \rightarrow \qquad |\Psi\rangle = \sum_{\mathbf{R}} e^{i\mathbf{k}\cdot\mathbf{R}}|\mathbf{R},i\rangle \tag{2.71}$$

is compatible with Bloch's theorem. When we have more than one atom per cell and when we consider spin, we can substitute $|\mathbf{R},i\rangle$ by a molecular orbital and write a $|\Psi\rangle$ for each of them. Another option is to substitute the $|\mathbf{R},i\rangle$ by a linear combination of the atomic orbitals within the corresponding $\mathbf{R}$ cell. Doing this we have:

$$|\Psi\rangle = \sum_{\mathbf{R}''} e^{i\mathbf{k}\cdot\mathbf{R}''}|\mathbf{R}'',\phi\rangle \tag{2.72}$$

with

$$|\mathbf{R}'',\phi\rangle = \sum_{l}\sum_{\sigma} c_{l,\sigma}|\mathbf{R}'',l,\sigma\rangle \tag{2.73}$$

and finally

$$\boxed{|\Psi\rangle = \sum_{\mathbf{R}''}\sum_{l}\sum_{\sigma} e^{i\mathbf{k}\cdot\mathbf{R}''}c_{l,\sigma}|\mathbf{R}'',l,\sigma\rangle}. \tag{2.74}$$

2.8.3 Eigenvalues

Operating the Hamiltonian on the Bloch function results in:

$$\hat{H}_0|\Psi\rangle = E|\Psi\rangle \tag{2.75}$$

$$\begin{aligned}
&\sum_{\mathbf{R}}\sum_{i}\sum_{\sigma}|\mathbf{R},i,\sigma\rangle\varepsilon_i\langle\mathbf{R},i,\sigma|\sum_{\mathbf{R}''}\sum_{l}\sum_{\sigma'}e^{i\mathbf{k}\cdot\mathbf{R}''}c_{l,\sigma'}|\mathbf{R}'',l,\sigma'\rangle \\
+\;&\sum_{\mathbf{R}}\sum_{i}\sum_{\mathbf{R}'}\sum_{j}\sum_{\sigma}|\mathbf{R},i,\sigma\rangle V_{(\mathbf{R},i),(\mathbf{R}',j)}\langle\mathbf{R}',j,\sigma|\sum_{\mathbf{R}''}\sum_{l}\sum_{\sigma'}e^{i\mathbf{k}\cdot\mathbf{R}''}c_{l,\sigma'}|\mathbf{R}'',l,\sigma'\rangle \\
=\;&E\sum_{\mathbf{R}''}\sum_{l}\sum_{\sigma'}e^{i\mathbf{k}\cdot\mathbf{R}''}c_{l,\sigma'}|\mathbf{R}'',l,\sigma'\rangle
\end{aligned} \tag{2.76}$$

$$\begin{aligned}
&\sum_{\mathbf{R}}\sum_{i}\sum_{\sigma}\varepsilon_i e^{i\mathbf{k}\cdot\mathbf{R}}c_{i,\sigma}|\mathbf{R},i,\sigma\rangle+\sum_{\mathbf{R}}\sum_{i}\sum_{\mathbf{R}'}\sum_{j}\sum_{\sigma}V_{(\mathbf{R},i),(\mathbf{R}',j)}e^{i\mathbf{k}\cdot\mathbf{R}'}c_{j,\sigma}|\mathbf{R},i,\sigma\rangle \\
=\;&E\sum_{\mathbf{R}''}\sum_{l}\sum_{\sigma'}e^{i\mathbf{k}\cdot\mathbf{R}''}c_{l,\sigma'}|\mathbf{R}'',l,\sigma'\rangle.
\end{aligned} \tag{2.77}$$

Projecting $\langle\mathbf{0},m,\sigma''|$ on the left:

$$\begin{aligned}
&\sum_{\mathbf{R}}\sum_{i}\sum_{\sigma}\varepsilon_i e^{i\mathbf{k}\cdot\mathbf{R}}c_{i,\sigma}\langle\mathbf{0},m,\sigma''|\mathbf{R},i,\sigma\rangle \\
+\;&\sum_{\mathbf{R}}\sum_{i}\sum_{\mathbf{R}'}\sum_{j}\sum_{\sigma}V_{(\mathbf{R},i),(\mathbf{R}',j)}e^{i\mathbf{k}\cdot\mathbf{R}'}c_{j,\sigma}\langle\mathbf{0},m,\sigma''|\mathbf{R},i,\sigma\rangle \\
=\;&E\sum_{\mathbf{R}''}\sum_{l}\sum_{\sigma'}e^{i\mathbf{k}\cdot\mathbf{R}''}c_{l,\sigma'}\langle\mathbf{0},m,\sigma''|\mathbf{R}'',l,\sigma'\rangle
\end{aligned} \tag{2.78}$$

$$\begin{aligned}
&\sum_{\mathbf{R}}\sum_{i}\sum_{\sigma}\varepsilon_i e^{i\mathbf{k}\cdot\mathbf{R}}c_{i,\sigma}\delta_{(\mathbf{0},m,\sigma''),(\mathbf{R},i,\sigma)} \\
+\;&\sum_{\mathbf{R}}\sum_{i}\sum_{\mathbf{R}'}\sum_{j}\sum_{\sigma}V_{(\mathbf{R},i),(\mathbf{R}',j)}e^{i\mathbf{k}\cdot\mathbf{R}'}c_{j,\sigma}\delta_{(\mathbf{0},m,\sigma''),(\mathbf{R},i,\sigma)} \\
=\;&E\sum_{\mathbf{R}''}\sum_{l}\sum_{\sigma'}e^{i\mathbf{k}\cdot\mathbf{R}''}c_{l,\sigma'}\delta_{(\mathbf{0},m,\sigma''),(\mathbf{R}'',l,\sigma')}
\end{aligned} \tag{2.79}$$

$$\varepsilon_m c_{m,\sigma''}+\sum_{\mathbf{R}'}\sum_{j}V_{(\mathbf{0},m),(\mathbf{R}',j)}e^{i\mathbf{k}\cdot\mathbf{R}'}c_{j,\sigma''}=Ec_{m,\sigma''} \tag{2.80}$$

$$\sum_{j}\sum_{\sigma}\mathscr{E}_{(m,\sigma'')(j,\sigma)}c_{j,\sigma}+\sum_{j}\sum_{\sigma}\mathscr{U}_{(m,\sigma'')(j,\sigma)}c_{j,\sigma}=Ec_{m,\sigma''} \tag{2.81}$$

where

$$\mathscr{U}_{(m,\sigma''),(j,\sigma)}=\delta_{\sigma'',\sigma}\sum_{\mathbf{R}'}V_{(\mathbf{0},m),(\mathbf{R}',j)}e^{i\mathbf{k}\cdot\mathbf{R}'} \tag{2.82}$$

$$\mathscr{E}_{(m,\sigma''),(j,\sigma)} = \delta_{(m,\sigma''),(j,\sigma)}\varepsilon_m. \tag{2.83}$$

Writing in matrix form we have:

$$\mathscr{H}\mathscr{C} = E\mathscr{C} \tag{2.84}$$

$$\boxed{(\mathscr{E}+\mathscr{U})\mathscr{C} = E\mathscr{I}\mathscr{C}}. \tag{2.85}$$

The matrix elements are

$$\mathscr{C}_{i,\sigma} = c_{i,\sigma} \tag{2.86}$$

$$\mathscr{I}_{(i,\sigma),(j,\sigma')} = \delta_{(i,\sigma),(j,\sigma')} \tag{2.87}$$

$$\mathscr{E}_{(i,\sigma),(j,\sigma')} = \varepsilon_i\delta_{(i,\sigma),(j,\sigma')} \tag{2.88}$$

$$\mathscr{U}_{(i,\sigma),(j,\sigma')} = \delta_{\sigma,\sigma'}\sum_{\mathbf{R}} V_{(\mathbf{0},i),(\mathbf{R},j)}e^{i\mathbf{k}\cdot\mathbf{R}} \tag{2.89}$$

and the eigenvalues are obtained from the equation:

$$\boxed{|\mathscr{H} - E\mathscr{I}| = 0}. \tag{2.90}$$

In one of the TBFOR inputs (see example in Appendix A), one has to provide the site energies and hopping parameters for 1^{st}, 2^{nd} and 3^{rd} neighbors. An internal subroutines then works the structure data (coordinates and lattice parameters) to identify the different n^{th}-nearest-neighbors for each atom. These information is the used by another subroutine that builds the hamitonian in Eq. 2.90 using Eqs. 2.82 and 2.83.

2.8.4 Hubbard model

So far we did not consider explicitly the interaction between two electrons with opposite spins occupying the same state. This is an important aspect to be considered in a number of systems as this interaction is responsible for non null balance between spin up and spin down occupations. A simple and well known example is provided by zigzag edges in graphitic materials. As discussed in Section 1.4.1, a ferromagnetic alignment is expected along these boundaries. Therefore, accounting for this short range interactions is fundamental for a concise and accurate description of such systems. The Hubbard model is a widely used method for computing this type of spin-spin interactions in molecules and solids. Within the one-orbital Hubbard model [30, 98], the Hamiltonian is written as a sum of two parts:

$$\hat{H} = \hat{H}_0 + \hat{H}' \tag{2.91}$$

where $\hat{H}_0$ is the usual tight-binding Hamiltonian and $\hat{H}'$ is the repulsive on-site Coulomb interaction given by:

$$\hat{H}' = U\sum_i \hat{n}_{i\uparrow}\hat{n}_{i\downarrow} \tag{2.92}$$

where $\hat{n}_{i\sigma} = c^\dagger_{i\sigma}c_{i\sigma}$ and $c^\dagger_{i\sigma}$ and $c_{i\sigma}$ are respectively the creation and annihilation operators for the orbital i with spin σ. The quantity U is a single parameter that measures the strength of the electron-electron on-site repulsion and it is obtained from first principles calculations [30]. We can write the densities in terms of the variations from the average value as:

$$\hat{n}_{i\sigma} = \langle\hat{n}_{i\sigma}\rangle + \delta\hat{n}_{i\sigma}. \tag{2.93}$$

Doing so, we can write:

$$\begin{aligned}\hat{H}' &= U\sum_i \Big(\langle\hat{n}_{i\uparrow}\rangle + \delta\hat{n}_{i\uparrow}\Big)\Big(\langle\hat{n}_{i\downarrow}\rangle + \delta\hat{n}_{i\downarrow}\Big) \\ &= U\sum_i \Big(\langle\hat{n}_{i\uparrow}\rangle\langle\hat{n}_{i\downarrow}\rangle + \delta\hat{n}_{i\uparrow}\langle\hat{n}_{i\downarrow}\rangle + \langle\hat{n}_{i\uparrow}\rangle\delta\hat{n}_{i\downarrow} + \delta\hat{n}_{i\uparrow}\delta\hat{n}_{i\downarrow}\Big).\end{aligned} \tag{2.94}$$

As far as we do not have sharp variations of the density from its corresponding mean value, we expect $\delta\hat{n}_{i\sigma}$ to be small so that $\sum_i \delta\hat{n}_{i\uparrow}\delta\hat{n}_{i\downarrow}$ is a minor contribution to $\hat{H}'$. If we ignore this last term, we obtain the so-called mean-field approximation [30]:

$$\hat{H}' = U\sum_i \Big(\langle\hat{n}_{i\downarrow}\rangle\hat{n}_{i\uparrow} + \langle\hat{n}_{i\uparrow}\rangle\hat{n}_{i\downarrow}\Big) - Uc\hat{1} \qquad c = \sum_i \langle\hat{n}_{i\uparrow}\rangle\langle\hat{n}_{i\downarrow}\rangle. \tag{2.95}$$

Writing it in a different notation we have:

$$\begin{aligned}\hat{H}' &= U\sum_{\mathbf{R}}\sum_i \Big(\langle n_{\mathbf{R},i,\downarrow}\rangle|\mathbf{R},i,\uparrow\rangle\langle\mathbf{R},i,\uparrow| + \langle n_{\mathbf{R},i,\uparrow}\rangle|\mathbf{R},i,\downarrow\rangle\langle\mathbf{R},i,\downarrow|\Big) \\ &\quad -Uc\sum_{\mathbf{R}}\sum_i \Big(|\mathbf{R},i,\uparrow\rangle\langle\mathbf{R},i,\uparrow| + |\mathbf{R},i,\downarrow\rangle\langle\mathbf{R},i,\downarrow|\Big)\end{aligned} \tag{2.96}$$

$$\hat{H}' = U\sum_{\mathbf{R}}\sum_i \Big(\big(\langle n_{\mathbf{R},i,\downarrow}\rangle - c\big)|\mathbf{R},i,\uparrow\rangle\langle\mathbf{R},i,\uparrow| + \big(\langle n_{\mathbf{R},i,\uparrow}\rangle - c\big)|\mathbf{R},i,\downarrow\rangle\langle\mathbf{R},i,\downarrow|\Big). \tag{2.97}$$

We can write

$$\langle\mathbf{0},m,\uparrow|\hat{H}'|\Psi\rangle = U\Big(\langle n_{\mathbf{0},m,\downarrow}\rangle - c\Big)\langle\mathbf{0},m,\uparrow|\sum_{\mathbf{R}''}\sum_l\sum_{\sigma'} e^{i\mathbf{k}\cdot\mathbf{R}''}c_{l,\sigma'}|\mathbf{R}'',l,\sigma'\rangle \tag{2.98}$$

$$\langle\mathbf{0},m,\uparrow|\hat{H}'|\Psi\rangle = U\Big(\langle n_{\mathbf{0},m,\downarrow}\rangle - c\Big)c_{m,\uparrow}. \tag{2.99}$$

So, our eigenvalue equation is rewritten as

$$\varepsilon_m c_{m,\sigma''} + \sum_{\mathbf{R}'} \sum_j V_{(\mathbf{0},m),(\mathbf{R}',j)} e^{i\mathbf{k}\cdot\mathbf{R}'} c_{j,\sigma''} + U\Big(\langle n_{\mathbf{0},m,\overline{\sigma''}}\rangle - c\Big) c_{m,\sigma''} = E c_{m,\sigma''} \tag{2.100}$$

$$\sum_j \sum_\sigma \mathscr{E}'_{(m,\sigma'')(j,\sigma)} c_{j,\sigma} + \sum_j \sum_\sigma \mathscr{U}_{(m,\sigma'')(j,\sigma)} c_{j,\sigma} = E c_{m,\sigma''} \tag{2.101}$$

where

$$\mathscr{U}_{(m,\sigma''),(j,\sigma)} = \delta_{\sigma'',\sigma} \sum_{\mathbf{R}'} V_{(\mathbf{0},m),(\mathbf{R}',j)} e^{i\mathbf{k}\cdot\mathbf{R}'} \tag{2.102}$$

$$\mathscr{E}'_{(m,\sigma''),(j,\sigma)} = \delta_{(m,\sigma''),(j,\sigma)} \Big(\varepsilon_m + U\langle n_{\mathbf{0},m,\overline{\sigma''}}\rangle - Uc\Big). \tag{2.103}$$

In matrix form, Eq. 2.103 becomes:

$$\mathscr{H}\mathscr{C} = E\mathscr{C} \tag{2.104}$$

$$\boxed{(\mathscr{E}' + \mathscr{U})\mathscr{C} = E\mathscr{I}\mathscr{C}}. \tag{2.105}$$

The matrix elements are

$$\begin{aligned}
\mathscr{C}_{i,\sigma} &= c_{i,\sigma} && (2.106)\\
\mathscr{I}_{(i,\sigma),(j,\sigma')} &= \delta_{(i,\sigma),(j,\sigma')} && (2.107)\\
\mathscr{E}'_{(i,\sigma),(j,\sigma')} &= \delta_{(i,\sigma),(j,\sigma')} \Big(\varepsilon_i + U\langle n_{\mathbf{0},i,\overline{\sigma''}}\rangle - Uc\Big) && (2.108)\\
\mathscr{U}_{(i,\sigma),(j,\sigma')} &= \delta_{\sigma,\sigma'} \sum_{\mathbf{R}} V_{(\mathbf{0},i),(\mathbf{R},j)} e^{i\mathbf{k}\cdot\mathbf{R}} && (2.109)
\end{aligned}$$

and the eigenvalues are obtained from the equation:

$$\boxed{|\mathscr{H} - E\mathscr{I}| = 0}. \tag{2.110}$$

Since the only effect of the Uc constant (added to every diagonal element) in $\mathscr{E}'_{(i,\sigma),(j,\sigma')}$ is to shift the whole energy spectrum, we can ignore it.

2.8.5 Self-consistency

Solving the TB problem including the Hubbard model is a very interesting numerical problem. This is because the Hamiltonian depends on the orbitals' occupations:

$$\langle n_{\mathbf{0},i,\sigma} \rangle = \frac{1}{\Delta \mathbf{k}} \int \left(\sum_{\alpha} f(E_\alpha) |c_{i,\sigma}(\mathbf{k},\alpha)|^2 \right) d\mathbf{k} \tag{2.111}$$

(where α enumerates the Hamiltonian eigenstates). However, these quantities depend on the solution so that there is no way to write the exact equation to be solved without knowing its solution. The usual method to solve this is by using an iterative approach to reach self-consistency. In this strategy, one starts with a initial guess for the occupation numbers $\langle n_{\mathbf{0},i,\sigma} \rangle$ and then write the corresponding Hamiltonian. After calculating the corresponding solution, new occupations are obtained and compared with those used to obtain the Hamiltonian. It is natural to expect, in the early steps of this process, that the output will be considerably different from the corresponding input. If this is the case, we mix the input and output densities and use the result as a new input, starting a new iteration step. On the other hand, if they are equal (or within an acceptable small difference), then self-consistency is reached. We carry on this procedure until we obtain a self-consistent solution. In this procedure, TBFOR uses a limited set of $\mathbf{k}$ points in the integral from Eq. 2.111 for each iteration. Once we finish this cycle, we use the self-consistent occupations to calculate the electronic structure over the Brillouin zone using a larger number of points.

2.8.6 Mixing schemes

Regarding the mixing performed at each iteration step, the most simple and intuitive one would be simply to substitute the input density by the corresponding output. However, this is usually not the most efficient method. A slightly different possibility is to make a simple mixing by:

$$n_{mix} = \beta n_{new} + (1-\beta) n_{old} \tag{2.112}$$

where β is a chosen real number, and use it in a new self-consistency cycle. The optimum value for β (which allows for the the fastest convergence) is system dependent and can only be determined by testing. In principle the larger the β the faster is the convergence. However the iterative procedure can become unstable, missing convergence, for excessively large β values. A small β yields slower convergence but it is more likely to result in a stable iterative procedure. For the systems we studied in this thesis, most cases converged with $\beta = 1$. In a minor part of

the simulations, we needed to use a smaller value ($\beta = 0.2$ to obtain convergence). The main difference from the first intuitive option is the consideration of a short-term memory, since we consider the last and the penultimate densities. A systematic and more efficient mixing scheme was proposed by Pulay [99]. In this method, we consider a linear combination of up to m previous input densities to build the next new input density n_{mix}:

$$n_{mix} = \sum_{i=1}^{m} \alpha_i n_i. \tag{2.113}$$

In order to obtain an optimal combination, we suppose the error R_{mix} associated with this optimal combination will be the corresponding linear combination of the errors R_i (difference between output and input densities) for the m previous inputs:

$$R_{mix} = \sum_{i=1}^{m} \alpha_i R_i, \qquad R_i = n_i' - n_i, \tag{2.114}$$

with n_i' being the corresponding output density for n_i. In the following, the α_i coefficients are determined by minimizing the quantity R:

$$R = R_{mix}^T \cdot R_{mix} = \sum_{i=1}^{m}\sum_{j=1}^{m} \alpha_i R_i^T \cdot R_j \alpha_j = [\alpha]^T \cdot [\overline{R}] \cdot [\alpha] \tag{2.115}$$

where $[\alpha]$ is the m-dimensional column vector with components α_i and $[\overline{R}]$ the $m \times m$ matrix with components $\overline{R}_{ij} = R_i^T \cdot R_j$. The minimization is made by considering a $[\delta\alpha]$ variation constrained by:

$$\sum_{i=1}^{m} \alpha_m = [\alpha]^T \cdot [\alpha] = 1. \tag{2.116}$$

Using a Lagrange multiplier λ for this condition we write the corresponding variation for R as:

$$\begin{aligned} \delta\Big(R - \lambda([\alpha]^T \cdot [\alpha] - 1)\Big) \;&=\; [\delta\alpha]^T \cdot [\overline{R}] \cdot [\alpha] + [\alpha]^T \cdot [\overline{R}] \cdot [\delta\alpha] \\ &\quad -\lambda([\delta\alpha]^T \cdot [\alpha] + [\alpha]^T \cdot [\delta\alpha]) = 0. \end{aligned} \tag{2.117}$$

But since we are working with real quantities we have $[\delta\alpha]^T \cdot [\overline{R}] \cdot [\alpha] = [\alpha]^T \cdot [\overline{R}] \cdot [\delta\alpha]$ and $[\delta\alpha]^T \cdot [\alpha] = [\alpha]^T \cdot [\delta\alpha]$, so that:

$$2[\delta\alpha]^T \cdot [\overline{R}] \cdot [\alpha] - 2\lambda[\delta\alpha]^T \cdot [\alpha] = 0 \tag{2.118}$$

which results in m equations given by:

$$\boxed{[\overline{R}] \cdot [\alpha] - \lambda[\alpha] = 0} \tag{2.119}$$

which together with Eq. 2.116 allows us to solve the system of $m+1$ variables λ, α_i, $i = 1,2,...,m$. An alternate version of this mixing procedure is to consider not only the input densities in the construction of the new trial density, but also take into account variations on them due to the iterative steps. In other words, we choose a new trial which also depend on the output densities n_i' corresponding to the n_i, $i = 1,2,3,...,m$ [100]. This is done by writing the new trial as:

$$n_{mix} = \sum_{i=1}^{m} \alpha_i (n_i + \beta R_i) \tag{2.120}$$

with β being an extra parameter free to our choice. The best β values is system dependent and, in principle, there is no simple rule to determine it, even though the chosen value is usually 0.8 [100].

2.9 Overview

In this Chapter we presented a general overview of some of the most used methodologies for the calculation of electronic properties in molecules and solids. Starting from the elementary Hartree's model, HF and DFT methods represented successive steps in constructing a satisfactory framework to treat the multi-electron problem within the independent-electrons approximation (which is actually treated exactly, in theory, within DFT). While highly accurate calculations demand a high computational cost, which makes the calculations sometimes prohibitive, simpler methods such as those based on the TB model can also be viewed as useful tools to access the properties of some, especially large, systems. Carbon sp^2 systems are considerably well described by TB calculations. For these systems, edge effects are straightforwardly treated within a Hubbard model Hamiltonian added to the usual TB model. Finally, our TBFOR package (which applies the TB+Hubbard model - TBU) was presented where we discussed important and specific details of the TBU implementation. This package was used to obtain most electronic structure results presented in Chapter 8 and the inputs needed for the electronic transport calculations shown in Chapter 9.

3 *Electronic transport at the nanoscale*

In this chapter we present the methods we applied to compute the electronic transport at the nanoscale. We start describing the general system under consideration for transport calculations and then introduce the Landauer approach. This formalism associates the quantum conductance through a nanoscopic system with the transmission probability for an electron impinging onto the system. In the following we introduce the Green's function and its relation to the transmission. We conclude the chapter discussing practical aspects related to semi-infinite electrodes and the use of non-orthogonal basis.

3.1 System description

The system under consideration in this chapter and that we worked out in the thesis is composed by a central scattering region (CSR) in contact with a number N of semi-infinite terminals as depicted in Fig. 3.1. Each terminal is composed by the repetition of a characteristic unit along a specific (periodic) direction.

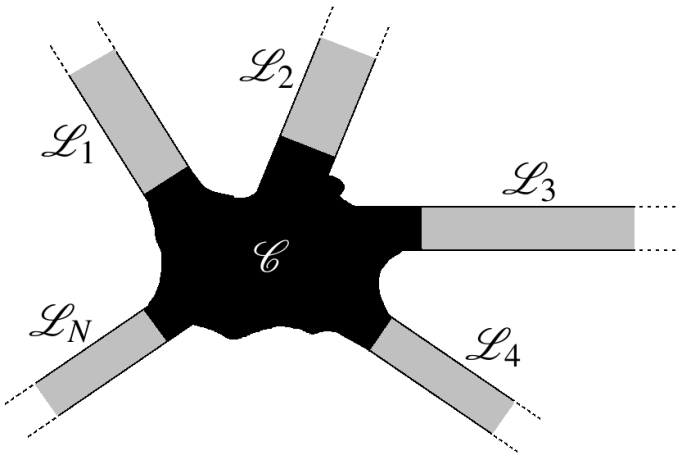

Figure 3.1: Basic system for electronic transport calculations. A central scattering region $\mathscr{C}$ coupled to the semi-infinite terminals $\mathscr{L}_1$, $\mathscr{L}_2$, $\mathscr{L}_3$, $\mathscr{L}_4$, ..., $\mathscr{L}_N$.

Note that each terminal can, in principle, be different from each other. Here we assume

that each of the terminal's cells is indistinguishable from the cell in the corresponding infinite system. This latter assumption will be referred to as *lead-bulk similarity* (LBS). In practice such condition is not a drastic restriction (as in the case of a simple TB calculation with hopping and overlap integrals given by constant parameters). However, additional care must be taken when using more sophisticated methods like DFT or TBU calculations in which a self-consistent procedure is carried out to obtain the electronic density. Nevertheless, the LBS can be achieved, within a good approximation and with controlled accuracy, by including a sufficient number of terminal unit cells within the CSR. A fundamental point to emphasize here is that we also apply the concept of principal layer (PL) to the electrodes. In other words, the terminal's unit cell is chosen so that it interacts only with the first-neighbor cells. This set of considerations allows us to write the problem in a convenient numerically solvable way.

3.2 Describing the terminals

The terminals $\mathscr{L}_n$ (where $n = 1,2,3,...,N$) are composed by periodic semi-infinite systems (as shown in Fig. 3.2) whose Hamiltonians are described by semi-infinite matrices. We label the unit cells within each terminal by the integer i where $i = 0$ for the cell closest to the CSR, $i = 1$ for the following cell and so on.

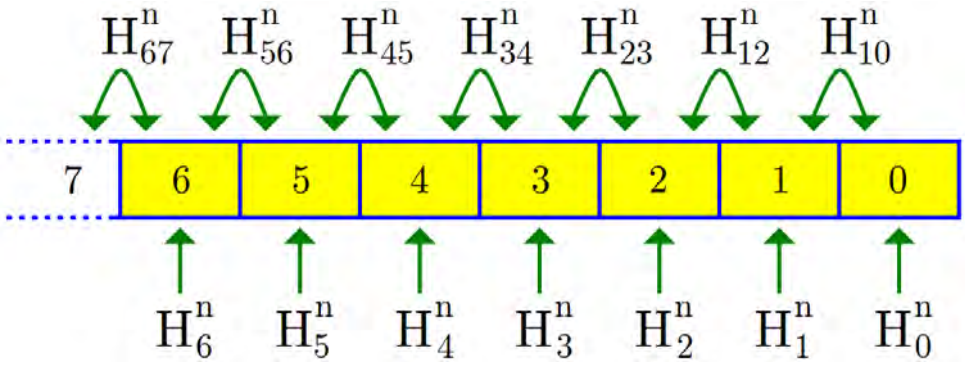

Figure 3.2: Semi-infinite terminal and the corresponding Hamiltonian sectors.

Under the conditions stated in the last section, we can write the Hamiltonian H_n corresponding to the n-th terminal $\mathscr{L}_n$ as:

$$H_n = \begin{bmatrix} H^n_0 & H^n_{01} & 0 & 0 & \dots \\ H^n_{10} & H^n_1 & H^n_{12} & 0 & \dots \\ 0 & H^n_{21} & H^n_2 & H^n_{23} & \dots \\ 0 & 0 & H^n_{32} & H^n_3 & \dots \\ \vdots & \vdots & \vdots & \vdots & \ddots \end{bmatrix} \tag{3.1}$$

where the matrix H_i^n describes the i-th terminal unit cell and $H_{i,j}^n$ describes the interaction between cells i and j (see Fig. 3.2). Note that $H_{i,j}^n = 0$ if $|i-j| > 1$, according to the PL condition. Both H_i^n and $H_{i,j}^n$ are square matrices having the size of the localized basis describing a unit cell of the terminal. Since the Hamiltonian is hermitian we have $H_{i,i+1}^n = (H_{i+1,i}^n)^\dagger$. The Hamiltonian can be further simplified by using the LBS to write:

$$H_i^n = H_0^n \qquad \text{and} \qquad H_{i,i+1}^n = H_{01}^n \qquad \text{for} \qquad i = 1,2,3,\ldots \tag{3.2}$$

The potential energy for the terminal presents two important characteristics, namely the periodicity along a given direction, say x_n, and the confinement in the orthogonal directions y_n and z_n. According to Bloch's theorem [95], we can write the energy eigenfunctions for the bulk system counterpart as:

$$\psi_{\alpha k} = e^{ikx_n} u_{\alpha k}(\mathbf{r}) \qquad \text{with} \qquad u_{\alpha k}(\mathbf{r}) = u_{\alpha k}(\mathbf{r} + j\mathbf{a}) \tag{3.3}$$

where $\mathbf{a}$ is the lattice vector along x_n. Here α is a quantum number relative to the confinement along $y_n - z_n$ and k is the wave vector corresponding to the periodic direction x_n (which we consider, by convention, positive as we move outwards the CSR). Turning the discussion to the semi-infinite terminal, this Bloch functional form can still be assumed for the eigenstates deep inside the lead. In the next section we use this result to describe electronic scattering when the electrons cross the CSR and introduce the Landauer formula.

3.3 Transmission and reflection

Suppose an electron in the terminal $\mathscr{L}_n$, having energy E_i and described by the Bloch state $\psi_{\alpha_i \overline{k_i}}^n$ (where $\overline{k_i} = -k_i$), is traveling towards the CSR. Once this state reaches the central conductor, its wavefunction is scattered to all the terminals and there is no simple approach to describe its behavior on the CSR and its vicinity. However, we know that the wavefunction deep into the electrodes is a linear combination of the outgoing Bloch functions. If we consider only energy conserving scattering events, the eigenfunction Ψ (corresponding to the electron with energy E_i) deep into a terminal $\mathscr{L}_m$ (other than $\mathscr{L}_n$) can be written as:

$$\Psi = \sum_l^{N_{E_i}^m} \mathscr{T}_{il} \psi_{\alpha_l k_l}^m \tag{3.4}$$

where $N_{E_i}^m$ is the number of Bloch states in $\mathscr{L}_m$ having energy E_i. In $\mathscr{L}_n$ the wavefunction has two contributions, one corresponding to the ingoing Bloch function $\psi_{\alpha_i \overline{k_i}}^n$ and the other

corresponding to the linear combination of the outgoing reflected waves:

$$\Psi = \psi^n_{\alpha_i \bar{k}_i} + \sum_l^{N^n_{E_i}} \mathscr{R}_{il} \psi^n_{\alpha_l k_l}. \tag{3.5}$$

The corresponding current density flowing deep inside the $\mathscr{L}_n$ terminal is given by:

$$\mathbf{j}_n(\mathbf{r}) = \langle \Psi_i | \hat{j} | \Psi_i \rangle = \frac{\hbar}{2im} \left(\Psi_i^* \frac{\partial \Psi_i}{\partial x_n} - \Psi_i \frac{\partial \Psi_i^*}{\partial x_n} \right) \hat{i}_n \tag{3.6}$$

where $\hat{i}_n$ is the canonical unit vector along the x_n direction. The current through a plane perpendicular to the x_n direction is given by:

$$I^n(E_j) = e \int_{-\infty}^{+\infty} \int_{-\infty}^{+\infty} dydz \langle \Psi_i | \hat{j} | \Psi_i \rangle \cdot \hat{i}_n. \tag{3.7}$$

As this current should not depend on the position of the plane inside the electrode, we can include integration over x within a terminal unit cell and divide it by the cell's length L_x^n

$$I^n(E_i) = \frac{e}{L_x^n} \int_{L_x^n} \int_{-\infty}^{+\infty} \int_{-\infty}^{+\infty} dxdydz \langle \Psi_i | \hat{j} | \Psi_i \rangle. \tag{3.8}$$

We observe that

$$\begin{aligned}
\Psi_i^* \frac{\partial \Psi_i}{\partial x} &= \left(\psi^{n*}_{\alpha_i k_i} + \sum_l^{N^n_{E_j}} \mathscr{R}^*_{il} \psi^{n*}_{\alpha_l k_l} \right) \left(-ik_i \psi^n_{\alpha_i k_i} + \sum_l^{N^n_{E_j}} ik_l \mathscr{R}_{il} \psi^n_{\alpha_l k_l} \right) && (3.9) \\
&= -ik_i \psi^n_{\alpha_i k_i} \psi^{n*}_{\alpha_i k_i} - ik_i \sum_l^{N^n_{E_j}} \psi^n_{\alpha_i k_i} \mathscr{R}^*_{il} \psi^{n*}_{\alpha_l k_l} && (3.10) \\
&\quad + \psi^{n*}_{\alpha_i k_i} \sum_l^{N^n_{E_j}} ik_l \mathscr{R}_{il} \psi^n_{\alpha_l k_l} + \sum_l^{N^n_{E_j}} \mathscr{R}^*_{il} \psi^{n*}_{\alpha_l k_l} \sum_{l'}^{N^n_{E_j}} ik_{l'} \mathscr{R}_{il'} \psi^n_{\alpha_{l'} k_{l'}} && (3.11)
\end{aligned}$$

and using the orthonormality condition for $\psi^n_{\alpha_p k_p}$ we end up with:

$$I^n(E_i) = \frac{e\hbar}{mL_x^n} \left(-k_i + \sum_l^{N^n_{E_j}} k_l |\mathscr{R}_{il}|^2 \right) = \left(-I_i(E_i) + \sum_l^{N^n_{E_j}} I_l(E_i) |\mathscr{R}_{il}|^2 \right) \tag{3.12}$$

where

$$I_p(E_i) = \frac{e\hbar k_p}{mL_x^n} = \frac{ev_p}{L_x^n}. \tag{3.13}$$

The quantity:

$$R_{il} = \frac{|I_l(E_i)|}{|I_i(E_i)|} |\mathscr{R}_{il}|^2 \tag{3.14}$$

is the reflection probability for an incident electron with momentum $\hbar k_i$ through the terminal $\mathscr{L}_n$ to be reflected elastically with momentum $\hbar k_l$ in the same lead. If we do the same process for any terminal $\mathscr{L}_m$ we end up with:

$$I^m(E_i) = \sum_l^{N_{E_j}^m} I_l(E_i)|\mathscr{T}_{il}|^2 \tag{3.15}$$

where

$$T_{il} = \frac{|I_l(E_i)|}{|I_i(E_i)|}|\mathscr{T}_{il}|^2 \tag{3.16}$$

is the transmission probability for an incident electron from $\mathscr{L}_n$ with momentum $\hbar k_i$ to be transmitted to $\mathscr{L}_m$ with momentum $\hbar k_l$ in an energy conserving process. Finally, in a steady state, the sum of all the terminal contributions has to result in zero (conservation of charge):

$$\sum_q I^q(E_i) = 0 \qquad \rightarrow \qquad \sum_l^{N_{E_j}^n} R_{il} + \sum_{m\neq n}\sum_{l'}^{N_{E_j}^m} T_{il'} = 1. \tag{3.17}$$

If we are interested in the net current $I^{n\rightarrow m}$ flowing from terminal $\mathscr{L}_n$ to terminal $\mathscr{L}_m$ we have to take the total charge flux from $\mathscr{L}_n$ to $\mathscr{L}_m$ and subtract the total charge flux from $\mathscr{L}_m$ to $\mathscr{L}_n$. For each of these currents we have to take a number of aspects into account:

1. Sum the contributions from all the states (or channels) with energy equal to E which transmit from one terminal to the other;
2. Multiply each contribution by the density of states;
3. Multiply each contribution by the Fermi distribution for the corresponding source electrode;
4. Integrate with respect to energy.

The final result reads

$$I^{n\rightarrow m} = 2\int dE \sum_j^{N_E^n}\sum_l^{N_E^m} f_n(E)D_j(E)I_j(E)T_{jl}(E) - 2\int dE \sum_l^{N_E^m}\sum_j^{N_E^n} f_m(E)D_l(E)I_l(E)T_{lj}(E). \tag{3.18}$$

The density of states in one dimension is given by:

$$D_j(E)dE = \frac{L_x}{2\pi}dk_i \qquad \rightarrow \qquad D_j(E) = \frac{L_x}{2\pi}dk_i/dE = \frac{L_x}{2\pi\hbar v_j(k_j)} \tag{3.19}$$

so that we have

$$I^{n\to m} = \frac{2e}{h}\int dE \sum_{j}^{N_E^n}\sum_{l}^{N_E^m} f_n(E)T_{jl}(E) - \frac{2e}{h}\int dE \sum_{l}^{N_E^m}\sum_{j}^{N_E^n} f_m(E)T_{lj}(E) \tag{3.20}$$

$$I^{n\to m} = \frac{2e}{h}\int dE \Big(f_n(E)\mathscr{T}_{nm}(E) - f_m(E)\mathscr{T}_{mn}(E) \Big) \tag{3.21}$$

with:

$$\mathscr{T}_{nm}(E) = \sum_{j}^{N_E^n}\sum_{l}^{N_E^m} T_{jl}(E) \qquad \mathscr{T}_{mn}(E) = \sum_{l}^{N_E^m}\sum_{j}^{N_E^n} T_{lj}(E). \tag{3.22}$$

If we consider an equilibrium situation where the levels filling is defined by a common Fermi energy E_F for the whole system we should have zero net current in every electrode. Under this circumstances we write:

$$I^{n\to m} = 0 \qquad \to \qquad \mathscr{T}_{nm}(E) = \mathscr{T}_{mn}(E). \tag{3.23}$$

Now, if we are interested in the non-eqilibrium situation at low bias case, we have $\mu_n - \mu_m \to 0$ (where μ_n and μ_m are the chemical potentials of the terminals n amd m, respectively) and we can write, at first order:

$$\frac{\partial f(E)}{\partial \mu} \approx \left.\frac{f_n(E) - f_m(E)}{\mu_n - \mu_m}\right|_{\mu_0} \qquad \to \qquad f_n(E) - f_m(E) \approx \left.\frac{\partial f(E)}{\partial \mu}\right|_{\mu_0} (\mu_n - \mu_m). \tag{3.24}$$

Since the Fermi-Dirac distribution has the form:

$$f(E) = \frac{1}{e^{(E-\mu)/k_B T} + 1} \tag{3.25}$$

we have:

$$\frac{\partial f(E)}{\partial \mu} = -\frac{\partial f(E)}{\partial E}. \tag{3.26}$$

Furthermore, if we consider the zero temperature limit we end up with:

$$\frac{\partial f(E)}{\partial E} = -\delta(E - \mu_0). \tag{3.27}$$

If we consider $\mu_0 = \mu_n$:

$$I^{n\to m} = \frac{2e}{h}(\mu_n - \mu_m)\mathscr{T}_{nm}(\mu_n). \tag{3.28}$$

On the other hand if we choose $\mu_0 = \mu_m$:

$$I^{n\to m} = \frac{2e}{h}(\mu_n - \mu_m)\mathscr{T}_{nm}(\mu_m). \tag{3.29}$$

As long as $\mathscr{T}_{nm}$ varies slowly, there is no significant difference in using Equation 3.28 or 3.29 or if we set $\mu_0 = E_F$ so that we do not need to worry in writing:

$$I^{n\to m} = \frac{2e}{h}(\mu_n - \mu_m)\mathscr{T}_{nm}(E_F). \tag{3.30}$$

Finally, the low bias conductance is defined as the ratio between I and the bias $V = (\mu_n - \mu_m)/e$:

$$G^{n\to m} = \frac{2e^2}{h}\mathscr{T}_{nm}(E_F). \tag{3.31}$$

However, if the transmission presents sharp variations around E_F we need to use Equation 3.21. In this case, it makes more sense to define the differential as:

$$G^{n\to m}(E) = \frac{2e}{h}\Big(f_n(E) - f_m(E)\Big)\mathscr{T}_{nm}(E). \tag{3.32}$$

These results express the essence of Landauer formalism, namely "conductance is transmission". This theory contains the nature of electronic transport at the nanoscale, being a clear departure from the top-down descriptions of electronic transport. While Ohm's law (successful for macroscopic systems) does not take into account the atomistic character of matter, it fails when predicting a vanishing resistance for a device with size going to zero. On the other hand, Landauer's formula is intrinsically based on the quantum mechanical description of matter within scattering theory and constitutes a truly bottom-up approach for the electronic current in nanoscale systems. Landauer's theory is today a widely used formalism for computing electronic transport properties of nanoscale systems with the aid of Green's function theory.

3.4 Experimental evidences of conductance quantization

For macroscopic systems, electrons undergo a huge number of scattering events (where energy is conserved or not) so that, as a final result, the electron can be assigned to a constant drag velocity. In this classical picture, transport is described within Ohm's law which states that the conductance (defined as the inverse of the electrical resistance) of a macroscopic conductor with length L and constant cross-sectional area A is given by:

$$G_{Ohm} = \sigma\frac{A}{L} \tag{3.33}$$

where σ is the material dependent conductivity. However, as we decrease L to lengths where the atomic character of matter becomes prominent (or in other words, when the device is smaller than the phase coherence length [101, 102]), quantum interference effects start to become important and Ohm's description no longer holds. At the nanoscale, we are out of this diffusive regime of transport and we have the onset of ballistic transport where electrons are likely to follow their paths free from being scattered (that is, like a bullet). Eventual scattering events at the nanoscale are described by the transmission within Landauer approach. In the special case of perfect ballistic transport we have complete transmission ($T_{jl}(E) = 1$) and the conductance at the zero temperature limit assumes quantized values that are multiple of the basic quantity

$$G_0 = \frac{2e^2}{h} \tag{3.34}$$

which is called quantum of conductance. The first experimental verification of this result was provided by van Wees [6] and Wharam [103] and their respective collaborators. They verified that quantum point contacts in a GaAs/AlGaAs interface present quantized conductance steps which are multiples of G_0, as shown in Fig. 3.3.

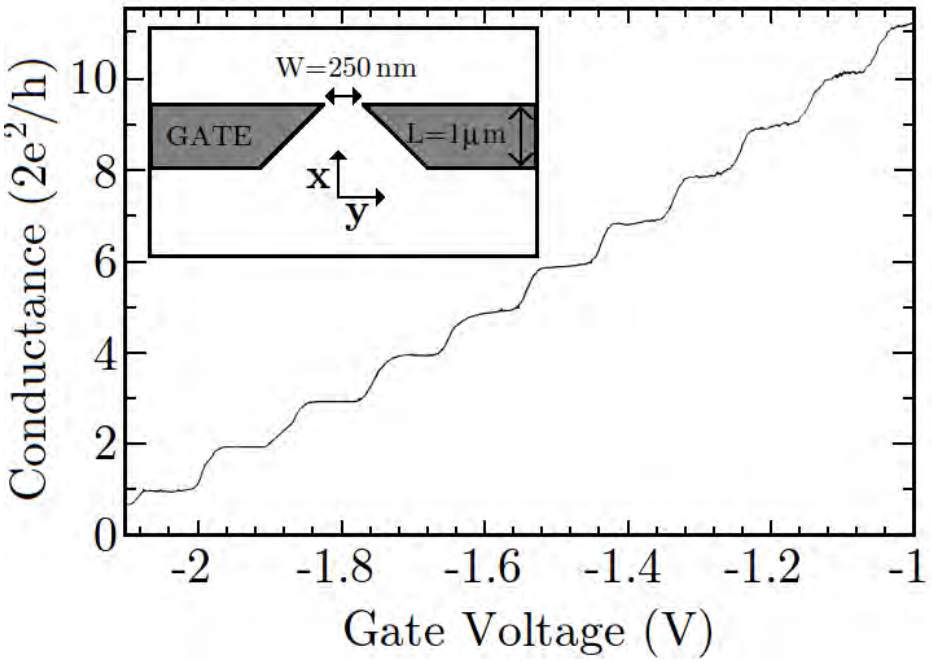

Figure 3.3: Dependence of the quantum conductance on the gate voltage for a quantum point contact in a GaAs/AlGaAs interface. Adapted from [6].

We observe that as the gate voltage varies, more channels are available inside the electrochemical potential window and we have a step-varying conductance. However, the apparatus used in these experiments was not a simple two terminal system [6, 103]. In fact, it corresponds to a four probe measurement where the current is measured between two probes and the volt-

age between another pair of terminals, so that direct comparison of the results in Fig. 3.3 and the Landauer formula is not appropriate [104, 105], even though it is sufficient to illustrate the quantized character of conductance.

3.5 The Green's function formalism

Scattering theory establishes a systematic approach to calculate the transmissions by means of an entity called Green's function (GF). Let $\hat{H}$ be a single particle Hamiltonian. Time-dependent Schrödinger equation then reads:

$$\hat{H}|\psi(t)\rangle = i\hbar\frac{d|\psi(t)\rangle}{dt} \tag{3.35}$$

which can be rewritten as

$$\left(i\hbar\frac{d}{dt} - \hat{H}\right)|\psi(t)\rangle = 0. \tag{3.36}$$

The corresponding Green's function for this problem is defined as the quantity obeying [104]:

$$\left(i\hbar\frac{d}{dt} - \hat{H}\right)\hat{G}(t) = \hat{1}\delta(t). \tag{3.37}$$

For this equation we have two solutions $\hat{G}^{\pm}$ corresponding to the following boundary conditions:

1. $\hat{G}^{+}(t) = 0$ for $t < 0$ (retarded);
2. $\hat{G}^{-}(t) = 0$ for $t > 0$ (advanced).

These solutions can be written as:

$$\hat{G}^{+} = -\frac{i}{\hbar}e^{-i\hat{H}t/\hbar}, \qquad t > 0; \tag{3.38}$$

$$\hat{G}^{-} = \frac{i}{\hbar}e^{-i\hat{H}t/\hbar}, \qquad t < 0. \tag{3.39}$$

Note that if the Hamiltonian is time independent, $\hat{G}^{+}$ can be identified with the time evolution operator (aside from a multiplicative constant), so that we can write [104]:

$$|\psi(t)\rangle = i\hbar\hat{G}^{+}(t)|\psi(0)\rangle, \tag{3.40}$$

with $t > 0$. In other words, $\hat{G}^+$ propagates $|\psi\rangle$ from a past time $t_0 = 0$ to a future time $t > 0$ (so the name "retarded"). Analogously, we can write:

$$|\psi(t)\rangle = -i\hbar\hat{G}^-(t)|\psi(0)\rangle, \tag{3.41}$$

with $t < 0$, so that $\hat{G}^-$ propagates $|\psi\rangle$ backwards from a time $t_0 = 0$ to a past time $t < 0$ (so the name "advanced").

Time independent versions of the GF can be obtained by Fourier transform:

$$\hat{G}^+(E) = \int dt e^{iEt/\hbar}\hat{G}^+(t) \tag{3.42}$$

$$= -\frac{i}{\hbar}\int dt e^{i(E-\hat{H})t/\hbar} \tag{3.43}$$

$$= -\frac{i}{\hbar}\frac{\hbar}{i}\frac{1}{E-\hat{H}}e^{i(E-\hat{H})t/\hbar}\Big|_0^{+\infty}. \tag{3.44}$$

In order to avoid poles on the real axis for the energy E, we add a $i\eta$ ($\eta \to 0^+$) term to the energy so that:

$$\hat{G}^+(E) = -\frac{1}{E+i\eta-\hat{H}}e^{i(E-\hat{H})t/\hbar}e^{-\eta t/\hbar}\Big|_0^{+\infty} = \frac{1}{E+i\eta-\hat{H}}. \tag{3.45}$$

Similarly for the advanced function:

$$\hat{G}^-(E) = \frac{1}{E-i\eta-\hat{H}}. \tag{3.46}$$

If we consider the multi-terminal basic system shown in Fig. 3.1, we can write its Hamiltonian in terms of a localized basis as:

$$H = \begin{bmatrix} H_C & h_{C1} & h_{C2} & h_{C3} & \dots & h_{CN} \\ h_{1C} & H_1 & 0 & 0 & \dots & 0 \\ h_{2C} & 0 & H_2 & 0 & \dots & 0 \\ h_{3C} & 0 & 0 & H_3 & \dots & 0 \\ \vdots & \vdots & \vdots & \vdots & \dots & \vdots \\ h_{NC} & 0 & 0 & 0 & \dots & H_N \end{bmatrix} \tag{3.47}$$

where H_C describes the CSR and H_i ($i = 1,2,3,...,N$) represents the semi-infinite lead $\mathscr{L}_i$ (see Eq. 3.1). Also, the Hamiltonian sectors representing the interaction between the CSR and the terminal $\mathscr{L}_i$ are h_{Ci} and h_{iC}. We do not consider the terminals interact directly with each other, so the corresponding zero elements in Eq. 3.47. If we define ε as $E+i\eta$ ($E-i\eta$) for the retarded

(advanced) GF, we can re-write Equation 3.45 (3.46) in matrix form as:

$$(\varepsilon\mathscr{I} - H)G = \mathscr{I} \tag{3.48}$$

$$\begin{bmatrix} \varepsilon I_C - H_C & -h_{C1} & -h_{C2} & \dots & -h_{CN} \\ -h_{1C} & \varepsilon I_1 - H_1 & 0 & \dots & 0 \\ -h_{2C} & 0 & \varepsilon I_2 - H_2 & \dots & 0 \\ \vdots & \vdots & \vdots & \dots & \vdots \\ -h_{NC} & 0 & 0 & \dots & \varepsilon I_N - H_N \end{bmatrix} \cdot \begin{bmatrix} G_C & G_{C1} & G_{C2} & \dots & G_{CN} \\ G_{1C} & G_{11} & G_{12} & \dots & G_{1N} \\ G_{2C} & G_{21} & G_{22} & \dots & G_{2N} \\ \vdots & \vdots & \vdots & \dots & \vdots \\ G_{NC} & G_{N1} & G_{N2} & \dots & G_{NN} \end{bmatrix} = \mathscr{I} \tag{3.49}$$

where $\mathscr{I}$ is the identity matrix. After performing the product we have

$$\begin{bmatrix} (\varepsilon I_C - H_C)G_C - \sum_i h_{Ci}G_{iC} & M_{C1} & M_{C2} & \dots & M_{CN} \\ -h_{1C}G_C + (\varepsilon I_1 - H_1)G_{1C} & M_{11} & M_{12} & \dots & M_{1N} \\ -h_{2C}G_C + (\varepsilon I_2 - H_2)G_{2C} & M_{21} & M_{22} & \dots & M_{2N} \\ \vdots & \vdots & \vdots & \dots & \vdots \\ -h_{NC}G_C + (\varepsilon I_N - H_N)G_{NC} & M_{N1} & M_{N2} & \dots & M_{NN} \end{bmatrix} = \begin{bmatrix} I_C & 0 & 0 & \dots & 0 \\ 0 & I_1 & 0 & \dots & 0 \\ 0 & 0 & I_2 & \dots & 0 \\ \vdots & \vdots & \vdots & \dots & \vdots \\ 0 & 0 & 0 & \dots & I_N \end{bmatrix}. \tag{3.50}$$

The upper left term gives us:

$$(\varepsilon I_C - H_C)G_C - \sum_i h_{Ci}G_{iC} = I_C \tag{3.51}$$

while the other terms in the first column give us

$$-h_{jC}G_C + (\varepsilon I_j - H_j)G_{jC} = 0 \tag{3.52}$$

$$G_{jC} = (\varepsilon I_j - H_j)^{-1}h_{jC}G_C = g_j h_{jC}G_C \qquad g_j = (\varepsilon I_j - H_j)^{-1}. \tag{3.53}$$

Then

$$(\varepsilon I_C - H_C)G_C - \sum_i h_{Ci}g_i h_{iC}G_C = (\varepsilon I_C - H_C)G_C - \Big(\sum_i h_{Ci}g_i h_{iC}\Big)G_C = I_C. \tag{3.54}$$

Using a simplified notation for the terms in the sum within the parenthesis we have:

$$(\varepsilon I_C - H_C)G_C - \Big(\sum_i \Sigma_i\Big)G_C = I_C \qquad \Sigma_i = h_{Ci}g_i h_{iC} \tag{3.55}$$

and finally isolating the conductor Green's function G_C we have:

$$G_C = (\varepsilon I_C - H_C - \Sigma_1 - \Sigma_2 - ... - \Sigma_N)^{-1}. \tag{3.56}$$

The matrix Σ_i is usually referred to as the *self-energy* of the lead $\mathscr{L}_i$. These terms can be interpreted as effective potentials which describe the effects of the semi-infinite terminals on the finite CSR. In other words, the sum of the CSR Hamiltonian with the self-energies represents a finite central conductor satisfying the boundary conditions corresponding to the attached electrodes $\mathscr{L}_i$, $i = 1,2,3,...,N$ [104, 106]. This is a remarkable result which allows us to reduce the problem of an extended infinite system to that of a finite central conductor as if it were isolated by using this modified Hamiltonian to describe it.

3.6 Green's function and density of electronic states

An important result is that the GF has a direct relation to the density of electronic states (DOS) of the system. If we consider a set of eigenstates with energy eigenvalues ε_α, the corresponding DOS is written as [95]:

$$D(E) = 2\sum_\alpha \delta(E-\varepsilon_\alpha) \tag{3.57}$$

where the factor 2 refers to the spin. The local density of states (LDOS) is obtained by multiplying each term in the sum with the density $|\psi_\alpha(\mathbf{r})|^2$ from the corresponding state:

$$D(\mathbf{r},E) = 2\sum_\alpha |\psi_\alpha(\mathbf{r})|^2 \delta(E-\varepsilon_\alpha). \tag{3.58}$$

This last quantity can be viewed as proportional to the diagonal element of the real space representation of a more general entity called spectral function [106]:

$$A(\mathbf{r},\mathbf{r}',E) = 2\pi\sum_\alpha \langle\mathbf{r}|\psi_\alpha\rangle\delta(E-\varepsilon_\alpha)\langle\psi_\alpha|\mathbf{r}'\rangle. \tag{3.59}$$

If we use the energy eigenstates representation, instead, we obtain:

$$A(E) = 2\pi \begin{bmatrix} \delta(E-\varepsilon_1) & 0 & 0 & \dots \\ 0 & \delta(E-\varepsilon_2) & 0 & \dots \\ 0 & 0 & \delta(E-\varepsilon_2) & \dots \\ \vdots & \vdots & \vdots & \ddots \end{bmatrix}. \tag{3.60}$$

On the other hand, the Dirac delta function can be written as (with $\eta \to 0^+$):

$$\begin{aligned} \delta(E-\varepsilon_\alpha) &= \frac{1}{2\pi}\frac{2\eta}{(E-\varepsilon_\alpha)^2+\eta^2} \\ &= \frac{i}{2\pi}\left(\frac{1}{E-\varepsilon_\alpha+\eta} - \frac{1}{E-\varepsilon_\alpha-\eta}\right) \end{aligned} \tag{3.61}$$

so that the spectral function becomes:

$$\begin{aligned} A(E) &= i\begin{bmatrix} \frac{1}{E-\varepsilon_1+\eta} & 0 & 0 & \dots \\ 0 & \frac{1}{E-\varepsilon_2+\eta} & 0 & \dots \\ 0 & 0 & \frac{1}{E-\varepsilon_3+\eta} & \dots \\ \vdots & \vdots & \vdots & \ddots \end{bmatrix} - i\begin{bmatrix} \frac{1}{E-\varepsilon_1-\eta} & 0 & 0 & \dots \\ 0 & \frac{1}{E-\varepsilon_2-\eta} & 0 & \dots \\ 0 & 0 & \frac{1}{E-\varepsilon_3-\eta} & \dots \\ \vdots & \vdots & \vdots & \ddots \end{bmatrix} \\ &= i\Big[G^r(E) - G^a(E)\Big]. \end{aligned} \tag{3.62}$$

From this last equation we obtain that the DOS is written in terms of the GF as:

$$D(E) = -\frac{1}{\pi} Tr\big(G^r(E)\big) \tag{3.63}$$

and the LDOS is given by the individual diagonal elements in the trace of $G^r(E)$.

3.7 Green's function and Landauer formalism

The conductor Green's function contains all the information about the electronic structure of the central region attached to the electrodes. In fact, as we will show in this section, the GF allows us to obtain not only the DOS, but also the quantum transmission needed to calculate the conductance using Landauer's formula.

Let us suppose an electron in the system depicted in Fig. 3.1 enters the CSR through terminal $\mathscr{L}_i$ and is described by an incoming wavefunction φ_i. Once it reaches the CSR, it is scattered to all the terminals (including $\mathscr{L}_i$). The wavefunction describing an outgoing electron in terminal $\mathscr{L}_j$ is denoted by ϕ_j and the wavefunction describing the electron in the CSR is ψ. Let us write time-independent Schrödinger equation in matrix form as:

$$\begin{bmatrix} H_C & h_{C1} & \dots & h_{Ci} & \dots & h_{Cj} & \dots & h_{CN} \\ h_{1C} & H_1 & \dots & 0 & \dots & 0 & \dots & 0 \\ \vdots & \vdots & \ddots & 0 & \dots & 0 & \dots & 0 \\ h_{iC} & 0 & 0 & H_i & \dots & 0 & \dots & 0 \\ \vdots & \vdots & \vdots & \vdots & \ddots & \vdots & \dots & \vdots \\ h_{jC} & 0 & 0 & 0 & \dots & H_j & \dots & 0 \\ \vdots & \vdots & \vdots & \vdots & \dots & \vdots & \dots & \vdots \\ h_{NC} & 0 & 0 & 0 & \dots & 0 & \dots & H_N \end{bmatrix} \begin{bmatrix} \psi \\ \phi_1 \\ \vdots \\ \varphi_i + \phi_i \\ \vdots \\ \phi_j \\ \vdots \\ \phi_N \end{bmatrix} = E \begin{bmatrix} \psi \\ \phi_1 \\ \vdots \\ \varphi_i + \phi_i \\ \vdots \\ \phi_j \\ \vdots \\ \phi_N \end{bmatrix}. \tag{3.64}$$

From this equation we can write:

$$h_{iC}\psi + H_i\phi_i + H_i\varphi_i = E\phi_i + E\varphi_i \quad \rightarrow \quad \phi_i + \varphi_i = g_i h_{iC}\psi \tag{3.65}$$

$$h_{jC}\psi + H_j\phi_j = E\phi_j \quad \rightarrow \quad \phi_j = g_j h_{jC}\psi. \tag{3.66}$$

The time-dependent version of Schrödinger equation is:

$$\begin{bmatrix} H_C & h_{C1} & \dots & h_{Ci} & \dots & h_{Cj} & \dots & h_{CN} \\ h_{1C} & H_1 & \dots & 0 & \dots & 0 & \dots & 0 \\ \vdots & \vdots & \ddots & 0 & \dots & 0 & \dots & 0 \\ h_{iC} & 0 & 0 & H_i & \dots & 0 & \dots & 0 \\ \vdots & \vdots & \vdots & \vdots & \ddots & \vdots & \dots & \vdots \\ h_{jC} & 0 & 0 & 0 & \dots & H_j & \dots & 0 \\ \vdots & \vdots & \vdots & \vdots & \dots & \vdots & \dots & \vdots \\ h_{NC} & 0 & 0 & 0 & \dots & 0 & \dots & H_N \end{bmatrix} \begin{bmatrix} \psi \\ \phi_1 \\ \vdots \\ \varphi_i + \phi_i \\ \vdots \\ \phi_j \\ \vdots \\ \phi_N \end{bmatrix} = i\hbar \begin{bmatrix} \dot{\psi} \\ \dot{\phi}_1 \\ \vdots \\ \dot{\varphi}_i + \dot{\phi}_i \\ \vdots \\ \dot{\phi}_j \\ \vdots \\ \dot{\phi}_N \end{bmatrix} \tag{3.67}$$

where a dot represents the derivate with respect to the time variable ($\dot{\psi} = d\psi/dt$). From this equation we can extract:

$$H_C\psi + h_{C1}\phi_1 + ... + h_{Ci}\phi_i + h_{Ci}\varphi_i + ... + h_{Cj}\phi_j + ... + h_{CN}\phi_N = i\hbar\dot{\psi} \tag{3.68}$$

which can be rewritten (after substituting Eqs. 3.65 and 3.66) as:

$$H_C\psi + \sum_l \Sigma_l\psi = i\hbar\dot{\psi} \quad \rightarrow \quad \dot{\psi} = \frac{1}{i\hbar}H_C\psi + \frac{1}{i\hbar}\sum_l \Sigma_l\psi. \tag{3.69}$$

The total charge flux I_{CSR} through the CSR is obtained from:

$$\begin{aligned} I_{CSR} &= -e\frac{d}{dt}\psi^\dagger\psi = -e\dot{\psi}^\dagger\psi - e\psi^\dagger\dot{\psi} \\ &= -e\left(-\frac{1}{i\hbar}(H_C\psi)^\dagger - \frac{1}{i\hbar}\sum_l(\Sigma_l\psi)^\dagger\right)\psi - e\psi^\dagger\left(\frac{1}{i\hbar}H_C\psi + \frac{1}{i\hbar}\sum_l\Sigma_l\psi\right) \\ &= -\frac{e}{i\hbar}\sum_l\psi^\dagger(\Sigma_l - \Sigma_l^\dagger)\psi = \frac{e}{\hbar}\sum_l\psi^\dagger\Gamma_l\psi = \frac{e}{\hbar}\sum_l Tr(\psi^\dagger\Gamma_l\psi) \\ &= \frac{e}{\hbar}\sum_l Tr(\Gamma_l\psi\psi^\dagger). \end{aligned} \tag{3.70}$$

However, this current corresponds to a single eigenstate. In order to have the complete current we have to sum over all the eigenstates and at the same time multiply each eigenstate contribution by the Fermi distribution (written relative to the chemical potential μ_i from $\mathscr{L}_i$). If we label

the different eigenstates by α we will have:

$$\begin{aligned} I_i &= \frac{e}{\hbar}\sum_\alpha f(\varepsilon_\alpha-\mu_i)Tr(\Gamma_i\psi_\alpha\psi_\alpha^\dagger) \\ &= \frac{e}{\hbar}\int dE\sum_\alpha f(E-\mu_i)Tr\Big(\Gamma_i\psi_\alpha\delta(E-\varepsilon_\alpha)\psi_\alpha^\dagger\Big) \\ &= \frac{e}{\hbar}\int dE f(E-\mu_i)Tr\Big(\Gamma_i\sum_\alpha\psi_\alpha\delta(E-\varepsilon_\alpha)\psi_\alpha^\dagger\Big). \end{aligned} \tag{3.71}$$

But we can identify the sum on α with the conductor's spectral function:

$$A_C=\sum_\alpha\psi_\alpha\delta(E-\varepsilon_\alpha)\psi_\alpha^\dagger=i\big[G_C^r(E)-G_C^a(E)\big]. \tag{3.72}$$

We can go further and work on this last expression to obtain:

$$\begin{aligned} A_C &= i\big[G_C^r(E)-G_C^a(E)\big] \\ &= iG_C^r(E)\Big[\big(G_C^a(E)\big)^{-1}-\big(G_C^r(E)\big)^{-1}\Big]G_C^a(E) \\ &= iG_C^r(E)\Big[\sum_l(\Sigma_l^r-\Sigma_l^a)\Big]G_C^a(E) \\ &= \sum_l G_C^r(E)\Gamma_l G_C^a(E) \end{aligned} \tag{3.73}$$

where $\Gamma_l=i(\Sigma_l-\Sigma_l^\dagger)$ represents the coupling between $\mathscr{L}_l$ and the conductor, while G_C^r (G_C^a) is the conductor retarded (advanced) GF [104, 106]. Analogously, it is possible to show that:

$$A_C=\sum_l G_C^a(E)\Gamma_l G_C^r(E). \tag{3.74}$$

Hence we can rewrite I_{CSR} as:

$$I_{CSR}=\sum_l\frac{e}{\hbar}\int dE f(E-\mu_i)Tr\Big(\Gamma_i G_C^r\Gamma_l G_C^a\Big)=\sum_l I_l^i \tag{3.75}$$

where

$$I_l^i=\frac{e}{\hbar}\int dE f(E-\mu_i)Tr\Big(\Gamma_i G_C^r\Gamma_l G_C^a\Big) \tag{3.76}$$

represents the current flowing through $\mathscr{L}_l$ from $\mathscr{L}_i$ for $l\neq i$. In the case of I_i^i, it represents the balance between the incoming current (related to φ_i) and the outcoming current (related to ϕ_i).

The results above were obtained from the perspective of an impinging electron coming from $\mathscr{L}_i$. If we make a similar calculation for an incoming electron from $\mathscr{L}_j$ we obtain:

$$I_{CSR}=\sum_l\frac{e}{\hbar}\int dE f(E-\mu_j)Tr\Big(\Gamma_j G_C^r\Gamma_l G_C^a\Big)=\sum_l I_l^j \tag{3.77}$$

so that if we consider the superposition of both currents, the net current I_{ij} coming from $\mathscr{L}_i$ to $\mathscr{L}_j$ is:

$$I_{ij} = I_j^i - I_i^j = \frac{e}{\hbar}\int dE f(E-\mu_i) Tr\Big(\Gamma_i G_C^r \Gamma_j G_C^a\Big) - \frac{e}{\hbar}\int dE f(E-\mu_j) Tr\Big(\Gamma_j G_C^r \Gamma_i G_C^a\Big). \quad (3.78)$$

But since we can also write $A_C = \sum_l G_C^a \Gamma_l G_C^r$, we have:

$$Tr\Big(\Gamma_j G_C^r \Gamma_i G_C^a\Big) = Tr\Big(\Gamma_j G_C^a \Gamma_i G_C^r\Big) = Tr\Big(\Gamma_i G_C^r \Gamma_j G_C^a\Big) \quad (3.79)$$

so that:

$$I_{ij} = I_j^i - I_i^j = \frac{e}{\hbar}\int dE \Big(f(E-\mu_i) - f(E-\mu_j)\Big) Tr\Big(\Gamma_i G_C^r \Gamma_j G_C^a\Big) \quad (3.80)$$

so that the transmissions in Landauer formula can be obtained from:

$$\mathscr{T}_{ij} = Tr(\Gamma_i G_C^r \Gamma_j G_C^a). \quad (3.81)$$

The first issue we have to deal with before going ahead on this problem is the calculation of the self-energies for the semi-infinite electrodes. Once we obtain such quantities, calculating the conductor GF is straightforward since it involves only a simple matrix inversion. However, depending on the size of the central region, we may have to deal with a second barrier. If the conductor is too large, the computational cost of the matrix inversion can make the calculation impractical. Additionally, one still has to take care with the memory handling in such case.

The self-energy calculation is treated in the next sections, while a powerful method to calculate G_C is presented in the next chapter.

3.8 Electrodes: infinite *versus* finite matrices

As shown in last section, the self-energy for a lead $\mathscr{L}_i$ is obtained from:

$$\Sigma_i = h_{Ci} g_i h_{iC}. \quad (3.82)$$

Writing down the matrices h_{Ci} and h_{iC} we have:

$$h_{Ci} = \begin{bmatrix} h_{Ci}^0 & 0 & 0 & \dots \end{bmatrix} \qquad h_{iC} = \begin{bmatrix} h_{iC}^0 \\ 0 \\ 0 \\ \vdots \end{bmatrix}$$

where h^0_{iC} and h^0_{Ci} represent the interaction Hamiltonian between the CSR and the the first unit cell (labeled by 0) from the terminal $\mathscr{L}_i$. Due to the PL condition, the cross terms between the CSR and the further cells are null. On the other hand, following the form in Eq. 3.1, g_i is written as:

$$g_i = \begin{bmatrix} g_i^{00} & g_i^{01} & g_i^{02} & \cdots \\ g_i^{10} & g_i^{11} & g_i^{12} & \cdots \\ g_i^{20} & g_i^{21} & g_i^{12} & \cdots \\ \vdots & \vdots & \vdots & \ddots \end{bmatrix}$$

where g_i^{nm} is the Green's function's cross sector between the terminal cells n and m. Even though these last three matrices are semi-infinite in at least one of their dimensions, we easily see that such multiplication reduces to the following finite matrix multiplication:

$$\Sigma_i = h^0_{Ci} g_i^{00} h^0_{iC} \tag{3.83}$$

due to the zeros in h_{Ci} and h_{iC}. Since the Hamiltonian matrix is usually known, the problem is now limited to obtaining the electrode's surface GF (g_i^{00}).

3.9 Electrode's surface GF: iterative method

In this section we summarize a method, developed by Lopez Sancho in [107], to calculate the surface GF for a semi-infinite system. In order to calculate g_i^{00} we write the GF defining equation for the semi-infinite lead:

$$\begin{bmatrix} (\varepsilon - h_i^{00}) & -h_i^{01} & 0 & 0 & \cdots \\ -h_i^{10} & (\varepsilon - h_i^{11}) & -h_i^{12} & 0 & \cdots \\ 0 & -h_i^{21} & (\varepsilon - h_i^{22}) & -h_i^{23} & \cdots \\ 0 & 0 & -h_i^{32} & (\varepsilon - h_i^{33}) & \cdots \\ \vdots & \vdots & \vdots & \vdots & \ddots \end{bmatrix} \begin{bmatrix} G_{00} & G_{01} & G_{02} & G_{03} & \cdots \\ G_{10} & G_{11} & G_{12} & G_{13} & \cdots \\ G_{20} & G_{21} & G_{22} & G_{23} & \cdots \\ G_{30} & G_{31} & G_{32} & G_{33} & \cdots \\ \vdots & \vdots & \vdots & \vdots & \ddots \end{bmatrix} =$$

$$= \begin{bmatrix} I & 0 & 0 & 0 & \cdots \\ 0 & I & 0 & 0 & \cdots \\ 0 & 0 & I & 0 & \cdots \\ 0 & 0 & 0 & I & \cdots \\ \vdots & \vdots & \vdots & \vdots & \ddots \end{bmatrix} \tag{3.84}$$

where, by symmetry, we can write $h_i^{jj} = h_i^{00}$, $h_i^{j,j+1} = h_i^{01}$ and $h_i^{j+1,j} = h_i^{10}$. By using the upper left term from this equation we have:

$$(\varepsilon - h_i^{00})G_{00} - h_i^{01}G_{10} = I$$

$$(\varepsilon - h_i^{00})G_{00} = I + h_i^{01}G_{10} \tag{3.85}$$

on the other hand, for the other terms from the first column, we have:

$$-h_i^{10}G_{X-1,0} + (\varepsilon - h_i^{00})G_{X0} - h_i^{01}G_{X+1,0} = 0$$

$$(\varepsilon - h_i^{00})G_{X0} = h_i^{10}G_{X-1,0} + h_i^{01}G_{X+1,0}. \tag{3.86}$$

Setting $X = 1$ in Equation 3.86 and substituting G_{10} into the expression for G_{00} we have:

$$(\varepsilon - h_i^{00})G_{00} = I + h_i^{01}(\varepsilon - h_i^{00})^{-1}\left(h_i^{10}G_{00} + h_i^{01}G_{2,0}\right) \tag{3.87}$$

$$(\varepsilon - h_i^{00} - h_i^{01}(\varepsilon - h_i^{00})^{-1}h_i^{10})G_{00} = I + h_i^{01}(\varepsilon - h_i^{00})^{-1}h_i^{01}G_{2,0} \tag{3.88}$$

$$(\varepsilon - \varepsilon_i^{1s})G_{00} = I + \alpha_i^1 G_{2,0}. \tag{3.89}$$

If we make $X \to X \pm 1$ in Equation 3.86 we have:

$$G_{X+1,0} = (\varepsilon - h_i^{00})^{-1}\left(h_i^{10}G_{X,0} + h_i^{01}G_{X+2,0}\right) \tag{3.90}$$

$$G_{X-1,0} = (\varepsilon - h_i^{00})^{-1}\left(h_i^{10}G_{X-2,0} + h_i^{01}G_{X,0}\right). \tag{3.91}$$

Substituting these in Eq. 3.86 we have:

$$(\varepsilon - h_i^{00})G_{X0} = h_i^{10}(\varepsilon - h_i^{00})^{-1}\left(h_i^{10}G_{X-2,0} + h_i^{01}G_{X,0}\right) + h_i^{01}(\varepsilon - h_i^{00})^{-1}\left(h_i^{10}G_{X,0} + h_i^{01}G_{X+2,0}\right) \tag{3.92}$$

$$\begin{aligned}(\varepsilon - h_i^{00} - h_i^{10}(\varepsilon - h_i^{00})^{-1}h_i^{01} - h_i^{01}(\varepsilon - h_i^{00})^{-1}h_i^{10})G_{X0} = \\ h_i^{10}(\varepsilon - h_i^{00})^{-1}h_i^{10}G_{X-2,0} + h_i^{01}(\varepsilon - h_i^{00})^{-1}h_i^{01}G_{X+2,0}\end{aligned} \tag{3.93}$$

$$(\varepsilon - \varepsilon_i^1)G_{X0} = \beta_i^1 G_{X-2,0} + \alpha_i^1 G_{X+2,0}. \tag{3.94}$$

Making $X \to 2X$ in the last two results we can identify the following analogy:

$$\begin{aligned}(\varepsilon - h_i^{00})G_{00} = I + h_i^{01}G_{10} \quad &\to \quad (\varepsilon - \varepsilon_i^{1s})G_{00} = I + \alpha_i^1 G_{2,0} \\ (\varepsilon - h_i^{00})G_{X0} = h_i^{10}G_{X-1,0} + h_i^{01}G_{X+1,0} \quad &\to \quad (\varepsilon - \varepsilon_i^{1})G_{2X,0} = \beta_i^1 G_{2(X-1),0} + \alpha_i^1 G_{2(X+1),0}.\end{aligned} \tag{3.95}$$

The new equations can be viewed as describing a new system with a unit cell equivalent to two unit cells from the original semi-infinite system and having the new Hamiltonian:

$$\begin{bmatrix} \varepsilon_i^{1s} & \alpha_i^1 & 0 & 0 & \dots \\ \beta_i^1 & \varepsilon_i^1 & \alpha_i^1 & 0 & \dots \\ 0 & \beta_i^1 & \varepsilon_i^1 & \alpha_i^1 & \dots \\ 0 & 0 & \beta_i^1 & \varepsilon_i^1 & \dots \\ \vdots & \vdots & \vdots & \vdots & \ddots \end{bmatrix}. \tag{3.96}$$

If we keep repeating this process $n-1$ more times, we will have a new system corresponding to 2^n unit cells. After doing that we will have the following set of equations:

$$(\varepsilon - \varepsilon_i^{ns})G_{00} = I + \alpha_i^n G_{2^n,0} \tag{3.97}$$

$$(\varepsilon - \varepsilon_i^{n})G_{2^nX,0} = \beta_i^n G_{2^n(X-1),0} + \alpha_i^n G_{2^n(X+1),0} \tag{3.98}$$

$$\varepsilon_i^{ns} = \varepsilon_i^{(n-1)s} + \alpha_i^{(n-1)}(\varepsilon - \varepsilon_i^{n-1})^{-1}\beta_i^{(n-1)} \tag{3.99}$$

$$\varepsilon_i^{n} = \varepsilon_i^{(n-1)} + \beta_i^{(n-1)}(\varepsilon - \varepsilon_i^{n-1})^{-1}\alpha_i^{(n-1)} + \alpha_i^{(n-1)}(\varepsilon - \varepsilon_i^{n-1})^{-1}\beta_i^{(n-1)} \tag{3.100}$$

$$\alpha_i^{n} = \alpha_i^{(n-1)}(\varepsilon - \varepsilon_i^{n-1})^{-1}\alpha_i^{(n-1)} \tag{3.101}$$

$$\beta_i^{n} = \beta_i^{(n-1)}(\varepsilon - \varepsilon_i^{n-1})^{-1}\beta_i^{(n-1)}. \tag{3.102}$$

Since the new unit cell corresponds now to 2^n unit cells from the original system, one expect that at some point the matrices α_i^n get very small, in such a way that we can ignore them and write (with the aid of Eq. 3.97):

$$(\varepsilon - \varepsilon_i^{ns})G_{00} = I \quad \to \quad G_{00} = (\varepsilon - \varepsilon_i^{ns})^{-1} \tag{3.103}$$

finally obtaining the surface GF for the terminal i.

This method is applied in the TRANSFOR package which will be described in the next chapter and that was used to obtain part of the results presented in this thesis.

3.10 Electrode's surface GF: transfer matrices

In this section we present another method, developed earlier by Lopez Sancho and coworkers [108], to determine the surface GF for the semi-infinite lead. If we take Eq. 3.86 we can write:

$$G_{X0} = t_0 G_{X-1,0} + \tilde{t}_0 G_{X+1,0} \tag{3.104}$$

with

$$t_0 = (\varepsilon - h_i^{00})^{-1} h_i^{10} \qquad \tilde{t}_0 = (\varepsilon - h_i^{00})^{-1} h_i^{01}. \tag{3.105}$$

On the other hand, we can write:

$$G_{X-1,0} = t_0 G_{X-2,0} + \tilde{t}_0 G_{X,0} \tag{3.106}$$

$$G_{X+1,0} = t_0 G_{X,0} + \tilde{t}_0 G_{X+2,0} \tag{3.107}$$

and substitute in Eq. 3.104:

$$G_{X0} = t_0 \left(t_0 G_{X-2,0} + \tilde{t}_0 G_{X,0}\right) + \tilde{t}_0 \left(t_0 G_{X,0} + \tilde{t}_0 G_{X+2,0}\right) \tag{3.108}$$

$$G_{X0} = t_1 G_{X-2,0} + \tilde{t}_1 G_{X+2,0} \tag{3.109}$$

$$t_1 = (I - t_0\tilde{t}_0 - \tilde{t}_0 t_0)^{-1} t_0^2 \qquad \tilde{t}_1 = (I - t_0\tilde{t}_0 - \tilde{t}_0 t_0)^{-1} \tilde{t}_0^2. \tag{3.110}$$

If we keep repeating this process we will end up with:

$$G_{X0} = t_l G_{X-2^l,0} + \tilde{t}_l G_{X+2^l,0} \tag{3.111}$$

$$t_l = (I - t_{l-1}\tilde{t}_{l-1} - \tilde{t}_{l-1} t_{l-1})^{-1} t_{l-1}^2 \tag{3.112}$$

$$\tilde{t}_l = (I - t_{l-1}\tilde{t}_{l-1} - \tilde{t}_{l-1} t_{l-1})^{-1} \tilde{t}_{l-1}^2. \tag{3.113}$$

If we make $X = 2^l + j$ and $l = 0, 1, 2, 3, ...$ we will have:

$$\begin{aligned} G_{j+1,0} &= t_0 G_{j,0} + \tilde{t}_0 G_{j+2,0} \\ G_{j+2,0} &= t_1 G_{j,0} + \tilde{t}_1 G_{j+4,0} \\ G_{j+4,0} &= t_2 G_{j,0} + \tilde{t}_2 G_{j+8,0} \\ &\vdots \\ G_{2^l+j,0} &= t_l G_{j,0} + \tilde{t}_l G_{2^{l+1}+j,0}. \end{aligned} \tag{3.114}$$

If we substitute the second, the third, the fourth and the other equations successively on the first one we will obtain:

$$\begin{aligned} G_{j+1,0} &= t_0 G_{j,0} + \tilde{t}_0 G_{j+2,0} \\ &= (t_0 + \tilde{t}_0 t_1) G_{j,0} + \tilde{t}_0 \tilde{t}_1 G_{j+4,0} \\ &= (t_0 + \tilde{t}_0 t_1 + \tilde{t}_0 \tilde{t}_1 t_2) G_{j,0} + \tilde{t}_0 \tilde{t}_1 \tilde{t}_2 G_{j+8,0} \\ &= (t_0 + \tilde{t}_0 t_1 + \tilde{t}_0 \tilde{t}_1 t_2 + \tilde{t}_0 \tilde{t}_1 \tilde{t}_2 t_3) G_{j,0} + \tilde{t}_0 \tilde{t}_1 \tilde{t}_2 \tilde{t}_3 G_{j+16,0} \\ &\vdots \\ &= (t_0 + \tilde{t}_0 t_1 + \tilde{t}_0 \tilde{t}_1 t_2 + \tilde{t}_0 \tilde{t}_1 \tilde{t}_2 t_3 + \cdots + \tilde{t}_0 \tilde{t}_1 \tilde{t}_2 \tilde{t}_3 \cdots \tilde{t}_{l-1} t_l) G_{j,0} + \tilde{t}_0 \tilde{t}_1 \tilde{t}_2 \tilde{t}_3 \cdots \tilde{t}_l G_{j+2^{l+1},0}. \end{aligned} \tag{3.115}$$

At some point, we will reach a situation in which t_l and $\tilde{t}_l$ are either zero or negligible. At this point we can write:

$$G_{2^l+j,0} = t_l G_{j,0} + \tilde{t}_l G_{2^{l+1}+j,0} \approx 0 \tag{3.116}$$

and:

$$G_{j+1,0} = T G_{j,0} \approx (t_0 + \tilde{t}_0 t_1 + \tilde{t}_0 \tilde{t}_1 t_2 + \tilde{t}_0 \tilde{t}_1 \tilde{t}_2 t_3 + \cdots + \tilde{t}_0 \tilde{t}_1 \tilde{t}_2 \tilde{t}_3 \cdots \tilde{t}_{l-1} t_l) G_{j,0} \tag{3.117}$$

where

$$T = t_0 + \tilde{t}_0 t_1 + \tilde{t}_0 \tilde{t}_1 t_2 + \tilde{t}_0 \tilde{t}_1 \tilde{t}_2 t_3 + \cdots \tag{3.118}$$

is the $j \to j+1$ matrix. An analogous procedure gives us the $j \to j-1$ matrix:

$$G_{j-1,0} = \overline{T} G_{j,0} \qquad \overline{T} = \tilde{t}_0 + t_0 \tilde{t}_1 + t_0 t_1 \tilde{t}_2 + t_0 t_1 t_2 \tilde{t}_3 + \cdots \tag{3.119}$$

If we set $j = 0$ we have $G_{1,0} = T G_{0,0}$. Substituting in Eq. 3.85 we finally obtain the surface GF for the terminal i:

$$G_{00} = (\varepsilon - h_i^{00} - h_i^{01} T)^{-1}. \tag{3.120}$$

This method is applied in the TRANSPLAYER package [109] which was used to obtain part of the transport results presented in this thesis.

3.11 Non-orthogonal basis

So far we considered an orthonormal basis. The corresponding extension for the non-orthogonal case is straightforward. In this scenario we have to modify Equation 3.48 to [110]:

$$(\varepsilon S - H)G = I \tag{3.121}$$

which can be rewritten in a suggestive form:

$$\Big(\varepsilon I - \big(H - \varepsilon(S-I)\big)\Big)G = (\varepsilon I - H')G = I \tag{3.122}$$

and we can take advantage of the tools described above, but now applied to the modified Hamiltonian $H' = H - \varepsilon(S-I)$.

3.12 The next step

In principle, we are now able to do transport calculations at the nanoscale (once we have the system's Hamiltonian). However, calculating the GF can be problematic as the system in consideration gets larger. This is because the computational cost involved in the GF calculation increases with N^3, where N is the system's size (since it involves a matrix inversion).

The next chapter is dedicated to this issue. There we present a powerful method to obtain the GF from Equation 3.56. In addition, we will also present the adaptation we developed to apply the method in a parallel scheme.

4 Conductor Green's function

4.1 Introduction

Calculating the Green's function (GF) is, in principle, a simple task within the LCAO method: once we have the Hamiltonian and self-energies, we only need to perform a matrix inversion. However, even though there are well-known algorithms and numerical packages to do such elementary algebra, this process can be computationally very expensive as inversion of a $N \times N$ matrix is a process which scales with N^3.

The knitting algorithm [111] (that will be presented in Section 4.4) is a powerful method to obtain the GF needed to describe the electronic transport in nanoscopic systems. In this procedure, the GF of a system composed of single orbital sites (or atoms) is obtained by a process in which the system is constructed site by site. At each step, one atom is "added" and a temporary GF corresponding to the incomplete system is computed. After the last step we end up with the GF for the whole system. One of the most important characteristics of this method is that no matrix inversion is performed. The GF at each step is obtained from the previous step by simple recurrence relations. In principle, one can apply the knitting algorithm to calculate the whole GF. However, the method can be restricted to the calculation of just a GF's subset. If one is interested only in transport properties like conductance, for instance, it is only necessary to calculate the GF elements among the atoms connected to the electrodes. This avoids a large amount of unnecessary work and makes the algorithm extremely fast. However, it is still possible to recover local information by using the sewing algorithm [111] (that will be presented in Section 4.5).

In this chapter, after presenting the original knitting and sewing algorithms in Sections 4.4 and 4.5, we develop an extension to a parallel approach in which the studied system is divided into a number of domains. In this patchwork algorithm, the different domains are then built simultaneously and independently by different processors in order to be joined up together later on, resulting in the final GF. Finally, we end the chapter describing the TRANSFOR package we developed to apply knitting and sewing algorithms in their patchwork extension. This pack-

age is used to perform part of the electronic transport calculations in this thesis (namely those presented in Chapter 9).

4.2 Dyson's equation

In each step of knitting-sewing algorithm, the fundamental tool to be used is the Dyson's equation. It relates the GF for a system before and after turning on a given perturbation. Let us consider a system with a Hamiltonian H_0 expressed in a localized basis. Its corresponding GF G_0 is:

$$G_0 = [\varepsilon I - H_0]^{-1}. \tag{4.1}$$

Let us now consider a perturbation V so that the new Hamiltonian describing the system is $H = H_0 + V$. The new GF G is obtained by:

$$G = [\varepsilon I - H_0 - V]^{-1}. \tag{4.2}$$

In principle, this can only be done for energies that are not poles of the GF. This problem is avoided by adding a small imaginary part to ε. If we multiply both side on the left by $[\varepsilon I - H_0 - V]$ we obtain:

$$[\varepsilon I - H_0 - V]G = I \quad \rightarrow \quad [\varepsilon I - H_0]G - VG = I \quad \rightarrow \quad G_0^{-1}G = I + VG \tag{4.3}$$

and finally multiplying by G_0 on the left:

$$\boxed{G = G_0 + G_0 V G} \tag{4.4}$$

which constitutes the Dyson's equation suitable for our problem. If we repeat the same process but going from the Hamiltonian H to H_0 by subtracting $-V$ (or by multiplying $[\varepsilon I - H_0 - V]$ on the right) we obtain:

$$\boxed{G = G_0 + G V G_0} \tag{4.5}$$

which is the Dyson's equation for the reverse process. The equations 4.4 and 4.5 are the basis of the methods described in this chapter and will be repeatedly used in the next sections.

4.3 Setup

We will present the knitting algorithm description by considering a finite isolated system. A way to understand the knitting algorithm is to consider that the system is already complete but with no interaction between the sites. In other words, we have a system described by a diagonal Hamiltonian having the site energies as diagonal elements. Since the inverse of a diagonal Hamiltonian is also diagonal, the GF for this initial system is diagonal with elements:

$$G^0_{XY} = \frac{\delta_{XY}}{E - \varepsilon_X}. \tag{4.6}$$

The act of "adding" an atom consists in turning on the interaction between it and all the atoms which have already been added before, as depicted for the 9-atom system shown in Fig. 4.1.

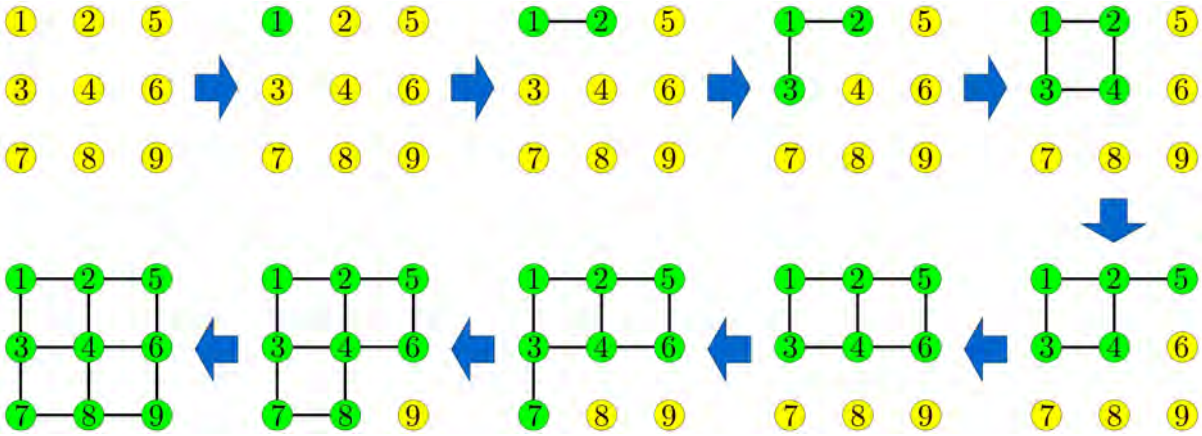

Figure 4.1: Illustration of the knitting procedure for a 9-site system with first-neighbor interactions only. We start with a set of non-interacting sites. By adding site number 2, we consider its interaction with the previous site number 1. When adding 3, we should account for its interaction with previous sites 1 and 2 (interaction 2-3 is null in this case). As the process is conducted, we finish by adding site 9 accounting for its interactions with all the previous atoms (non-null only for sites 6 and 8 in this case). After adding all the sites we have the final GF.

Let $G^{\mathscr{A}-1}$ represent the GF just before the $\mathscr{A}$ step and $G^{\mathscr{A}}$ represent the GF just after the $\mathscr{A}$ step. Dyson's equation gives us:

$$G^{\mathscr{A}} = G^{\mathscr{A}-1} + G^{\mathscr{A}-1} V G^{\mathscr{A}} \tag{4.7}$$

$$G^{\mathscr{A}}_{XY} = G^{\mathscr{A}-1}_{XY} + \sum_{ZW} G^{\mathscr{A}-1}_{XZ} V_{ZW} G^{\mathscr{A}}_{WY} \tag{4.8}$$

where V represents the interaction between $\mathscr{A}$ and the already added atoms. It is also convenient to write this equation in its reverse form:

$$G^{\mathscr{A}-1} = G^{\mathscr{A}} - G^{\mathscr{A}} V G^{\mathscr{A}-1} \tag{4.9}$$

$$G^{\mathscr{A}-1}_{XY} = G^{\mathscr{A}}_{XY} - \sum_{ZW} G^{\mathscr{A}}_{XZ} V_{ZW} G^{\mathscr{A}-1}_{WY}. \tag{4.10}$$

The values for all the elements involving atoms not added yet are still those from G^0.

Let us focus on the step where we have constructed the system until the $(\mathscr{A}-1)$ site and we are about to add the $\mathscr{A}$ site. There are special designations for the atoms involved in this knitting step:

- $\mathscr{A}$ site: the site which will be added in the current step;
- *Connected Atoms* (CA): those atoms (or sites) which have already been added in the knitting and that interact with $\mathscr{A}$ by means of non-null Hamiltonian elements. These atoms will be labeled by σ;
- *Surface Atoms* (SA): those atoms which have already been added during the knitting, but that have neighbors which have not been added yet. By neighbors we mean two atoms interacting by means of non-null Hamiltonian elements. SAs will be labeled by Latin letters. Note that the CAs are a special kind of SA;
- *Greek Atoms* (GA): those atoms belonging to the conductor, but which are connected to the terminals through nonzero Hamiltonian elements. These atoms will be labeled by Greek letters (except σ).

When we refer to an atom and we do not know which kind of atom it is, we will represent it by a capital Latin letter.

For our isolated system, the Hamiltonian has elements:

$$\mathbf{H}_{isolated} = [h_{XY}] \quad \rightarrow \quad h_{XX} = \varepsilon_X \tag{4.11}$$

$$\rightarrow \quad h_{XY} = t_{XY} \quad X, \text{ and } Y \text{ neighbors} \tag{4.12}$$

$$\rightarrow \quad h_{XY} = 0 \quad X, \text{ and } Y \text{ not neighbors.} \tag{4.13}$$

With this terminology, we can write the V_{ZW} for the isolated system as:

$$V_{ZW} = \sum_{\sigma} \delta_{Z\sigma}\delta_{W\mathscr{A}} t_{\sigma\mathscr{A}} + \sum_{\sigma} \delta_{Z\mathscr{A}}\delta_{W\sigma} t_{\mathscr{A}\sigma} \tag{4.14}$$

or in another way:

$$\begin{aligned} V_{\sigma\mathscr{A}} &= t_{\sigma\mathscr{A}} \\ V_{\mathscr{A}\sigma} &= t_{\mathscr{A}\sigma} \\ V_{ZW} &= 0 \quad \text{otherwise.} \end{aligned} \tag{4.15}$$

In the case of a finite conductor attached to a number of semi-infinite electrodes, represented by the self-energies Σ^n, we can map the conductor part of this system onto an isolated system with a new Hamiltonian defined by:

$$\mathbf{H}_{isolated} = \mathbf{H}_{conductor} + \sum_{terminals} \Sigma^n = [H_{XY}] \tag{4.16}$$

$$H_{XY} = h_{XY} + \sum_{terminals} \Sigma^n_{XY} \tag{4.17}$$

and apply the knitting algorithm by using the CA, SA and GA concepts to this new Hamiltonian. Now we will show how to apply Dyson's equation to conduct the knitting and sewing steps.

4.4 Knitting Algorithm

Let $G^{\mathscr{A}}$ denote the Green's function for the $\mathscr{A}$-th step. We can calculate the $G^{\mathscr{A}}_{\mathscr{A}\mathscr{A}}$ element by inverting a 1×1 Hamiltonian and describing the remaining system by a self energy $\Sigma^{\mathscr{A}-1}$

$$\boxed{G^{\mathscr{A}}_{\mathscr{A}\mathscr{A}} = \frac{1}{E - H_{\mathscr{A}\mathscr{A}} - \Sigma^{\mathscr{A}-1}}} \tag{4.18}$$

with

$$\Sigma^{\mathscr{A}-1} = \sum_{\sigma\sigma'} H_{\mathscr{A}\sigma} G^{\mathscr{A}-1}_{\sigma\sigma'} H_{\sigma'\mathscr{A}}. \tag{4.19}$$

For X being a SA or a GA ($X = i, \alpha$) we can write:

$$G^{\mathscr{A}}_{X\mathscr{A}} = G^{\mathscr{A}-1}_{X\mathscr{A}} + \sum_{ZW} G^{\mathscr{A}-1}_{XZ} V_{ZW} G^{\mathscr{A}}_{W\mathscr{A}} \tag{4.20}$$

$$\boxed{G^{\mathscr{A}}_{X\mathscr{A}} = \sum_{\sigma} G^{\mathscr{A}-1}_{X\sigma} H_{\sigma\mathscr{A}} G^{\mathscr{A}}_{\mathscr{A}\mathscr{A}}} \tag{4.21}$$

and (using the reverse form from Dyson equation - Eq. 4.5):

$$G^{\mathscr{A}-1}_{\mathscr{A}X} = G^{\mathscr{A}}_{\mathscr{A}X} - \sum_{ZW} G^{\mathscr{A}}_{\mathscr{A}Z} V_{ZW} G^{\mathscr{A}-1}_{WX} \tag{4.22}$$

$$\boxed{G^{\mathscr{A}}_{\mathscr{A}X} = \sum_{\sigma} G^{\mathscr{A}}_{\mathscr{A}\mathscr{A}} H_{\mathscr{A}\sigma} G^{\mathscr{A}-1}_{\sigma X}.} \tag{4.23}$$

Also, for $X,Y = i,\alpha$ we have:

$$G^{\mathscr{A}}_{XY} = G^{\mathscr{A}-1}_{XY} + \sum_{ZW} G^{\mathscr{A}-1}_{XZ} V_{ZW} G^{\mathscr{A}}_{WY} = G^{\mathscr{A}-1}_{XY} + \sum_{\sigma} G^{\mathscr{A}-1}_{X\sigma} H_{\sigma\mathscr{A}} G^{\mathscr{A}}_{\mathscr{A}Y} \tag{4.24}$$

$$G^{\mathscr{A}}_{XY} = G^{\mathscr{A}-1}_{XY} + \left(\sum_{\sigma} G^{\mathscr{A}-1}_{X\sigma} H_{\sigma\mathscr{A}} \right) G^{\mathscr{A}}_{\mathscr{A}Y} \tag{4.25}$$

but from Equation 4.21 for the $G^{\mathscr{A}}_{X\mathscr{A}}$ term we have:

$$G^{\mathscr{A}}_{X\mathscr{A}} = \sum_{\sigma} G^{\mathscr{A}-1}_{X\sigma} H_{\sigma\mathscr{A}} G^{\mathscr{A}}_{\mathscr{A}\mathscr{A}} \tag{4.26}$$

$$\sum_{\sigma} G^{\mathscr{A}-1}_{X\sigma} H_{\sigma\mathscr{A}} = G^{\mathscr{A}}_{X\mathscr{A}} \frac{1}{G^{\mathscr{A}}_{\mathscr{A}\mathscr{A}}} \tag{4.27}$$

so that:

$$\boxed{G^{\mathscr{A}}_{XY} = G^{\mathscr{A}-1}_{XY} + G^{\mathscr{A}}_{X\mathscr{A}} \frac{1}{G^{\mathscr{A}}_{\mathscr{A}\mathscr{A}}} G^{\mathscr{A}}_{\mathscr{A}Y}.} \tag{4.28}$$

In each knitting step, we use Equation 4.18 and Equations 4.21, 4.23 and 4.28 for $X,Y = i,\alpha$, that is, for the surface and Greek atoms. The reason to use this set of equations for the Greek atoms is straightforward, since the elements involving these atoms will give us the conductance between all the pairs of terminals. The reason for calculating the elements for all the SA (and not only for the CAs from the next step) is that they will be CAs in the future and we must update them in every step (before adding all their neighbors) in order to have them when they are needed.

In the end of this process, we will have all the GF elements between the GAs and we will be able to calculate the conductance between all the terminals. We will not have, however, the diagonal elements (necessary to calculate the DOS) and other elements necessary to calculate local properties. For these elements, we have to use another procedure called "sewing" algorithm, which will be explained in the following section.

4.5 Sewing Algorithm

Let $\mathscr{A}$ be an arbitrary atom from the conductor. Consider the case in which we are interested in three kinds of GF elements:

- $G_{\mathscr{A}\alpha}$ and $G_{\alpha\mathscr{A}}$ - elements between $\mathscr{A}$ and the GAs;

- $G_{\mathscr{A}n_{\mathscr{A}}}$ and $G_{n_{\mathscr{A}}\mathscr{A}}$ - elements between $\mathscr{A}$ and all its neighbors $n_{\mathscr{A}}$;
- $G_{\mathscr{A}\mathscr{A}}$ - the diagonal element involving $\mathscr{A}$.

These terms can be calculated by the so called sewing algorithm. The sewing procedure can only be started once we finish the knitting. Then the sewing is conducted backwards by sewing the sites on the reverse order (starting from the last atom to the first). In order to sew the site $\mathscr{A}$ and obtain the desired terms, we consider the knitting step just after adding the site $\mathscr{A}$. We then consider two processes:

1. Adding the remaining system (after $\mathscr{A}$) at once, obtaining the final GF;
2. The inverse process in which we remove the remaining system (from $\mathscr{A}+1$ to the end) from the complete system.

We will now consider separately the atoms from both sides of the interface corresponding to these two processes. Namely, the *left* system (from the beginning to $\mathscr{A}$) and the *right* system (from $\mathscr{A}+1$ to the end). We then have to clarify a new terminology:

- *Left Surface Atoms* (LSA): already added atoms (that is, atoms to the "left" of $\mathscr{A}$) which have not already added neighbors. They will be represented by Latin letters without a prime;
- *Right Surface Atoms* (RSA): atoms still to be added (that is, atoms to the "right" of $\mathscr{A}$) which have neighbors who have already been added. They will be represented by Latin letters with a prime;
- *Undefined Surface Atoms* (USA): the set of atoms encompassing both left and right surfaces. When we do not know from which surface the atoms is, we will refer to it as an USA. They will be represented by double primed Latin letters;
- *Left Greek Atoms* (LGA): GAs which have already been added before $\mathscr{A}$. They will be represented by Greek letters without a prime;
- *Right Greek Atoms* (RGA): GAs which have not been added yet before $\mathscr{A}$. They will be represented by Greek letters with a prime.

When we refer to atoms which can be either a surface or a Greek atom, they will be identified by a capital Latin letter without a prime when they are "left" atoms (that is, when they have already been added before $\mathscr{A}$) and by a primed capital Latin letter when they are "right" atoms

(that is, when they have not been added yet before $\mathscr{A}$). Capital double primed Latin letters can represent either a right or a left atom. Dyson equation allows us to write the following equations for the two processes:

$$1^{st} \quad \rightarrow \quad G_{X\mathscr{A}} = G^{\mathscr{A}}_{X\mathscr{A}} + \sum_{Y''Z''} G^{\mathscr{A}}_{XY''} V_{Y''Z''} G_{Z''\mathscr{A}} \tag{4.29}$$

$$1^{st} \quad \rightarrow \quad G_{\mathscr{A}X} = G^{\mathscr{A}}_{\mathscr{A}X} + \sum_{Y''Z''} G^{\mathscr{A}}_{\mathscr{A}Y''} V_{Y''Z''} G_{Z''X} \tag{4.30}$$

$$2^{nd} \quad \rightarrow \quad G^{\mathscr{A}}_{X\mathscr{A}} = G_{X\mathscr{A}} - \sum_{Y''Z''} G_{XY''} V_{Y''Z''} G^{\mathscr{A}}_{Z''\mathscr{A}} \tag{4.31}$$

$$2^{nd} \quad \rightarrow \quad G^{\mathscr{A}}_{\mathscr{A}X} = G_{\mathscr{A}X} - \sum_{Y''Z''} G_{\mathscr{A}Y''} V_{Y''Z''} G^{\mathscr{A}}_{Z''X} \tag{4.32}$$

but:

$$V_{ij'} = H_{ij'}; \quad V_{i'j} = H_{i'j}; \quad V_{Y''Z''} = 0 \quad \text{(all other cases)}$$

and

$$G^{\mathscr{A}}_{i'\mathscr{A}} = G^{\mathscr{A}}_{Xi'} = G^{\mathscr{A}}_{j'X} = G^{\mathscr{A}}_{\mathscr{A}i'} = 0$$

so that

$$1^{st} \quad \rightarrow \quad G_{X\mathscr{A}} = G^{\mathscr{A}}_{X\mathscr{A}} + \sum_{ij'} G^{\mathscr{A}}_{Xi} H_{ij'} G_{j'\mathscr{A}} \tag{4.33}$$

$$1^{st} \quad \rightarrow \quad G_{\mathscr{A}X} = G^{\mathscr{A}}_{\mathscr{A}X} + \sum_{ij'} G^{\mathscr{A}}_{\mathscr{A}i} H_{ij'} G_{j'X} \tag{4.34}$$

$$2^{nd} \quad \rightarrow \quad G_{X\mathscr{A}} = G^{\mathscr{A}}_{X\mathscr{A}} + \sum_{i'j} G_{Xi'} H_{i'j} G^{\mathscr{A}}_{j\mathscr{A}} \tag{4.35}$$

$$2^{nd} \quad \rightarrow \quad G_{\mathscr{A}X} = G^{\mathscr{A}}_{\mathscr{A}X} + \sum_{i'j} G_{\mathscr{A}i'} H_{i'j} G^{\mathscr{A}}_{jX}. \tag{4.36}$$

But the equations for the first process are also valid for the $G_{Xi'}$ and $G_{\mathscr{A}i'}$ terms (needed for the equations for the second process). So, if we change $\mathscr{A}$ (only in the subscripts) to i' in the first equation and X to i' in the second, we will have:

$$G_{Xi'} = G^{\mathscr{A}}_{Xi'} + \sum_{ij'} G^{\mathscr{A}}_{Xi} H_{ij'} G_{j'i'} = \sum_{ij'} G^{\mathscr{A}}_{Xi} H_{ij'} G_{j'i'} \tag{4.37}$$

$$G_{\mathscr{A}i'} = G^{\mathscr{A}}_{\mathscr{A}i'} + \sum_{ij'} G^{\mathscr{A}}_{\mathscr{A}i} H_{ij'} G_{j'i'} = \sum_{ij'} G^{\mathscr{A}}_{\mathscr{A}i} H_{ij'} G_{j'i'} \tag{4.38}$$

which, when substituted in the equations for the second process, give:

$$G_{X\mathscr{A}} = G^{\mathscr{A}}_{X\mathscr{A}} + \sum_{i'j}\sum_{ij'} G^{\mathscr{A}}_{Xi} H_{ij'} G_{j'i'} H_{i'j} G^{\mathscr{A}}_{j\mathscr{A}} = G^{\mathscr{A}}_{X\mathscr{A}} + \sum_{ij} G^{\mathscr{A}}_{Xi} \left(\sum_{i'j'} H_{ij'} G_{j'i'} H_{i'j} \right) G^{\mathscr{A}}_{j\mathscr{A}} \tag{4.39}$$

$$G_{\mathscr{A}X} = G^{\mathscr{A}}_{\mathscr{A}X} + \sum_{i'j}\sum_{ij'} G^{\mathscr{A}}_{\mathscr{A}i} H_{ij'} G_{j'i'} H_{i'j} G^{\mathscr{A}}_{jX} = G^{\mathscr{A}}_{\mathscr{A}X} + \sum_{ij} G^{\mathscr{A}}_{\mathscr{A}i} \left(\sum_{i'j'} H_{ij'} G_{j'i'} H_{i'j} \right) G^{\mathscr{A}}_{jX} \tag{4.40}$$

$$\boxed{G_{X\mathscr{A}} = G^{\mathscr{A}}_{X\mathscr{A}} + \sum_{ij} G^{\mathscr{A}}_{Xi} S_{ij} G^{\mathscr{A}}_{j\mathscr{A}}} \tag{4.41}$$

$$\boxed{G_{\mathscr{A}X} = G^{\mathscr{A}}_{\mathscr{A}X} + \sum_{ij} G^{\mathscr{A}}_{\mathscr{A}i} S_{ij} G^{\mathscr{A}}_{jX}} \tag{4.42}$$

with:

$$S_{ij} = \sum_{i'j'} H_{ij'} G_{j'i'} H_{i'j}. \tag{4.43}$$

Finally, if we use the first equation from the second process and the second equation from the first process by changing X to X' we will have:

$$\boxed{G_{X'\mathscr{A}} = \sum_{i'j} G_{X'i'} H_{i'j} G^{\mathscr{A}}_{j\mathscr{A}}} \tag{4.44}$$

$$\boxed{G_{\mathscr{A}X'} = \sum_{ij'} G^{\mathscr{A}}_{\mathscr{A}i} H_{ij'} G_{j'X'}.} \tag{4.45}$$

At each step, we also use equations 4.41, 4.42, 4.44 and 4.45 to compute the $G_{\mathscr{A}X''}$ and $G_{X''\mathscr{A}}$ terms, where X'' ranges among all the GAs and RSAs. By doing this, in the end of the algorithm we will have the GF elements between every atom in the conductor and all the GAs. In addition, we will have all the elements between any atom and its neighbors. This is because in the $\mathscr{A}$ step we calculate all the elements between $\mathscr{A}$ and its neighbors on the right. If $\mathscr{A}$ has any neighbor on its left it will be in the right surface for the future steps corresponding to its left neighbors and the terms between $\mathscr{A}$ and their left neighbors will be calculated.

Finally, we can calculate the diagonal element involving $\mathscr{A}$ using either equation 4.41 or 4.42 by substituting X by $\mathscr{A}$:

$$\boxed{G_{\mathscr{A}\mathscr{A}} = G^{\mathscr{A}}_{\mathscr{A}\mathscr{A}} + \sum_{ij} G^{\mathscr{A}}_{\mathscr{A}i} S_{ij} G^{\mathscr{A}}_{j\mathscr{A}}.} \tag{4.46}$$

4.6 Multiple Knitting and Domains Approach - Patchwork Algorithm

Here we adapt the original knitting and sewing algorithms into a suitable parallel procedure where our system is composed of parts called domains. Here we use one processor for each domain. When the domains are done, they are merged two-by-two until we end up with the complete system. These steps are described in this and in the next sections.

Let us start by breaking up our system into a number of domains. Inside each domain, we can identify two different types of atoms:

1. Domain Surface Atoms (DSA): atoms which have atoms from other domains as neighbors;

2. Domain Internal Atoms (DIA): atoms which do not have neighbors outside its domain.

The basic idea in the patchwork algorithm is to construct the system's domains in parallel by adding the DIAs (leaving the DSAs for the future) through the knitting algorithm. In this case, the calculation for the GF elements inside a certain domain does not interfere, at all, with the calculation of the elements from the other domains. After adding all the DIAs, we start a new patchwork step by merging the domains, two by two for example, in order to obtain a new collection of domains. Doing so, some of the DSAs from the old set of domains will become DIAs. These new DIAs will be added via the knitting algorithm. We repeat this process until we have just one domain and when we finally add all the remaining atoms, thereby completing the system. This procedure is illustrated for the finite 2D lattice shown in Fig. 4.2 with four initial domains (where we consider only first-neighbors interactions. In the first patchwork stage we have four domains where the DSAs are colored in red and the DIAs which will be added are colored in green. Once we add all the green atoms, we move to the second patchwork stage where we merge the domains two-by-two. We then redefine the DIAs and DSAa (the already added DIAs are painted in in blue). The process ends in the third stage where we have only one domain and no DSAs. After completing this third step we have the final GF.

So, considering the knitting algorithm, instead of constructing the system atom-by-atom, we perform the same operation by adding sets of up to d atoms each time (where d is the number of domains in the patchwork step). Now we will label each set by $\mathscr{A}$ and each atom in the set as $\mathscr{A}_i$ ($i = 1,2,3,..,d$). Note that some of the $\mathscr{A}_i$ may be missing since the number of DIAs is not necessarily the same for all the domains. Analogously to the original knitting

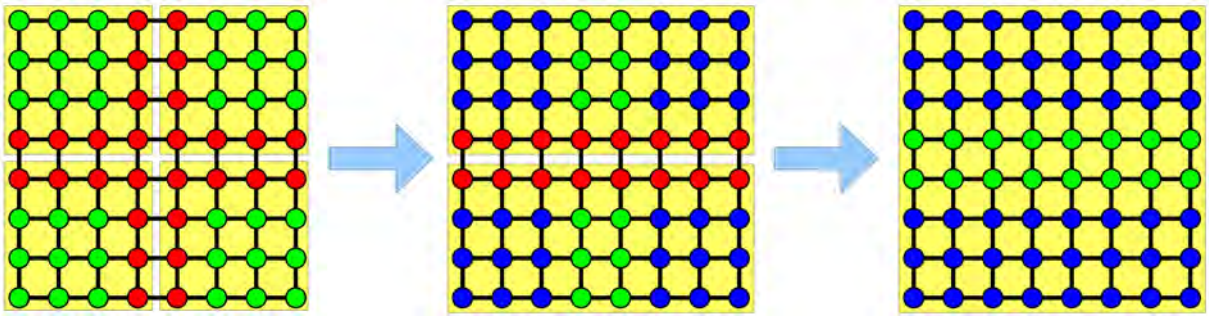

Figure 4.2: Illustration of the patchwork algorithm for a finite 2D system with only first-neighbor interactions and initially divided into four domains. The first patchwork step consists in adding all the DIAs (green atoms) from each domain, while not considering the DSAs (red atoms). Once we add all the DIAs we redefine the domains by merging them two-by-two. Some previously DSAs become DIAs which will be added in this second patchwork step (DIAs added in a previous patchwork step are painted in blue). We carry out this process until we have a single domain which, after having all its DIAs added, provides the final GF.

scheme, the $G^{\mathscr{A}}_{\mathscr{A}_i\mathscr{A}_j}$ elements are obtained by:

$$\boxed{G^{\mathscr{A}}_{\mathscr{A}_i\mathscr{A}_j} = [\mathbf{G}^{\mathscr{A},m}]_{ij} \qquad \mathbf{G}^{\mathscr{A},m} = \frac{1}{E\mathbf{I}^m - \mathbf{H}^{\mathscr{A}} - \Sigma^{\mathscr{A}-1}}} \tag{4.47}$$

where $\mathbf{I}^m$ is the $m \times m$ identity matrix and $\mathbf{H}^{\mathscr{A}}$ is the $m \times m$ (diagonal) Hamiltonian for the isolated $\mathscr{A}$ set. The self energy $\Sigma^{\mathscr{A}-1}$ for the system composed by the previous $\mathscr{A}-1$ steps is given by

$$[\Sigma^{\mathscr{A}-1}]_{\mathscr{A}_i\mathscr{A}_j} = \sum_{\sigma\sigma'} H_{\mathscr{A}_i\sigma} G^{\mathscr{A}-1}_{\sigma\sigma'} H_{\sigma'\mathscr{A}_j}. \tag{4.48}$$

Since the GF elements between atoms in different domains in each patchwork step are zero, the $\Sigma^{\mathscr{A}-1}$ matrix will also be diagonal.

For X being a GA or an atom in the p-th domain internal surface (not in the domain-domain surface, X is a DIA, not a DSA) we have:

$$G^{\mathscr{A}}_{X\mathscr{A}_p} = G^{\mathscr{A}-1}_{X\mathscr{A}_p} + \sum_{ZW} G^{\mathscr{A}-1}_{XZ} V_{ZW} G^{\mathscr{A}}_{W\mathscr{A}_p} = \sum_{\sigma}\sum_{q} G^{\mathscr{A}-1}_{X\sigma} H_{\sigma\mathscr{A}_q} G^{\mathscr{A}}_{\mathscr{A}_q\mathscr{A}_p} \tag{4.49}$$

$$\boxed{G^{\mathscr{A}}_{X\mathscr{A}_p} = \sum_{\sigma} G^{\mathscr{A}-1}_{X\sigma} H_{\sigma\mathscr{A}_p} G^{\mathscr{A}}_{\mathscr{A}_p\mathscr{A}_p}} \tag{4.50}$$

and (using the reverse form on Dyson equation):

$$G^{\mathscr{A}-1}_{\mathscr{A}_pX} = G^{\mathscr{A}}_{\mathscr{A}_pX} - \sum_{ZW} G^{\mathscr{A}}_{\mathscr{A}_pZ} V_{ZW} G^{\mathscr{A}-1}_{WX} \quad \rightarrow \quad G^{\mathscr{A}}_{\mathscr{A}_pX} = \sum_{\sigma}\sum_{q} G^{\mathscr{A}}_{\mathscr{A}_p\mathscr{A}_q} H_{\mathscr{A}_q\sigma} G^{\mathscr{A}-1}_{\sigma X} \tag{4.51}$$

$$\boxed{G^{\mathscr{A}}_{\mathscr{A}_p X} = \sum_{\sigma} G^{\mathscr{A}}_{\mathscr{A}_p \mathscr{A}_p} H_{\mathscr{A}_p \sigma} G^{\mathscr{A}^{-1}}_{\sigma X}.} \tag{4.52}$$

In addition, for X from the p-th domain and for Y from the q-th domain we have:

$$G^{\mathscr{A}}_{XY} = G^{\mathscr{A}^{-1}}_{XY} + \sum_{ZW} G^{\mathscr{A}^{-1}}_{XZ} V_{ZW} G^{\mathscr{A}}_{WY} \tag{4.53}$$

$$G^{\mathscr{A}}_{XY} = \sum_{\sigma} \sum_{r} G^{\mathscr{A}^{-1}}_{X\sigma} H_{\sigma \mathscr{A}_r} G^{\mathscr{A}}_{\mathscr{A}_r Y} \tag{4.54}$$

$$G^{\mathscr{A}}_{XY} = \sum_{\sigma} G^{\mathscr{A}^{-1}}_{X\sigma} H_{\sigma \mathscr{A}_q} G^{\mathscr{A}}_{\mathscr{A}_q Y}. \tag{4.55}$$

Note that $H_{\sigma \mathscr{A}_q}$ will be non zero only for σ in the q-th domain. On the other hand, for those σ, we have $G^{\mathscr{A}^{-1}}_{X\sigma} = 0$, and so will be for $G^{\mathscr{A}}_{XY}$. But if X and Y are in the p-th domain we have:

$$G^{\mathscr{A}}_{XY} = G^{\mathscr{A}^{-1}}_{XY} + \sum_{ZW} G^{\mathscr{A}^{-1}}_{XZ} V_{ZW} G^{\mathscr{A}}_{WY} \tag{4.56}$$

$$G^{\mathscr{A}}_{XY} = G^{\mathscr{A}^{-1}}_{XY} + \sum_{\sigma} \sum_{r} G^{\mathscr{A}^{-1}}_{X\sigma} H_{\sigma \mathscr{A}_r} G^{\mathscr{A}}_{\mathscr{A}_r Y} \tag{4.57}$$

$$G^{\mathscr{A}}_{XY} = G^{\mathscr{A}^{-1}}_{XY} + \sum_{\sigma} G^{\mathscr{A}^{-1}}_{X\sigma} H_{\sigma \mathscr{A}_p} G^{\mathscr{A}}_{\mathscr{A}_p Y}. \tag{4.58}$$

From the $G^{\mathscr{A}}_{X\mathscr{A}_p}$ equation we have:

$$G^{\mathscr{A}}_{X\mathscr{A}_p} = \sum_{\sigma} G^{\mathscr{A}^{-1}}_{X\sigma} H_{\sigma \mathscr{A}_p} G^{\mathscr{A}}_{\mathscr{A}_p \mathscr{A}_p} \tag{4.59}$$

$$\sum_{\sigma} G^{\mathscr{A}^{-1}}_{X\sigma} H_{\sigma \mathscr{A}_p} = \frac{G^{\mathscr{A}}_{X\mathscr{A}_p}}{G^{\mathscr{A}}_{\mathscr{A}_p \mathscr{A}_p}} \tag{4.60}$$

and

$$\boxed{G^{\mathscr{A}}_{XY} = G^{\mathscr{A}^{-1}}_{XY} + G^{\mathscr{A}}_{X\mathscr{A}_p} \frac{1}{G^{\mathscr{A}}_{\mathscr{A}_p \mathscr{A}_p}} G^{\mathscr{A}}_{\mathscr{A}_p Y}.} \tag{4.61}$$

These results allow us to work on the knitting procedure for each domain as if the others did not exist. At the end of each patchwork step, we merge the domains so as to form a reduced set of domains in a process which results, at the end, in a single domain which finally will give us the final GF. In the next section we explain how to adapt the sewing algorithm within this patchwork approach.

4.7 Sewing algorithm in the domain approach

The sewing algorithm can be readily applied into the domain approach. We obviously start from the last patchwork step, in which we have only one domain. We sew all the DIAs which were added in that last patchwork step. After doing that, we go to the previous patchwork step (where we have two domains) and we apply the sewing algorithm (for all the DIA added in the corresponding patchwork step) for each domain pretending the other one does not exist since the sewing equations from one domain contain no terms from the other domains. We can continue to do that until we have sewed all the sites.

4.8 The TRANSFOR project

Knitting and sewing algorithms in their patchwork parallel version are implemented within our TRANSFOR code. The lead self-energies are calculated by the method described in Section 3.9 and the Hamiltonian and overlap matrices are directly provided to the program by input files. The program is able to work with multi-terminal structures and the number of domains is provided by the user in the main input file.

In Fig. 4.3, we show the conductance (using knitting algorithm) and DOS (using sewing algorithm) for the nanotubes $(8,0)$, $(7,7)$ and $(12,0)$ within a first-neighbor TB model (with $\gamma = 3.0$ eV and $s = 0$). As discussed in Section 1.3.2, the nanotube $(8,0)$ is semiconducting, while $(7,7)$ and $(12,0)$ are metallic.

In addition, we compared TRANSFOR and TRANSPLAYER in an extra test to assess TRANSFOR's accuracy. We ran three carbon nanotube based systems composed by a torus seamlessly attached to two semi-infinite terminals making an angle of 180° (these systems are studied in Chapters 5 and 6). We considered systems based on the $(6,6)$, $(12,0)$ and $(10,0)$ nanotubes. In Figure 4.4 we plot the conductance as a function of energy for these systems calculated by both packages. A first-neighbor TB model with $\gamma = 3.0$ eV and $s = 0$ was used. From the plots one observes that both TRANSPLAYER and TRANSFOR give the same answer.

An additional procedure applied in the code is to modify the conductor Hamiltonian so as to minimize the matrix bandwidth[1]. The goal of such Hamiltonian reorganization is to minimize the size of the knitting-sewing surfaces and save time. Here we perform the bandwidth reduction using the GPSKCA subroutine [112] which is available in Ref. [113].

In order to illustrate the efficiency of the patchwork algorithm, let us consider the example

[1] If a matrix A is so that $A_{ij} = 0$ for both $j < i - k_1$ and $j > i + k_2$, so the matrix bandwidth is defined as $k_1 + k_2$.

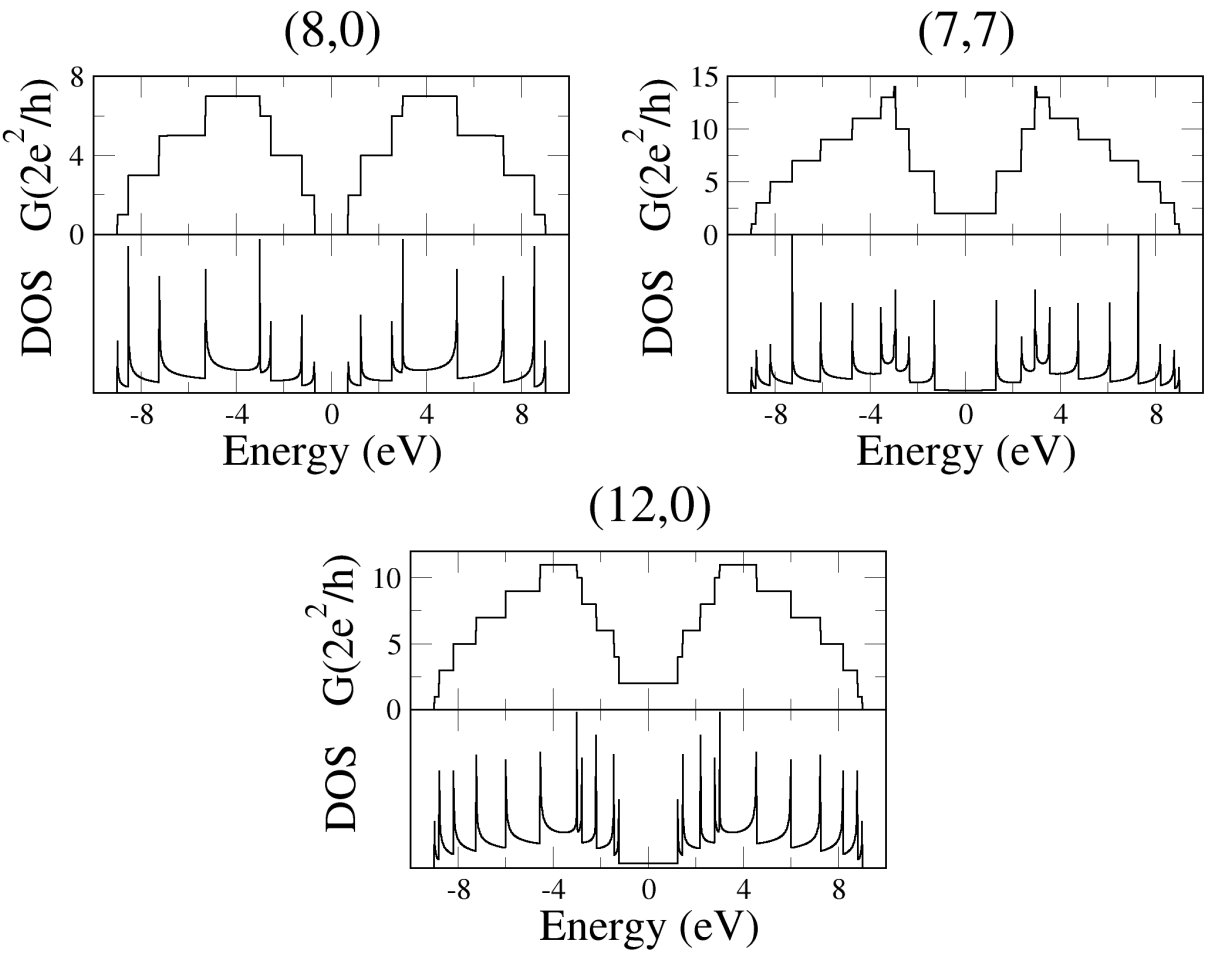

Figure 4.3: Quantum conductance (using knitting algorithm) and DOS (using sewing algorithm) for the nanotubes $(8,0)$, $(7,7)$ and $(12,0)$. We used a first-neighbor TB model with $\gamma = 3.0$ eV and $s = 0$. The Fermi energy is set to 0.0.

of a $(10,10)$ nanotube (whose unit cell's length is about 2.5 nm) with 1250 cells (50000 atoms) as CSR (in *tbc* mode with a first-neighbor TB Hamiltonian). In Fig. 4.5 we show the time corresponding to 10 knitting steps as a function of the number np of initial domains ($np = 1,2,...,12$) in a direct (red line in the upper panel) and logaritmic (red line in the lower panel) scales. In order to minimize fluctuations due to processing loading on the machines, we repeated each calculation 10 times and take the average of these data for each np.

One observes that one has a fast decrease in the execution time for increasing number of processors. In fact, we can observe that the time saving is very close to that of perfect scaling (black lines in Figure 4.5) where the calculation using np processors takes np less time. Additionally, TRANSFOR has a second level of parallelization, namely on the energy points. The processors are then distributed in ne groups of processors so that one needs $np \times ne$ processors to calculate ne energy points at the same time and using np domains for each energy point.

Memory allocation can be a problem, specially when treating systems with a huge number

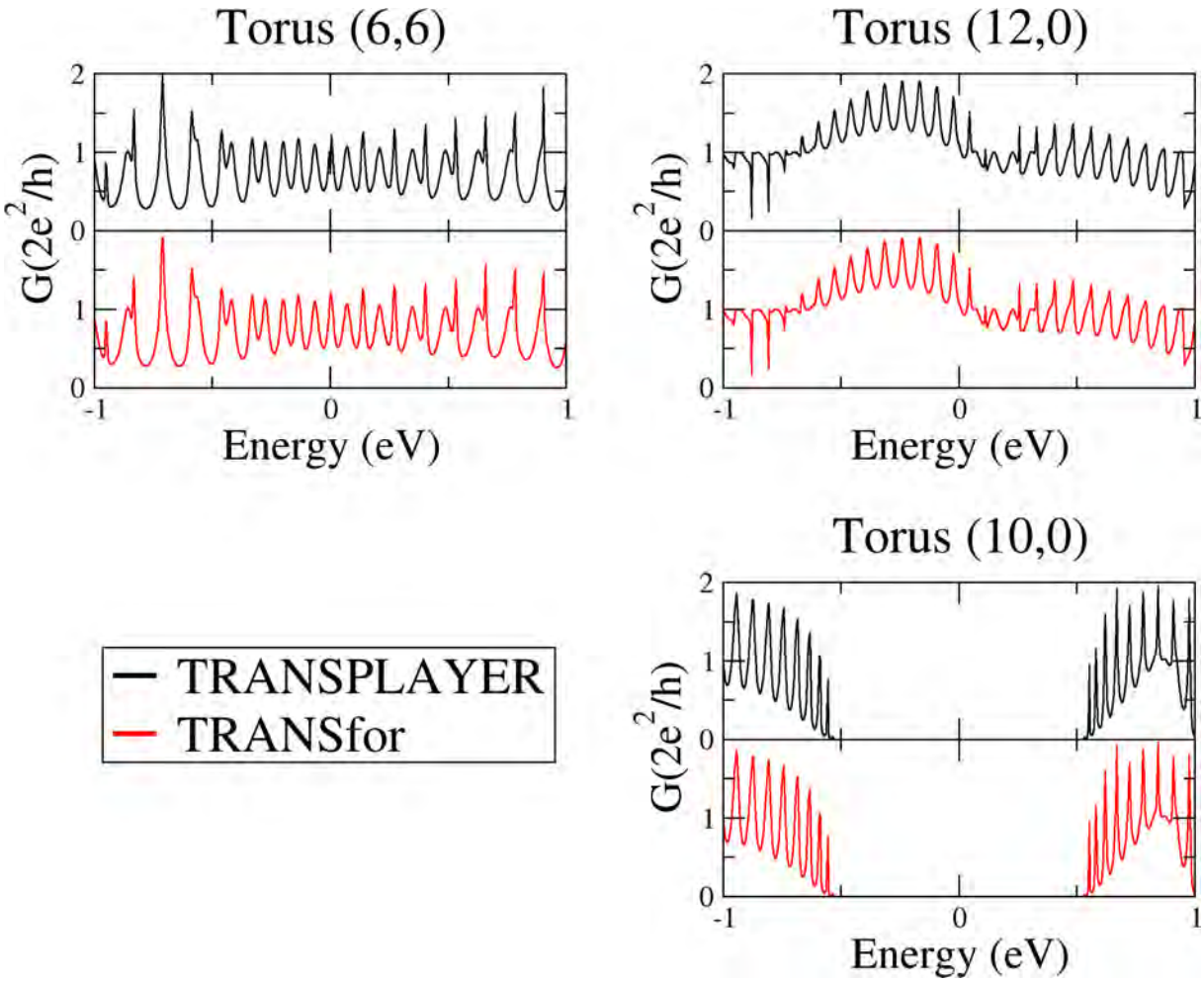

Figure 4.4: Quantum conductance as a function of energy for $(6,6)$, $(12,0)$ and $(10,0)$ carbon nanotube based tori attached to two semi-infinite terminals making an angle of 180° calculated by the TRANSPLAYER (black lines) and TRANSFOR (red lines) packages. We used a first-neighbor TB model with $\gamma = 3.0$ eV and $s = 0$. The Fermi energy is set to 0.0.

of atoms. However, Hamiltonians written in terms of localized basis are usually very sparse (in other words, containing a considerable number of zeros). For this reason, TRANSFOR uses Yale form to store sparse matrices. In this representation we do not waste memory by storing zeros and a $n \times m$ matrix A is represented by three vectors: AY, IA and JA. These vectors' sizes are, respectively, nnz, $n+1$ and nnz (where nnz is the number of non zero elements in A). The vector AY contains the non zero elements, while JA contains the column indexes for the corresponding elements in AY. In AY and JA, we first list the non zero elements in the first row by increasing column index, the the same for the second row, the third and successively. The i-th element in IA contains the position in AY of the first non zero element in row i. The $(n+1)$-th IA element is always equal to nnz. In this way, the number of non-zero elements in row i is simply given by $IA(i+1) - IA(i)$. This strategy allows for a great memory saving, allowing the calculation of extremely big systems.

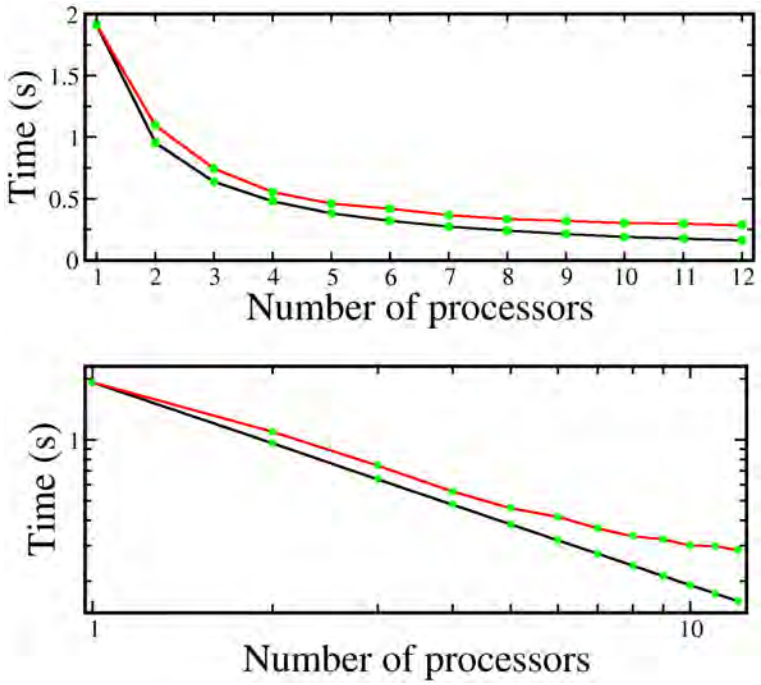

Figure 4.5: Time for 10 knitting steps versus number of processors (red lines) for a $(10, 10)$ nanotube with 1250 cells as CSR (average over 10 calculations) in direct (upper panel) and logaritmic (lower panel) scales. Black lines represent the corresponding curves for perfect scaling.

Finally the sums in the knitting and sewing equations are performed by matrix multiplications using BLAS and LAPACK [114]. The use of such routines is extremely advantageous, specially for systems with large knitting-sewing surfaces.

4.9 Overview

In this chapter we presented the original knitting and sewing algorithms [111] and developed the patchwork procedure which allows for parallelization over the knitting domains. In the end of the chapter we presented our TRANSFOR package which apply these methods and the methods described in Chapter 3. TRANSFOR was used to obtain part of the results on transport calculations (namely, the transport calculations on the GNWs, presented in Chapter 9).

Part II

Nanotori

5 *Toroidal carbon nanostructures - two terminal systems*

In this chapter we study toroidal carbon nanostructures attached to two nanotube terminals. Here we describe the geometries and electronic structure of both the tori and the junctions. Such discussion is crucial to understand the numerical results for the conductance as a function of both energy and angle between terminals. Finally, we present a simple continuum model which describes qualitatively well the conductance-energy-angle relation based on simple assumptions.

5.1 Carbon nanorings

Carbon nanostructures composed of a single nanotube bended into a ring (and in principle free of pentagonal and heptagonal defects) were first observed in carbon nanotube samples synthesized by means of laser ablation and they were named crop circles [67]. Transmission electron microscopy (TEM) analysis showed that $0.1 - 1\%$ of the nanotorus samples in that early work were in fact circular formations of single-wall carbon nanotube ropes. The absence of buckles in the structures supported the idea that these nanorings were free of pentagon and heptagon defects and were likely made up of bent nanotubes whose ends are joined by covalent bonds. Some controversy emerged in the following years about the actual existence of these perfect tori since other experiments pointed out that similar structures were in reality coiled nanotubes, given the large variation of wall thickness around the circumference [68, 69]. In that case, the energy penalty associated with bending is balanced by the wall-to-wall van der Waals adhesion. In spite of this, a large number of theoretical studies have focused on studying mechanical stability to show that it is thermodynamically possible for these structures to be formed [66, 70, 71, 72].

From simple energy balance considerations between elastic energy (bending) and chemical energy (bonding of the two initially open ends), it is clear that the larger the diameter, the

more energetically favorable defect-free carbon nanotori are. Furthermore, it was predicted by means of elastic theory [73] that the critical diameter at which the stress due to bending is just balanced by the covalently bonding energy is $D_{threshold} = 180$ nm. An updated value for the Young's modulus of $Y = 0.75TPa$ [115] (in the case of a (10, 10) nanotube) in Equation (1) from [73]:

$$D_{threshold} = \frac{\pi r^2 Y}{2\sigma} \tag{5.1}$$

(where r is the nanotube radius and σ is the surface tension of graphite perpendicular to the basal planes) yields a smaller value $D_{threshold} = 130$ nm for the critical diameter. Other atomistic simulations indicate that experimentally observed diameters are significantly larger than those obtained theoretically [66, 70, 71, 72]. This discrepancy is likely related to the fact that experiments are conducted at near equilibrium conditions under which the energy barrier needed to create the small ring geometries cannot be overcome [66].

Theoretical investigations have indicated that metallic nanotube based carbon nanotoroids possess giant paramagnetic moments [74]. Such a property is common to all tori made up of metallic nanotubes whose bands cross at the Fermi level at the Γ point and for selected radii for those metallic tubes where the band crossing happens at $2/3$ of the Brillouin zone. This behavior is due to the specific boundary conditions related to the circumferential confinement of the nanotube axial wave vector.

Since the radius of curvature in a carbon nanotorus is uniquely defined for a given nanotube, this structure can be used to understand the changes in the electronic properties of bent carbon nanotubes [75]. By gradually decreasing the radius of a nanotorus made of a (5,5) nanotube, Liu et al. observed that the toroidal structure evolves from a simple stretching/compression of the outer/inner walls (for radii greater than 19.6 Å) to the collapse of these walls for radii smaller than 13.3 Å in a finite number of positions along the torus circumference, where carbon atoms undergo re-hybridization from sp^2 to sp^3. After adding two pristine terminals to a sector containing such collapsed structure, a 75% reduction of the conductance at the Fermi level was predicted when compared to a pristine nanotube. Regarding the transport properties of these rings, a recursive Green's function approach was used to determine the density of states, transmission and current of a (3,3) based carbon nanotorus attached to two metallic electrodes as a function of the angle between the terminals and the magnetic flux [76]. A magnetic flux was shown to enhance the transmission probability, notably close to van Hove singularities, for specific angle values. In addition, investigations such as those of Herrera and Terrones have demonstrated that sp^2 junctions are experimentally feasible [54, 57], thereby confirming the need for a deep understanding of the transport properties of carbon nanostructures covalently

attached to carbon-based electrodes. Similarly, Chou et al. [77] computed conductance curves for nanotori attached to nanotube electrodes in an sp^3 free structure, showing that the conductance depends strongly on the local structure of the junction.

Carbon structures with sp^2 nanotube junctions constitute interesting materials to study transport in nanoscale. In particular, electronic interference phenomena are very likely in the toroidal geometry where paths for the interfering electrons are closely related to the distance between terminals. As the effects of the length variation have not been taken into account by previous works, we carried out a study focusing on the electronic transport properties of carbon sp^2 systems in the toroidal geometry. To that end, we performed theoretical calculations to study carbon nanorings covalently attached to two identical carbon nanotube terminals with a varying angle between them [7]. A detailed understanding of the electronic transport in such systems constitutes an important step to enable their future use in nanoelectronics.

5.2 Atomic configurations

The atomic coordinates for a defect-free carbon nanoring can be obtained in a very simple way. First, one constructs a nanotube with a number M of unit cells having the axis x, for example, as the nanotube's axis (Fig. 5.1a). Second, we displace the nanotube by a distance $R = MT/2\pi$ (T is the lenght of the nanotube's translational vector) along the y axis (Fig. 5.1b). Third, we apply the following transformation to the nanotube coordinates:

$$x' = y\sin(x/y) \tag{5.2}$$

$$y' = y\cos(x/y) \tag{5.3}$$

$$z' = z \tag{5.4}$$

in order to obtain a ring having z as its axis perpendicular to the torus plane (Fig. 5.1c).

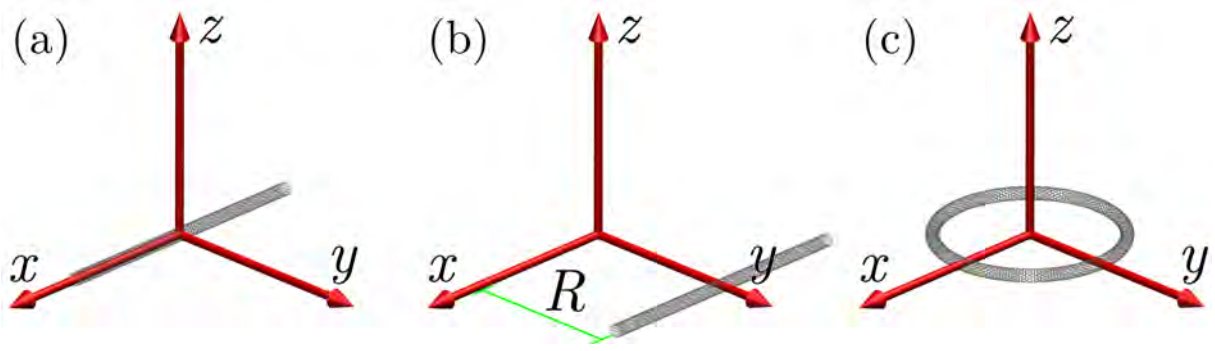

Figure 5.1: Systematic procedure to generate a torus from a nanotube.

We also adopted a systematic procedure to calculate the atomic coordinates for the geometry of carbon nanorings coupled to external leads. Firstly, we built up the structure of a simple joint, made up of a small ring sector connected normally to a straight tube section (note that no dangling bonds were present after this process). Secondly, we created the lowest α structure, where α is the angle between terminals, by fusing a second junction structure to the first one. More specifically, α is defined as the angle between the axes from the nanotubes composing the two terminals as presented in Fig. 5.2. Finally, a large nanotorus sector was added to complete the structure.

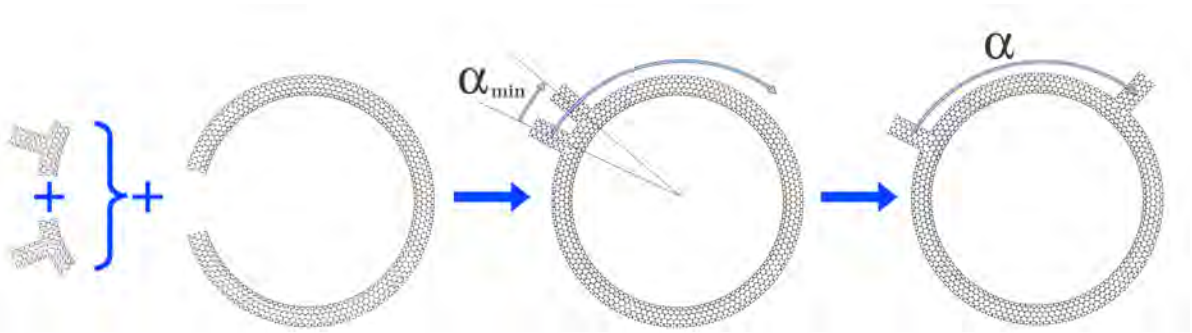

Figure 5.2: Schematic representation of the procedure adopted for the systematic structure construction.

The configurations are labeled $(n,m)_r-(l,p)_t$, where $(n,m)_r$ stands for the chirality of the tube making up the ring and $(l,p)_t$ for that making up the terminals. The configurations considered here are depicted in Fig. 5.3. The tori were assembled with 120 nanotube unit cells along the circumference. This particular length was chosen for reasons that will become clear below. It corresponds to torus radii $R = 46.97$ Å, 81.36 Å, 81.36 Å, and 124.28 Å for the $(6,6)$, $(10,0)$, $(12,0)$, and $(8,2)$ nanotube based tori, respectively. This approach presents the advantage that each configuration can be easily modified into a structure corresponding to a different α. The transformation proceeds by transferring pristine nanotube unit cells from the longer to the shorter arm. For each case studied here, we prepared two types of junctions (shown in Fig. 5.3): one with the transversal part over the center of a nanotube unit cell from the ring and another over the intersection between two cells. This enabled us to create series of structures with a $180/120 = 1.5$ step (which correspond to $\alpha = 1.5^\circ$) since all the systems have 120 nanotube cells along the circumference and each nanotube unit cell correspond to an arc of 3°.

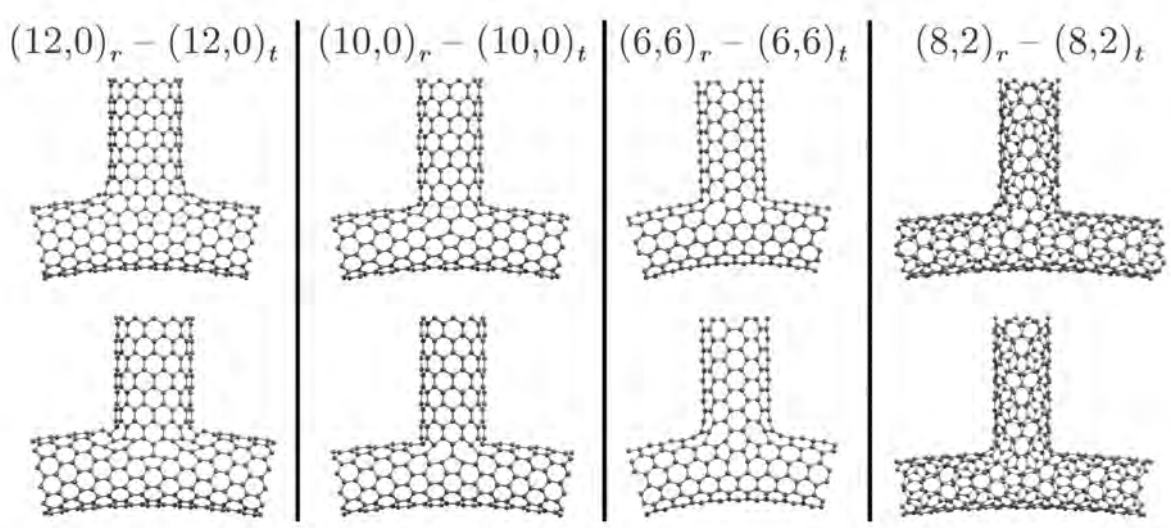

Figure 5.3: List of studied configurations.

5.3 Electronic structure

Since carbon nanorings and nanotube structures are formed from the same building blocks, their electronic structures are closely related. Within the single-orbital tight-binding model, the electronic structure for an infinite carbon nanotube can be obtained from graphene's 2D electronic dispersion relation (as we showed in Section 2.7):

$$E(\mathbf{k}) = E_F \pm \gamma\sqrt{3+2\cos\mathbf{k}\cdot\mathbf{a}_1+2\cos\mathbf{k}\cdot\mathbf{a}_2+2\cos\mathbf{k}\cdot(\mathbf{a}_1-\mathbf{a}_2)} \tag{5.5}$$

where $E_F = 0$ is the Fermi level of the system, $\mathbf{a}_{1,2}$ are the unit cell vectors of graphene and $\mathbf{k}$ is a vector in the corresponding first Brillouin zone. Quantum confinement along the nanotube circumference ($2\pi r$, where r is the tube radius) constrains the wavevector along this direction to be quantized as follows:

$$k_c = \frac{2\pi q}{|\mathbf{C}_h|} = \frac{q}{r} \quad \rightarrow \quad q = 0,1,2,...,N-1, \tag{5.6}$$

where q is an integer, $\mathbf{C}_h = n\mathbf{a}_1 + m\mathbf{a}_2$ is the nanotube chiral vector (whose length is the tubule circumference), and N is the number of hexagons in a unit cell of the nanotube (see Section 1.3.2). The axial component of $\mathbf{k}$ is free to assume continuous values in the $[-\pi/T, +\pi/T[$ range where T is the length of the nanotube translational vector. In addition, carbon nanotori present a confinement of the electron density along the translational vector direction. This additional level of confinement forces the axial component of $\mathbf{k}$ to be restricted to the following

discrete set of values:

$$k_a = \frac{2\pi p}{L} = \frac{p}{R} \quad \rightarrow \quad p = 0,1,2,...,M-1, \tag{5.7}$$

where p is an integer and M is the number of nanotube unit cells along the torus circumference of radius R ($L = MT$). It follows that the electronic structure of carbon nanotori is determined by a set of discrete $\mathbf{k}$ points positioned at the crossing of two families of mutually orthogonal lines. Such a grid captures explicitly some effects of the curvature as the spacing between these lines is determined by the curvatures of the nanotube ($1/r$) and the nanotorus ($1/R$). Note, however, that curvature effects are not included in the hopping parameter description employed here; in other words the electronic properties computed here depend only on the topology (i.e. table of atomic neighbors) of the structure, but not on the details of the atomic positions. We illustrate such a 2D mesh of lines mapped on the graphene Brillouin zone and their defining boundary conditions in Fig. 5.4.

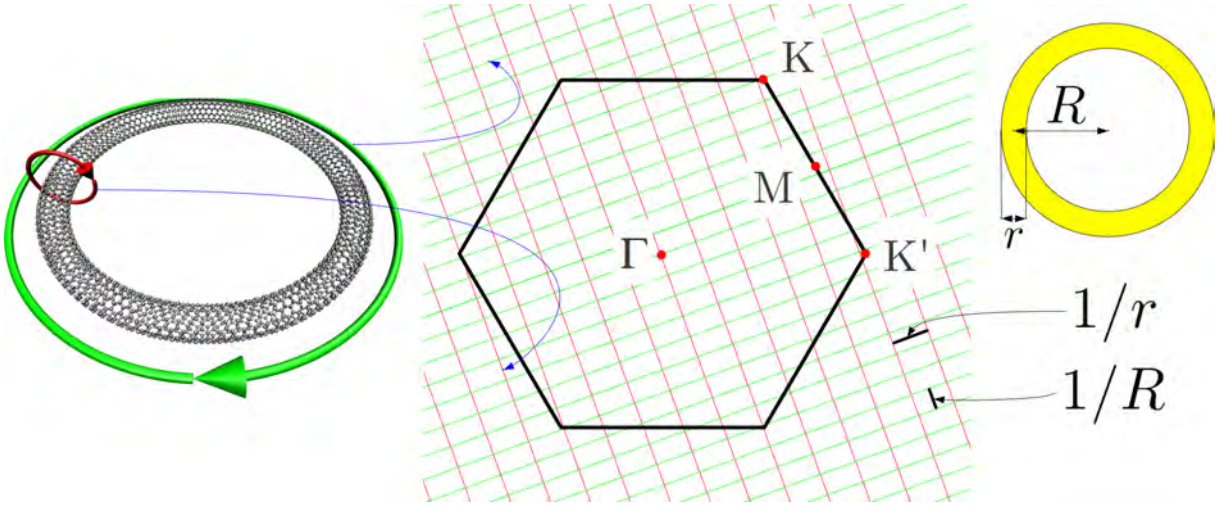

Figure 5.4: Illustration of the different levels of quantum confinement and the corresponding cutting lines for a carbon nanoring mapped on the 2D graphene Brillouin Zone. The spacing for the two families of lines are directly related to the curvatures of the nanotube ($1/r$) and the nanotorus ($1/R$).

It is well established that within a simple tight-binding approach such as the one used here, carbon nanotubes can be metallic under two distinct conditions (see [116] and Section 1.3.2). Denoting the greatest common denominator (gcd) of n and m as d , the two types of metallic systems are:

- M1: $(n-m)$ is a multiple of 3 but not of $3d$; and
- M2: $(n-m)$ is a multiple of $3d$.

In the first group, the valence and conduction bands touch at the Fermi level at the Γ point ($k_a = 0$). This crossing occurs at $k_a = \pm 2\pi/3T$ in the second group. On the one hand, it is

clear that all the tori made up from M1 nanotubes will be metallic (i.e. the HOMO-LUMO gap is zero) since the Γ point along the axis will always be allowed by the band-folding picture explained above. On the other hand, for tori made up of M2 nanotubes, the additional condition that M has to be a multiple of three must be fulfilled to ensure a zero gap at the Fermi level. In Fig. 5.5(a)-(c) we show the cutting lines near a graphene K point for the M2 $(8,2)$ nanotorus for $M = 119, 120$ and 121, respectively. We can see that the cutting lines cross at K (highlighted by a red circle) only for the $M = 120$ system. Fig. 5.5(d) shows the DOS for this type of torus while Fig. 5.5(e) presents the DOS for the $(6,6)$ based torus with $M = 120$.

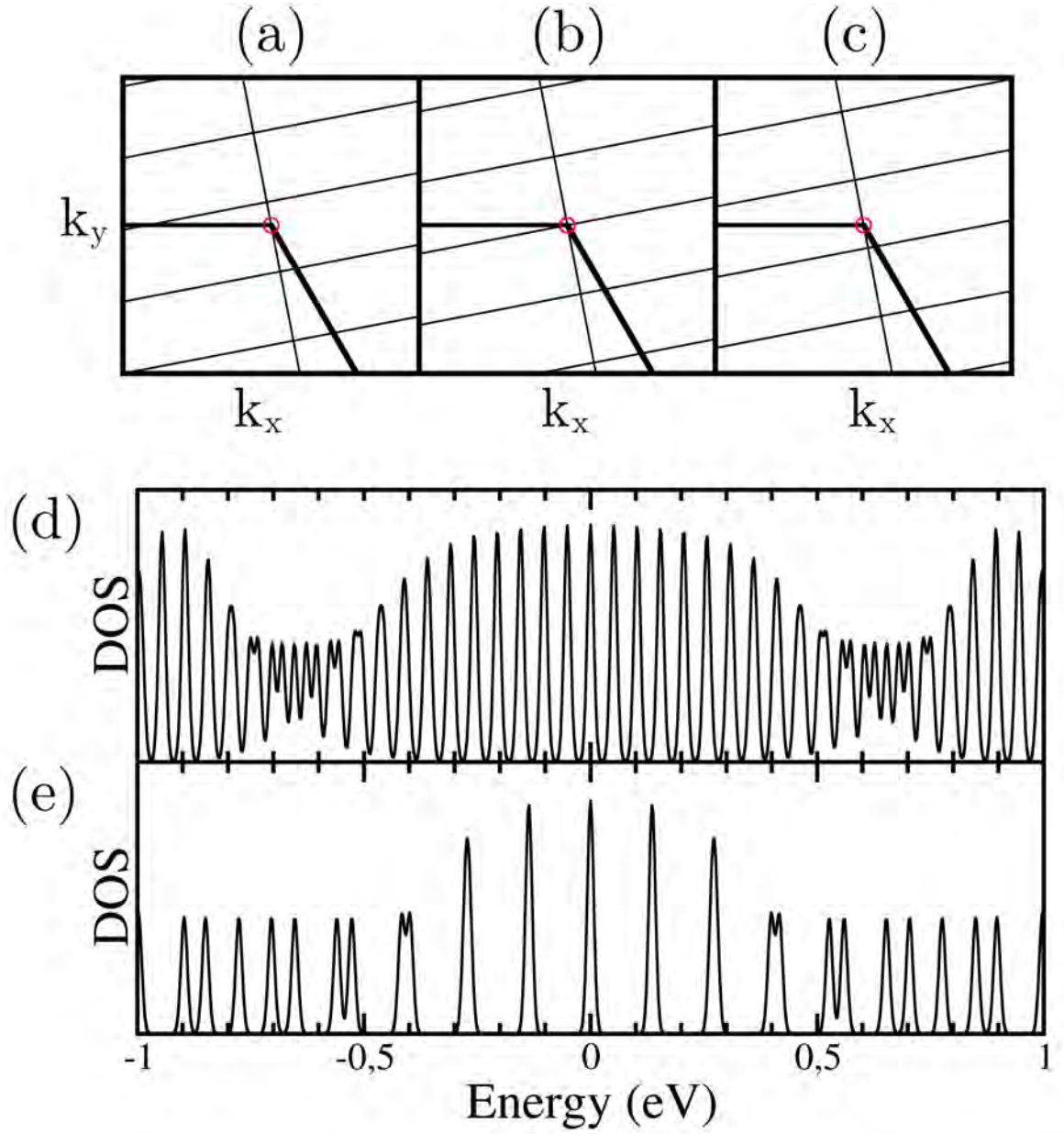

Figure 5.5: (a)-(c): Cutting lines near a K point for $(8,2)$ nanoring with 119 (a), 120 (b) and 121 (c) nanotube units cells, respectively; (d)-(e): Electronic density of states for the (8,2) and (6,6) nanotori made up of 120 nanotube cells [7].

In addition, the levels near the Fermi level are nearly equally spaced. This last aspect turns to be an important feature of the torus' electronic structure and it is the result of the interplay between the allowed wavevectors (allowed by confinement determined by the boundary conditions along the circumferences of the nanotube and nanotorus) and the details of the electronic structure around E_F. Using the notation of Saito et al. [18] and the results previously discussed in this section we write:

$$\mathbf{k} = \frac{2\pi q}{|\mathbf{C}_h|}\frac{\mathbf{K}_1}{|\mathbf{K}_1|} + \frac{2\pi p}{MT}\frac{\mathbf{K}_2}{|\mathbf{K}_2|} = q\mathbf{K}_1 + \frac{p}{M}\mathbf{K}_2 \tag{5.8}$$

where:

$$\mathbf{K}_1 = \frac{1}{N}\left(\frac{2n+m}{d_r}\mathbf{b}_1 + \frac{n+2m}{d_r}\mathbf{b}_2\right) \quad \text{and} \quad \mathbf{K}_2 = \frac{1}{N}(m\mathbf{b}_1 - n\mathbf{b}_2) \tag{5.9}$$

are, respectively, the lattice vectors along the nanotube's circumferential and axial directions and d_r is the gcd of $2n+m$ and $n+2m$. In addition, to get a metallic nanotorus, the K point of the graphene Brillouin zone must be present among the allowed wavevectors. For instance, we should have:

$$\mathbf{k} = \mathbf{K} = \frac{2}{3}\mathbf{b}_1 + \frac{1}{3}\mathbf{b}_2. \tag{5.10}$$

A system of two equations involving q and p can be obtained from Equation 5.8 to 5.10 and the corresponding solutions yield the following conditions on q and p:

$$q = \frac{2n+m}{3} \quad \text{and} \quad p = M\frac{m}{d_r}. \tag{5.11}$$

With $q = (2n+m)/3$ and $p = i + Mm/d_r$ (with i an small integer), we can write the allowed wavevectors around the K point as:

$$\mathbf{k} = \frac{1}{3}(2\mathbf{b}_1 + \mathbf{b}_2) + \frac{i}{MN}(m\mathbf{b}_1 - n\mathbf{b}_2). \tag{5.12}$$

Imposing $E_F = 0$ in Equation 5.5 and using the results above we find:

$$[E(\mathbf{k})]^2/\gamma^2 \;=\; 3 - 2\cos\delta^+\cos\delta^- + 2\sqrt{3}\sin\delta^+\cos\delta^- - \cos 2\delta^+ - \sqrt{3}\sin 2\delta^+ \tag{5.13}$$

where:

$$\delta^{\pm} = \frac{i(m \pm n)\pi}{NM}. \tag{5.14}$$

For a large nanotorus we can show[1] that we end up with:

$$E(\mathbf{k}) = \pm \frac{\gamma \pi d_r}{M\sqrt{n^2+m^2+nm}}|i| \tag{5.15}$$

and i is given by:

$$i = p - Mm/d_r. \tag{5.16}$$

For a M1 nanotube, $d_r = d$, where d is the *gcd* of n and m. It follows that we have $i = p - lM$ (where $l = m/d$ is an integer) which is equivalent to $i = p$ after a translation into the first Brillouin zone.

For a M2 nanotube, $d_r = 3d$ and $i = p - lM/3$. However, the integer l is not allowed to be a multiple of 3 in this last case and therefore i will always be equivalent to $i = p \pm M/3$ (which are also equivalent by reflections on a Bragg plane). The fact that l is not a multiple of 3 can be proven by reductio ad absurdum[2].

For M2 nanotubes, the levels described by Equation 5.15 present a twofold degeneracy. Such degeneracy occurs in the torus consisting of M2 nanotubes because the linear relation has the same slope for both bands and two k_a symmetrically positioned relative to $2\pi/3T$ correspond to the same energy value. However, as we move far away from $k_a = 2\pi/3T$, the linear relation no longer holds and the two branches have different slopes. It follows that the energies corresponding to the two allowed k_a symmetrically positioned around the crossing k_a no longer match. This is the reason why the levels start to split for the $(8,2)$ and $(6,6)$ nanorings as we move away from the Fermi energy. Eventually, we recover the double degeneracy when the splitting is large enough to promote a new match between levels coming from different pairs of splitting levels. This effect is illustrated in Fig. 5.5(d) where the energy match is recovered near

[1]Note that for a large nanotorus we have $\delta^{\pm} << 1$, and we can therefore use the first terms of the Taylor expansion for the trigonometric functions to find

$$[E(\mathbf{k})]^2/\gamma^2 \quad = \quad 3(\delta^+)^2 + (\delta^-)^2 - \frac{1}{2}(\delta^+)^2(\delta^-)^2 - \sqrt{3}\delta^+(\delta^-)^2$$

which becomes (after considering only the leading terms):

$$[E(\mathbf{k})]^2/\gamma^2 \quad = \quad 3(\delta^+)^2 + (\delta^-)^2.$$

Finally, after algebric manipulations, we obtain:

$$E(\mathbf{k}) = \pm \frac{\gamma \pi d_r}{M\sqrt{n^2+m^2+nm}}|i|.$$

[2]First, suppose $l = 3l'$ (l' integer) and that d is the *gcd* of n and m, we can write $m = 3l'd$ and $n = n'd$ (n' integer). We would then have $2n+m = d(2n'+3l')$ and $n+2m = d(n'+6l')$. So, in order to have $d_r = 3d$ (for the M2 case) we would have to have n' as a multiple of 3 which is impossible since the *gcd* of n and m would then be $3d$ rather than d.

$E = \pm 1.0\ eV$ for the $(8,2)$ based nanotorus.

Based on these results, we chose representative nanotubes from each of the two groups ($(12,0)$ for M1; $(6,6)$ and $(8,2)$ for M2) as well as the semiconducting $(10,0)$ nanotube to form the set of systems studied in this work. The choice of $M = 120$ is made to ensure that all tori made up of an M2 nanotube are metallic.

5.4 Numerical Results

We studied the transport properties of a number of tori while systematically changing the angle α between the two identical electrodes. The quantum conductance was computed using a Green's function and transfer-matrix-based approach for computing transport in extended systems implemented in the TRANSPLAYER package [109]. Here we used a simple first-neighbor tight-binding Hamiltonian with $\gamma_0 = 3.0$ eV. While the method is applicable to any general Hamiltonian that can be described within a localized-orbital basis, we are here restricted to a simple nearest-neighbor description, given the size of the systems under investigation (the largest system contained 7074 atoms). Nevertheless, this Hamiltonian model is known to reproduce well the electronic structure of carbon nanostructures [117, 118]. As already mentioned in the previous section, our model does not explicitly consider curvature effects. It follows that the physical description of our system does not depend on the details of the atomic positions, but only on the table of neighbors of the structure. Consequently, it is not necessary to perform geometry optimization since it will not affect the transport results. In the figures reproduced here, we plotted the conductance as a function of the impinging electron energy and angle α . Note that a uniform pattern for the conductance is not expected for the $\alpha = 3j$ and $\alpha = 3(j+1/2)$ systems since they have been constructed from integer and half-integer multiples of nanotube unit cells for the arms of the nanotori, as explained early in this chapter. For this reason we label each family as $\alpha^{\Delta\alpha}_{\alpha^\circ_m}$ where α_m represents the greatest α in the series and $\Delta\alpha$ is the angle step. Here, all the systems have 120 nanotube unit cells along the ring in such a way that each unit cell corresponds to a 3° arc. The terminals in the $\alpha^{3^\circ}_{180^\circ}$ series possess two symmetrical joint geometries (with the transverse nanotube over the center of a nanotube cell from the ring), unlike the $\alpha^{3^\circ}_{178.5^\circ}$ systems where the second terminal is placed between two cells. In the $(6,6)_r - (6,6)_t$ systems, for instance, each of the terminal geometries in the first family contains $N^0_5 = 2$ pentagons and $N^0_7 = 8$ heptagons, while in the second set the second junction has $N^0_5 = 4$ and $N^0_7 = 10$ (see Table 5.1). Note that the relative numbers of five- and seven-membered rings

obey[3]:

$$N_5 - N_7 = 12 \times (1 - g) \tag{5.17}$$

for a surface of genus $g = 2$ (that is, a surface with two 'holes' or 'handles', considering that the electrodes meet at infinity) and $N_5 = 2N_5^0$ and $N_7 = 2N_7^0$ for the $\alpha_{180^\circ}^{3^\circ}$ case (for the $\alpha_{178.5^\circ}^{3^\circ}$ series the $N_{5/7}$ are obtained by summing the values of $N_{5/7}^0$ from each junction).

It is established that pentagon and heptagon defects act as localized scatterers that modify significantly the transport properties of carbon nanostructures [121]. It is therefore quite unsurprising for the conductances of the two families of angles to behave differently as α varies. Even for configurations presenting the same number of pentagons and heptagons (Table 5.1) we expect to observe different behaviors for $\alpha_{180^\circ}^{3^\circ}$ and $\alpha_{178.5^\circ}^{3^\circ}$ since the spatial distributions of defects are different for the two types of junction, leading for dissimilar transport properties.

Table 5.1: Number of pentagons and heptagons in the junction structures for the $\alpha = (3j)^\circ$ (both terminals) and $\alpha = (3j+1.5)^\circ$ (second terminal) systems. The first terminal structure in $\alpha = (3j+1.5)^\circ$ family is identical to the $\alpha = (3j)^\circ$ terminals.

System	N_5^0/N_7^0 for $\alpha = (3i)^\circ$	N_5^0/N_7^0 for $\alpha = (3i+1.5)^\circ$
$(6,6)_r - (6,6)_t$	2/8	4/10
$(10,0)_r - (10,0)_t$	2/8	2/8
$(12,0)_r - (12,0)_t$	6/12	4/10
$(8,2)_r - (8,2)_t$	3/9	0/6

Figures 5.6(a) and (b) represent the α and energy dependences for the conductance of the $(12,0)_r - (12,0)_t$ systems. Note that a linear interpolation was performed in order to facilitate the visualization. As expected, the $\alpha_{180^\circ}^{3^\circ}$ and $\alpha_{178.5^\circ}^{3^\circ}$ series show characteristic trends. We observe that the $\alpha_{180^\circ}^{3^\circ}$ family presents an almost symmetrical electron-hole behavior. However, the occupied levels possess high conductance corresponding to red islands of conductance, along with merged green islands, which are absent in the unoccupied states region. The situation is reversed for the $\alpha_{178.5^\circ}^{3^\circ}$ series: the conductance for $E < 0$ decreases as we move away from the Fermi energy. In other words the conduction shifts from *p*- to *n*-type as the relative geometry of the two terminals changes.

We also observe that the conductance does not depend on α for $E = 0$. In fact, as the nanotube composing the torus is a M1 nanotube, the levels at the the Fermi energy ($E = 0$) correspond to a wave vector at the Γ point ($k_a = 0$). Since this corresponds to an infinitely large wavelength, we expect no dependence on α for this particular energy value.

The geometry of the second terminal also plays an important role in determining the trans-

[3]This equation is obtained using Euler's rule togheter with other concepts like the Gauss-Bonnet theorem [119, 120].

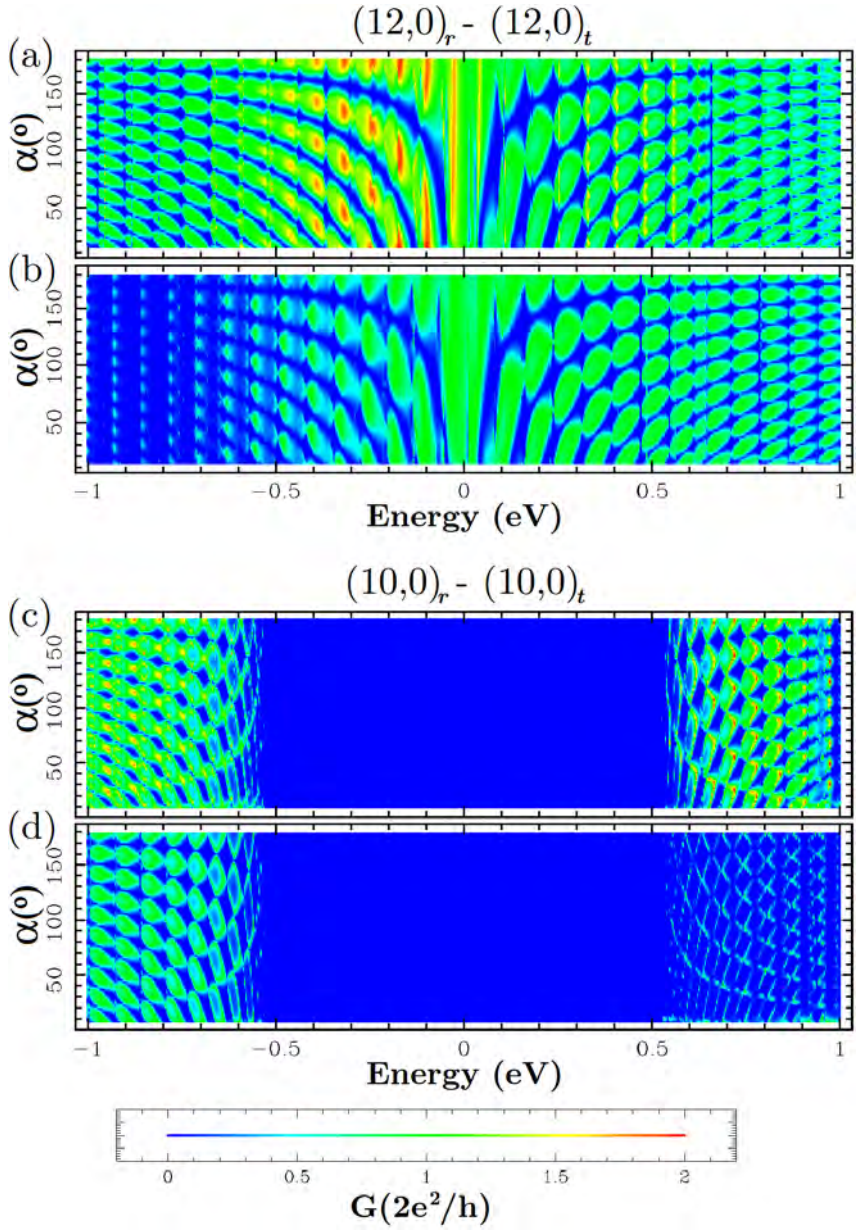

Figure 5.6: Conductance *versus* energy and α for the $\alpha^{3^\circ}_{180^\circ}$ and $\alpha^{3^\circ}_{178.5^\circ}$ series for the $(12,0)_r-(12,0)_t$ (a-b) and $(10,0)_r-(10,0)_t$ systems (c-d), respectively [7].

port properties of the $(10,0)_r-(10,0)_t$ structures. As can be seen in Fig. 5.6(c)-(d), the systems are characterized by a large region of zero conductance around the Fermi level due to the semiconducting character of the (10, 0) nanotube. For energies far away from $E=0$ we observe that the conductance diminishes significantly for $\alpha^{3^\circ}_{178.5^\circ}$ compared to $\alpha^{3^\circ}_{180^\circ}$. This lowering is remarkably more intense for $E>0$ in such a way that the conduction through the empty levels almost completely vanishes. This effect is due to charge localization related to the junction geometry. To confirm this, we show, in Fig. 5.7(a) and (b), the DOS and conductance for the $\alpha=180^\circ$ and 178.5° systems along with the LDOS for the indicated energies. In the first case while there is a clear accumulation of charge on two atoms shared by two heptagons, there is

also a significant charge spread over the terminals. It follows that conduction is possible at those energies. Conversely, there is no such spread in either of the terminals in the $\alpha = 178.5°$ configuration, thereby explaining the suppression of conductance.

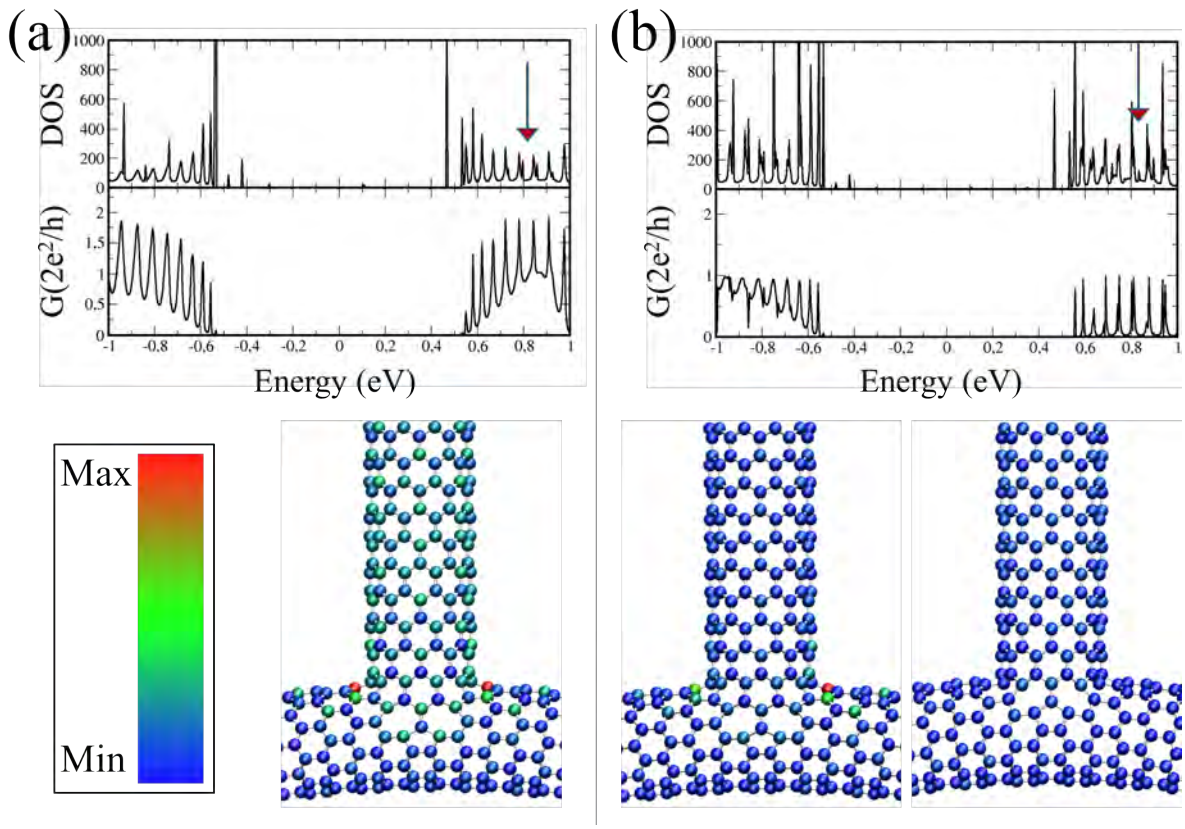

Figure 5.7: DOS, conductance, and LDOS for the $\alpha = 180°$ (a) and 178.5° (b) in the $(10,0)_r - (10,0)_t$ systems [7].

Turning to the metallic $(6,6)$ nanotube, the separated plots into the two $\alpha^{3°}_{180°}$ and $\alpha^{3°}_{178.5°}$ series are not sufficient to yield well defined patterns for the $(6,6)_r - (6,6)_t$ system. However, one can recover systematic patterns by splitting the two main series into three subgroups: $\alpha^{3°}_{180°}$ gives rise to the $\alpha^{9°}_{180°}$, $\alpha^{9°}_{177°}$ and $\alpha^{9°}_{174°}$ subgroups (Figures 5.8(a)-(c)), while $\alpha^{3°}_{178.5°}$ can be separated into $\alpha^{9°}_{178.5°}$ (Fig. 5.8(d)), $\alpha^{9°}_{175.5°}$ and $\alpha^{9°}_{172.5°}$. In each subgroup, the α configurations are separated by 9° steps, equivalent to three nanotube unit cells along the ring.

The existence of subgroups can be understood in terms of the torus electronic structure. When we attach two electrodes to the ring, the torus is effectively divided into two arms with lengths $L_i = M_i T$, $i = 1,2$ where $i = 1$ denotes the smaller section and $L_1 + L_2 = L$. The allowed wavevectors along these two paths are given by $k_a = 2\pi p_i / L_i$, assuming a node in the wavefunction at the torus-terminal junction. Note that we again observe the $mod(M_i, 3) = 0$ condition for metallic arms since $(6,6)$ is an M2 nanotube. It follows that the transport properties for M2 based rings present a periodicity corresponding to arc lengths that are a multiple of

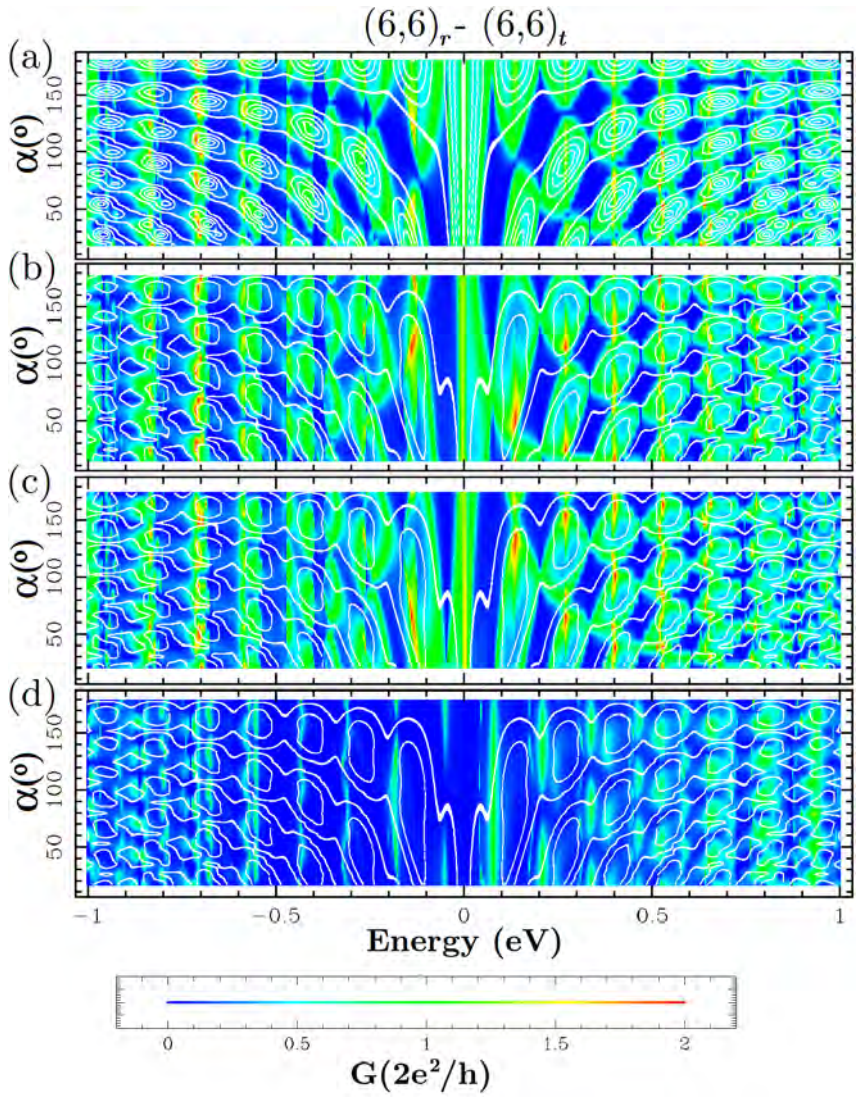

Figure 5.8: Conductance *versus* energy and α for the $\alpha^{9^\circ}_{180^\circ}$ (a), $\alpha^{9^\circ}_{177^\circ}$ (b), $\alpha^{9^\circ}_{174^\circ}$ (c) and $\alpha^{9^\circ}_{178.5^\circ}$ (d) series for the $(6,6)_r-(6,6)_t$ system. The white lines are isocountour lines for the model described in Section 5.5 [7].

$3T$ since the states close to the Fermi level correspond to such an electron wavelength. In our simulations, since $M = 120$, this step corresponds to a 9° periodicity. Arms that are not of the $\alpha = (9j)^\circ$ type present two different phase differences that split them into the $\alpha = (9j+3)^\circ$ and $\alpha = (9j+6)^\circ$ subgroups, each with a characteristic behavior. In addition, the second terminal geometry reduces significantly the overall conductance for the $\alpha^{9^\circ}_{178.5^\circ}$, $\alpha^{9^\circ}_{175.5^\circ}$ and $\alpha^{9^\circ}_{172.5^\circ}$ systems, so that the conductance is almost completely suppressed compared to the other series. In Figures 5.9(a) and (b) we plotted the DOS, conductance, and LDOS around the Fermi energy for $\alpha = 180^\circ$ (a) and 178.5° (b). We can see, as for the $(10,0)_r-(10,0)_t$ system, that the charge in the $\alpha = 180^\circ$ case is spread over the terminals in spite of a high charge density located on the heptagons. Since the system is metallic, such charge delocalization is extended to both arms, corresponding to a large conductance. The $3T$ wavelength character is easily observed along

the ring in the LDOS plot since the anti-nodes (green LDOS portions) are spaced by $1.5T$. In the $\alpha = 178.5^\circ$ case the charge distribution is limited to the smaller arm by the junctions and it is not extended to the terminals, thereby explaining the reduced conductance.

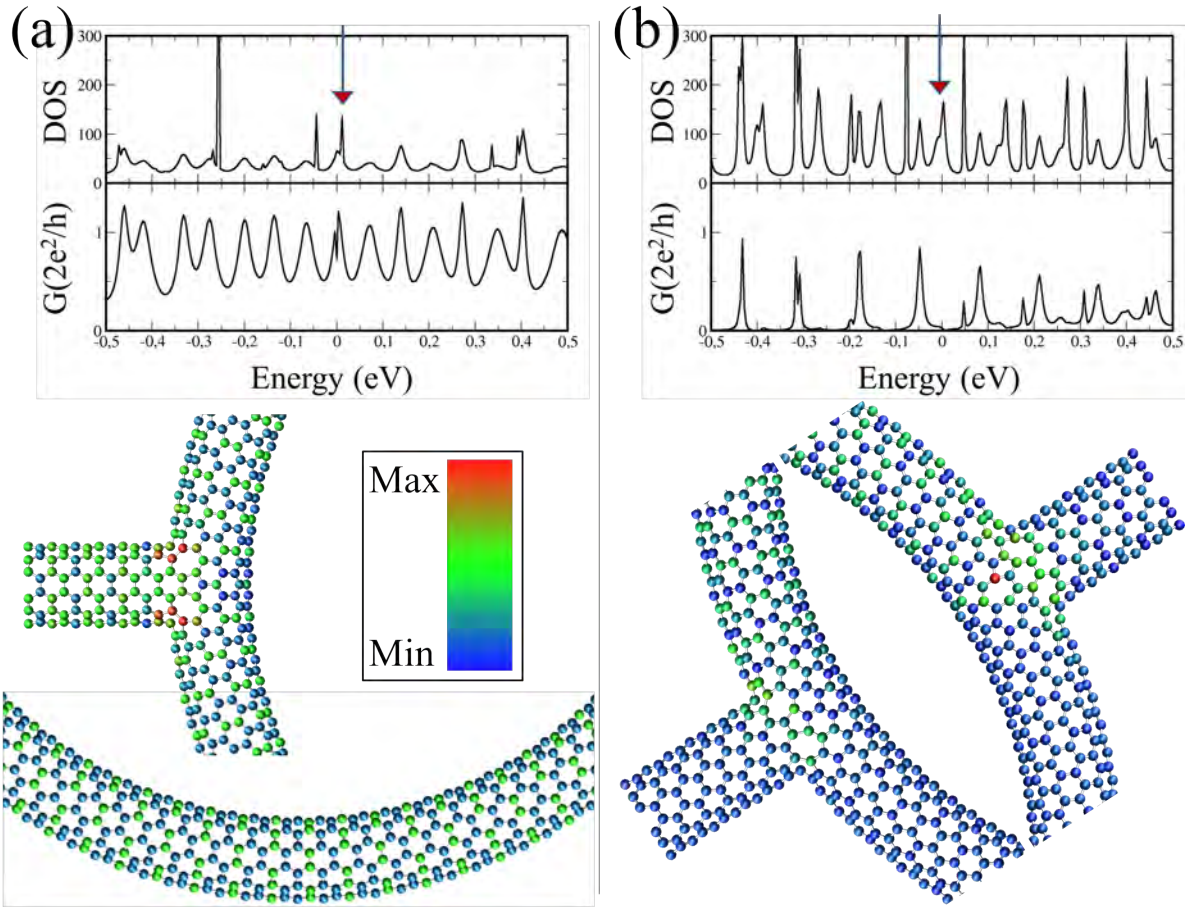

Figure 5.9: DOS, conductance, and LDOS for the $\alpha = 180^\circ$ (a) and 178.5° (b) in the $(6,6)_r - (6,6)_t$ system [7].

The same family grouping is needed to categorize the transport properties of the $(8,2)_r - (8,2)_t$ systems since $(8,2)$ is an M2 nanotube. The conductance is slightly asymmetric with higher conductance for the occupied states for the $\alpha^{9^\circ}_{180^\circ}$, $\alpha^{9^\circ}_{177^\circ}$ and $\alpha^{9^\circ}_{174^\circ}$ sets (Figures 5.10(a)-(c)). However, we do not observe conductance suppression for $\alpha^{9^\circ}_{178.5^\circ}$ (Fig. 5.10(d)), $\alpha^{9^\circ}_{175.5^\circ}$ and $\alpha^{9^\circ}_{172.5^\circ}$.

One readily notices two differences between the $(8,2)_r - (8,2)_t$ and $(6,6)_r - (6,6)_t$ systems. First, the former system presents a greater number of large conductance islands compared to the latter. Second, the conductance pattern in $(6,6)r - (6,6)_t$ approaches a vertical line at the Fermi energy, while the corresponding pattern consists of two distinct vertical lines near $E = \pm 1.0$ eV for the $(8,2)_r - (8,2)_t$ case. The difference in the number of conductance maxima can be understood in terms of chirality. Chirality indeed determines the relative incli-

nation between the axial cutting lines and the hexagonal Wigner-Seitz cell over the graphene Brillouin zone. As these lines cut differently the set of wrapped trigonal isoenergy surfaces near the K points for the $(8,2)$ and $(6,6)$ cases, they produce distinct slopes for the frontier energy bands. For energies close to the Fermi level, Equation 5.15 gives $E = (\pi\sqrt{3}/M)|i|$ and $E = (3\pi\sqrt{21}/21M)|i|$ for the $(6,6)$ and $(8,2)$ nanotubes. Since the $(8,2)$ tube presents a smaller slope, a greater number of states are present in the energy range shown in the plots, leading to a larger number of high-conductance spots. On the other hand, the characteristic behavior of the $(8,2)_r - (8,2)_t$ systems near $E = \pm 1.0$ eV is due to the increased DOS near these energy values, because of the energy matching for these levels, as described in Section 5.3.

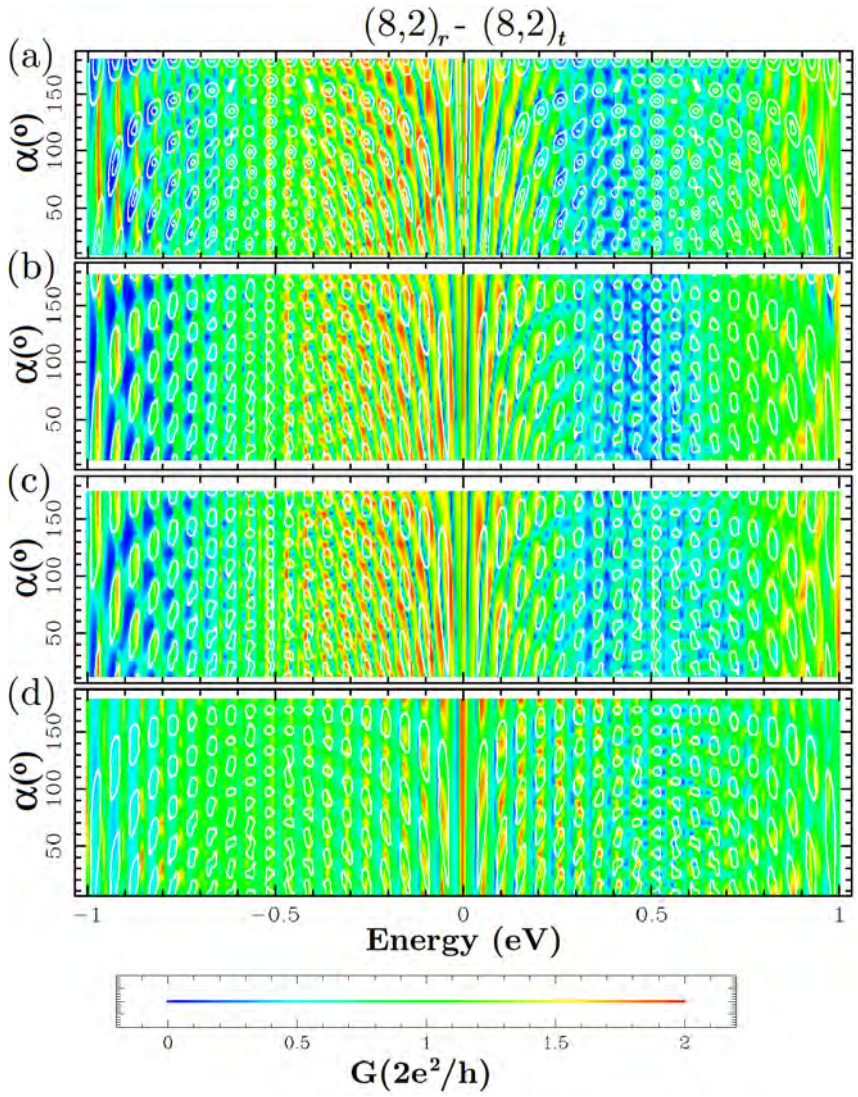

Figure 5.10: Conductance *versus* energy and α for the $\alpha^{9^\circ}_{180^\circ}$ (a), $\alpha^{9^\circ}_{177^\circ}$ (b), $\alpha^{9^\circ}_{174^\circ}$ (c) and $\alpha^{9^\circ}_{178.5^\circ}$ (d) series for the $(8,2)_r - (8,2)_t$ systems. The white lines are isocontour lines for the model described in Section 5.5 [7].

5.5 Quantum interference model

We now develop further the analysis made in Section 5.4 by exploiting the details of the tori's electronic structure. The analysis presented here enables the construction of a qualitative and general model describing electronic transport in nanorings by considering electron wavefunctions traveling ballistically from the first to the second terminal through the two different arms. We will describe the two electronic paths using $e^{ik_a x_i}$ waves (where x_i is the position along arm i), as ilustrated in Fig. 5.11a.

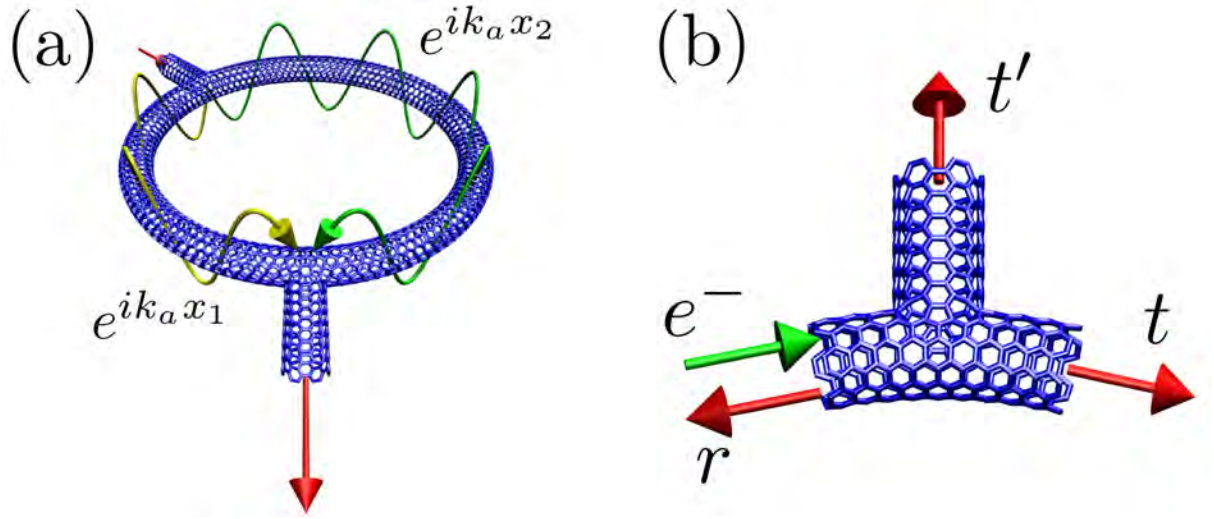

Figure 5.11: (a) Concept of the wave interference model. (b) Scaterring processes undergoing in the junctions.

Before entering the second terminal, these electrons can undergo scattering processes when passing across the junctions. An electron coming to a junction can be reflected back to the arm it comes from (with probability amplitude r), be transmitted to the other arm (with probability amplitude t), or be transmitted to the lead (with probability amplitude t'). After each passage, the wave amplitude is therefore multiplied by r, t or t', depending on whether the electron is reflected or transmitted to the other arm or to the second terminal, respectively (Fig. 5.11b). Because of current conservation, these coefficients obey

$$|r|^2 + |t|^2 + |t'|^2 = 1. \tag{5.18}$$

If the electron i undergoes θ_i arm-to-arm transmissions and ϕ_i reflexions before entering the second terminal, it will have (after entering the electrode) an amplitude A_i and a path length L_i given by

$$A_i = t' t^{\theta_i} r^{\phi_i} \tag{5.19}$$

$$\mathscr{L}_i = L_i + u_i L_1 + v_i L_2. \tag{5.20}$$

Here, u_i and v_i are integers which are functions of both θ_i and ϕ_i as well as of the time order in which the scattering processes occur. Two electrons entering the terminal produce an interference pattern with an amplitude $\mathscr{A}$:

$$\mathscr{A} = \sqrt{A_1^2 + A_2^2 + 2A_1A_2\cos\Big(k_a(\mathscr{L}_2 - \mathscr{L}_1)\Big)}. \tag{5.21}$$

In first approximation, we can associate the conductance to the sum of the squared amplitudes from these interference waves after considering all the possible Feynman paths. Let us represent any pair of possible paths for the two electrons (identified by θ_1, θ_2, ϕ_1, ϕ_2 and the order in which the events occur) by Ω. Doing this we can write:

$$I = \sum_{\Omega} |\mathscr{A}_{\Omega}|^2. \tag{5.22}$$

Since the interference pattern is determined by path difference and by the allowed k_a vectors, we can write the total intensity as a function of α (as the path difference depends on the number of nanotube cells in the arms) and energy (as it depends on k_a). We can write:

$$L_1 = R\alpha \qquad L_2 = R(2\pi - \alpha) \tag{5.23}$$

so that:

$$\mathscr{L}_2 - \mathscr{L}_1 = 2\pi R(1 + v_2 - v_1) + (u_2 - u_1 - v_2 + v_1 - 2)R\alpha. \tag{5.24}$$

For k_a we need to invert the $E(\mathbf{k})$ relation from each branch:

$$E(\mathbf{k}) = \pm\gamma\sqrt{3 + 2\cos\mathbf{k}\cdot\mathbf{a}_1 + 2\cos\mathbf{k}\cdot\mathbf{a}_2 + 2\cos\mathbf{k}\cdot(\mathbf{a}_1 - \mathbf{a}_2)} \tag{5.25}$$

with

$$\mathbf{k} = \frac{2\pi q}{|\mathbf{C}_h|}\frac{\mathbf{K}_1}{|\mathbf{K}_1|} + k_a\frac{\mathbf{K}_2}{|\mathbf{K}_2|} = q\mathbf{K}_1 + k_a\frac{\mathbf{K}_2}{|\mathbf{K}_2|} \tag{5.26}$$

and

$$\mathbf{K}_1 = \frac{1}{N}(-t_2\mathbf{b}_1 + t_1\mathbf{b}_2) \tag{5.27}$$

$$\mathbf{K}_2 = \frac{1}{N}(m\mathbf{b}_1 - n\mathbf{b}_2) \tag{5.28}$$

which results in:

$$\begin{aligned}[E(\mathbf{k})/\gamma]^2 = 3 + 2\cos(\frac{-2\pi q t_2}{N} + \frac{2\pi k_a m}{K_2 N}) + 2\cos(\frac{2\pi q t_1}{N} - \frac{2\pi k_a n}{K_2 N}) \\ + 2\cos(\frac{-2\pi q(t_1 + t_2)}{N} + \frac{2\pi k_a(n+m)}{K_2 N}).\end{aligned} \tag{5.29}$$

Further analysis is easier conducted by selecting a specific tube of interest[4].

By considering that interfering electrons undergo four processes before entering the second terminal we find the pattern depicted in Fig. 5.12(a) in the $(12,0)_r-(12,0)_t$ case and in Fig. 5.12(b) for the $(10,0)_r-(10,0)_t$ systems. Note that, for the energy range used in these plots, it is sufficient to consider only the bands which touch the Fermi level (or those closest to E_F in the semiconducting case) to express k_a as a function of energy. For illustrative purposes we choose $t=t'=0.63$ and $r=0.45$ (note however that t, t', and r , in general can assume complex values). These values seem reasonable from the transmission numbers presented in Section 5.4.

This simple $e^{ik_a x}$ model reproduces remarkably well the conductance behavior as a function of electron energy and α for both metallic and semiconducting systems (Fig. 5.12). However, it cannot account for the asymmetries around $E=0$, since it does not describe explicitly the details of the lattice (i.e. the presence of pentagons and heptagons, responsible for electron-hole asymmetry). The intrinsic structure of Y junctions, for instance, is known to have significant

[4]If one is interested in the bands crossing at the Fermi level for a M1 nanotube, we make $k_a=0$ so that:

$$[E(\mathbf{k})/\gamma]^2 = 3+2\cos(\frac{-2\pi q t_2}{N})+2\cos(\frac{2\pi q t_1}{N})+2\cos(\frac{-2\pi q(t_1+t_2)}{N}) \tag{5.30}$$

which clearly will result in 0 for q obeying:

$$\frac{2\pi q t_1}{N}=\frac{2\pi}{3}+2i\pi \qquad \text{and} \qquad \frac{2\pi q t_2}{N}=\frac{2\pi}{3}+2j\pi. \tag{5.31}$$

For a $(n,0)$ M1 nanotube ($mod(n,3)=0$) we can show that:

$$k_a=\frac{2}{T}\arccos\left(1-\frac{1}{2}[E(\mathbf{k})/\gamma]^2\right). \tag{5.32}$$

If we turn our attention now for a M2 nanotube, we make $k_a=2\pi/3T$ and the following equation

$$\begin{aligned}[E(\mathbf{k})/\gamma]^2 = 3+2\cos(\frac{-2\pi q t_2}{N}+\frac{2\pi m}{3N})+2\cos(\frac{2\pi q t_1}{N}-\frac{2\pi n}{3N}) \\ +2\cos(\frac{-2\pi q(t_1+t_2)}{N}+\frac{2\pi(n+m)}{3N})\end{aligned} \tag{5.33}$$

will result in 0 for q such that:

$$\frac{-2\pi q t_2}{N}=-\frac{2\pi m}{3N}\pm\frac{2\pi}{3}+2i\pi \qquad \text{and} \qquad \frac{2\pi q t_1}{N}=\frac{2\pi n}{3N}\mp\frac{2\pi}{3}+2j\pi \tag{5.34}$$

one can show that the right signs to use are those obeying:

$$mod(-m\pm N,3)=0 \quad \text{and} \quad mod(n\mp N,3)=0. \tag{5.35}$$

For a (n,n) metallic nanotube we have $N=2n$ and we use the lower signs. Then we end up with:

$$k_a=\frac{2}{T}\arccos\left(\frac{1}{2}\pm\frac{E(\mathbf{k})}{2\gamma}\right) \tag{5.36}$$

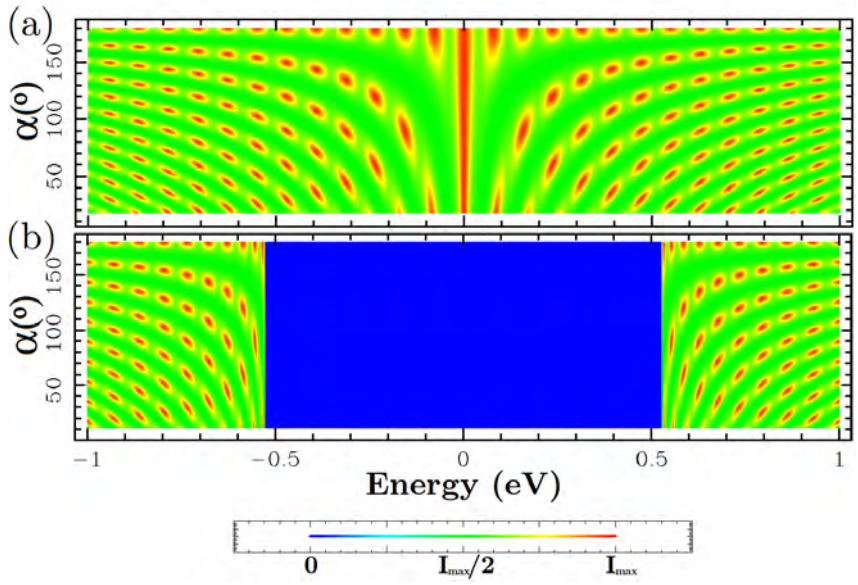

Figure 5.12: Conductance *versus* energy and α for the $\alpha^{3^\circ}_{180^\circ}$ in the $(12,0)_r-(12,0)_t$ (a) and $(10,0)_r-(10,0)_t$ systems according to the model described in Section 5.5 [7].

influence on the transport properties of the junction [122] and it is likely that similar effects related to the ring-terminal junctions are responsible for the asymmetries in the conductance obtained numerically. Since our goal is to model interference effects for an idealized geometry, the simple algebraic approach in this section does not include effects related to the atomistic details of the junction. Nevertheless, the simple model succeeds in predicting the positions and distribution of the maxima and minima of conductance on the $E-\alpha$ plane. We illustrate this result for the $(6,6)_r-(6,6)_t$ and $(8,2)_r-(8,2)_t$ configurations as white isocontour lines superimposed in Figures 5.8, 5.10. We can see that the model is not able to describe shifts in the tori energy levels due to the contacts as shown in the small differences in the conductance maxima in comparison to the numerical results.

5.6 Overview

In this chapter we discussed the electronic and transport properties of carbon nanotori attached to two semi-infinite terminals within a first-neighbor tight-binding model. We observed that three aspects which have a strong influence on the electronic transport in these rings, namely the type of nanotube composing the torus, the joint geometry and the position of the terminals along the torus. We were able to make a qualitative description of the influence of this last aspect (angle between terminals) by a simple continuum model. On the other hand, we stated that other features like the asymmetric conductance curves around E_F are the result of the scattering due the the pentagonal and heptagonal defects. In the next chapter we extend the study for

structures with many terminals, as well as to ring structures made up of graphene nanoribbons.

6 *Toroidal carbon nanostructures - multi terminal systems*

In this chapter, we significantly extend the previous study of the electronic transport/structure relationship of tubular nanorings (TNs) attached to two nanotube terminals of variable positions [7] by considering the effect of up to twelve terminals on the transport properties of these toroidal systems [8]. Additionally, we consider a "Flat Nanoring" (FN) structure made up of an one-atom-thick wall. In other words, these FNs have a graphene nanoribbon as their basic building block. This alternative approach to carbon nanotoroids is attractive given the properties of nanoribbons. As shown in Chapter 5, these structures occupy a special position in the rich family tree of carbon nanomaterials since they have an intermediate structure between carbon nanotubes and graphene and they present remarkable physical properties depending on their width and the geometry of edges [34, 123].

Even though we are a step behind in the experimental realization of such multi-terminal structures, they constitute a good test bed to study transport and interference effects.

6.1 Tubular and flat nanorings

The presence of a large number of terminals offers significant freedom in assembling complex nanocircuits using nanotori as elementary components. This makes it indispensable to develop a rigorous understanding of the impact of multiterminal on the transport properties of the systems. Since there is a characteristic relationship between electronic properties and geometry for carbon nanotubes and nanoribbons, those structures present unusual properties, especially when assembled into a toroidal geometry. One also expects enhanced mechanical stability for FNs since bonds need to be compressed or stretched on only one direction.

Here, a given TN is built using the same nanotube for the ring and the terminals connected to it. Similar to previous chapter, we choose a representative metallic tube from each family in this work: $(12,0)$ and $(6,6)$ for M1 and M2, respectively. For the FNs we use the zigzag and

armchair edged ribbons obtained after unrolling the $(6,6)$ and $(12,0)$ nanotubes. This procedure results in a zigzag ribbon with 12 zigzag strips and an armchair ribbon with 24 $C-C$ bonds along the width, respectively. The terminals are made from the same nanotube from which the ribbon is obtained. For both sets of TNs and FNs, rings with 120 unit cells were set up in order to construct symmetric structures with 2, 3, 4, 5, 6, 8, 10, and 12 terminals. We label the TN configurations as $(n_1,n_2)_n$ where n_1 and n_2 identify the nanotube composing the structure and n is the number of terminals. For the FN systems, we use the $[n_1,n_2]_n$ notation, where n_1 and n_2 identify the nanotube corresponding to the ribbon. The geometric construction of such systems is performed in a way similar to the approach described previously in Chapter 5 [7]: the junction geometry is assembled using a number of nanotube or nanoribbon unit cells in order to construct a sector with $120/n$ cells (where n is the number of terminals). This structure is then repeated to form the multiterminal toroid (Fig. 6.1).

We will present our results from the perspective of an electron impinging from an arbitrary terminal. Because of symmetry, all the other terminals are classified from their position relative to the symmetry mirror plane perpendicular to the torus and passing through the starting terminal so that the number of nonequivalent paths is the largest integer smaller than $n/2$. Each possible path is denoted as $(n_1,n_2)_n^{i\to j}$, where i (j) labels the source (drain) terminal. The source is numbered as 1 and the other terminals labeled counterclockwise as in Fig. 6.1.

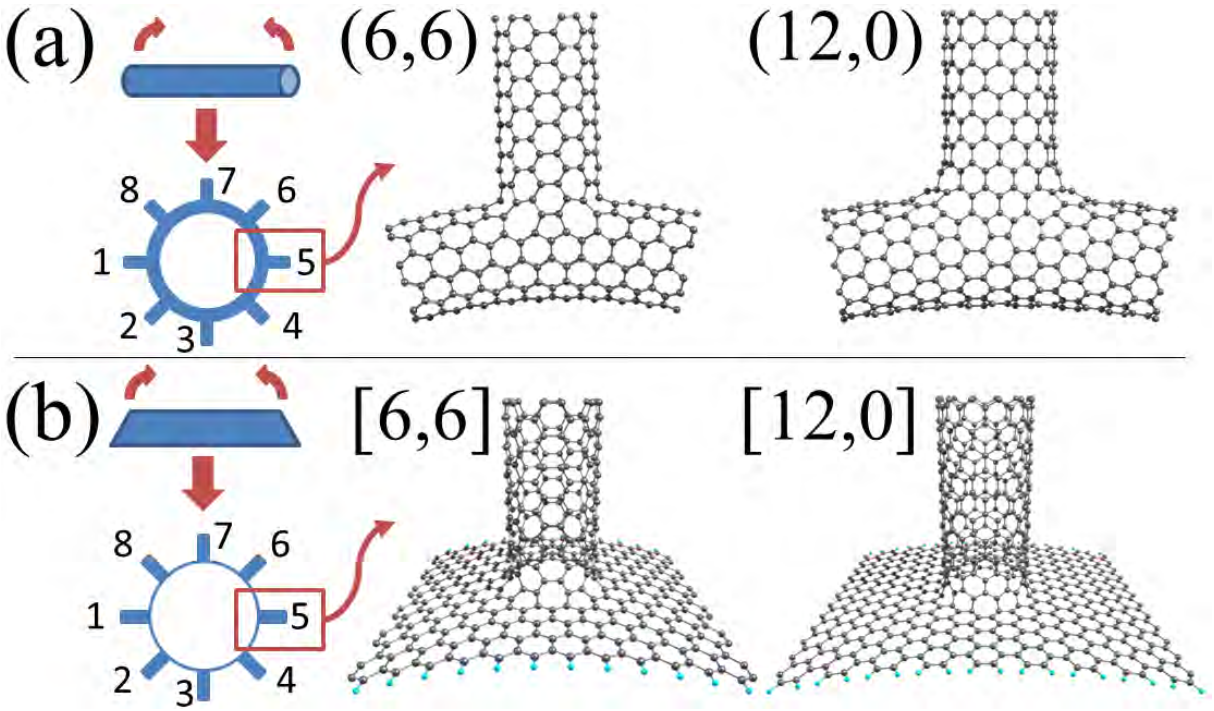

Figure 6.1: Carbon nanotoroid structures studied in this chapter: (a) TNs and (b) FNs [8].

6.2 Numerical results - TNs

The electronic properties of a given toroidal system are dictated by the corresponding elementary building block and by boundary conditions along its circumference [7]. It is important to note than the properties of a given ring are expected to depend on the number and positions of terminals since each geometry is characterized by a set of specific electronic paths, which give rise to a set of different electronic interference patterns. These correspond to the onset of resonances in the transmission spectra. Because of symmetry, some of these resonances will take place at the same energy value for configurations with different number of terminals. In addition, the atomistic details (such as the presence of pentagons and heptagons) of the connections between the ring and the terminals constitute sources of electronic scattering [7, 122]. All-in-all, these effects are responsible for rich transmission spectra for various ring geometries connected to a varying number of terminals, as we will now examine in details.

We start discussing the results for TNs. The conductance curves for the $(12,0)_n$ and $(6,6)_n$ systems with $n = 2,3,4,5,6$ are represented on Fig. 6.2. An important result is that sets of paths share the same conductance pattern with a pronounced dependence on the energy. For instance, an electron with energy around -0.32 eV transmits with high probability through $(6,6)_2^{1\to2}$ and $(6,6)_4^{1\to3}$ but not along $(6,6)_5^{1\to2}$ and $(6,6)_5^{1\to3}$. Conversely, an electron with energy 0.4 or -0.24 eV has a large probability to transmit along $(6,6)_5^{1\to2}$ but not $(6,6)_5^{1\to3}$. In addition, an electron with energy -0.2 eV travels more easily along $(6,6)_3^{1\to2}$ compared to $(6,6)_4^{1\to2}$ and $(6,6)_4^{1\to3}$. Note also that $(12,0)_3^{1\to2}$ is not an allowed path for electrons at energies around -0.06 and 0.36 eV, while both paths in the $(12,0)_5$ system are excluded for energies close to -0.09 eV. These examples show that once integrated into a complex nanocircuit, these structures have the potential to function as a path controlling tool since one can determine the electronic path by tuning the energy of the impinging electron.

The strong energy-dependent selectivity of the conductance paths is also present inside the same structure as observed in the $(6,6)_5$ system. This is particularly verified when the number of terminals is large. For instance, an electron has high probability to be transmitted along the $(6,6)_6^{1\to2}$ and $(6,6)_6^{1\to4}$ paths while it will avoid the $(6,6)_6^{1\to3}$ paths for an energy around either -0.04 or 0.34 eV. By switching the energy of the entering electron to any of the peaks surrounding -0.04 or 0.34 eV the current will flow in all the three possible paths in the $(6,6)_6$ structure. Therefore the six terminals behave as two separate groups of conducting paths which can be accessed by the electronic energy. A similar feature is observed in the $(12,0)_6$ case. For energies around 0.33 eV the electron flow is driven along $(12,0)_6^{1\to2}$, while it transmits through all the paths for the conductance peaks surrounding this particular energy values.

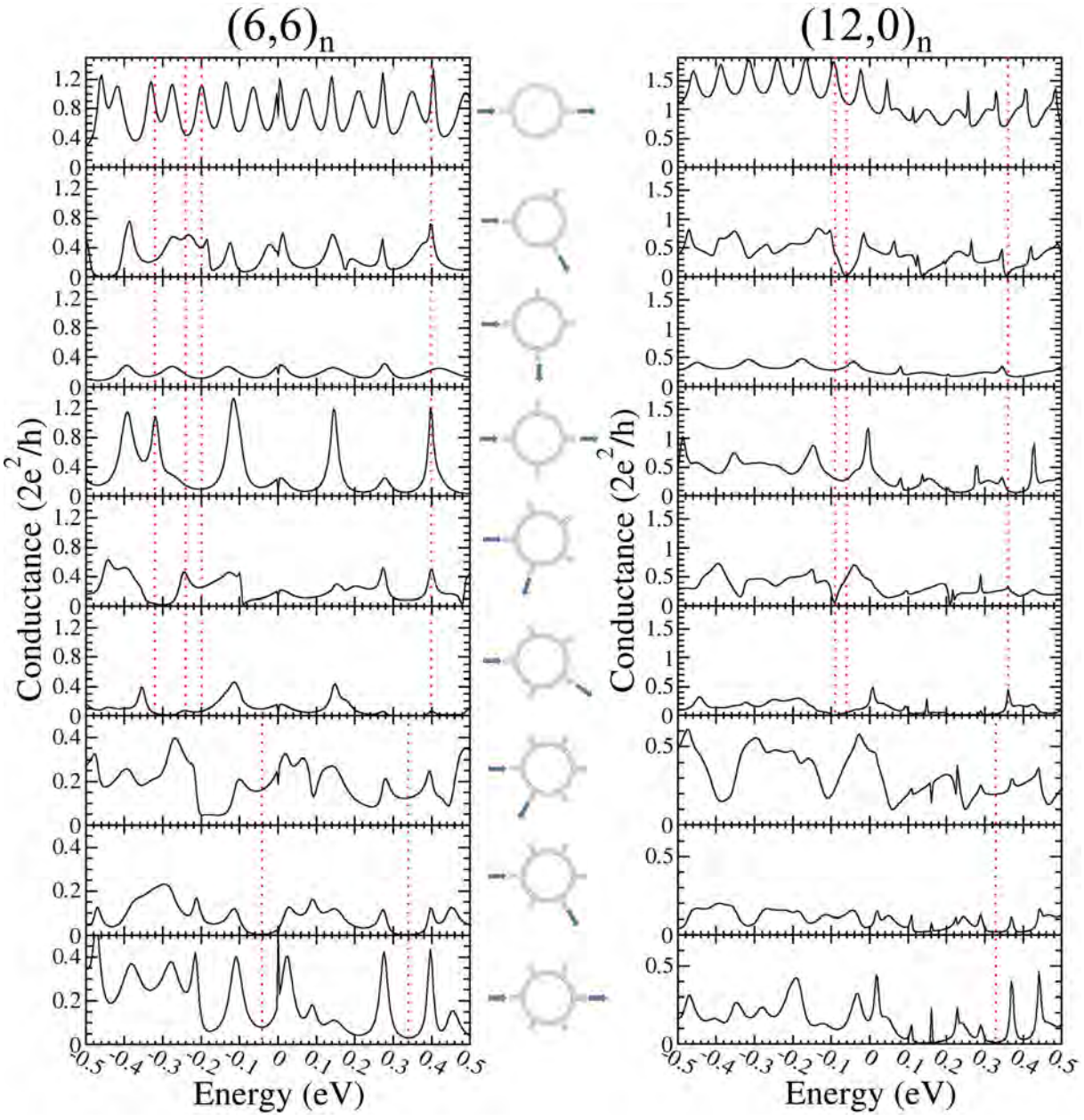

Figure 6.2: Conductance for the different paths on the $(6,6)_n$ and $(12,0)_n$, $n = 2,3,4,5,6$ structures [8].

In Figures 6.3 and 6.4 we show the results for the $(6,6)_n$ and $(12,0)_n$ with $n = 8,10,12$. From these plots we can observe that as the number of terminals increases, the effects of tunneling become more pronounced (as the terminals get closer to their neighbors). This is explicited by the fact that paths $(n_1,n_2)_n^{1\to j}$ with smaller j have much higher conductance than paths with j close to $n/2$..

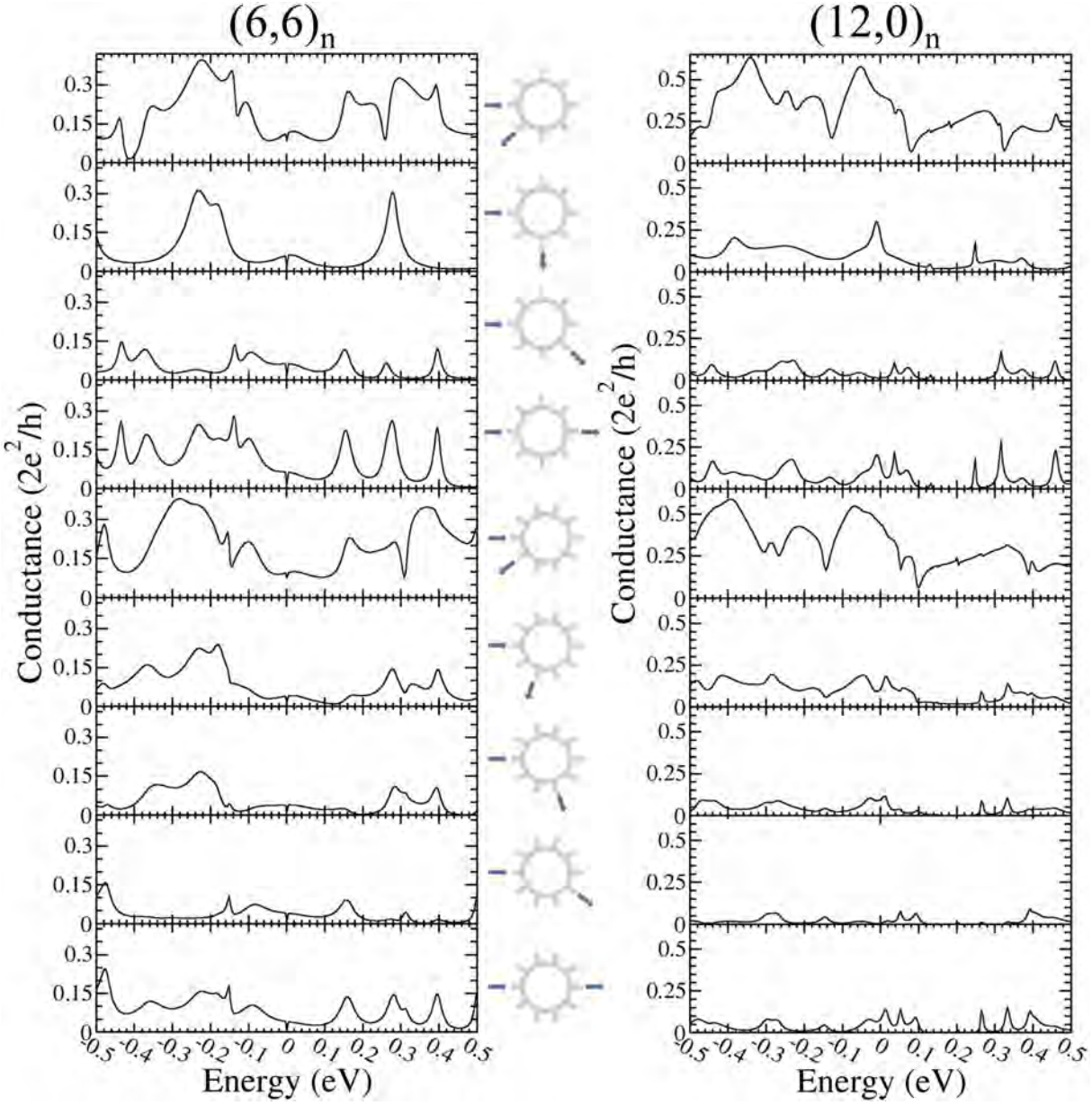

Figure 6.3: Conductance for the different paths on the $(6,6)_n$ and $(12,0)_n$, $n = 8,10$, structures [8].

6.3 Numerical results - FNs

Turning to the FN systems, we observe a number of similitudes and differences with the tubular ring systems. For instance, in the zigzag edged FNs, electron conductance is significant

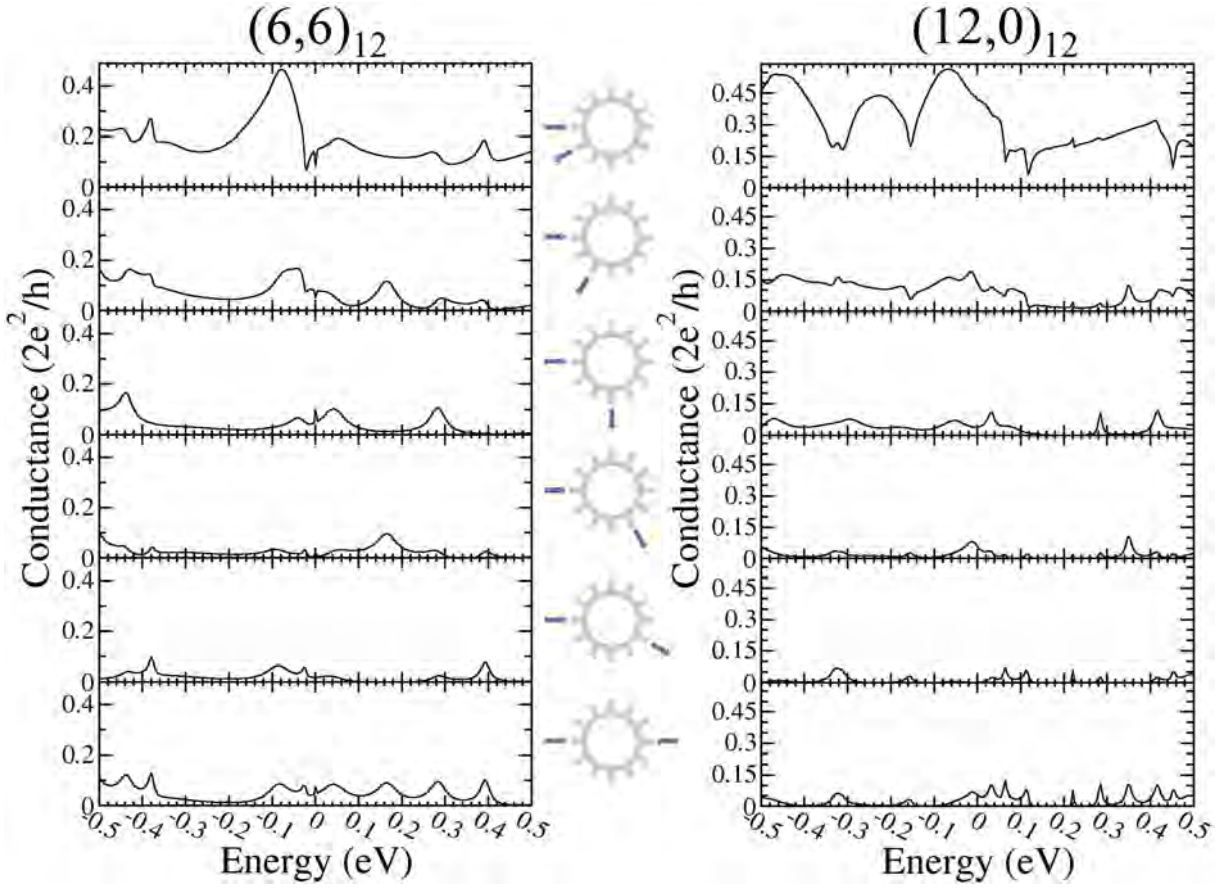

Figure 6.4: Conductance for the different paths on the $(6,6)_{12}$ and $(12,0)_{12}$ structures [8].

for $[6,6]_n$, $n = 2,3,4$, and 5 systems for the following electronic energies: -0.15 eV, -0.125 eV, -0.105 eV, and -0.065 eV, respectively (Fig. 6.5).

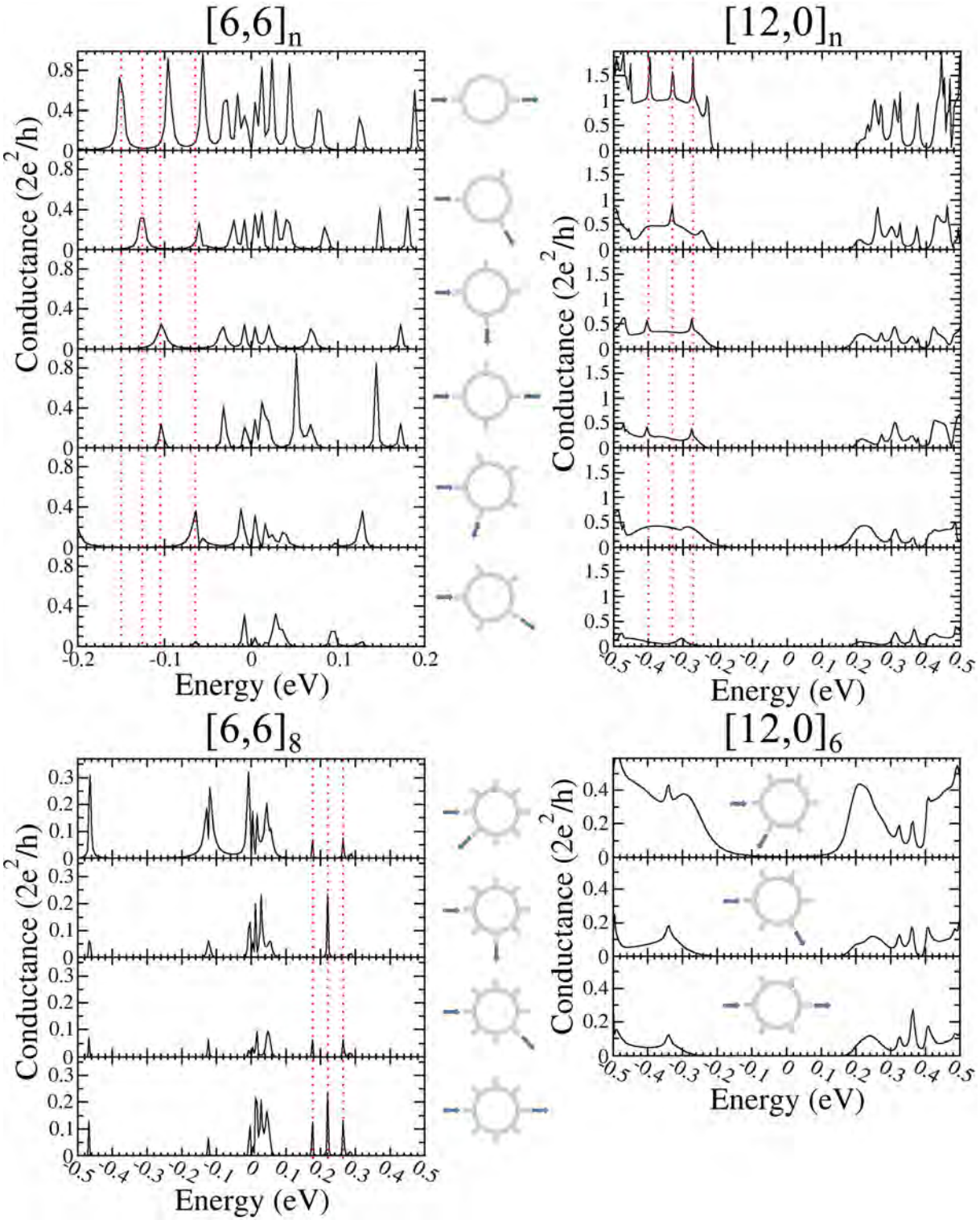

Figure 6.5: Conductance for the different paths on the $[6,6]_n$ ($n = 2,3,4,5,8$) and $[12,0]_n$ ($n = 2,3,4,5,6$) [8].

Conversely, a 0.4 eV gap is noticeable in all $[12,0]_n$, $n = 2,3,4,5$ systems. Focusing on

negative energies, one observes three conductance peaks in the $[12,0]_2$ system. Only the one located around -0.33 eV is present in $[12,0]_3$, two peaks (around -0.40 and -0.27 eV) appear in $[12,0]_4$, and none of them appears in the $[12,0]_5$ system. The presence of this set of peaks can be exploited to increase the current in a selective way by tuning the incoming electron energy to the specific energy values. A similar behavior is also apparent in $[6,6]_8$, as seen in Fig. 6.5, between 0.16 and 0.28 eV. The opening of these conducting channels forces the current to switch between two different patterns. In the first one, corresponding to electron energies close to 0.18 or 0.26 eV, the current proceeds between any possible path, with the notable exception of $[6,6]_8^{1\to3}$. In the second one, corresponding to 0.21 eV, the $[6,6]_8^{1\to2}$ and $[6,6]_8^{1\to4}$ conducting paths are blocked while $[6,6]_8^{1\to5}$ remains conducting and $[6,6]_8^{1\to3}$ is turned on. Since these peaks are much more pronounced for the zigzag edged ring than the previous peaks in the armchair edged systems we have a robust *on/off* switch from peak to peak and not only a raising/lowering regime, comparable to the armchair case. Finally, now looking at the $[12,0]_{12}$ systems with a larger number of terminals, as the $[12,0]_6$ case in Fig. 6.5, we observe that the energy gap around the Fermi level becomes smaller as the terminals are closer to each other. This is a direct manifestation of electron tunnelling when the path along the semiconductor ring is shorter than the Debye length [124, 125].

Similar features are present in the other $[6,6]_n$ and $[12,0]_n$ as shown in Figures 6.6 and 6.7.

6.4 Overview

In this chapter we discussed the effect of multi-terminal structures on the transport properties of toroidal carbon nanostructures. The presence of multiple electrodes brings a series of new interesting properties to these structures in comparison to the two-terminal case. Here we demonstrated that the path for the electrical current can be controlled by the electronic energy through a intricate set of rules. This result is an important step toward the development of new nanodevices as this structures provides a systematic way to control the current in nanocircuits.

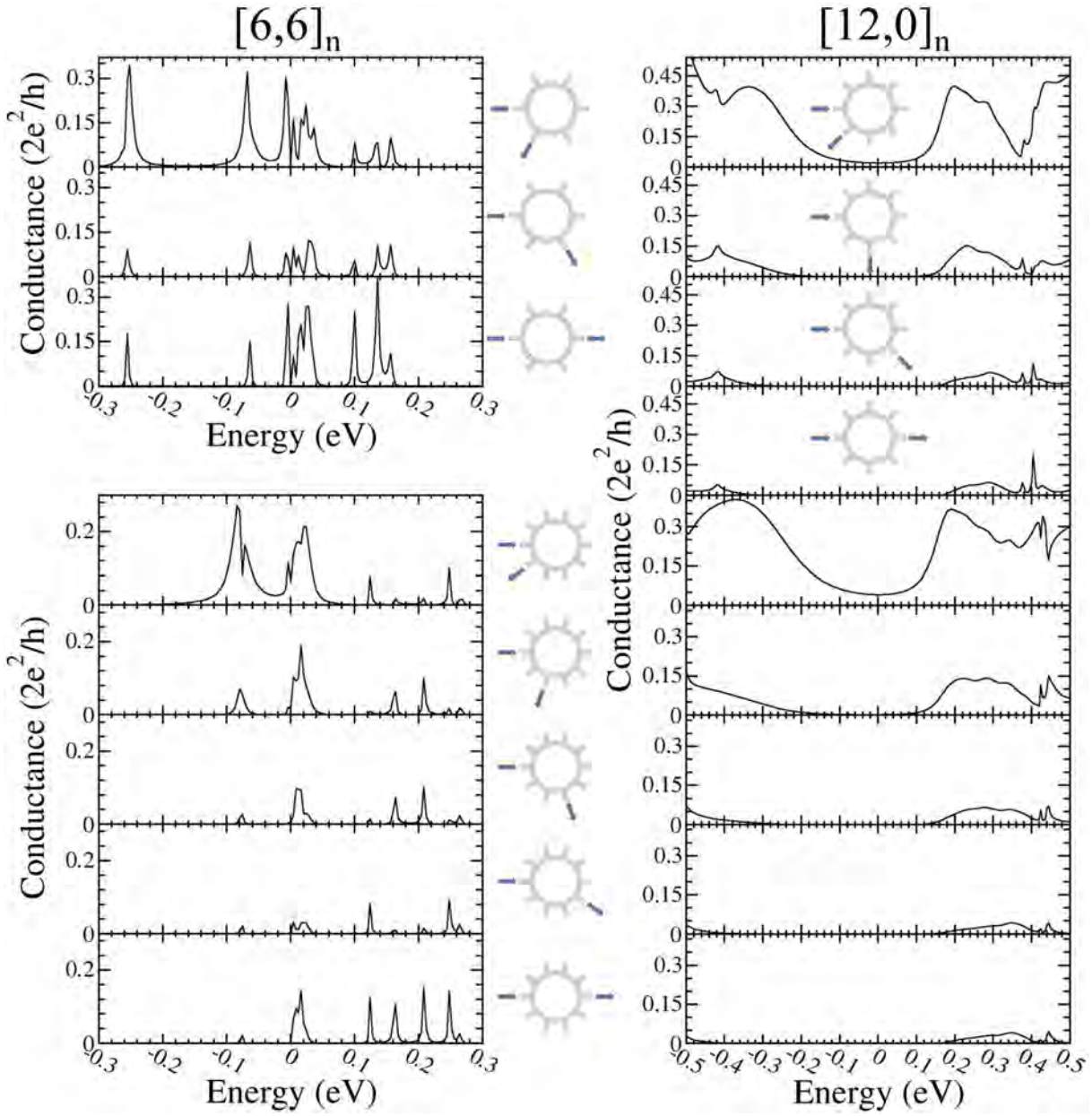

Figure 6.6: Conductance for the different paths on the $[6,6]_n$ ($n = 6, 10$) and $[12,0]_n$, ($n = 8, 10$), structures [8].

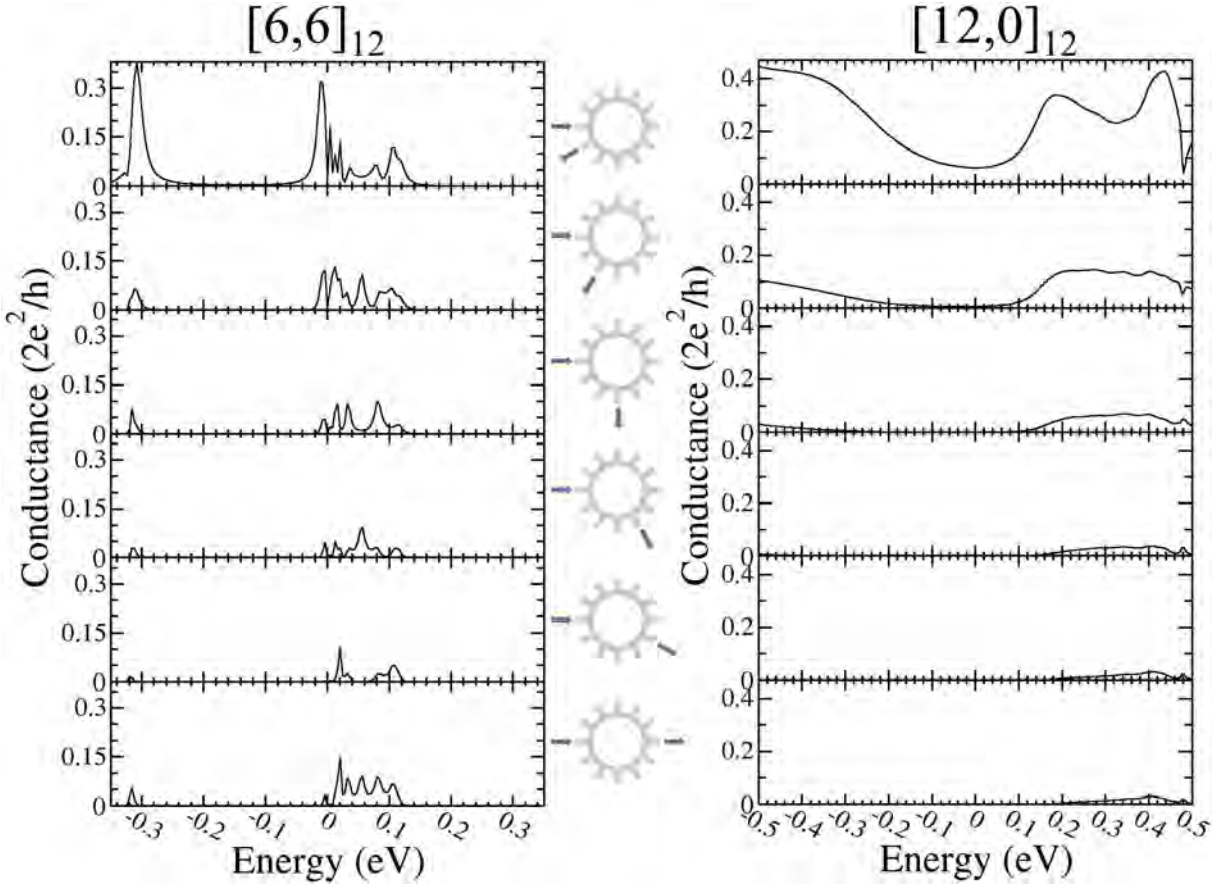

Figure 6.7: Conductance for the different paths on the $[6,6]_{12}$ and $[12,0]_{12}$ structures [8].

Part III

Nanowiggles

7 *Graphene carbon nanowiggles - geometric considerations*

In this chapter we will present a geometric description of the novel carbon nanostructures so called graphitic nanowiggles (GNWs). The structural properties of GNWs are discussed having carbon nanoribbons (GNRs) as basic building blocks. In the following two chapters we will discuss the electronic structure and electronic transport properties of these structures which are strongly dependent on GNW's geometry.

7.1 Introduction

Theory predicts that the materials properties needed for technological applications of GNRs demand narrow structures (width$<$10nm) with clean edges. To obtain such structures, a set of synthesis techniques, including both top-down and bottom-up approaches, has been developed to enable the precise and controlled fabrication of narrow and defect-free systems [51]. Most notably in the block-to-block approach devised by Cai et al. [4], small aromatic molecules are chemically assembled into highly crystalline narrow ribbons. In this method, a cyclo-dehydrogenation reaction proceeds on a metallic substrate that facilitates both the coupling and the thermally-activated fusion of individual aromatic molecules [4]. This method not only leads to the synthesis of high-quality GNRs, but has also demonstrated the possibility of creating more complex structures, with a variety of shapes such as multi-terminal GNRs and other wiggle-like one-dimensional systems. Those graphitic nanowiggles are characterized by a periodic repetition of graphene nanoribbon junctions (Fig. 7.1). Compared to other theoretically proposed structures,[35, 36, 37, 38] GNWs are particular attractive, owing to the existence of a practical synthesis technique. In addition, as we will demonstrate in the next chapter, GNW nanostructures possess unique properties that are superior to the simple sum of those of their GNR constituents: these atypical properties include electronic and magnetic behaviors which emerge from the interaction between the GNRs building blocks. The study performed in this

thesis does not only highlight the general principles guiding the properties of the major possible subclasses of GNWs, it also establishes a road-map for the synthesis of GNWs with desired optoelectronic and magnetic behaviors.

7.2 GNW's structure

GNWs consist in successive repetitions of parallel and oblique (relative to the GNW's periodic direction) GNR domains seamlessly stitched together without the need of structural defects. Their general structure is illustrated in Fig. 7.1a. If we restrict the discussion to achiral GNWs, we can denote the parallel and oblique sectors by P_α and O_β, respectively, with $\alpha, \beta = A, Z$ depending on the type of sector (armchair (A) or zigzag (Z)). This gives rise to the armchair-armchair (AA-GNW - Fig. 7.1b), armchair-zigzag (AZ-GNW - Fig. 7.1c), zigzag-armchair (ZA-GNW - Fig. 7.1d) and zigzag-zigzag (ZZ-GNW - Fig. 7.1e) geometries, named after the parallel and oblique edges, respectively.

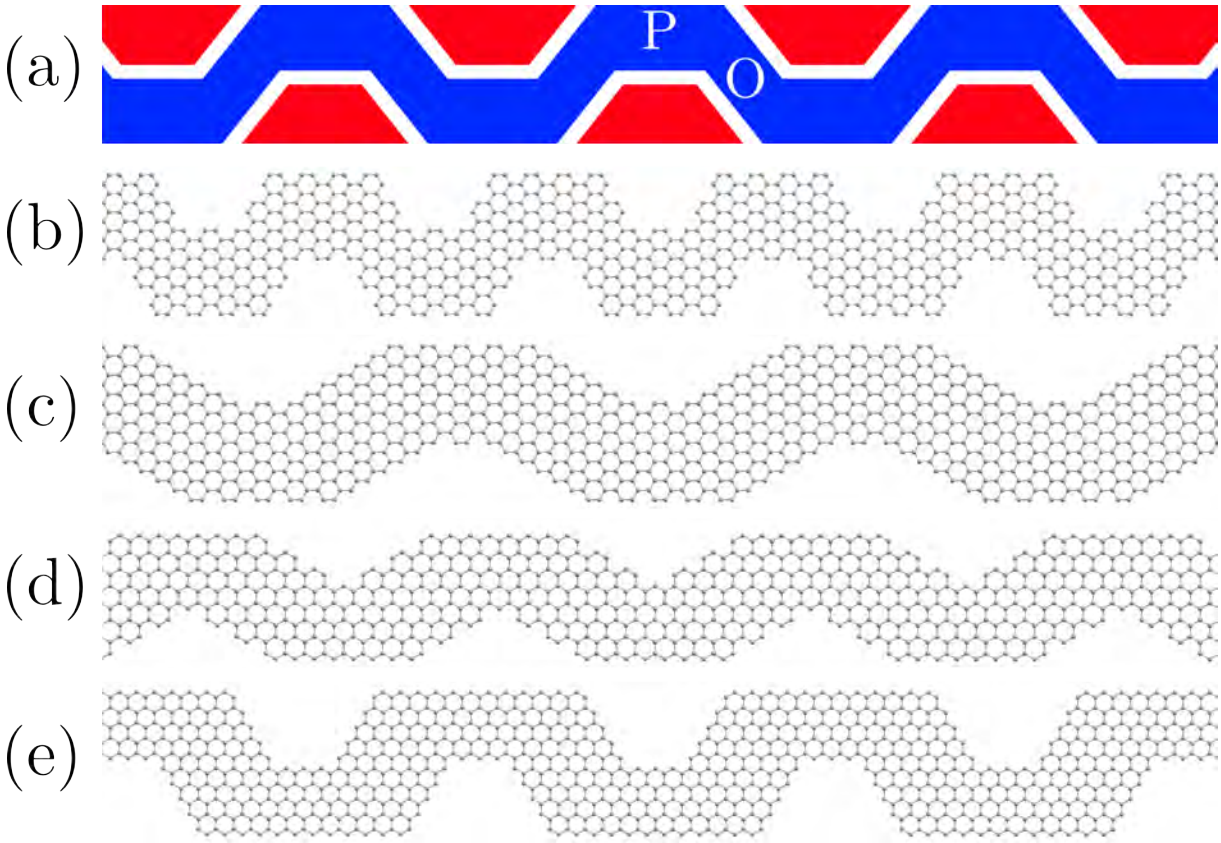

Figure 7.1: (a) Geometry and nomenclature of a GNW made up of successive oblique and parallel cuts in armchair (A) or zigzag (Z) patches. (b-e) Examples of an AA (b), AZ (c), ZA (d) and ZZ (e) GNW.

GNWs can also be conceptually viewed as armchair or zigzag GNRs over which trapezoidal wedges are carved away on alternating edges as depicted for the four achiral GNW types in

Fig. 7.2. We observe that $\alpha = \beta$ if the non-parallel sides from the trapezoidal wedges make an angle of 60° and $\alpha \neq \beta$ when this angle is 30°. Here we are restricted to these two cases (leaving the limiting case in which the trapezoid becomes a rectangle - 90° - for future studies).

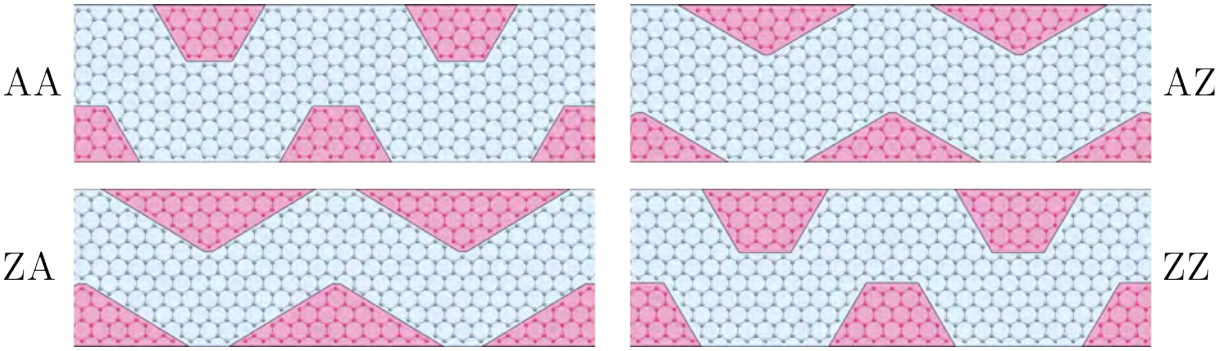

Figure 7.2: Schematic construction of the four achiral GNWs: initial GNR and the trapezoidal wedges needed to transform it into a GNW.

Each GNW is characterized by four parameters. The first two, W_p and W_o, represent the number of $C-C$ bonds or zigzag strips along the width of the parallel and oblique sectors (depending on their armchair or zigzag symmetry), respectively. These two quantities are illustrated for an AZ-GNW in Fig. 7.3. The other two numbers, L_p and L_o, are related to the sectors' lengths. While we identify L_o as the number of $C-C$ lines or zigzag strips along the width of the wedge healed GNW (similarly to the definition of W_p and W_o), the L_p length is the number of a_{CC}[1] lengths ($\alpha = A$) or the number of zigzag tips ($\alpha = Z$) along the smallest basis of the trapezoid formed by the GNW's edge atoms (as shown in Fig. 7.4). With the 4 parameters set $(P_\alpha, O_\beta) - (p_\alpha, o_\beta)$ the GNW structure is uniquely defined (where P_α, O_β, p_α and o_β represent W_p, W_o, L_p and L_o, respectively). In the next two chapters, we will restrict the values of L_p and L_o so that L_p is defined as the smallest possible and L_o such that at least one $C-C$ line or zigzag strip (along the GNW length) is not interrupted by the wedges. Under these restrictions, we represent a general GNW by the reduced symbol (P_α, O_β) since the other two parameters are implicitly determined by $L_p = 2$ (for AA- and AZ-GNWs) or $L_p = 1$ (for ZZ- and ZA-GNWs) and $L_o = 2W_p - 1$.

7.3 Lattice parameter

7.3.1 General approach

An important GNW's quantity is its unit cell length $\mathscr{L}$. In order to determine this value as function of W_p, L_p, W_o and L_o, we define the set (b,c,d,e,h,l,w,x,y) of characteristic lengths

[1] Where a_{CC} is the carbon-carbon distance in graphene.

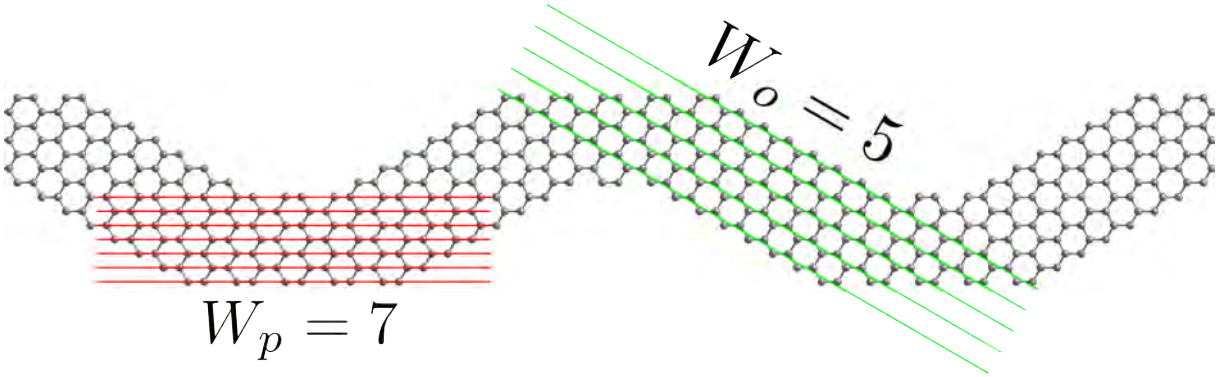

Figure 7.3: Definition of the W_p and W_o parameters as the lines of $C-C$ lines or zigzag strips along the width of each sector. Here the example of an AZ-GNW with $W_p = 7$ (red lines) and $W_o = 5$ (green lines).

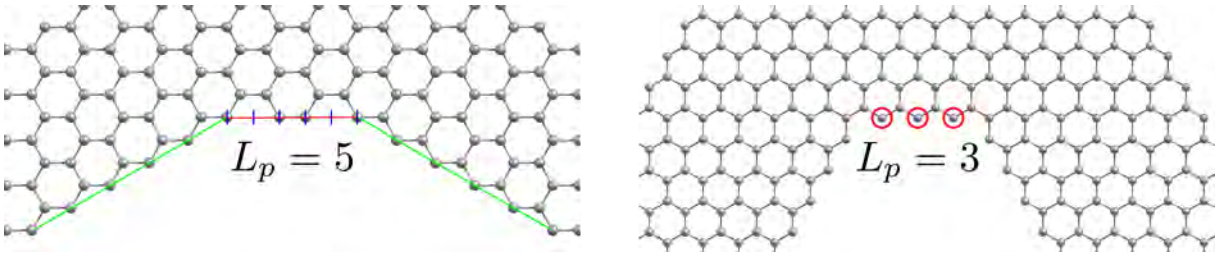

Figure 7.4: Definition of the L_p as the number of a_{CC} lengths (AA- and AZ-GNWs) or zigzag tips (ZA- and ZZ-GNWs) along the smallest basis of the trapezoid formed by the GNW's edge atoms. Here the example of an AZ-GNW with $L_p = 5$ (left) and a ZZ-GNW with $L_p = 3$ (right).

for a general GNW unit cell as in Fig. 7.5. The angle θ is either 60° (for AA- and ZZ-GNWs) or 30° (for AZ- and ZA-GNWs). In this figure we define the limits of the blue area as being the lines containing the frontier carbon atoms from the wiggle.

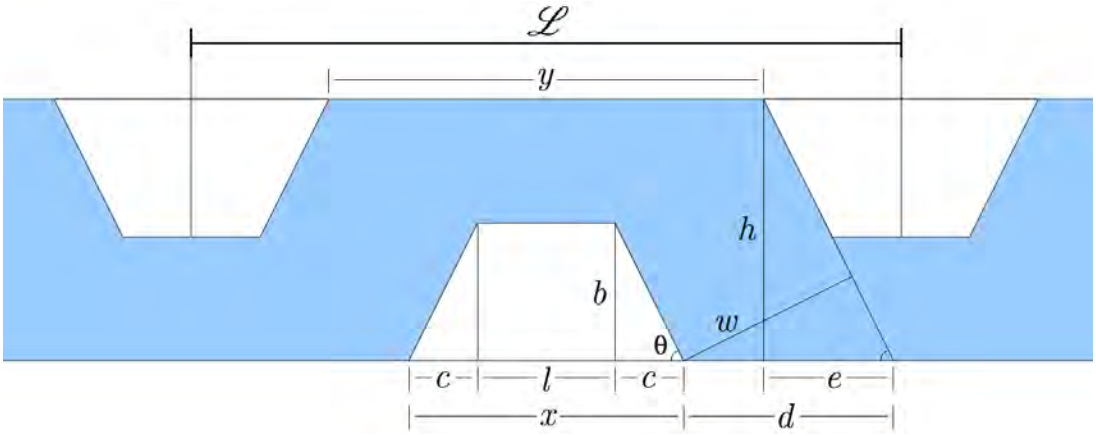

Figure 7.5: Auxiliary lengths to determine the lattice parameter of a general GNW unit cell.

From Fig. 7.5, we easily see that the lattice constant $\mathscr{L}$ for the GNW unit cell is given by:

$$\mathscr{L} = x + y. \tag{7.1}$$

We can also write:

$$x = l + 2c \qquad \text{and} \qquad c = b/\tan\theta \tag{7.2}$$

and

$$y = 2d + x - 2e; \qquad d = w/\sin\theta \qquad e = h/\tan\theta \tag{7.3}$$

so that:

$$\mathscr{L} = \frac{2w}{\sin\theta} + 2l + \frac{4b}{\tan\theta} - \frac{2h}{\tan\theta}. \tag{7.4}$$

Depending on the values for w, l, b, h and θ, we have different equations for each type of GNW.

7.3.2 The l length

By definition, l is trivially determined for AA- and AZ-GNWs by:

$$l = L_p a_{CC}. \tag{7.5}$$

A careful observation of the ZA-GNW structures (see example in Fig. 7.6a) allows us to write l for the ZA case as the distance between the two extreme zigzag tips on the wedge's parallel edge:

$$l = (L_p - 1)a \tag{7.6}$$

while we have to add a length $2f$ (defined in Fig. 7.6b) to this last result to obtain the corresponding length for the ZZ case. The value of f is easily obtained with the help of Fig. 7.6b as being:

$$f = a - \frac{a_{CC}/2}{\cos 30^\circ} = \frac{2a}{3} \tag{7.7}$$

so that

$$l = (L_p + \frac{1}{3})a. \tag{7.8}$$

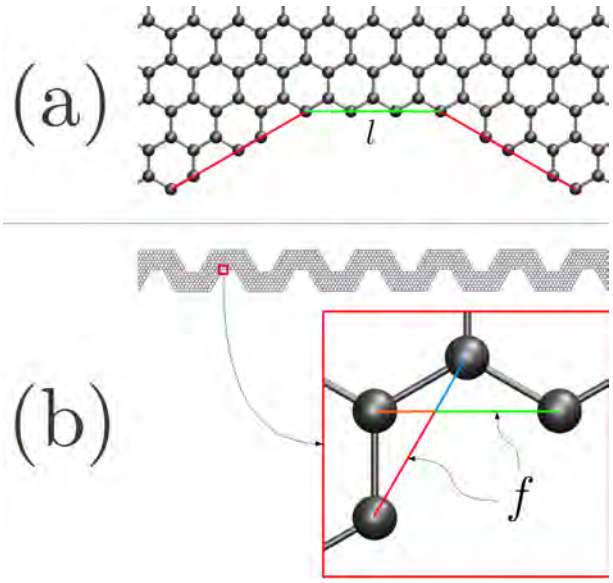

Figure 7.6: Auxiliary length l for ZA-GNWs (a) and increment f for ZZ-GNWs (b).

7.3.3 The w, h and b lengths

As a set of n $C-C$ parallel lines in graphene is $(n-1)a/2$ wide (where $a = a_{CC}\sqrt{3}$) and the width for a set of n zigzag strips is $(3n-2)a_{CC}/2$, w is easily obtained by:

$$w = \frac{(W_o - 1)a}{2} \qquad \text{for AA- and ZA-GNWs} \tag{7.9}$$

$$w = \frac{(3W_o - 2)a_{CC}}{2} \qquad \text{for AZ- and ZZ-GNWs.} \tag{7.10}$$

For the same reason we can write h as:

$$h = \frac{(L_o - 1)a}{2} \qquad \text{for AA- and AZ-GNWs} \tag{7.11}$$

$$h = \frac{(3L_o - 2)a_{CC}}{2} \qquad \text{for ZA- and ZZ-GNWs} \tag{7.12}$$

and finally b is obtained by:

$$b = h - \frac{(W_p - 1)a}{2} = \frac{(L_o - W_p)a}{2} \qquad \text{for AA- and AZ-GNWs} \tag{7.13}$$

$$b = h - \frac{(3W_p - 2)a_{CC}}{2} = \frac{3(L_o - W_p)a_{CC}}{2} \qquad \text{for ZA- and ZZ-GNWs.} \tag{7.14}$$

7.3.4 Lattice parameter relations

With the previous results it is trivial to write:

$$\mathscr{L}_{AA} = (2W_o + L_o + 2L_p - 2W_p - 1)a_{CC} \tag{7.15}$$

$$\mathscr{L}_{AZ} = (6W_o + 3L_o + 2L_p - 6W_p - 1)a_{CC} \tag{7.16}$$

$$\mathscr{L}_{ZA} = (2W_o + 3L_o + 2L_p - 6W_p - 2)a_{CC}\sqrt{3} \tag{7.17}$$

$$\mathscr{L}_{ZZ} = (2W_o + L_o + 2L_p - 2W_p)a_{CC}\sqrt{3}. \tag{7.18}$$

7.4 Number of atoms

Another important number defining a given GNW is how many atoms $\mathscr{N}$ are contained within a unit cell. In order to calculate $\mathscr{N}$ we first calculate the area corresponding to the wedge-healed GNW. We then carve out the area from the trapezoidal wedges. Observe that the non-parallel sides and the smallest basis from these trapezoids are midway between the corresponding sides on the trapezoids composed by the GNW's edge atoms and the edge atoms from the removed graphene flakes (as depicted in Fig. 7.7). An analogous definition is made for the lines determining the limits of the healed ribbon. The important quantities to determine are shown in Fig. 7.7. With these definitions we can write:

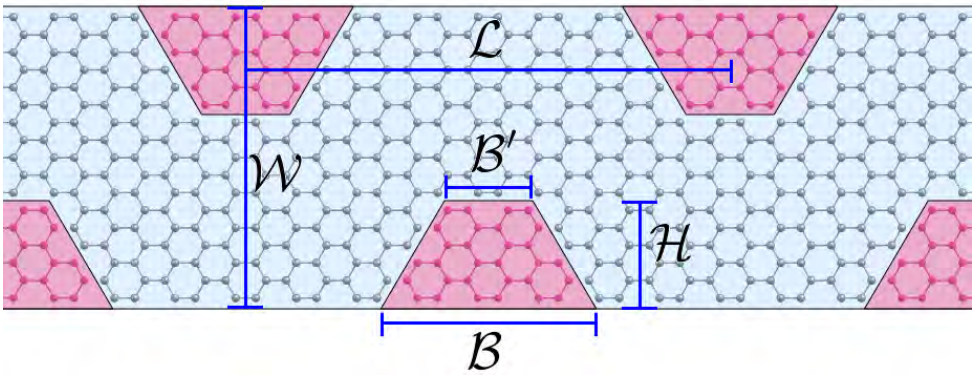

Figure 7.7: Auxiliary lengths used to determine the number $\mathscr{N}$ of atoms in a GNW's unit cell.

$$\mathscr{N} = \Big(\mathscr{L}\mathscr{W} - (\mathscr{B} + \mathscr{B}')\mathscr{H}\Big)/(3a_{CC}a/4) \tag{7.19}$$

where $\mathscr{L}$ is the length of the GNW's unit cell, $\mathscr{W}$ is the healed GNW's width, $\mathscr{H}$ is the height of the deleted trapezoids and $\mathscr{B}$ and $\mathscr{B}'$ are, respectively the largest and smallest basis from the trapezoids. Again, we have specific results for each GNW kind.

7.4.1 Healed GNW's width $\mathscr{W}$ and wedge's height $\mathscr{H}$

Based on the considerations from Section 7.3.3 we can write $\mathscr{W}$ as:

$$\mathscr{W} = L_o a/2 \qquad \text{for AA- and AZ-GNWs} \tag{7.20}$$

$$\mathscr{W} = 3L_o a_{CC}/2 \qquad \text{for ZA- and ZZ-GNWs,} \tag{7.21}$$

where we had to add $a/2$ in the first case and a_{CC} in the second since the lines defining the limits of the healed GNW's area are midway between the GNR frontier atoms and those from the carved graphene structure. In a similar way, we can came up with expressions for $\mathscr{H}$:

$$\mathscr{H} = (L_o - W_p)a/2 \qquad \text{for AA- and AZ-GNWs} \tag{7.22}$$

$$\mathscr{H} = 3(L_o - W_p)a_{CC}/2 \qquad \text{for ZA- and ZZ-GNWs.} \tag{7.23}$$

7.4.2 Wedge's basis $\mathscr{B}$ and $\mathscr{B}'$

Consider the trapezoid formed by the lines passing through the frontier atoms from the deleted flakes. Let l' and l'' be the smallest and largest basis from this trapezoid. For AA- and AZ-GNWs this value is $l' = l - a_{CC}$. So $\mathscr{B}'$ is given by:

$$\mathscr{B}' = \frac{l + l'}{2} = L_p a_{CC} - a_{CC}/2. \tag{7.24}$$

For the ZA-GNWs case we have $l' = l$ and:

$$\mathscr{B}' = \frac{l + l'}{2} = (L_p - 1)a. \tag{7.25}$$

In ZZ-GNWs we have $l' = l - f$ and:

$$\mathscr{B}' = \frac{l + l'}{2} = L_p a. \tag{7.26}$$

In order to obtain $\mathscr{B}$ we also consider the trapezoid defined by the frontier atoms from 2D graphene after carving out the trapezoidal flakes. Let l''' be the largest basis from this trapezoid. For AA-GNWs we have $l'' = l + 2c - 2a_{CC}$ and $l''' = l + 2c + a_{CC}$ so that:

$$\mathscr{B} = \frac{l'' + l'''}{2} = (L_p + L_o - W_p - \frac{1}{2})a_{CC} \tag{7.27}$$

For AZ-GNWs we have $l'' = l + 2c - 4a_{CC}$ and $l''' = l + 2c + 3a_{CC}$ so that:

$$\mathscr{B} = \frac{l'' + l'''}{2} = (L_p + 3L_o - 3W_p - \frac{1}{2})a_{CC} \tag{7.28}$$

Moving to ZA-GNWs, we have $l'' = l + 2c - 2a$ and $l''' = l + 2c + 2a$ and:

$$\mathscr{B} = \frac{l'' + l'''}{2} = (L_p + 3L_o - 3W_p - 1)a. \tag{7.29}$$

Finally, ZZ-GNWs are such that $l'' = l + 2c - 2f$ and $l''' = l + 2c + a$, resulting in:

$$\mathscr{B} = \frac{l'' + l'''}{2} = (L_p + L_o - W_p)a \tag{7.30}$$

7.4.3 Formulas for $\mathscr{N}$

The previous results allow us to write:

$$\begin{aligned}
\mathscr{N}_{ZZ} &= 4W_oL_o + 4L_pW_p - 2W_p^2 && (7.31)\\
\mathscr{N}_{ZA} &= 4W_oL_o + 4L_pW_p - 6W_p^2 - 4W_p && (7.32)\\
\mathscr{N}_{AZ} &= (12W_oL_o + 4L_pW_p - 6W_p^2 - 2W_p)/3 && (7.33)\\
\mathscr{N}_{AA} &= (4W_oL_o + 4L_pW_p - 2W_p^2 - 2W_p)/3. && (7.34)
\end{aligned}$$

7.4.4 Corrections on the AA-GNW case

Note that Eq. 7.34 does not give us the correct result in all the cases. The reason is that when calculating the area from the two trapezoids, we are actually calculating the area of a parallelogram composed by the two trapezoids in a construction similar to that shown in Fig. 7.8a,b. However, the simple superposition of the two trapezoids may not be compatible with the bonds made by the carbon atoms depending on the defining parameters of the GNW. By simple observation, the superposition of the two trapezoids is correct when:

- $mod(L_p, 3) = 2$ and $mod(L_o - W_p, 3) = 0$ (see example in Fig. 7.8a);
- $mod(L_p, 3) = 1$ and $mod(L_o - W_p, 3) = 2$ (see example in Fig. 7.8b).

The method has to be adapted for the other cases. Let us consider first the case $mod(L_p, 3) = 2$. When $L_o - W_p = 3i + 2$, we should shift each trapezoid in Fig. 7.8a by $a/2$ (perpendicular to their basis, one up and the other down), in such a way that the smallest line of $C - C$ bonds get out of the parallelogram (see example in Fig. 7.8c). So, the deleted atoms are composed by those inside the new parallelogram plus the atoms in the two $C - C$ lines outside the the parallelogram ($2(L_p + 1)/3$ in each). The part of each trapezoid included in the parallelogram has a smallest basis a_{CC} bigger and a height $a/2$ shorter. So, the number of atoms will be given

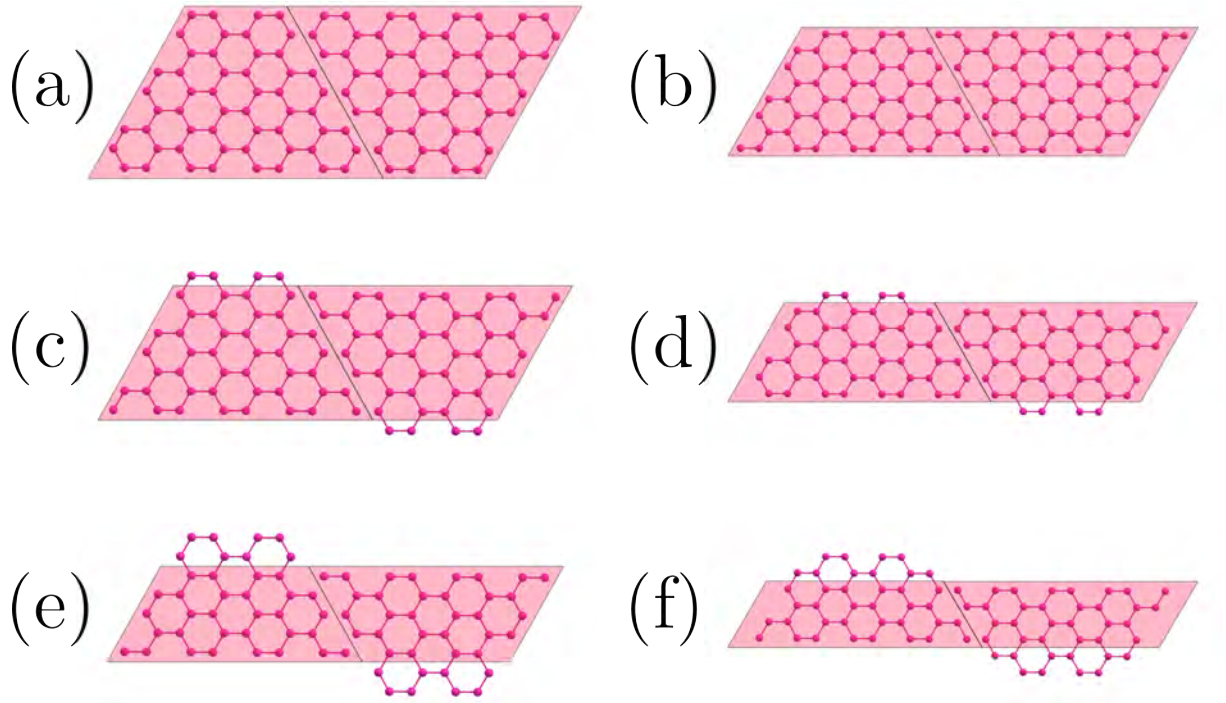

Figure 7.8: Auxiliary scheme to calculate the number of deleted atoms in a GNW's wedge.

by:

$$\mathcal{N}_{AA} = (4W_oL_o + 4L_pW_p - 2W_p^2 - 2W_p - 4)/3. \tag{7.35}$$

When $L_o - W_p = 3i + 1$, we should shift each trapezoid in Fig. 7.8a by a (perpendicular to their basis, one up and the other down), in such a way that the two smallest lines of $C-C$ bonds get out of the parallelogram (see example in Fig. 7.8e). It follows that the deleted atoms are composed by those inside the new parallelogram plus the atoms in the four $C-C$ lines outside the parallelogram ($2(L_p+1)/3$ in each). The part of each trapezoid included in the parallelogram has a smallest basis $2a_{CC}$ bigger and a height a shorter. So, the number of atoms will be given by:

$$\mathcal{N}_{AA} = (4W_oL_o + 4L_pW_p - 2W_p^2 - 2W_p - 4)/3. \tag{7.36}$$

Let us now consider the case $mod(L_p,3) = 1$. When $L_o - W_p = 3i + 1$, we should shift each trapezoid in Fig. 7.8b by $a/2$ (perpendicular to their basis, one up and the other down), in such a way that the smallest line of $C-C$ bonds get out of the parallelogram (see example in Fig. 7.8d). So, the deleted atoms are composed by those inside the new parallelogram plus the atoms in the two $C-C$ lines outside the parallelogram ($2(L_p-1)/3$ in each). The part of each trapezoid included in the parallelogram has a longer smallest basis (a_{CC} longer) and a shorter height ($a/2$

shorter). So, the number of atoms will be given by:

$$\mathcal{N}_{AA} = (4W_oL_o + 4L_pW_p - 2W_p^2 - 2W_p + 4)/3. \tag{7.37}$$

When $L_o - W_p = 3i$, we should shift each trapezoid in Fig. 7.8b by a (perpendicular to their basis, one up and the other down), in such a way that the two smallest lines of $C-C$ bonds get out of the parallelogram (see example in Fig. 7.8f). So, the deleted atoms are defined by those inside the new parallelogram plus the atoms in the four $C-C$ lines outside the parallelogram ($2(L_p-1)/3$ in each of the smallest two and $2+2(L_p-1)/3$ in each of the others). The part of each trapezoid included in the parallelogram has a smallest basis which is $2a_{CC}$ larger and a height being a shorter. Therefore, the number of atoms will be given by:

$$\mathcal{N}_{AA} = (4W_oL_o + 4L_pW_p - 2W_p^2 - 2W_p)/3 \tag{7.38}$$

so that the downsizing on the trapezoids area and the addition of the two lines of atoms compensate each other so that we end up with the same formula as for the cases exemplified in Fig. 7.8a-b.

In addition, an examination on Fig. 7.8c,f reveals that we have to subtract 4 atoms from the cases $mod(L_p,3) = mod(L_o - W_p) = 2$ and $mod(L_p,3) = 1$ $mod(L_o - W_p) = 0$ to eliminate four single bonded atoms at the corners of the outer parallel edges.

As we will see in the next section, we do not need to worry about the $mod(L_p,3) = 0$ case as this particular length is not allowed for AA-GNWs.

7.5 Geometric restrictions

Although any GNW is uniquely defined by the set of four parameters W_p, W_o, L_p and L_o, it is not true that any set of four numbers will define a valid GNW. In this section we discuss some of the restrictions that have to be applied to these parameters.

First, for all the four groups of achiral GNWs we have to have:

$$W_o, W_p \geq 2; \qquad L_o \geq W_p \qquad \text{and} \qquad L_p \geq L_p^{min} \tag{7.39}$$

with $L_p^{min} = 2$ for AA- and AZ-GNWs and $L_p^{min} = 1$ for ZZ- and ZA-GNWs. Additional specific restrictions applies for each case.

For AA-GNWs, the L_p parameter has to obey $2 \leq L_p \neq 3i$ in order to avoid rings with only one missing atom, as shown in Fig. 7.9. On the other hand, we should be restricted to the case

where $L_p = 3i+2$ for AZ-GNWs (values of L_p such that $L_p = 3i$ will give the same structures as $L_p = 3i+2$, while the $2 \leq L_p = 3i+1$ case will produce a lot of carbon atoms having only one neighbor).

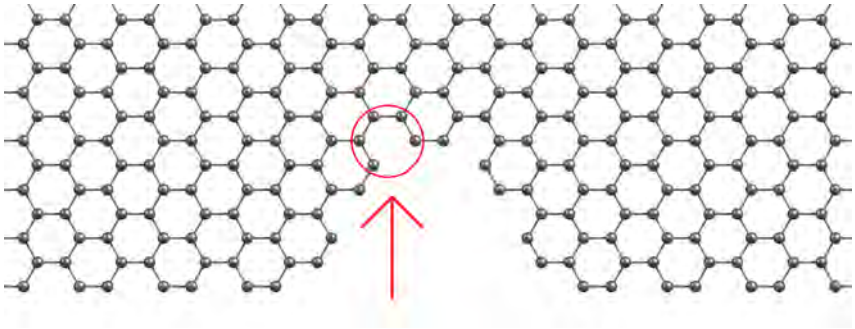

Figure 7.9: AA-GNW structure avoided by the $L_p \neq 3i$ condition.

The specific structure of AA-GNWs imposes an additional condition on $\mathscr{L}_{AA}$ which must be a multiple of $3a_{CC}$. Using the lattice parameter relation from Eq. 7.15, this restriction takes the form:

$$2W_o + L_o + 2L_p - 2W_p - 1 = 3l \quad \text{(AA-GNWs)} \tag{7.40}$$

where l is an integer. A similar restriction should also be applied to AZ-GNWs, but the corresponding equation is automatically satisfied since $L_p = 3j+2$ in this case.

Finally, the length y corresponding to the outer edge of the parallel sector (Fig. 7.5) has a specific lower bound value for each GNW type. For AA-GNWs, this value is $y_{min} \times a_{CC}$ with $y_{min} = 3$, $y_{min} = 1$ or $y_{min} = 5$ for $mod(y/a_{CC}, 3) = 0, 1, 2$, respectively, as illustrated in Fig. 7.10a-c. For AZ-, ZA- and ZZ-GNWs, this treshold value is a_{CC}, 0 and $2a_{CC}\sqrt{3}/3$, respectively, as exemplified in Fig. 7.10d-f.

After using the expression for y in Appendix A for each GNW class we end up with:

$$AA \quad \rightarrow \quad 2W_o + L_p - W_p - 1 \geq y_{min}; \tag{7.41}$$

$$AZ \quad \rightarrow \quad 6W_o + L_p - 3W_p \geq 2; \tag{7.42}$$

$$ZA \quad \rightarrow \quad 2W_o + L_p - 3W_p \geq 1; \tag{7.43}$$

$$ZZ \quad \rightarrow \quad 2W_o + L_p - W_p \geq 1. \tag{7.44}$$

7.6 Summary of results

In this chapter we presented a detailed description of the four classes of achiral GNW structures: AA, AZ, ZA and ZZ. We demonstrated that the whole GNW structure can be defined

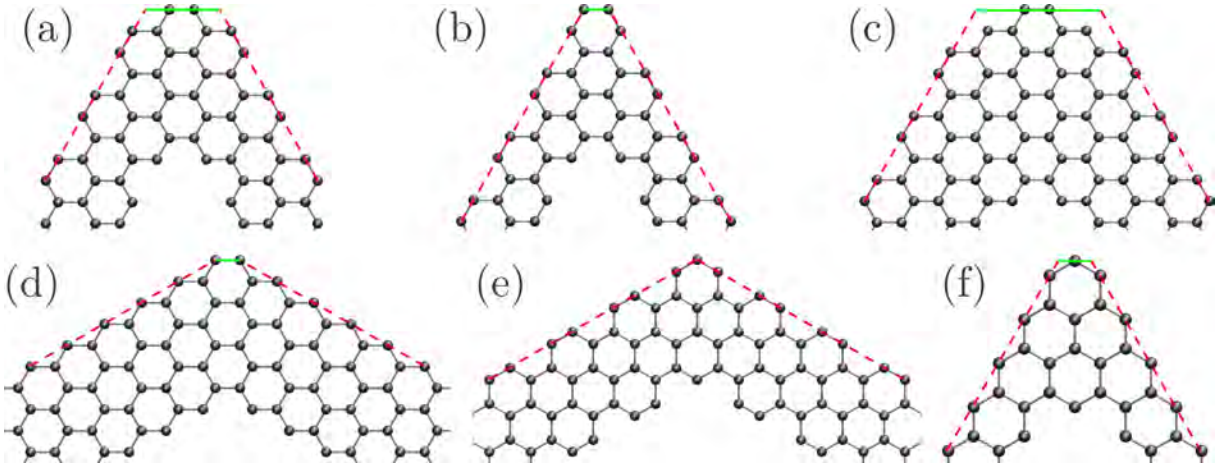

Figure 7.10: Examples for the minimum value of the length y of the outer parallel edge (full green lines) in AA- (a-c), AZ- (d), ZA- (e) and ZZ-GNWs (f).

by a set of four integer parameters:

$$(W_p, L_p, W_o, L_o) \tag{7.45}$$

where W_p and W_o are related to the widths of the periodic and oblique sectors, respectively, whose successive alternate repetition defines the periodic GNW structure. The L_p and L_o define the lengths of these sectors. In fact, important quantities defining the GNW are uniquely determined by these four numbers. The GNW's unit cell's length is calculated by a specific formula for each GNW type, as summarized in Table 7.1.

Table 7.1: GNW's lattice parameter as a function of W_p, W_o, L_p and L_o for the four achiral GNW classes.

XX	$\mathscr{L}_{XX}$
AA	$(2W_o + L_o + 2L_p - 2W_p - 1)a_{CC}$
AZ	$(6W_o + 3L_o + 2L_p - 6W_p - 1)a_{CC}$
ZA	$(2W_o + 3L_o + 2L_p - 6W_p - 2)a_{CC}\sqrt{3}$
ZZ	$(2L_p - 2W_p + 2W_o + L_o)a_{CC}\sqrt{3}$

Similarly, the number of atoms within a unit cell is easily obtained by relations listed on Table 7.2.

Table 7.2: Number of atoms within a GNW unit cell as a function of W_p, W_o, L_p and L_o for the four achiral GNW classes. The value of i for AA-GNWs depends on the W_p, L_p and L_o values.

XX	$\mathscr{N}_{XX}$
AA	$(4W_oL_o + 4L_pW_p - 2W_p^2 - 2W_p + i - j)/3$
AZ	$(12W_oL_o + 4L_pW_p - 6W_p^2 - 2W_p)/3$
ZA	$4W_oL_o + 4L_pW_p - 6W_p^2 - 4W_p$
ZZ	$4W_oL_o + 4L_pW_p - 2W_p^2$

In Table 7.2, the i and j parameters for AA-GNWs depend on the W_p, L_p and L_o values by specific rules[2].

We finished the chapter by describing a set of restrictions one has to apply to the four parameters in order to construct a valid GNW structure. In the following chapters we use a shorter notation:

$$(P_\alpha, O_\beta) \tag{7.46}$$

where P_α and O_β represent W_p and W_o, respectively, and α and β identify if the corresponding sector has an armchair or zigzag edge geometry. In this case, L_p and L_o are implicitly determined so that L_p assumes the smallest allowed value and L_o is such that at least one zigzag strip or $C-C$ line is not interrupted along the GNW's periodic direction.

A simple tool to generate atomic coordinates of GNWs is provided in Appendix B.

[2]Here $i = 0$ for the cases $[mod(L_p,3); mod(L_o - W_p,3)] = [1;0],[1;2],[2;0]$, $i = -4$ for $[mod(L_p,3); mod(L_o - W_p,3)] = [2;1],[2;2]$ and $i = 4$ for $[mod(L_p,3); mod(L_o - W_p,3)] = [1;1]$. The other cases are not valid. We also have $j = 4$ for the cases $[mod(L_p,3); mod(L_o - W_p,3)] = [1;0],[2;2]$ (and $j = 0$ otherwise) to eliminate four single bonded atoms at the corners of the outer parallel edges for the corresponding structures.

8 *Graphene carbon nanowiggles - Electronic properties*

In this chapter we present the calculation of the electronic structure and spin ordering of the four GNW types. By changing the structural parameters we have generated band gap maps for different magnetic arrangements. Our calculations predict the emergence of physical phenomena which are absent in their constituents graphene nanoribbons. These new properties result from the interplay between the properties of the building blocks, the symmetry of the structure and the bipartition of graphene lattice.

8.1 Introduction

After developing a general framework to classify nanowiggles according to their geometry in Chapter 7, we now present a discussion of their electronic structure. The nanowiggles reported experimentally in Ref. [4] are AA-GNWs corresponding to $(9_A, 6_A)$, as shown on Fig. 8.1b. Here, we will consider the extended set of systems in which the P_α and O_β edges can assume AA (e.g. $(9_A, 6_A)$, Fig. 8.1b), AZ (e.g. $(6_A, 7_Z)$, Fig. 8.1c), ZA (e.g. $(4_Z, 9_A)$, Fig. 8.1d) or ZZ (e.g $(7_Z, 7_Z)$, Fig. 8.1e) geometries. In this extended set, the length of the O sector is chosen such that at least one full zigzag or armchair strip along the GNW is not cut by the wedges, while the P sector is defined to have the shortest allowed length (as explained in Section 7.2).

We carried out a systematic study, by varying the P_α and O_β widths, using the TBU method implemented in the TBFOR package as described in Chapter 2. Representative structures from each GNW family are also studied within state-of-the-art DFT calculations to establish the TBU suitability and accuracy for the study of these graphitic systems.

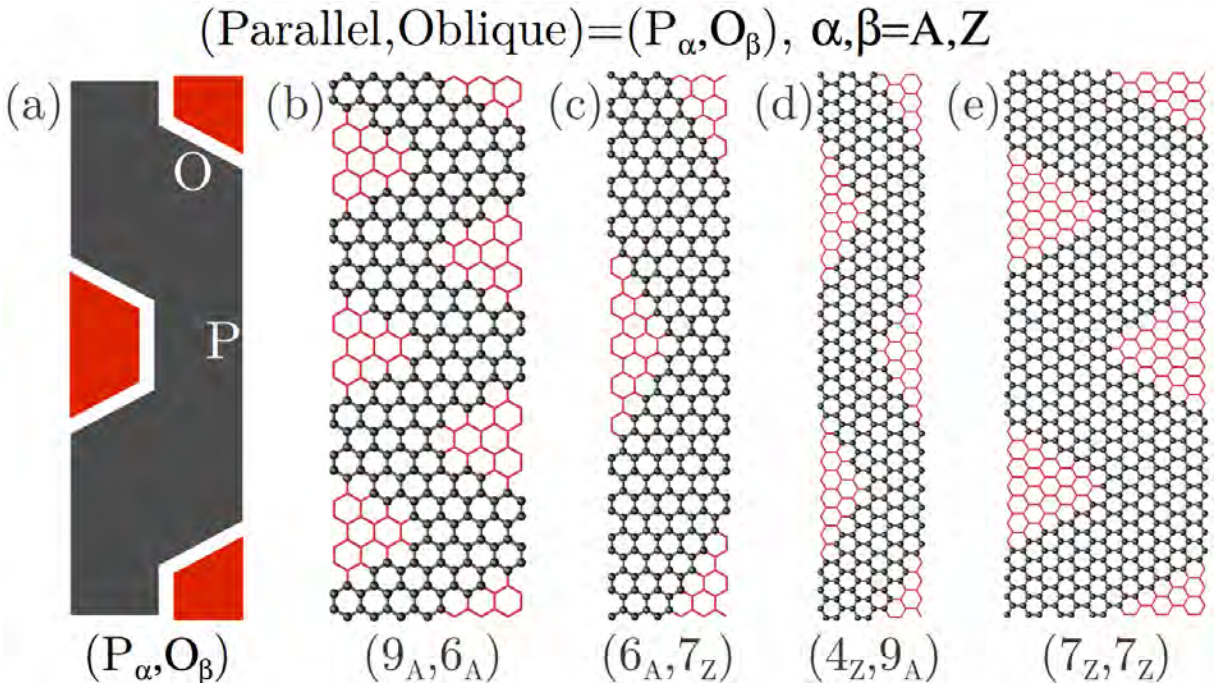

Figure 8.1: (a) Geometry and nomenclature of a GNW made up of successive oblique and parallel cuts in armchair (A) or zigzag (Z) patches. (b-e) Examples of an $(9_A,6_A)$ AA (b), $(6_A,7_Z)$ AZ (c), $(4_Z,9_A)$ ZA (d) and $(7_Z,7_Z)$ ZZ (e) GNW. One (c), two (d,e) and three (b) unit cells of the periodic systems are shown [9].

8.2 Theoretical Methods

The electronic properties of the systems depicted in Fig. 8.1 have been calculated within a GGA-based density functional theory (DFT) approach implemented in VASP [92, 93]. We computed the electronic properties after full atomic relaxation, using a fine k-point sampling and PAW pseudo-potentials, with a cut-off energy of 400 eV for the plane-wave basis set. DFT is too computationally demanding to perform a systematic study of the relationship between the details of the geometry and the electronic properties of GNWs of any size. Fortunately, compared to DFT, the less expensive π-band tight-binding approach yields a good quantitative description of the electronic properties of carbon nanostructures. The present self-consistent tight-binding + U (TBU) calculations were performed with the TBFOR package (see Section 2.8) and are based on the model developed in Ref. [126] with first-, second-, and third- nearest neighbor hopping integrals given by $t_1 = 3.2$ eV, $t_2 = 0$ eV and $t_3 = 0.3$ eV, respectively. The different chemical environment at the edges was accounted for by including a $\Delta t_1 = 0.2$ eV correction to the t_1 parameter for the frontier atoms [126]. Further, a precise description of the magnetic interaction in GNRs has been shown to be tractable when the total Hamiltonian includes an explicit Hubbard-like term where spin-spin interactions are treated in a mean-field fashion. This is accomplished by introducing a positive U parameter that quantifies the magnitude of the on-

site electron-electron interaction. In practice, this TBU model has been shown to capture the most relevant physical aspects of magnetic states in a number of graphitic systems, including zigzag GNRs [30], as we showed in Chapter 1 using the TBFOR package. A precise value of the U interaction strength is chosen to match the TBU and DFT band structures for the systems depicted on Fig. 8.1 considering all their magnetic configurations. The one-parameter fit results in $U = 0.92t_1$. As we will show in the next section, the two methods agree remarkably well for all the systems of Fig. 8.1.

8.3 Multiple magnetic states

In both DFT and TBU calculations, we observe that the final result from the self-consistent procedure for the spin distribution depends on the initial guess for the spin-up and -down densities as shown in Fig. 8.2 for the systems depicted in Fig. 8.1. This is a signature of the presence of multiple metastable magnetic states. While the AA geometry presents only a paramagnetic distribution (with null spin-polarization for all the sites), all the other cases present a set of different magnetic states (whose spin distribution nature is illustrated on the top of the band structure plot for each state). This is remarkable for the AZ and ZZ structures as they present up to four different magnetic states (as discussed in the next sections).

The TBU and DFT results for the band structure are shown in solid and dashed lines, respectively, in Fig. 8.2. This figure indicates a relatively good agreement between the DFT and TBU results which becomes remarkable for the bands close to the Fermi energy, and gives us confidence in using the TBU model to study a broader set of GNWs. The DFT calculations were performed with edge atoms properly saturated with hydrogen atoms, as implicitly included in the TBU model. An additional point to be emphasized is that all the TBU results were obtained with the same parameters, showing that the TBU approach constitutes an excellent tool for the study of the different classes of GNWs. Convinced by this good DFT-TBU agreement for the systems in Fig. 8.1, we used the model Hamiltonian to carry out a systematic study aimed at understanding the influence of the GNW geometry on the electronic properties by simulating a total of 393 AA, 153 AZ, 75 ZA and 171 ZZ structures corresponding to a wide range of P and O sector widths. Other geometrical parameters, such as the length of each sector, could also be varied but we found that the range of properties is well represented by the structures considered here.

The existence of multiple magnetic states is a major signature of the rich properties of GNWs (Fig. 8.2). This finding can be rationalized from the properties of individual zigzag

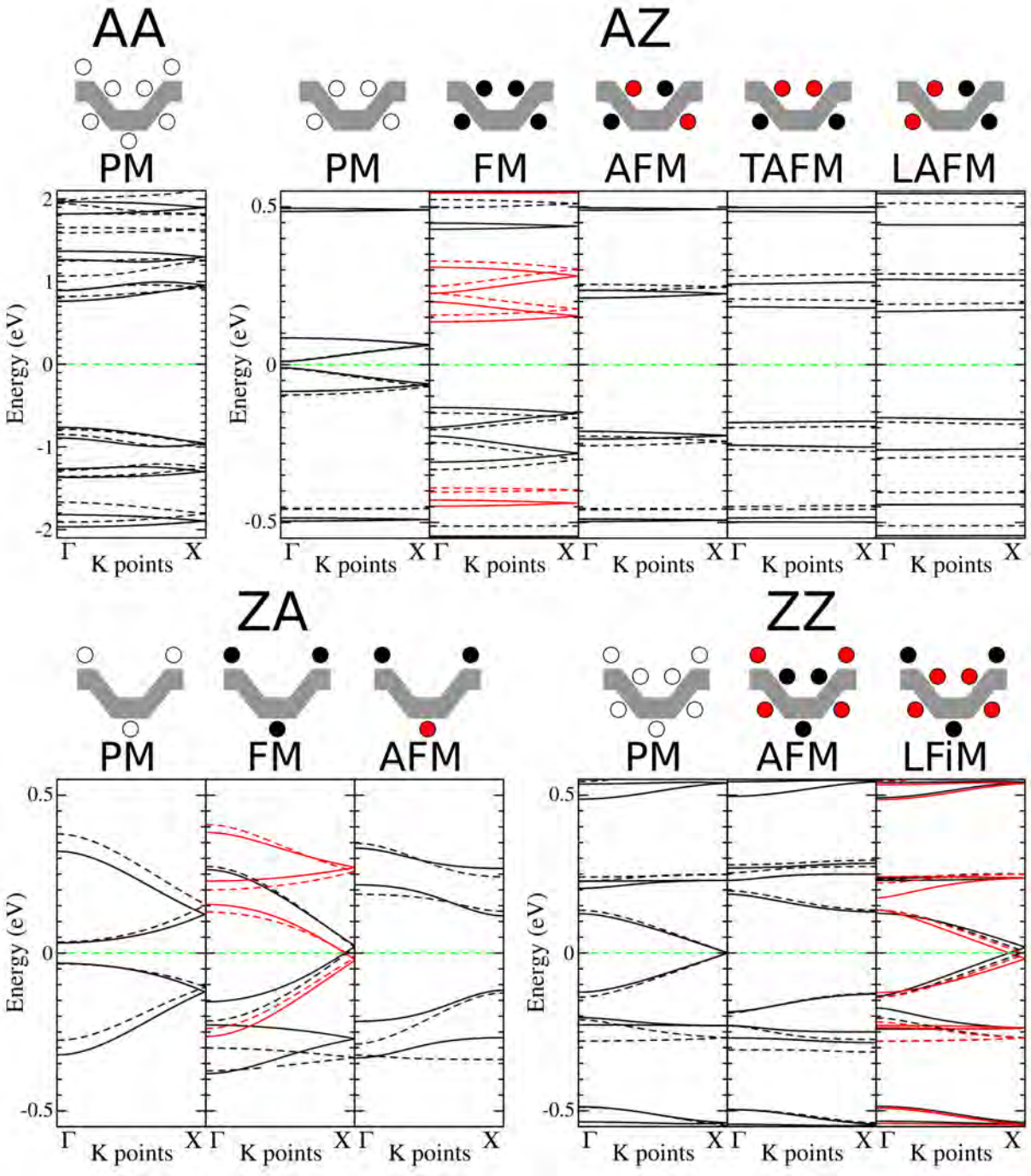

Figure 8.2: DFT (dash lines) and TBU (solid lines) electronic band structures corresponding to the different magnetic states for the representative AA, AZ, ZA and ZZ GNWs shown in Fig 8.1. The schematic spin distributions (black: up, red: down, white: no polarization) are shown on top of each panel [9].

and armchair edged GNRs: while armchair systems are non-magnetic, the zigzag systems' ground state is anti-ferromagnetic with possible metastable non-magnetic and ferromagnetic spin configurations [31], as we discussed in Chapter 1.

In the next section we discuss the case of each achiral GNW geometry in details, as well as the corresponding systematic TBU studies.

8.4 AA-GNWs

We observe that the AA systems only exist in a non-magnetic electronic configuration. The large band-gap (1.5 eV) observed in the AA-GNW of Fig. 8.1b is compatible with the properties of the individual armchair sectors $(9_A, 6_A)$ which present large band-gaps since P_A and O_A are multiple of 3 [31].

As discussed in Section 8.3, the TBU model provides a good description of GNW's electronic structure. This encourages us to conduct a systematic study in order to understand the relation between electronic structure and geometry for these GNWs. In such study, we performed TBU calculations for a variety of AA-GNWs so that O_A and P_A were varied from 4 to 25. The energy gaps around the Fermi energy (E_F) are plotted as a function of O_A and P_A in Fig 8.3. The systems can be classified according the multiple-of-three rules, as evidenced by grids evenly spaced in units of 3. The fact that the energy gap Δ_N for armchair edged nanoribbons with a number $N = (3i + j)$ of $C-C$ lines obey the relation $\Delta_{3i+1} > \Delta_{3i} > \Delta_{3i+2}$ [31], also explains why structures with P_A and O_A sectors that are multiple of 3 + 2 possess the smallest gaps (shown in dark blue patterns in Fig. 8.3).

8.5 AZ-GNWs

In contrast to the AA-GNW case, AZ-GNW structures have possible paramagnetic or ferromagnetic spin alignments along the zigzag edges, giving rise to a number of dissimilar spin configurations. The specific bands of the $(6_A, 7_Z)$ GNW in Fig 8.1c are shown in Fig. 8.2. The paramagnetic (PM) state has four spin-degenerated bands characterized by a very small dispersion (< 0.1 eV) around E_F. Those bands show a two-by-two folded structure relative to the X point in the Brillouin Zone (also present in the AA-GNW structure). This degeneracy is due to the presence of an improper translation symmetry ($\mathbf{a}/2$ translation + C_2 axis in the molecular plane - Fig. 8.4) in the atomistic structure (i.e. the spin distribution displays the full symmetry of the atomic structure, including the order 2 rotation). Deliberate choices of the initial guess for

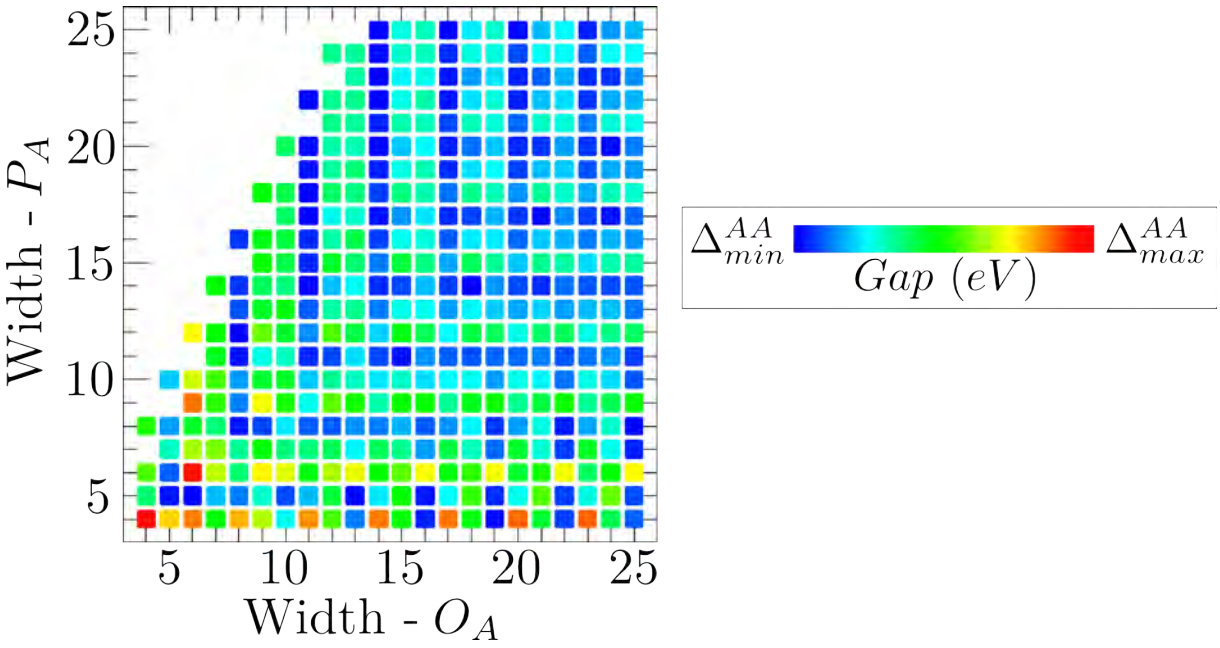

Figure 8.3: Energy band-gap as a function of P and O widths for the PM state in AA-GNWs. The minimum and maximun are $\Delta^{AA}_{min} = 1$ meV and $\Delta^{AA}_{max} = 1.7$ eV. The points absent on the upper-left corner of the graph correspond to geometries not allowed by the particular choice for the lengths of the P and O sectors.

Figure 8.4: Improper rotation symmetry for the GNW's unit cell.

the on-site occupations allow the self-consistent process to converge into four different magnetic states. These states are schematically plotted on top of Fig. 8.2 and their presence can be understood from the properties of individual Z-GNRs. The plot highlights the origin of each spin configurations compatible with periodic boundary conditions. They are labeled according to the edge-to-edge spin orientations: ferromagnetic (FM), anti-ferromagnetic (AFM), trans-anti-ferromagnetic (TAFM), and longitudinal-anti-ferromagnetic (LAFM). In each of those states, the spin polarization is maximal on the zigzag edges, where it has a local ferromagnetic ordering. The polarization decreases quickly from the center of the edges to the corner where the zigzag edge meets the armchair geometry. The FM state presents a splitting between spin up and down bands, which opens a $\Delta_{TBU} = 0.27$ eV ($\Delta_{DFT} = 0.30$ eV) energy gap. The spin polarized valence state corresponds to the polarization localized at the edges. This polarization is favored while electron-electron interaction pushes the (minority spin) conduction band to higher energy. The other three configurations have no net polarization and their electronic bands are all spin-degenerated. The AFM state has a $\Delta_{TBU} = 0.42$ eV ($\Delta_{DFT} = 0.46$ eV) band-gap, and

the bands closest to E_F present very little dispersion, because the spatial spin distribution is restricted to the portion of the nanowiggle with a zigzag edge (e.g. the zigzag portion behaves like a quantum dot, in a way similar to reported anti-dot graphene [59]). The TAFM and LAFM states present features similar to those mentioned for the AFM configuration. However, the symmetry of the spin distributions in these last two states is reduced since they break the helical symmetry and the degeneracy is lifted at the X point.

DFT total energy calculations can be used to assess the relative stability of the various phases. Note that in all the systems studied in this work, careful (DFT) geometry relaxation does not yield appreciable differences between the various magnetic states of a given GNW, thereby ruling out the possibility of spin-Peierls transition. The TBU band-structure energy provides another operational way to compare structure stability. It is easily computed as:

$$E_{\mathrm{TBU}} = \int_{-\infty}^{E_F} En(E)dE \tag{8.1}$$

where $n(E)$ is the density of states. As shown below, this approximate expression turns out to provide a good predictive framework, compared to the more accurate and computationally expensive DFT approach. We found the AFM state to be the most stable: compared to the AFM, DFT (TBU) relative energy is 0.29 eV (0.85 eV) for PM, 0.020 eV (0.027 eV) for TAFM, 0.025 eV (0.027 eV) for LAFM and 0.045eV (0.046 eV) for FM. These results give us confidence to use the TBU band-structure energy as a tool to understand how the relative energy difference among the multi magnetic states behaves as we change the AZ-GNWs geometry. We calculated a series of AZ-GNWs which spans sector widths P_A and O_Z from 5 to 17. In Fig. 8.5 we show the energy differences for any pair of magnetic states as a function of the sectors' widths. The $|\Delta E|_{max}$ value for each pair of states is listed in Table 8.1.

Table 8.1: $|\Delta E|_{max}$ values for the different pairs of magnetic states in AZ-GNWs.

$\lvert\Delta E\rvert_{max}$ (eV)	AFM	TAFM	LAFM	FM
PM	4.995	4.914	4.875	4.799
FM	0.830	0.504	0.478	–
LAFM	0.559	0.476	–	–
TAFM	0.479	–	–	–

In the lower right plot of Fig. 8.5 we see that the PM state is in general higher than the AFM case. This is remarkably for GNWs with larger parallel width, while narrower P_A sectors give a PM state closer in energy to AFM. This can be explained by the fact that for a given oblique width, a wider parallel width produces longer O_Z sectors and the energy necessary to have a non-polarized zigzag edge increases as these edges get larger. Conversely, as P_A gets narrower, the oblique sector becomes shorter and the parallel sector longer, so that the GNW

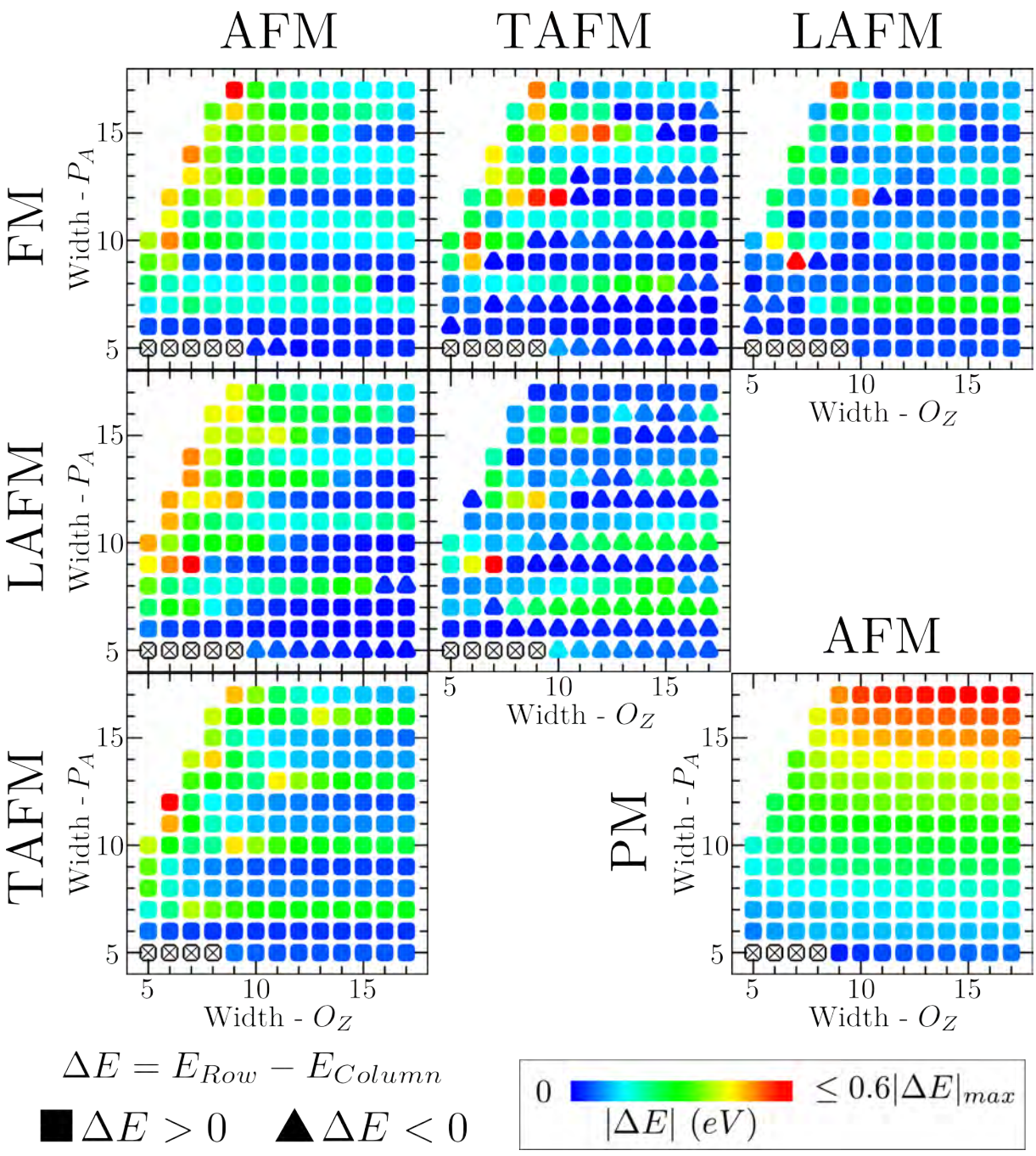

Figure 8.5: Band-Structure energy difference among the different magnetic states as a function of P_A and O_Z. The points absent on the upper-left corner of each graph correspond to geometries not allowed by the particular choice for the lengths of the P and O sectors. Systems that do not possess a stable AFM, TAFM, LAFM or FM distribution of spins are marked by a cross. The $|\Delta E|_{max}$ values for the different plots are shown in Table 8.1. Positive (negative) values for ΔE are represented by squares (triangles).

edge structure is predominantly armchair, favoring a paramagnetic distribution for the spin. The other plots involving the PM state (PM-FM, PM-LAFM and PM-TAFM) present the same features as the PM-AFM plot.

All the other magnetic states are closer in energy to each other. As a general trend, we observe that the states obey the following order for increasing energy: AFM $<$ TAFM $<$ LAFM $<$ FM $<$ PM. We do observe some exceptions like the $(9_A, 7_Z)$ GNW for the LAFM-FM pair and some set of horizontal lines (corresponding to $mod(P_A, 3) = 1$) in the LAFM-TAFM plot. We do observe other set of points in discordance with the energy order above, but we also note that the absolute value of the energy difference is very low (dark blue triangles) and is likely to be within the method's error.

In addition, we note that the energy differences between TAFM and AFM and between FM and LAFM are notably higher for the $mod(P_A, 3) = 1$ family. We can understand this behavior in terms of the spin distributions along the zigzag edges (from the oblique sector) and the properties of the parallel sector. As the occupied (unoccupied) energy bands are pushed down (up) for a semiconducting system, a larger gap is a factor which, in principle, lowers the value of E_{TBU}. Note that in the AFM state, the edges with similar majority spin (edges 1 and 4 or 2 and 3 in the left of Fig. 8.6) are likely to be farther away from each other than in the TAFM distribution (edges 1 and 3 or 2 and 4 in the left of Fig. 8.6), as seen in the right of Fig. 8.6. In the TAFM state, this contributes to form more extended states (favoring the lowering of the gap). This effect is similar but opposite in the AFM case, thus contributing to a bandgap increase, and in turn to a band-structure energy reduction. So, as A-GNRs with a number N of $C-C$ lines along its width will have the largest gaps for $mod(N, 3) = 1$, parallel sectors with $mod(P_A, 3) = 1$ are likely to correspond more stable structures. Our results show that this trend is more pronounced for the AFM state than for the TAFM distribution, leading to a larger TAFM-AFM energy difference. A similar argument can be applied for the FM-LAFM difference.

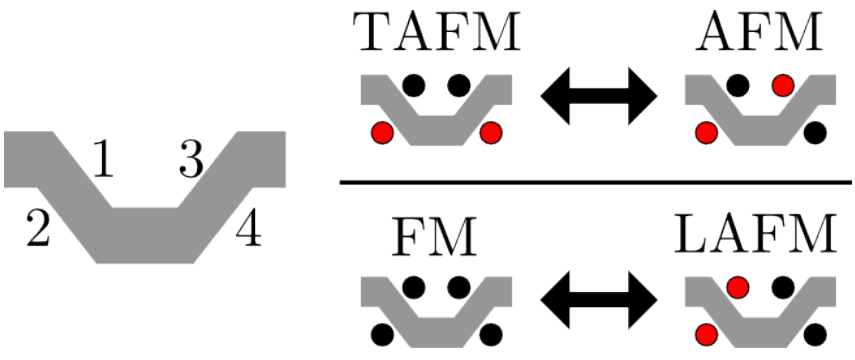

Figure 8.6: Pair of magnetic states which give the largest energy separation for $mod(P_A, 3) = 1$.

We observe a similar raising in the LAFM-AFM and FM-TAFM differences for systems with $mod(P_A,3) = 2$. Let us consider edge 1 in the left of Fig. 8.7, for instance. It is close to the edges 2 and 3, so let us call 1 and 2 or 1 and 3 as "neighbors". While a zigzag edge with a given spin polarization has one "neighbor" zigzag edge with the same polarization in LAFM, the corresponding edge on the AFM state has no "neighbors" with the same majority spin. So LAFM has a more pronounced tendency to present a small gap than AFM. At the same time, A-GNRs with a number N of $C-C$ lines along its width will have the smallest gaps for $mod(N,3) = 2$. So, parallel sectors with $mod(P_A,3) = 2$ are likely to produce less stable structures. Our results show that this last tendency is more pronounced for the LAFM state than for the AFM case, rendering a larger LAFM-AFM energy difference. A similar discussion can applied for the FM-TAFM difference in energy.

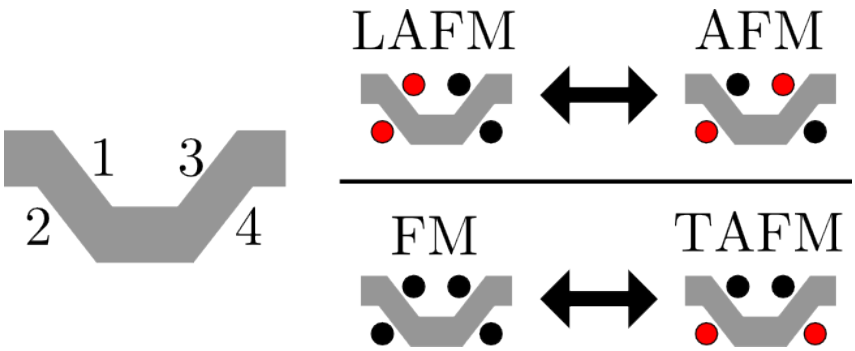

Figure 8.7: Pair of magnetic states which give the largest energy splitting for $mod(P_A,3) = 2$.

Finally, we applied the systematic band-gap study for each of the five different spin distributions. The electronic band-gap as a function of P_A and O_Z for each state is plotted in Fig. 8.8. The minimum (Δ^{AZ}_{min}) and maximum (Δ^{AZ}_{max}) values for the gaps in each spin-configuration are shown in Table 8.2.

Table 8.2: Minimum (Δ^{AZ}_{min}) and maximum (Δ^{AZ}_{max}) values for the gaps in each spin-configuration for AZ-GNWs.

	AFM	TAFM	LAFM	FM	PM
Δ^{AZ}_{min} (meV)	183	22	7	0	0
Δ^{AZ}_{max} (meV)	446	396	428	347	393

We observe that except for the systems with narrow parallel sectors, the PM state is always metallic. As explained in the discussion on energetics, for a fixed O_Z, the wider the P_A is, the longer our oblique sector becomes. So, for larger P_A, the AZ-GNWs properties are dominated by the O_Z sector (which are metallic in their PM state), except by the 120° turn made by the Z-GNR sector as it finds the short A-GNR sector. However, the plot tells us that the small parallel sector influence is not sufficient to render the structure a semiconducting character in this PM state.

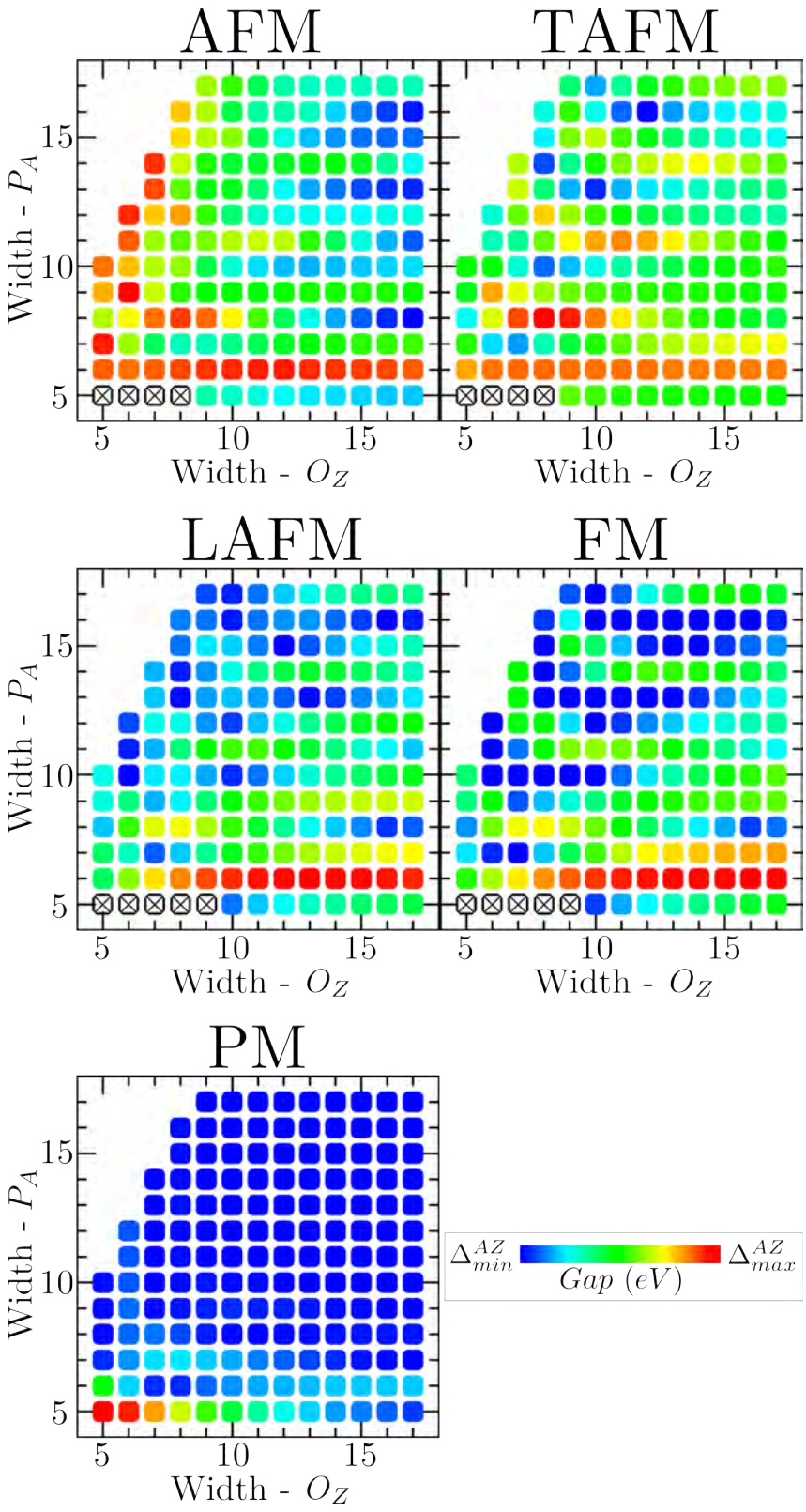

Figure 8.8: Energy band-gap as a function of *P* and *O* widths for the multi-magnetic states in AZ-GNWs. The points absent on the upper-left corner of each graph correspond to geometries not allowed by the particular choice for the lengths of the P and O sectors. Systems that do not possess a stable AFM, TAFM, LAFM or FM distribution of spins are marked by a cross. The minimum and maximum values for the gap in each plot are shown in Table 8.2.

Moving to the other magnetic states, we observe three distinct behaviors corresponding to sector widths P_A with mod$(P_A,3)$ =0, 1, or 2. Scanning horizontally across the chart, the electronic band-gap oscillates for small O_Z values and gradually converges to a P_A-dependent constant that we associate with a pristine A-GNR corresponding to the wedge-healed GNW. These characteristics related to the non-PM states show that the P_A sector has a pronounced influence on the AZ-GNWs' electronic properties, even for short parallel pieces. If we look at the specific case of the FM state we notice that the P_A sector influences sufficiently the electronic structure to open a gap even for longer oblique sectors (corresponding to wider parallel sectors), which are composed by Z-GNRs in their FM metallic state (see the LAFM and FM AZ-GNW states). For the LAFM state we have an additional factor to consider, namely that successive FM O_Z sectors have alternating spin orientations. This separates the atoms with identical majority spin orientation to portions far from each other, contributing to form localized states (like the example in Fig. 8.1c whose bands are shown in Fig. 8.2) that also affect the opening of a band gap. These aspects show that the interplay between A- and Z-GNRs in GNWs is not only restricted to the simple sum of their individual properties, but it is in fact extremely dependent on the specific way how these pieces are assembled into the GNW.

8.6 ZA-GNWs

Similar to the AZ-GNW shown on Fig. 8.1c, the PM state of the $(4_Z,9_A)$ ZA-GNW system displayed on Fig. 8.1d presents four spin-degenerated bands around E_F. As noted before, these four states can be unfolded in pairs according to the structure's improper translation symmetry. The possible spin configurations include a series of magnetic states with local ferromagnetic alignments along the zigzag edges similar to the AZ-GNWs. These configurations are either ferromagnetic (FM) or anti-ferromagnetic (AFM) depending on the relative arrangement of the spin on opposite edges.

The FM state has a total magnetic moment $M_{TBU} = 1.8\mu_B$ ($M_{DFT} = 1.9\mu_B$) and is characterized by electronic bands with opposite spins crossing at E_F. In contrast to the PM and FM configurations, the AFM spin distribution breaks the improper translational symmetry of the lattice, and the corresponding bands do not simply fold at the X point. However, the symmetry of the spin distribution guarantees a zero total magnetization and, in turn, a spin-degenerate set of bands. The diffraction at the Bragg plane at X yields a fairly large $\Delta_{TBU} = 0.23$ eV ($\Delta_{DFT} = 0.26$ eV) band-gap. In each configuration, the bands around E_F are significantly more dispersed compared to the AZ-GNW systems, indicating a true 1D behavior and a significant attenuation of the quantum-dot effect observed in the AZ-GNW considered above. Total energy

calculations using DFT (TBU) show that the AFM state is more stable than both the PM and FM configurations, by 0.13 eV (0.44 eV) and 0.057 eV (0.13 eV), respectively.

Next, we conducted a systematic study using the TBU method by varying the GNW sector widths P_Z and O_A from 2 to 10 and 6 to 17, respectively. In general we observe the order AFM<FM<PM regarding energy stability. The values for $|\Delta E|_{max}$ are listed in Table 8.3. The PM state energy is remarkably higher than the other two states for a intermediate parallel width between the minimum and maximum value of P_Z, specially for wider oblique sectors. This is the result of two different factors. First, for narrow parallel sectors, the zigzag edges at opposite sides of the GNW are close to each other, which lowers the magnetic instability of the paramagnetic state [31]. On the other hand, wide P_Z sectors present shorter zigzag edges for a given O_A, lowering the instability associated with the PM state. These two opposite tendencies balance for some value of P_Z where the PM instability reaches its maximum value for a given oblique width (with $O_A \approx 3$ or 4). When comparing FM and AFM, we see that narrower P_Z blocks produce a higher AFM-FM splitting similar to Z-GNRs [31] since the zigzag edges from opposite GNW's sides are close to each other.

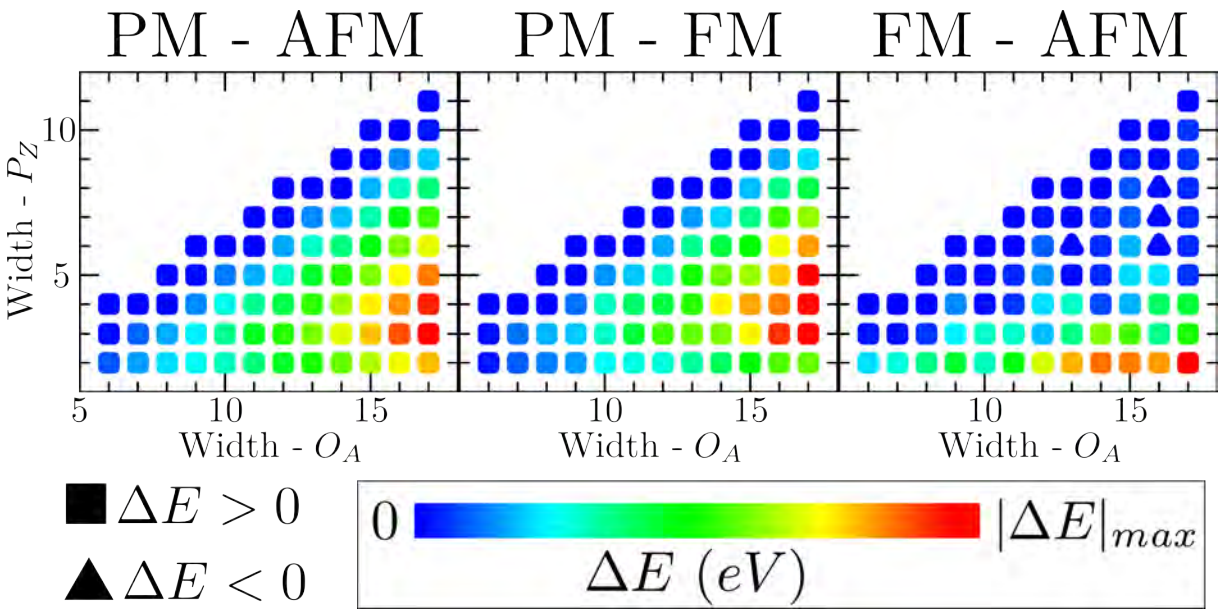

Figure 8.9: Band-Structure energy difference among the different magnetic states as a function of P_A and O_Z. The points absent on the upper-left corner of each graph correspond to geometries not allowed by the particular choice for the lengths of the P and O sectors. The $|\Delta E|_{max}$ values for the different plots are shown in Table 8.3. Positive (negative) values for ΔE are represented by squares (triangles).

Table 8.3: $|\Delta E|_{max}$ values for the different pairs of magnetic states in ZA-GNWs.

$\|\Delta E\|_{max}$ (eV)	AFM	FM
PM	3.357	2.860
FM	0.993	–

When analyzing the systematic study results of the energy gap of the AFM and FM states, we note that the general features of the 2D plot show a clear distinction between 3 families as we move along the plot's vertical direction (i.e. as P_Z changes). These three families correspond to different values of O_A such that mod$(O_A, 3)$ =0, 1, and 2, for reasons similar to those explained for the AZ systems. Also we note that the AFM state is always a semiconductor, while the FM state sometimes presents a metallic structure. While most ZA-GNWs are metallic in their PM state, nanostructures with large P_Z present a wide band-gap. This is due to the fact that the zigzag sectors are short for wide parallel blocks so that the electronic properties are dominated by the semiconducting (armchair oblique) sectors.

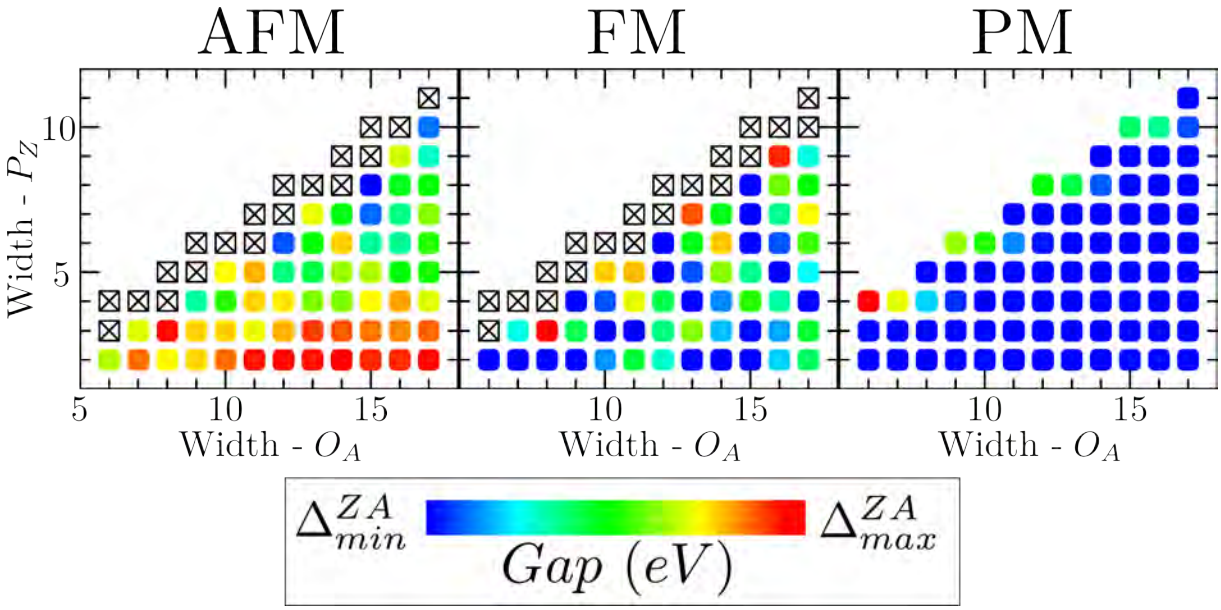

Figure 8.10: Energy band-gap as a function of P and O widths for the multi-magnetic states in ZA-GNWs. The points absent on the upper-left corner of each graph correspond to geometries not allowed by the particular choice for the lengths of the P and O sectors. Systems that do not possess a stable AFM or FM distribution of spins are marked by a cross. The minimum and maximum values for the gap in each plot are 107 meV and 477 meV for the AFM state, 0 and 360 meV for FM and 0 and 1527 for PM.

8.7 ZZ-GNWs

ZZ-GNWs constitute the fourth possibility of assembling achiral GNRs into GNWs (Fig. 8.1e). For the $(7_Z, 7_Z)$ system depicted in Fig. 8.1e, the PM state is a zero-gap system where the frontier bands meet at the X-point of the Brillouin zone (Fig. 8.2). This behavior contrasts with that of straight Z-GNRs where the frontier bands meet some distance before the X point [30, 31]. Interestingly, neither DFT nor TBU predict a stable FM state for this particular $(7_Z, 7_Z)$ system. A detailed analysis of the A and B graphene sub-lattices explains the absence of a FM state. The coexistence of spin up along the entire length of the ZZ-GNW edge would indeed require

the local spin on sites belonging to both A and B sub-lattices on connected P_Z and O_Z sectors to be aligned. This configuration is not stable for reasonable values of spin-spin interactions. We verified that assumption by employing the self-consistent TBU model with an excessively large value of U and found the FM state to be artificially stabilized. The A-B bipartitioning of the lattice does not preclude the presence of other ferromagnetic-like spin configurations (see top of Fig. 8.2) for this $(7_Z, 7_Z)$ structure. For example, in the AFM state, the edge atoms belonging to a given graphene sub-lattice present the same type of majority spin. This spin distribution breaks the helical symmetry of the atomic lattice and a $\Delta_{TBU} = 0.26$ eV ($\Delta_{DFT} = 0.25$ eV) gap opens at the X point. In addition to the AFM spin distribution, the ZZ-GNWs also allow for a more intriguing longitudinal-ferrimagnetic (LFiM) state as shown on Fig. 8.2. Because of the quasi-AFM spin distribution (due to the A-B bipartitioning of the lattice), the total magnetization of LFiM is quite small ($M_{TBU} = 0.07\mu_B$, $M_{DFT} = 0.01\mu_B$). However, symmetry arguments do not ensure the total polarization to completely vanish (hence the ferrimagnetic character of the configuration). In addition, except for a small spin-up – spin-down splitting, the LFiM bands are very similar to those of the PM configuration. DFT (TBU) predicts the AFM state to be more stable than the PM or LFiM states, by 0.055 eV (0.446 eV) and 0.056 eV (0.397 eV), respectively.

In the following we carried out the systematic study for P_Z and O_Z covering the range of values from 4 to 17. While we were not able to find any other spin configuration for the particular $(7_Z, 7_Z)$ system than PM, AFM and LFiM, a set of other magnetic states were also adopted by other systems. We found that ZZ-GNWs can present the PM state and up to four other spin configurations: AFM, LFiM, FM and TAFM. These distributions are illustrated in Fig. 8.11.

Figure 8.11: Different spin distributions for ZZ-GNWs.

In Fig. 8.12 we plot the electronic band gap for all these magnetic states as a function of P_Z and O_Z. Note that, as in the case of the $(7_Z, 7_Z)$ system, some structures do not present all these states, specially the narrowest structures in the bottom-left part of each plot (where some values are absent). Here we choose to not consider the magnetic states where the maximum polarization of a orbital in the structure is less than $0.01\mu_B$. In these plots we used the same values for the Δ^{ZZ}_{min} and Δ^{ZZ}_{max} pair for all the magnetic states, namely $\Delta^{ZZ}_{min} = 0$ and $\Delta^{ZZ}_{max} = 0.45$

eV. In order to analyze the data, we found convenient to define four different regions on the P_Z–O_Z–gap plot as shown in Fig. 8.12: (I) bottom-left, (II) upper-left, (III) bottom and (IV) diagonal regions. The narrowest structures are in (I), where we have most of the structures with missing magnetic states since narrow structures have a reduced paramagnetic instability [31]. Region (II) is characterized by structures whose outer parallel edge is short enough so that this edge does not present significant spin polarization. In this case we observe that the AFM and TAFM states look alike, while we note the same for the FM and LFiM states. A similar picture occurs in region (III) as the structures over this region present short oblique edges where the spin polarization does not assume significant values. One observes that the plots over regions (II) and (III) are practically the same for the AFM-TAFM and FM-LFiM pairs. The main differences reside in region (IV) where the wide structures present a high value for the paramagnetic instability, allowing spin polarization along all the edges on the ZZ-GNW.

For all magnetic states, we observe that the combined variations along the horizontal and vertical directions explain why the gap tends to get smaller along the chart's diagonal (to eventually vanish as the 2D graphene character is recovered).

In Fig. 8.13, we plot the TBU band energy difference for different pairs of states (the values for $|\Delta E|_{max}$ in each case are shown in Table 8.4). The PM-AFM energy difference is plotted in the lower right plot of Fig. 8.13. We observe that the energy separation for these two states is always positive (in other words, AFM is always lower) and increases as we move away from region (I) in the plot. This is a clear manifestation of the increasing (lowering) of the paramagnetic instability as the system gets wider (narrower). We observe the same features for the PM-X (X=AFM, FM, LFiM, TAFM) energy difference. Moving to the other cases, regions (II) and (III) in the plots for the TAFM-AFM and FM-LFiM differences are predominantly dark blue (corresponding to zero energy difference), as expected from the early discussion in the section. Finally, if we focus on region (IV), we note an overall PM>FM>TAFM>LFiM>AFM energetic order for the magnetic states (except for some points in the FM-TAFM plot).

Table 8.4: $|\Delta E|_{max}$ values for the different pairs of magnetic states in ZZ-GNWs.

$\|\Delta E\|_{max}$ (eV)	AFM	LFiM	TAFM	FM
PM	6.014	5.872	5.373	5.364
FM	0.851	0.658	0.623	–
TAFM	0.872	0.638	–	–
LFiM	0.474	–	–	–

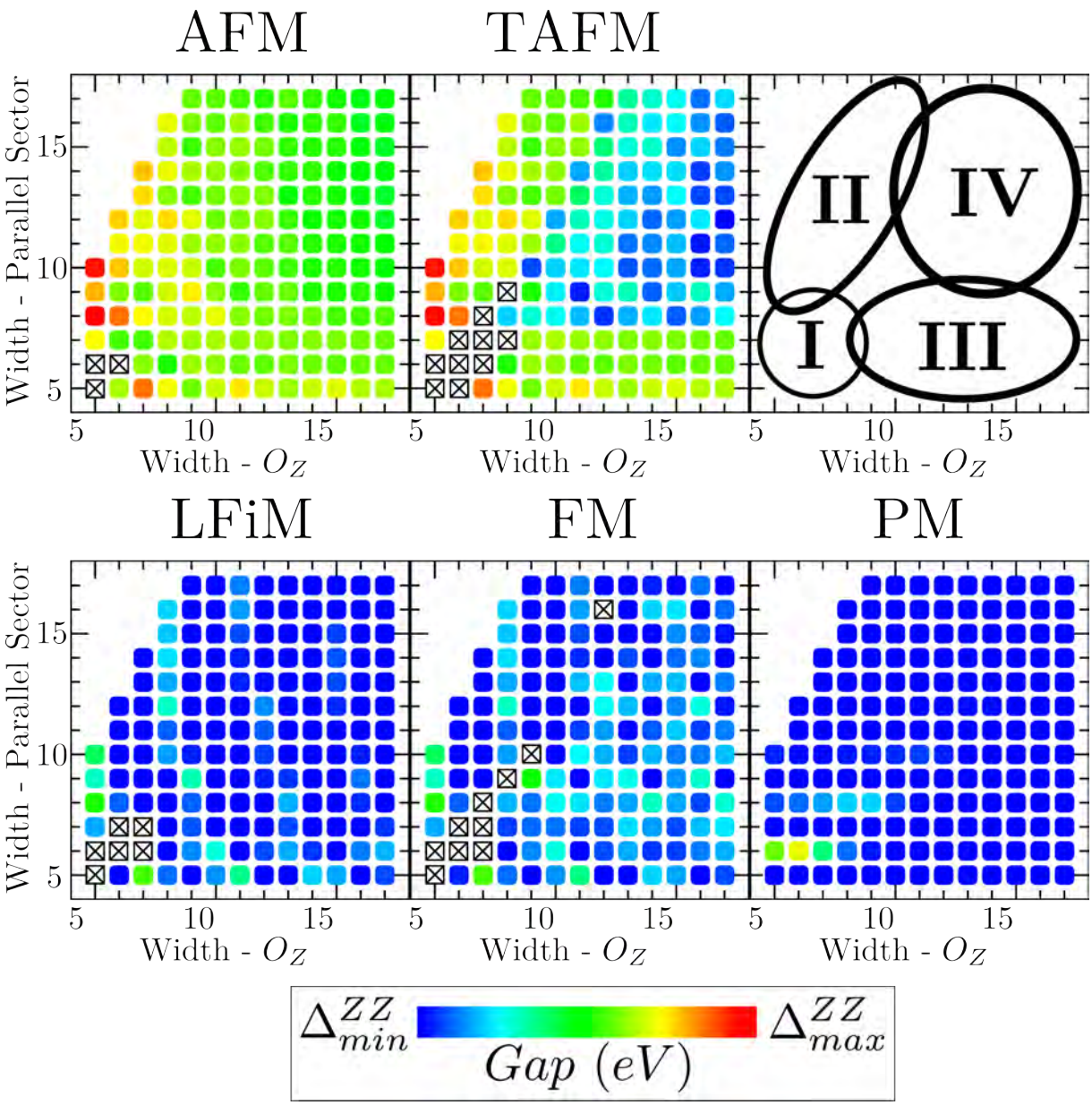

Figure 8.12: Energy band-gap as a function of P and O widths for the multi-magnetic states in ZZ-GNWs. The points absent on the upper-left corner of each graph correspond to geometries not allowed by the particular choice for the lengths of the P and O sectors. Systems that do not possess a stable AFM, LFiM, TAFM or FM distribution of spins are marked by a cross. The minimum and maximum gap values are $\Delta^{ZZ}_{min} = 0$ and $\Delta^{ZZ}_{max} = 0.45$ eV, respectively.

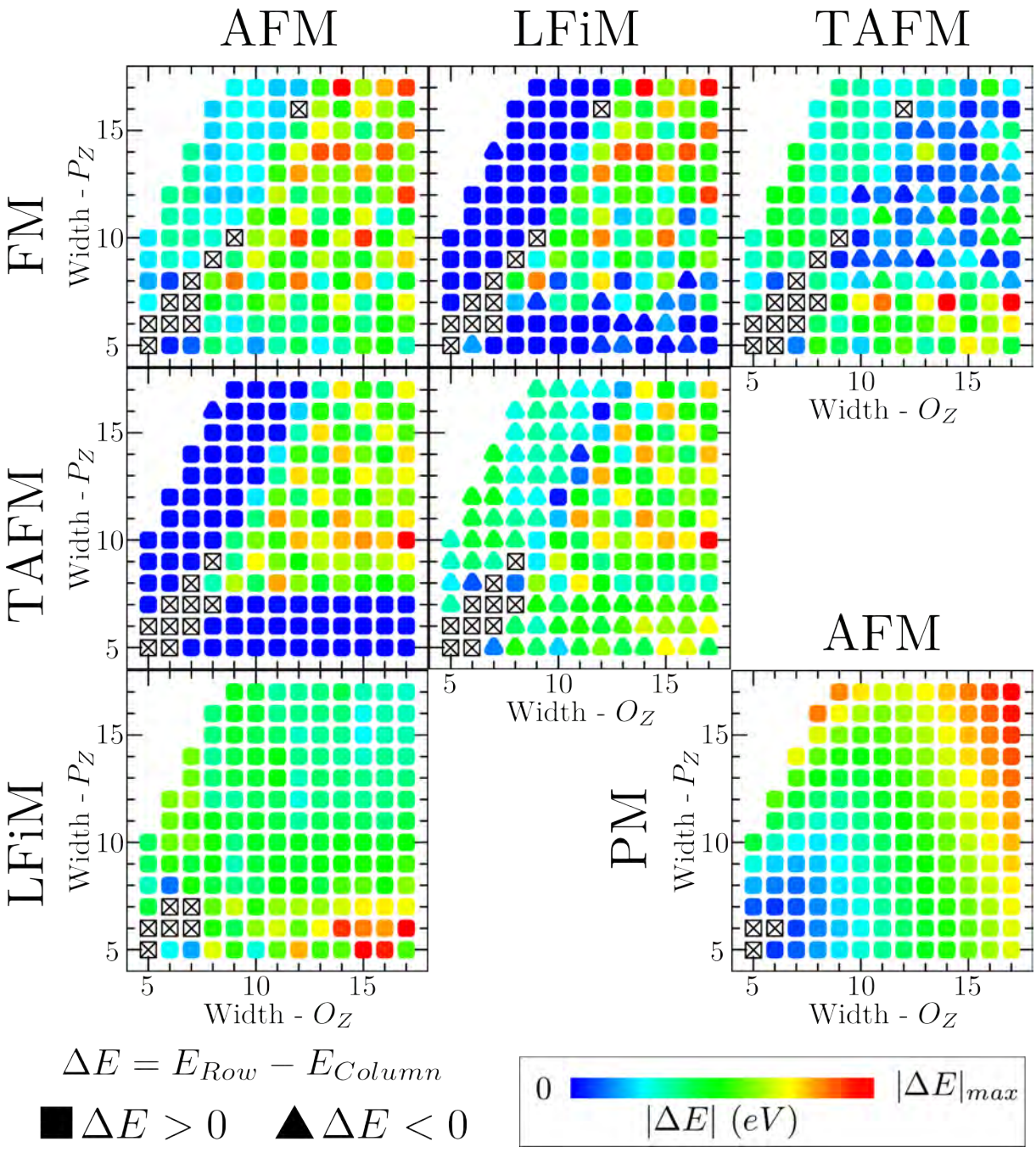

Figure 8.13: Band-Structure energy difference among the different magnetic states as a function of P_Z and O_Z. The points absent on the upper-left corner of each graph correspond to geometries not allowed by the particular choice for the lengths of the P and O sectors. Systems that do not possess a stable AFM, LFiM, TAFM or FM distribution of spins are marked by a cross. The $|\Delta E|_{max}$ values for the different plots are shown in Table 8.4. Positive (negative) values for ΔE are represented by squares (triangles).

8.8 Overview

In this chapter we presented and discussed the rich set of electronic properties of GNWs. These systems show a variety of magnetic states which is even richer than the properties of their GNR building blocks (while A-GNRs have only a PM state and Z-GNRs have also other 2 - AFM and FM - magnetic states, GNWs can present up to four distinct spin distributions different from the PM case on a single unit cell). In general, GNWs present an AFM ground state (whose spin distribution obeys the bipartition of graphene's lattice) which is always semiconducting. The dependence of the energy gap around E_F is in general dictated by the armchair or zigzag character of the sectors composing the GNW. However, we observe a non trivial interplay between the different wiggle sectors so that GNWs properties can not be viewed simply as the superposition of the properties of their component GNR sectors. In addition, according to the TBU results, the multiple magnetic states present a well defined order in energy. We Note that the PM state is much higher in energy than the other states for wide systems. As we move to narrow GNWs, the PM state gets closer in energy to the other states, while some states cease to be stable. This results constitute a useful huide to the synthesis of graphitic nanostructures with desired electronic properties.

9 *Graphene carbon nanowiggles - electronic transport properties*

In this chapter we examine the electronic transport properties of GNWs in two particular configurations. In the first case we consider a periodic GNW structure (the GNW unit cell is used as CSR and as terminals - see Chapter 3 for the concept of CSR). In the second case, we calculate the transport through a single GNW cell attached to two GNR terminals. An intermediate structure where we include a varying number of GNW unit cells between the GNR electrodes is also considered. This enables us to study how the GNW-between-GNRs system evolves to recover characteristics of the periodic system as we increase the number of unit cells between the GNR terminals. In addition, we verify that the multiple magnetic states present different conductance versus energy curves, opening a promising path for potential spintronics applications of GNWs as nanodevices.

9.1 Methods

The results obtained in this chapter for the quantum conductance of GNWs were obtained using the TRANSFOR package we developed during this thesis. The methods implemented in TRANSFOR were presented in the Chapters 3 and 4. In order to obtain the Hamiltonian to be read by TRANSFOR, a previous run is made on TBFOR. In the case of the GNW-between-GNRs systems, we include a large number of electrode cells in the run so as to have a good approximation for the BLS condition (see Chapter 3 for the concept of bulk-lead similarity - BLS). Namely, we used either 20 A-GNR (AZ-GNW case) or 35 Z-GNR (ZA- or ZZ-GNWs) unit cells for each terminal. The TBFOR output for the $\langle \hat{n}_{i\sigma} \rangle$ densities is then used to construct the Hamiltonian in the localized orbitals representation to be used by TRANSFOR.

9.2 AZ-GNWs

We start by considering the AZ-GNW case, focusing on the $(11_A, 6_Z)$ GNW. First we consider the periodic GNW case. As shown in the last chapter, AZ-GNWs present up to four possible magnetic states (AFM, FM, LAFM and TAFM) which are different from the trivial non-magnetic case (PM). We illustrate the five different spin distributions in Fig. 9.1. In Fig. 9.2 we plot the quantum conductance as a function of the energy around the Fermi energy ($E_F = 0$).

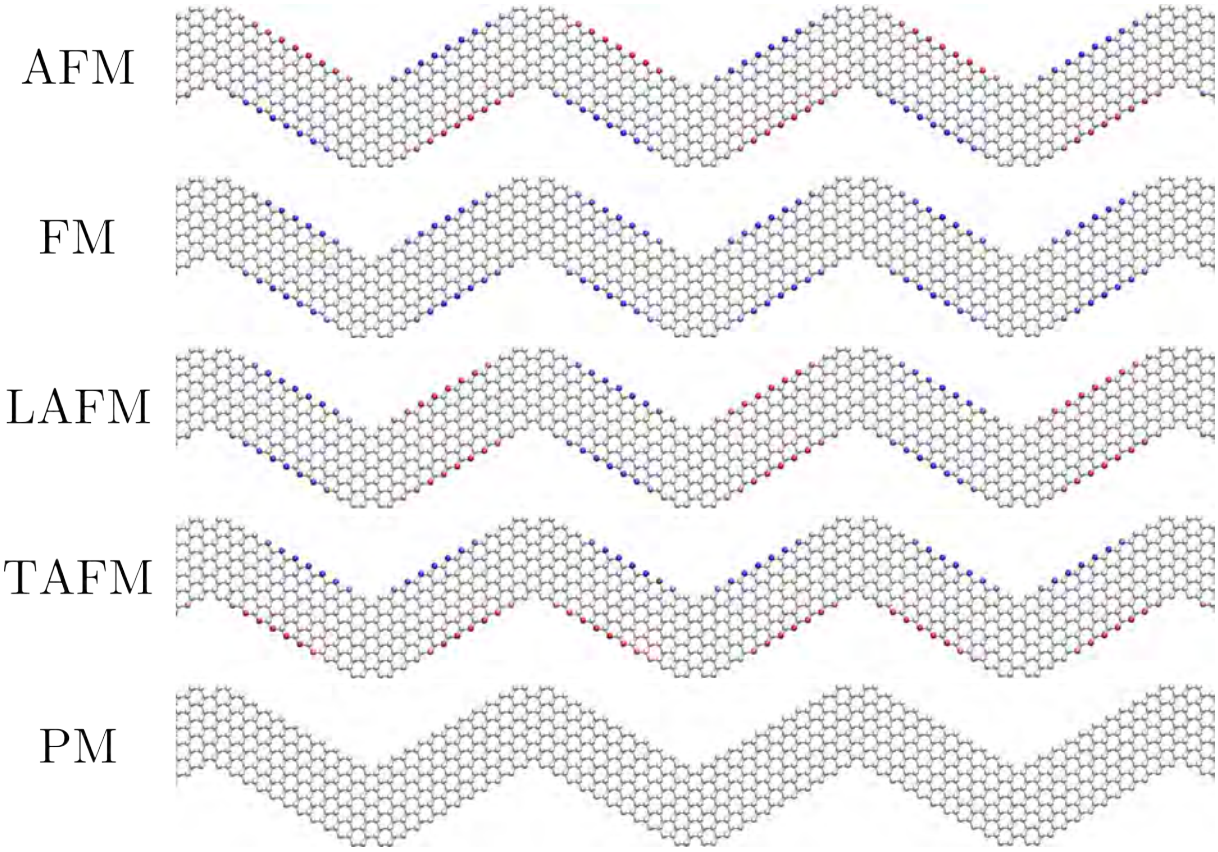

Figure 9.1: Five possible spin distributions for the periodic $(11_A, 6_Z)$ AZ-GNW. In the plots, blue (red) represents the maximum polarization for spin up (down), while white denotes no spin-polarization.

By observing the conductance curves for spin-up and -down states we note that, following the electronic structure (as discussed in the last chapter), the FM state is the only one to present different behaviors for the two spin orientations because it has a net magnetization. In all other cases we have identical curves for both spins. In addition, the electronic transport is ballistic through these GNWs (in fact, this is a trivial case where the step-like conductance curves could be simply obtained by counting the bands for each energy value). We also have remarkable differences for the conductance profile between different magnetic states. While FM is the only state with non-zero conductance at the Fermi level, the LAFM case presents a tiny gap (≈ 20 meV) around $E = 0$ eV and PM has two peaks of conductance about ± 20 meV close to E_F.

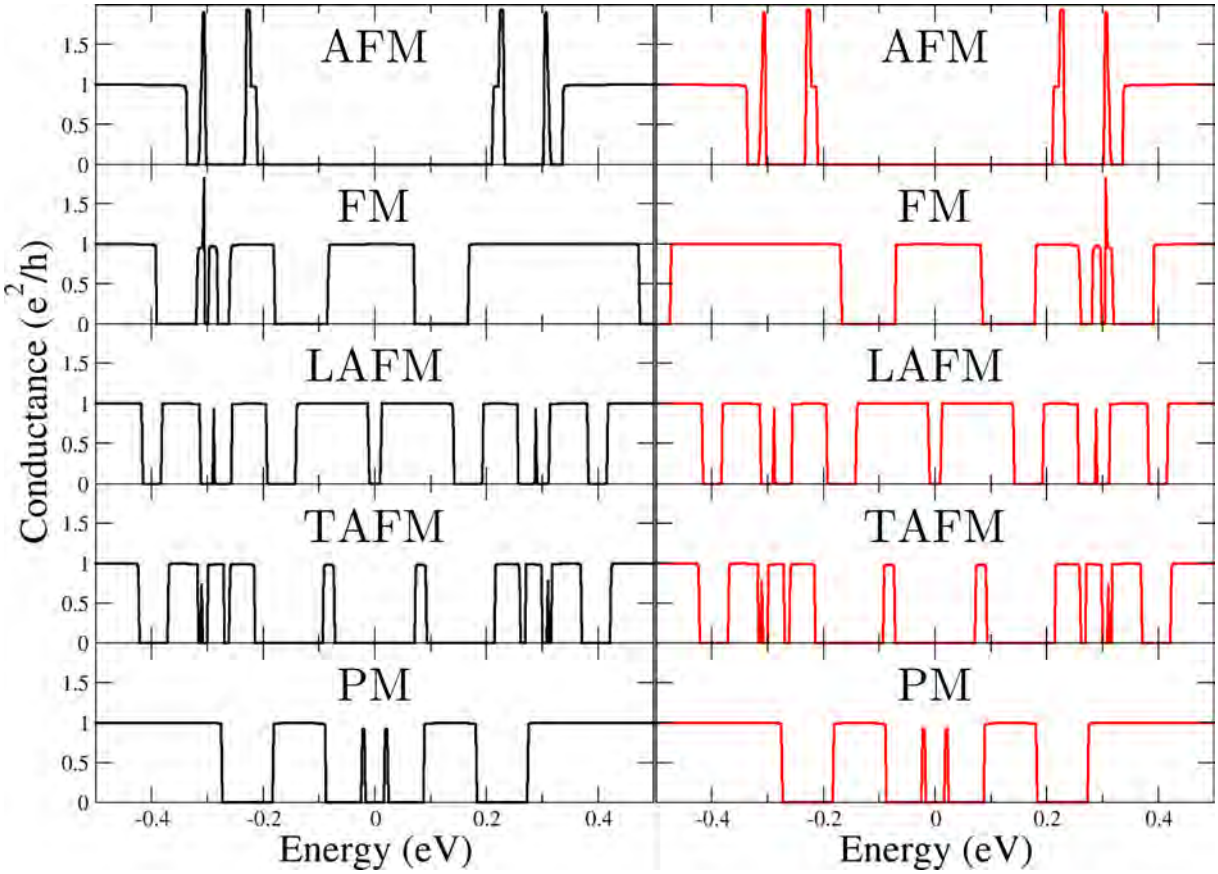

Figure 9.2: Quantum conductance as a function of energy for the five possible spin distributions for the periodic $(11_A, 6_Z)$ AZ-GNW structure. Spin-up curves are in black (left) while spin-down curves are in red (right). Here the Fermi energy is set to $E_F = 0$.

The AFM state possess the widest conductance gap, followed by the TAFM case.

Selectivity rules in energy can be applied to control the electronic flux in a GNW-based nanodevice in a similar fashion as in multi-terminal tori (whose rules were discussed in Chapter 6). If we look at energies around 0.4 eV, for example, the impinging electron is transmitted when the GNW is in its AFM, FM (spin up channel) or PM state, while it is blocked for the LAFM and TAFM states. A set of different rules can be obtained by tuning the energy of the incoming electron. In the case of the FM state this selectivity can additionally involve the electronic spin. This is an important result which makes GNWs eligible for prototype devices owing to these interesting physical properties. With experimental control over their multi magnetic states, GNWs could be embedded in nanocircuits, to act as nano-switch devices for instance, which operate in different regimes depending on their magnetic state.

We can further exploit the AZ-GNWs properties by investigating their behavior when attached to A-GNR electrodes. We start by using a single AZ-GNW unit cell as central scatterer. This structure and its corresponding magnetic states are depicted in Fig. 9.3. In this case, the GNW cell breaks the translational symmetry of the infinite 11-A-GNR corresponding to the

terminals. This promotes significant scattering so that the conductance curves no longer have a step-like profile, as shown in Fig. 9.4.

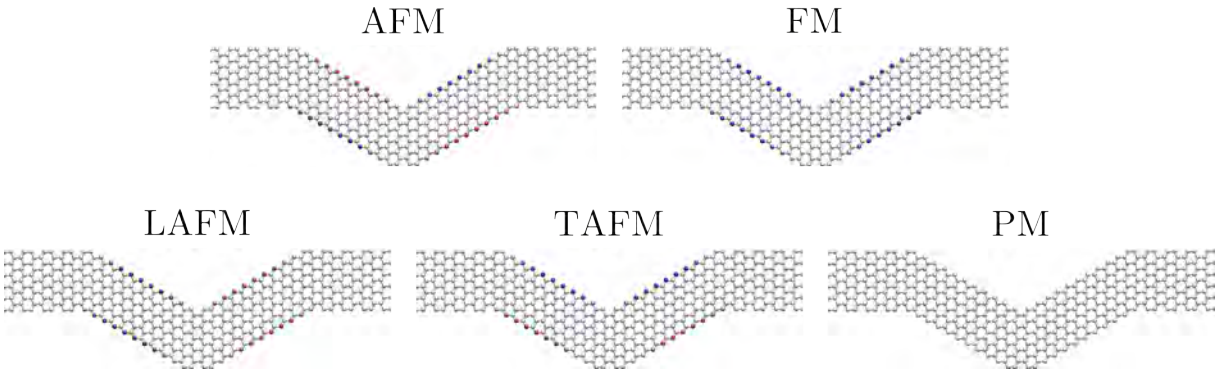

Figure 9.3: Five possible spin distributions for a single $(11_A, 6_Z)$ AZ-GNW cell attached to two semi-infinite 11-A-GNR electrodes. In the plots, blue (red) represents the maximum polarization for spin up (down), while white denotes no spin-polarization.

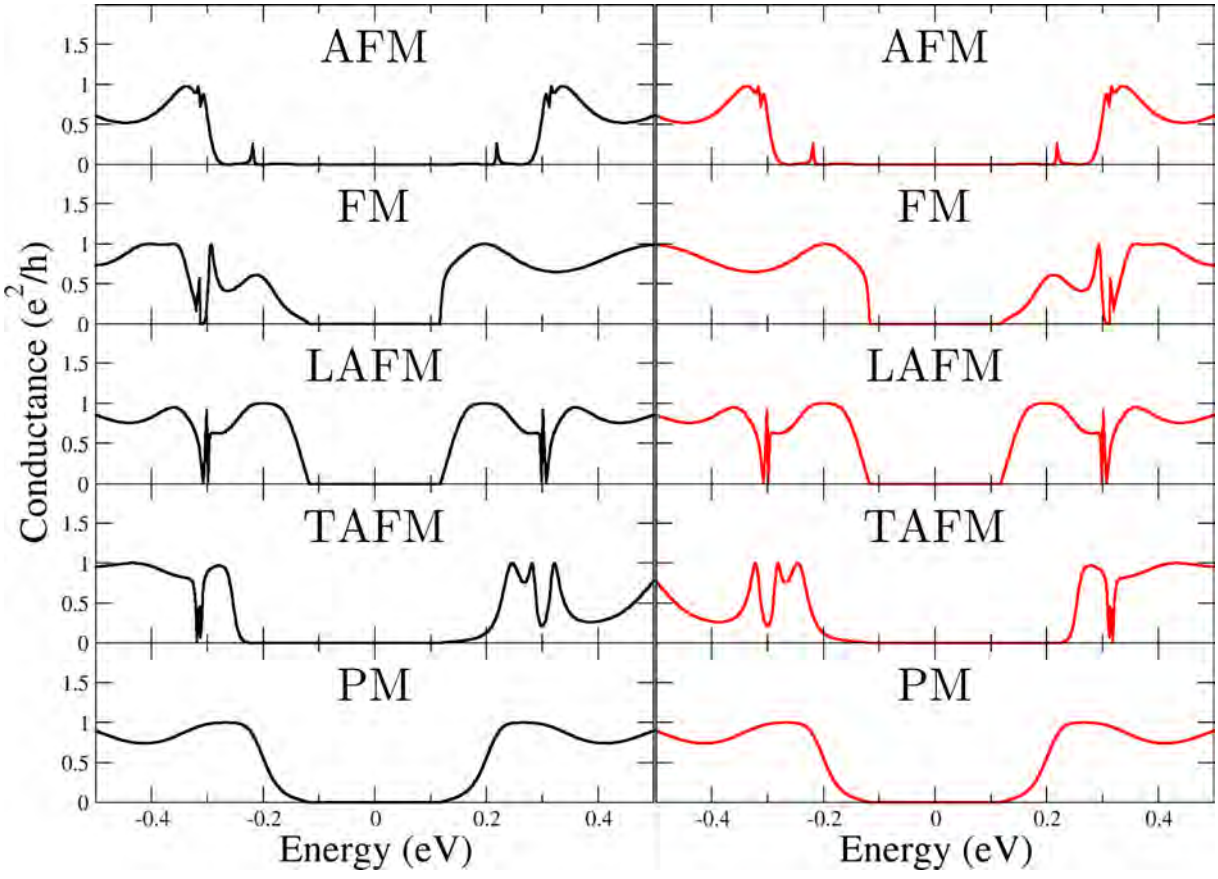

Figure 9.4: Quantum conductance as a function of energy for the five possible spin distributions for a single $(11_A, 6_Z)$ AZ-GNW unit cell attached to two semi-infinite 11-A-GNR terminals. Spin-up curves are in black (left) while spin-down curves are in red (right). Here the Fermi energy is set to $E_F = 0$.

By symmetry, the structure has a zero total magnetization for the AFM, LAFM and PM cases, while FM clearly has a non-zero value for the same quantity, as in the periodic case. This produces spin degenerated conductance for AFM, LAFM and PM, while FM presents different

curves for the two spin orientations. However, in contrast to the periodic system (which has zero total magnetization), the one-cell system in the TAFM state does not have a symmetric distribution for majority spin-up and -down spin. In fact, this structure has a non-zero total magnetization as evidenced by the different spin-up and -down conductance curves. In addition to the spin-dependent electronic transport for the FM and TAFM states, the conductance gap can also be tuned by selecting the magnetic state, as observed in Fig. 9.4.

A clear distinction between the periodic and the one-cell systems is that in the second case one has to switch the magnetic state only for a finite extend from the structure (since the terminals are armchair and non-magnetic). This is different from the periodic case where the state switching has to be conducted through the whole periodic structure or, in practical terms, at least through a much broader spatial extension. This is an essential practical aspect to be considered by experimentalists regarding the manipulation of these magnetic states at the experimental level.

Note that, unlike the periodic case, the one cell always has a gap (greater than 0.2 eV). This is compatible with the electrode properties since a perfect periodic 11-A-GNR has a conductance gap of ≈ 236 meV, as shown in Fig. 9.5. As this band gap is a natural characteristic from A-GNRs, the conductance for the energies close to the Fermi level is always blocked in the one-cell system composed of a AZ-GNW (unless the particular AZ-GNW has a wide parallel sector so as to render a tiny gap for the terminals).

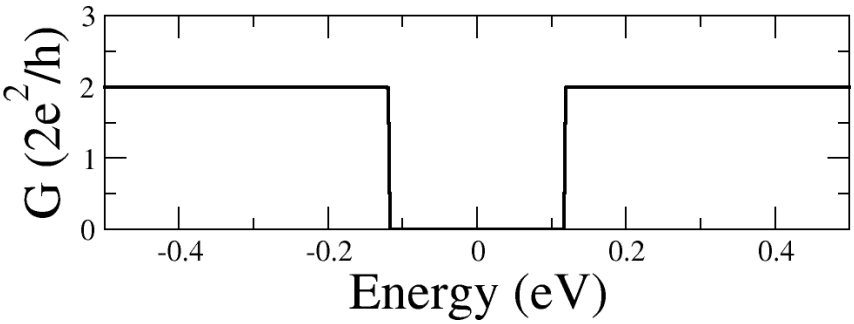

Figure 9.5: Quantum conductance as a function of energy for a periodic 11-A-GNR in its paramagnetic state. Here the Fermi energy is set to $E_F = 0$. The method used to construct this curve is the same used in the calculation of GNWs transport properties.

9.3 ZA-GNWs

We follow a similar procedure to study the transport properties of ZA-GNWs. Here we choose a $(5_Z, 13_A)$ ZA-GNW as a representative example from this group. This system in its periodic configuration presents a reduced set of magnetic states in comparison to a AZ-GNW.

The spin polarization for the PM, AFM and FM ZA-GNW states are depicted in Fig. 9.6.

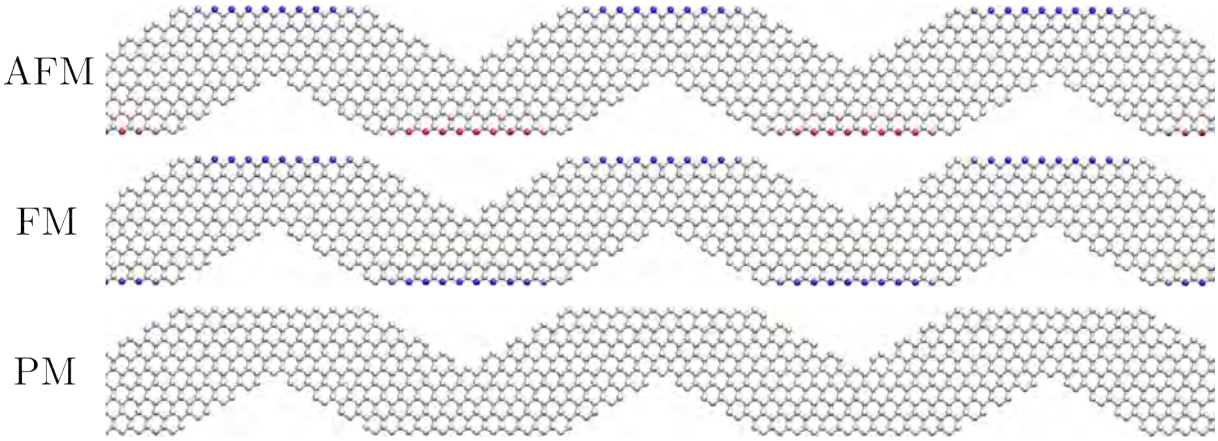

Figure 9.6: Three possible spin distributions for the periodic $(5_Z, 13_A)$ ZA-GNW. In the plots, blue (red) represents the maximum polarization for spin up (down), while white denotes no spin-polarization.

In Fig. 9.7 we plot the quantum conductance for the different spin channels in the AFM, FM and PM states. As expected, AFM and PM have spin degenerated curves for the conductance due to their symmetric spin distribution. The AFM state has a ≈ 265 meV gap around the Fermi energy. Moving to the PM case, we have a highly localized conductance peak at the zero energy point which is surrounded by two conductance plateaus having a tiny gap (≈ 34 meV) between them. Finally, the FM state presents a ≈ 30 meV gap. However, in contrast with the AFM and PM cases, the gap in the FM case is between a pure spin-up and spin-down levels. It follows that the spin character of the current can be controlled by setting the impinging electron energy slightly above or below the Fermi energy.

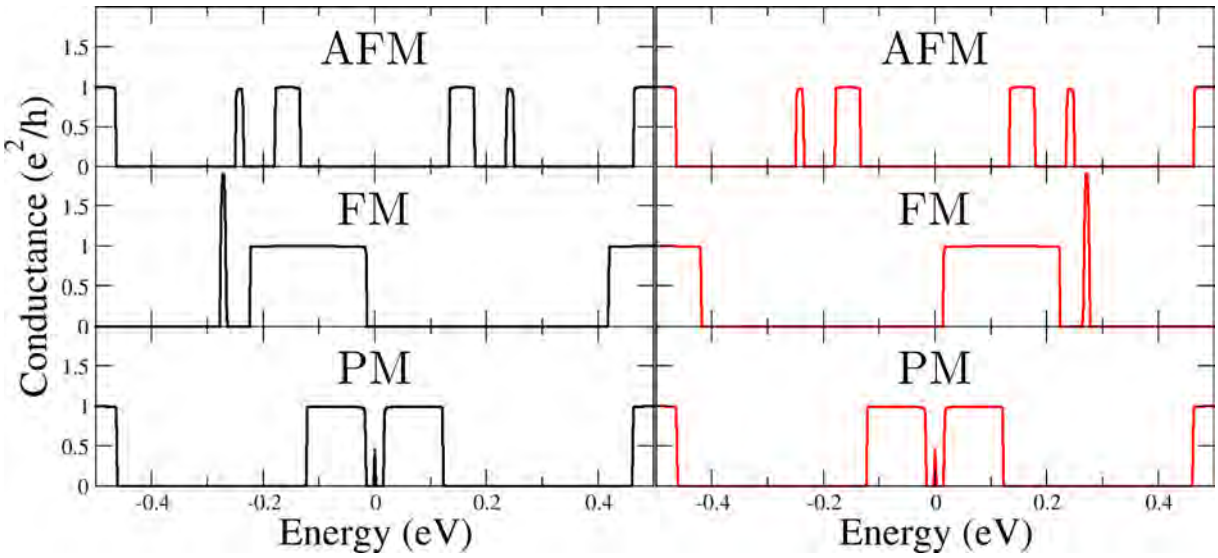

Figure 9.7: Quantum conductance as a function of energy for the three possible spin distributions for the periodic $(5_Z, 13_A)$ ZA-GNW structure. Spin-up curves are plotted in black (left) while spin-down curves are in red (right). Here the Fermi energy is set to $E_F = 0$.

In the following, we consider one ZA-GNW cell sandwiched between two semi-infinite 5-Z-GNR terminals. Despite of having only two magnetic states (other than the PM case), we have four possibilities for the spin distribution in this one-cell system. This is due to the two possibilities for the spin distribution along the Z-GNR terminals for each state from the GNW unit cell. We will label these distributions according to the GNW cell state plus an index which can be either 1 (when the GNR terminals have the same distribution as the GNW) or 2 (when the GNR terminals do not have the same distribution as the GNW). These are depicted in Fig. 9.8.

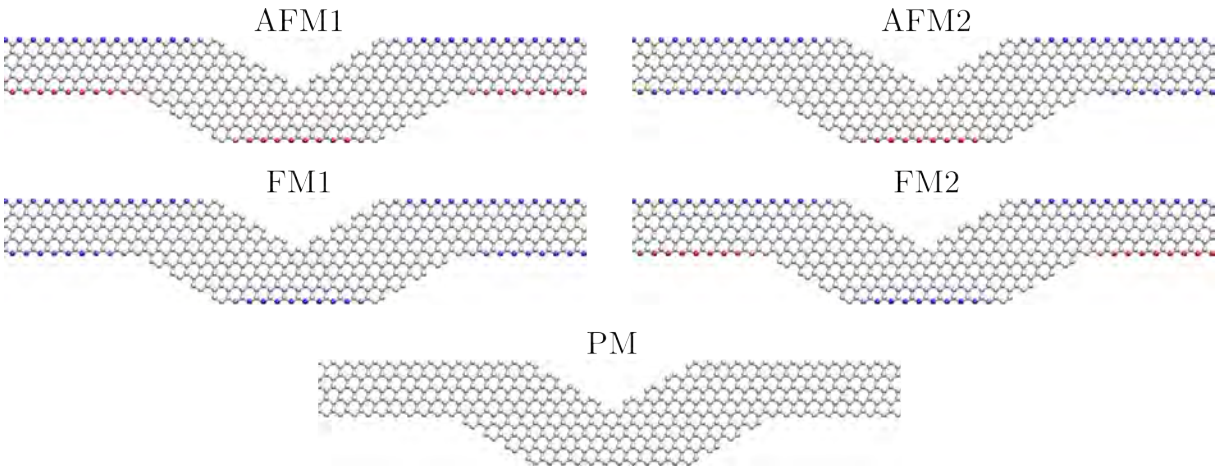

Figure 9.8: Five possible spin distributions for a single $(5_Z, 13_A)$ AZ-GNW cell attached to two semi-infinite 5-Z-GNR electrodes. In the plots, blue (red) represents the maximum polarization for spin up (down), while white denotes no spin-polarization.

The conductance curves for these one-cell states are ploted in Fig. 9.9. We observe that the conductance is substantially suppressed for the $[-0.5eV, +0.5eV]$ interval for the AFM1 case. After a gap of about 0.5 eV, the conductance starts to increase, but in a slow pace. The same behavior is observed for FM2, except for conductance spikes located close to ± 0.25 eV and ± 0.35 eV. This is directly related to the terminals properties since these are in their AFM state which presents a ≈ 0.5 eV conductance gap around the Fermi energy (see Fig. 9.10).

On the other hand, the AFM2 and FM1 states have Z-GNR terminals in their FM state (which is metallic - see Fig. 9.10). In the FM1 case we note two broader conductance peaks (centered close to -112 and -222 meV) on the left of E_F for electrons with spin up (majority spin) and two symmetrically positioned peaks (112 and 222 meV) on the right of E_F for spin-down electrons. This is compatible with the properties of both 5-Z-GNR terminals and the $(5_Z, 13_A)$ system. Since the periodic 5-Z-GNR system possess constant non zero conductance along the extension over the energy axis corresponding to these peaks, the periodic ZA-GNW system has 208 meV wide conductance plateaus in the same energy intervals. We observe that, around the Fermi energy, the conductance relative to the occupied states ($E < 0$) corresponds to the majority spin, while the electron-electron interaction pushes the opposite spin levels to

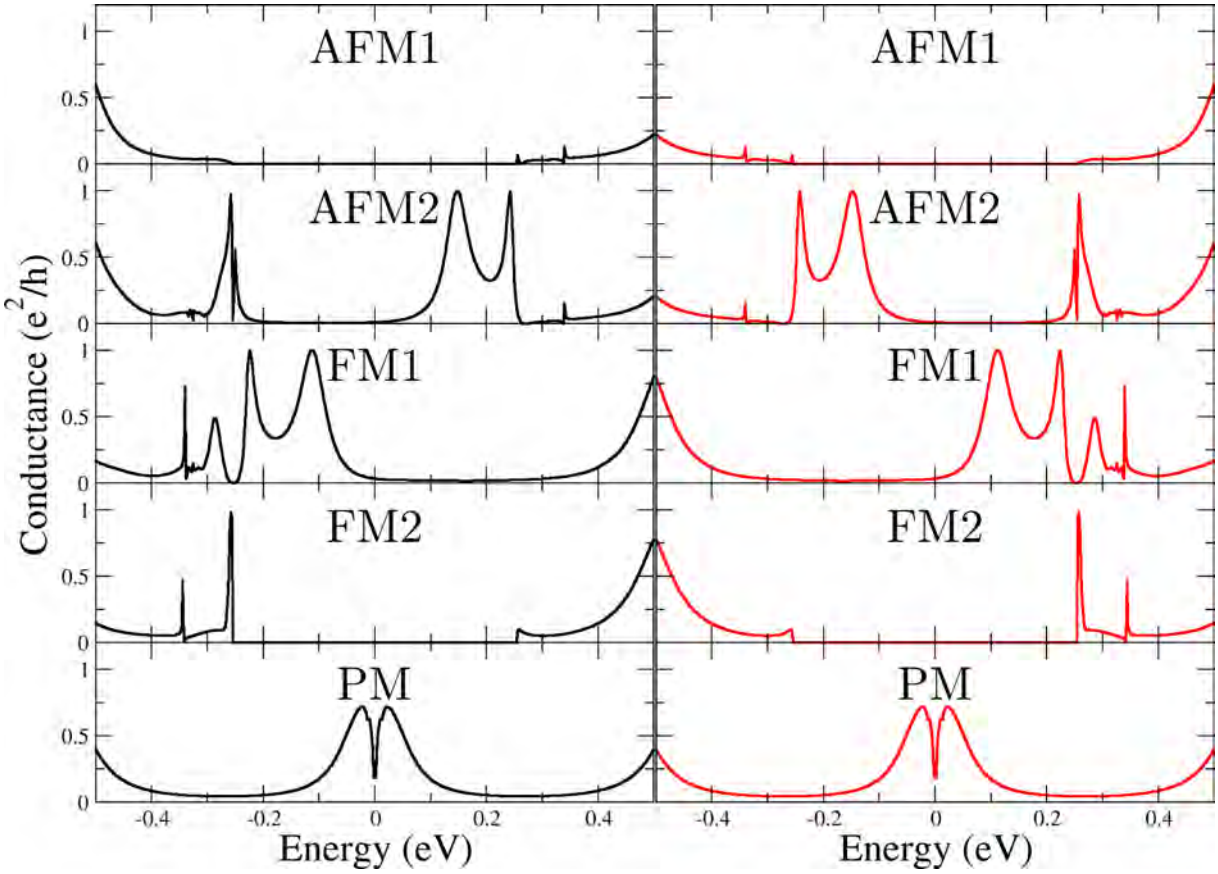

Figure 9.9: Quantum conductance as a function of energy for the five possible spin distributions for a single $(5_Z, 13_A)$ ZA-GNW unit cell attached to two semi-infinite 5-Z-GNR terminals. Spin-up curves are in black (left) while spin-down curves are in red (right). Here the Fermi energy is set to $E_F = 0$.

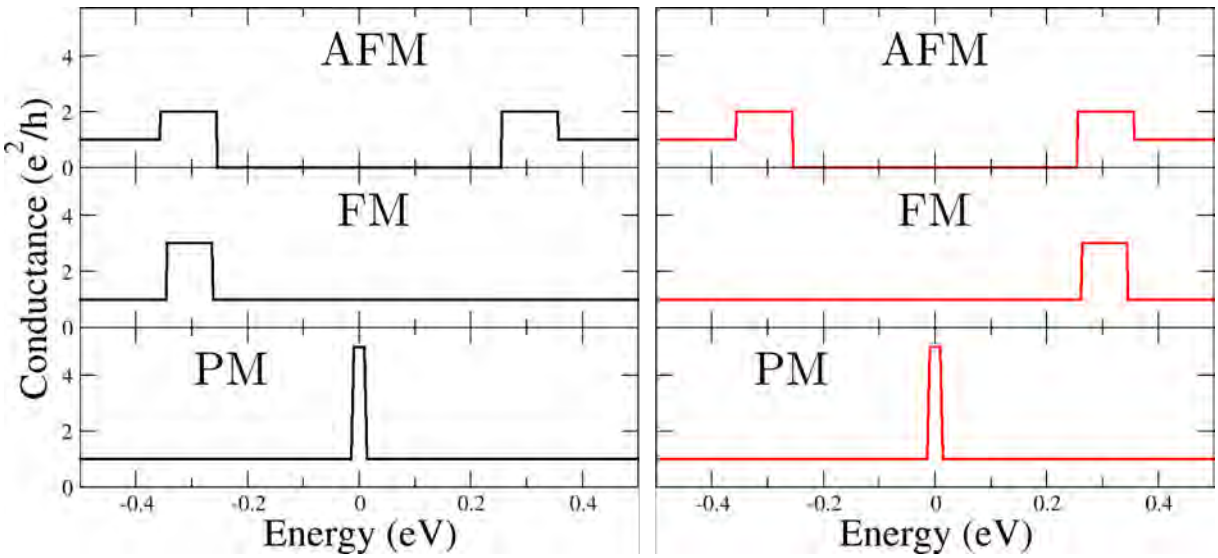

Figure 9.10: Quantum conductance as a function of energy for the three possible spin distributions for a periodic 5-Z-GNR. Spin-up curves are plotted in black (left) while spin-down curves are in red (right). Here the Fermi energy is shifted to $E_F = 0$.

higher energies so that the conductance for the unoccupied levels ($E > 0$) is dominated by the minority spin levels.

Switching to the AFM2 state (which also has 5-Z-GNR terminals on their FM state), we still have these two peaks for each spin channel, but their positions relative to the Fermi level are inverted: the conductance close to the Fermi level for occupied states is now dominated by the spin down electrons (minority spin on the Z-GNR terminals), while the conductance for the unoccupied states is in turn dominated by spin up electrons (majority spin on the terminals). This can be surprising, in principle, as we could expect the majority (minority) spin electrons to be responsible for the conductance from the occupied (unoccupied) states. However, an analysis on the DOS sheds light on the origins of the AFM2 state behavior. The sewing algorithm implemented in the TRANSFOR package (see Chapters 3 and 4) allows us to access local properties like the DOS as it provides a systematic way to obtain the GF's diagonal elements.

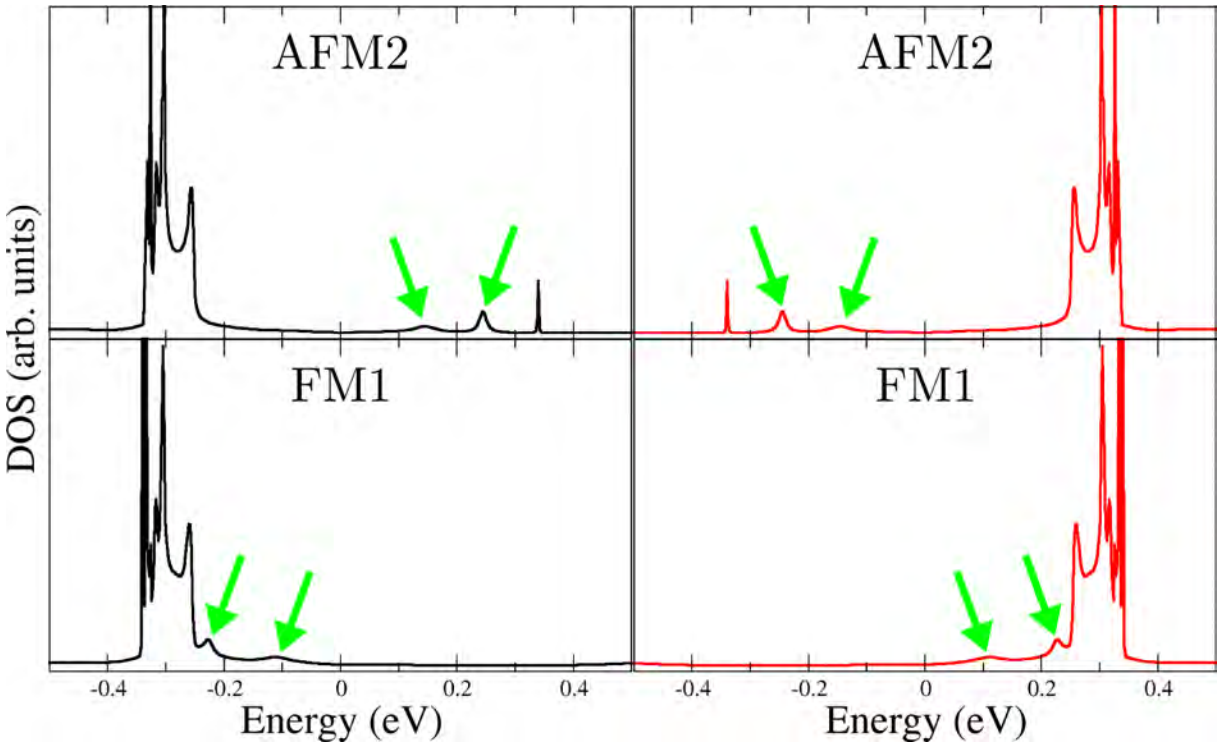

Figure 9.11: DOS as a function of energy for the AFM2 and FM1 spin distributions for a single $(5_Z, 13_A)$ ZA-GNW unit cell attached to two semi-infinite 5-Z-GNR terminals calculated using the sewing algorithm implemented in the TRANSFOR package. Spin-up curves are in black (left) while spin-down curves are in red (right). Here the Fermi energy is set to $E_F = 0$.

As we can see from Fig. 9.11, most of the DOS below (above) E_F corresponds to the majority (minority) spin in both FM1 and AFM2. The states corresponding to the AFM2 and FM1 conductance peaks close to E_F (in Fig. 9.9) are those marked by green arrows in the DOS plots from Fig. 9.11. As we can see, these particular states behave differently from most of the states close to E_F and change their position relative to the zero energy level as we go from the FM1 to the AFM2 distribution. Therefore, the conductance for states below and above the Fermi energy can be switched between spin-up and -down conduction by switching the spin

polarization along the zigzag edge sector indicated by the green arrows in Fig. 9.12.

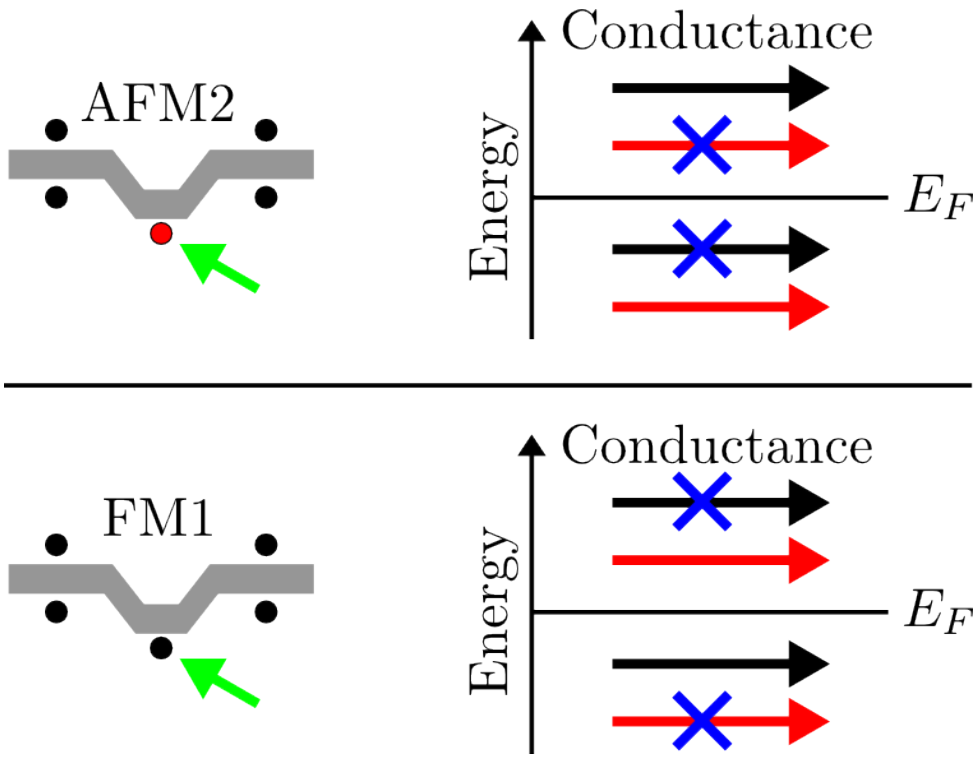

Figure 9.12: Switching mechanism for the spin-up and -down conductance involving the AFM2 and FM1 states in a single $(5_Z, 13_A)$ ZA-GNW unit cell attached to two semi-infinite 5-Z-GNR terminals. Spin up (down) is represented by black (red) circles and arrows.

Finally, the PM distribution presents two symmetric conductance peaks around the Fermi level.

9.4 ZZ-GNWs

For this last case considered here, we choose a $(5_Z, 8_Z)$ ZZ-GNW. Since the oblique sectors are too short in this system, no significant spin polarization is developed along its oblique edges so that the AFM and TAFM distributions are (in practice) indistinguishable, similarly to FM and LFiM. Although this particular system does not present 5 different spin distributions within a single unit cell as most ZZ-GNWs, it is a good example to be compared with the ZA-GNW case presented in the last section. This is because in their one-cell system the semi-infinite GNRs composing the terminals will be the same, namely 5-Z-GNR ribbons. In addition the lengths of the outer parallel edges on their unit cell (which is where spin polarization assumes significant values for this $(5_Z, 8_Z)$ system) will also be the same. So the geometrical differences between $(5_Z, 13_A)$ and $(5_Z, 8_Z)$ in the one-cell system will be restricted to the oblique sectors which will lead to dissimilar transport properties for one case to the other. In fact, the one-cell system

has five possibilities for the spin distribution which are analogous the the five corresponding distributions on the ZA-GNW one-cell system (Fig 9.8).

In Fig. 9.13 we plot the conductance versus energy curves for the periodic $(5_Z, 8_Z)$ systems in the AFM FM and PM states. The AFM state presents a 338 meV conductance gap around the Fermi energy surrounded by three short conductance plateaus from each side. In the PM case, we have a metallic system (nonzero conductance at E_F) and, in addition, two more conductance plateaus symmetrically arranged around the Fermi level. Both AFM and PM states have degenerated spin-up and -down conductance curves due to the symmetry of their spin distributions.

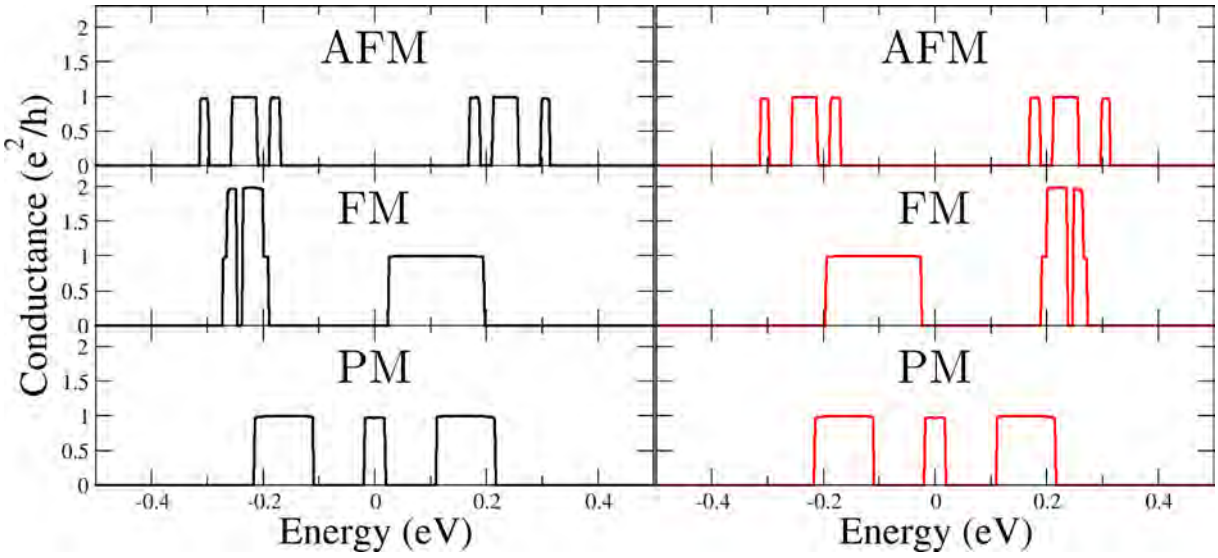

Figure 9.13: Quantum conductance as a function of energy for the three possible spin distributions for the periodic $(5_Z, 8_Z)$ ZZ-GNW structure. Spin-up curves are in black (left) while spin-down curves are in red (right). Here the Fermi energy is set to $E_F = 0$.

Finally, the FM state presents two conductance windows around the Fermi energy, one for the (majority) spin-up ($E > 0$) and other for the (minority) spin-down ($E < 0$) states. This is similar to what happens to the periodic $(5_Z, 13_A)$ structure in its FM state, but with one noteworthy difference: the conducting levels below (above) the Fermi energy corresponds to the minority (majority) spin. This behavior is opposite to the $(5_Z, 13_A)$ case where the conductance plateau just below E_F for the FM state corresponds to the majority spin. These aspects related to the conductance of frontier levels in $(5_Z, 8_Z)$ also differ from the $(6_A, 7_Z)$ AZ-GNW system whose electronic structure was described in last chapter. As we discussed before, the $(6_A, 7_Z)$ structure in its FM state presents valence bands populated by majority spin, pushing the minority spin levels to higher energies in the conduction band.

When analyzing the one-cell system data, we observe that both AFM1 and FM2 states have a ≈ 555 meV conductance gap around E_F. In the AFM1 case we note two asymmetric conductance peaks from which the sharpest is suppressed in the FM1 state. So, switching

between AFM1 and FM2 can be used to turn the conductance on and off for these particular values of energy.

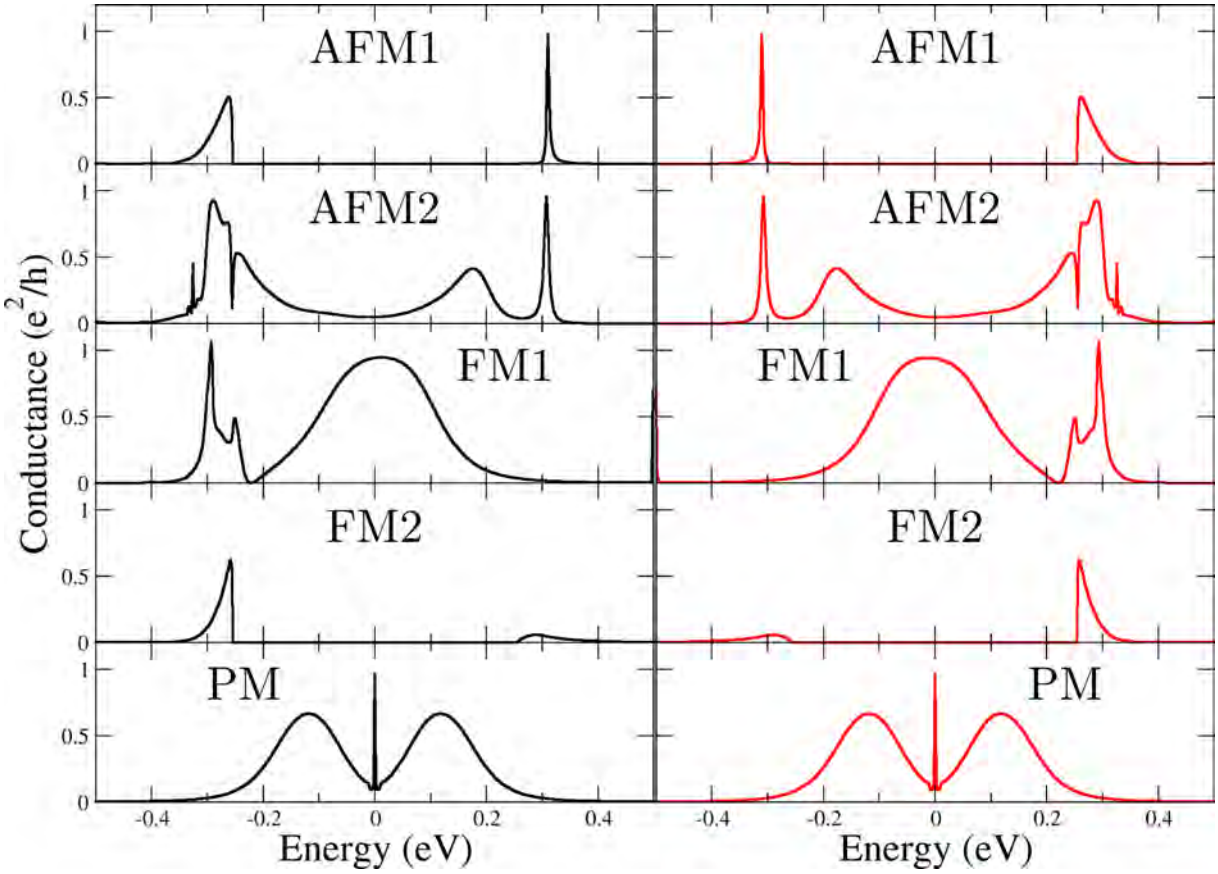

Figure 9.14: Quantum conductance as a function of energy for the five possible spin distributions for a single $(5_Z, 8_Z)$ ZZ-GNW unit cell attached to two semi-infinite 5-Z-GNR terminals. Spin-up curves are in black (left) while spin-down curves are in red (right). Here the Fermi energy is set to $E_F = 0$.

The FM1 state possesses a broad conductance peak over the Fermi level which is slightly asymmetric for spin-up and -down states. In addition, we have some peaks of conductance on the left (right) of the broad peak for spin-up (-down) in this same state. When flipping the spin polarization on the zigzag edge highlighted in Fig. 9.12 we obtain the AFM2 state and the central broad peak is turned off while we preserve peaks of conductance on the left (right) of E_F for spin-up (-down) electrons. Another change is the appearance of two peaks on the right (left) of E_F for spin-up (-down). We see that all the changes are conducted by a local change on the orientation for the spin along the finite parallel edge from the central GNW cell. The PM states behaves similarly to the ZA-GNW case, except for the presence of broader peaks and a sharp peak on the Fermi level.

9.5 From the one cell system to the periodic system

In the last three sections we studied the transport properties of GNWs from two complementary points of view. Namely, we considered two different cases: a periodic system and a one cell structure attached to two semi-infinite GNR electrodes. In this section we aim at describing how the transport properties behave as we gradually go from one system to the other. In order to do this, we consider a series of intermediate systems were we have $n = 1,2,3,4,5,6,7$ GNW unit cells between two semi-infinite GNR leads as depicted in Fig. 9.15.

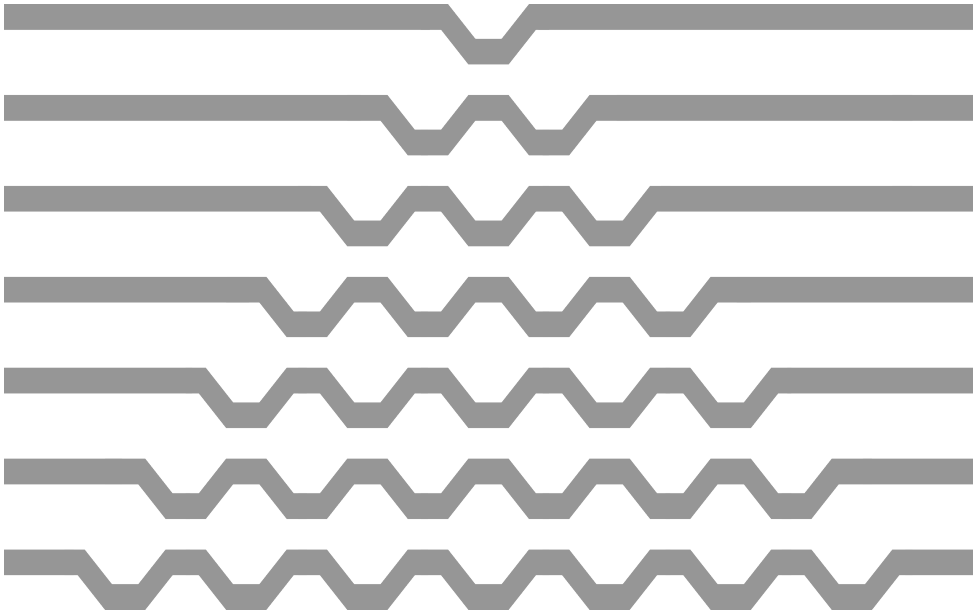

Figure 9.15: Systems of $n = 1,2,3,4,5,6,7$ $(11_A, 6_Z)$ unit cells attached to two semi infinite 11-A-GNR electrodes.

Here we focus on the $(11_A, 6_Z)$ structure. In Fig. 9.16 we show the conductance curves for the five different spin distributions in this AZ-GNW.

We observe a common behavior for all the possible AZ-GNW states: as we add more and more GNW cells between the two semi-infinite A-GNR terminals, an increasing number of conductance peaks appear within the plotted energy window. In addition, these peaks start to concentrate in groups which look closer and closer to the conductance plateaus from the periodic system as the number of sandwiched GNW cells gets large. This is expected since as we have an increasing number of cells, the GNW's electronic states gradually cease to behave like localized scatterers to start forming bands of energy, allowing the ballistic conduction through them as the number of cells tends to be infinite. Nevertheless, we can already have a good approximation to the periodic system behavior only with a limited number of GNW cells, as can be seen in special for the 7-cell systems.

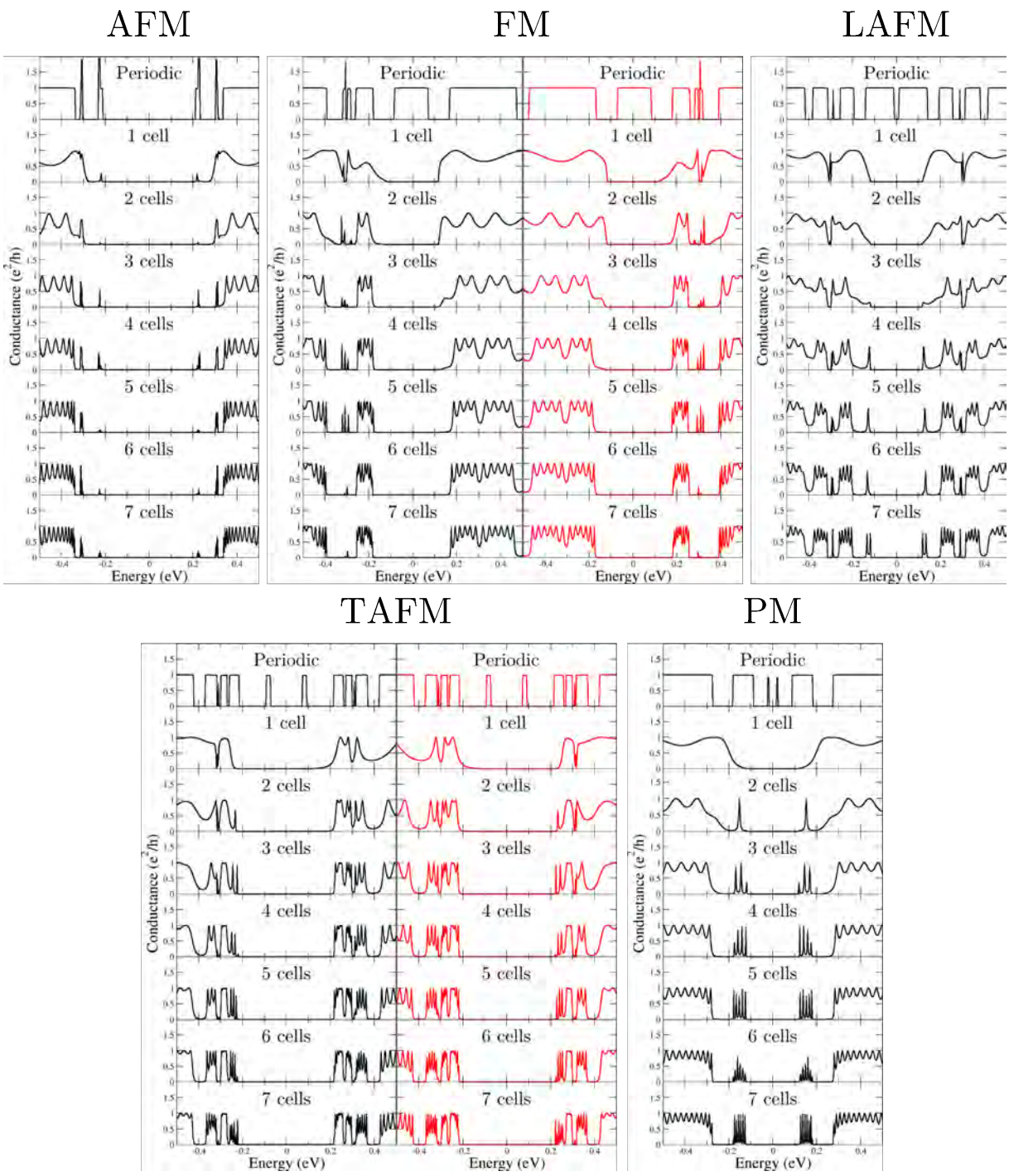

Figure 9.16: Quantum conductance as a function of energy for the five possible spin distributions in a periodic $(11_A,6_Z)$ AZ-GNW and in systems composed by $n = 1,2,3,4,5,6,7$ $(11_A,6_Z)$ AZ-GNW unit cells attached to two semi-infinite 11-A-GNR terminals. Spin-up curves are in black while spin-down curves are in red. For the AFM, LAFM and PM cases, we present only the spin-up results (the spin-down curves are identical). Here the Fermi energy is set to $E_F = 0$.

However, the resemblance between the multi-cell systems and their periodic counterpart does not hold true for the conductance plateaus around the Fermi energy. This is clearly imposed by the leads properties as the 11-A-GNR system is semiconductor (see Fig.9.5). One observes that in all the states for all systems, the conductance is null on the energy interval corresponding

to the A-GNR gap. In the periodic-LAFM case, for example, the two step-like conductance portions close to E_F have part within the A-GNR gap window and part outside it. If one observes the corresponding 7-cells system, for instance, it is noticed that the GNW conductance levels condensate only within the region associated with the outside part of the periodic system's plateau. A similar situation occurs in the PM state. All the other conductance plateaus (from the periodic systems) which are inside the A-GNR gap are suppressed in the multi-cell systems.

9.6 Summary

In this chapter we concluded the GNWs study by computing the electronic transport of these structures in two different configurations: a periodic GNW system and a one-cell system where a single GNW unit cell is placed between two semi-infinite GNR electrodes. While the first case is characterized by conductance plateaus (onset of ballistic transport), the GNW in the one-cell systems presents a source of electronic scattering resulting in sets of conductance peaks which can be tuned by switching the GNW's magnetic state. In addition, we were able to see that a larger number of GNW unit cells sandwiched between semi-infinite GNR electrodes gradually recovers the conductance aspects of the periodic systems as the number of GNW cells increases (unless for energies close to E_F whose conductance is blocked when we have semiconducting electrodes).

Conclusions

We conclude this document by presenting a summary of the findings made during the course of this thesis. After a general introduction and a detailed discussion of the methods employed for our research, we started presenting our findings. These results can be separated into two main parts: toroidal systems and graphene nanowiggles.

Before discussing the results, we developed (in Chapter 4) the patchwork algorithm we implemented in the TRANSFOR software. This method is based on the knitting and sewing algorithms proposed recently. The patchwork algorithm adapts knitting and sewing to work in parallel by dividing the system into smaller parts, or domains. In this way we can use multiple processors so that each one takes care of one domain. This tool can be very useful for future studies, especially if we intend to simulate much larger systems. While the time saving can be only modest for small systems, the use of multiple processors can lower significantly the execution time in the calculation of huge systems (as we pointed out in Chapter 4).

In Chapter 5 we presented a theoretical study of the electronic transport properties of carbon nanorings (made from the bending of a carbon nanotube) attached to two identical nanotube electrodes. Our findings indicate that the transmission amplitude depends strongly on the distance between terminals (since this distance determines the electronic paths) and on the place on the torus where the terminals are anchored (since different joint geometries produce dissimilar conductance dependence on the energy and angle between terminals owing to different scattering at the junctions). They confirm that a highly controlled approach needs to be adopted in the design of such nanoscale devices, especially in terms of how the electrodes are positioned relative to the nanoring. In addition, the choice of the nanotube composing the torus has an explicit influence on the torus transport properties. Namely, the nanotube type determines characteristic families of behaviors for the conductance dependence with the angle between the terminals. This is in fact expected since each tube has a specific energy-momentum relation (electronic structure) which results in different dependence of the interfering patterns as a function of energy. Part of these conclusions were rationalized using a continuum model for the interference of reflected and transmitted waves along the different arms forming the torus. This model is shown to explain well the observed numerical results. However, this simple model is not able to reproduce energy asymmetries around the Fermi energy since it does not include specific de-

tails of the atomic arrangements on the junctions (presence of pentagons and heptagons which produce electronic scattering).

Moving to Chapter 6, our work demonstrated that nanotube- and nanoribbon-based nanorings attached to multiple electrodes represent opportunities for designing devices at the nanoscale with complex properties. These properties include energy-specific transmission selectivity related to nontrivial resonance patterns and the presence of specific quantum states allowed by cyclic boundary conditions. This is an interesting result that opens up the possibility of using multi-terminal carbon nanorings as path controlling devices in complex nanocircuits using the impinging electron energy as path-tuning parameter.

After presenting our work on toroidal structures, we started the discussion on new complex ribbon structures, called graphene nanowiggles (GNWs). In Chapter 7 we defined these structures, showing a systematic way to describe and construct GNWs. We showed that the specific geometry we worked on can be completely determined by four parameters that determine the widths and the lengths of the parallel and oblique GNR sectors whose successive periodic repetition defines the GNW's lattice. Other structural quantities like the lattice parameter and the number of atoms are easily obtained from that four defining parameters.

Chapter 8 is dedicated to describing GNW's electronic structure. Our calculations predict the emergence of physical phenomena in GNWs that are absent in their constitutive GNRs. The emergence of these properties is the result of the interplay between the properties of the GNR constituents, the symmetry of the atomic structure, and the bipartition of the graphene lattice. The relationship between the gap and the geometry is dictated by the armchair or zigzag character of the corresponding parallel and oblique sectors, enabling GNWs to offer a broad set of geometrical parameters to tune the electronic structure compared to GNRs. Spin ordering is found to be restricted to zigzag edges, while armchair sectors dictate the formation of magnetic nanodomains whose size can be fine tuned depending on how GNW sectors are assembled. All GNWs with at least one zigzag sector have an antiferromagnetic ground state, in large part due to the bipartition of the graphene lattice. Our calculations also suggest the existence of a number of possible metastable spin distributions, thereby elevating GNWs as potential components of spintronic devices. We plotted the gap *versus* atomic structure relation for all these magnetic states, showing that each achiral GNW type has a specific map for the gap as a function of the widths of both parallel and oblique sectors.

Transport properties of GNWs containing at least one zigzag edge are discussed in Chapter 9. The transport in these GNWs is controlled by the structure's magnetic state. As a result, we can have completely different conductance patterns for the same atomic arrangement by

selecting the nature of the spin distribution. This behavior is present in both atomic configurations we studied: periodic GNW and one GNW cell sandwiched between two semi-infinite GNR electrodes. Such transport tuning also involves switching between spin-up and -down currents by selecting the magnetic state and/or impinging electron energy. This feature is notably observed in the one-cell case. This is because symmetric up-down spin distributions in the periodic ribbon become asymmetric in the non-periodic system, rendering different spin-up and -down conductance curves. Electronic scattering is significant to the one-cell system, as evidenced by peaks in the conductance *versus* energy plot. Finally, the properties of periodic systems are gradually recovered by including more GNW cells in the on-cell system. The non-periodic system gradually presents the features of a periodic system even for a small number of sandwiched GNW cells (≈ 7) as sets of peaks steadily concentrate along energy ranges defined by the periodic system's plateaus. However, the formation of such sets is avoided for energies close to the Fermi energy when we have semiconducting leads. We anticipate the present study to provide an ideal bridge between the recently synthesized GNWs and their future developments into nanodevices.

Perspectives

While we believe that we have a good collection of promising results in this thesis, we see a lot of interesting problems to be considered in the future.

As we showed in Chapters 5 and 6, the presence of multiple possible paths for the electronic flow in toroidal structures allows to tune the electrical current by choosing the impinging electron energy and by selecting specific geometries. In the systems we studied, we restricted the presence of defects to the joints. However, defects can play a broader influence on the transport properties of carbon nanorings (specially when in an extended distribution), since they can act as an additional tuning factor to obtain structures with desired physical properties. As stated in Chapter 1, the production of structures with specific arrangement of defects is a developing area at the experimental level and considering extended arrangements of defects in toroidal systems is an interesting problem to be considered by us in the following of this thesis.

While the transport formalism used in this thesis is based on coherent (energy conserving) scattering. The inclusion of decoherence effects is a problem of great importance as we start to look at increasingly larger systems. Such effects have already been considered in nanostructured systems [127] and definitely constitute a pertinent problem to be considered for both toroidal structures and GNWs.

We believe that our results on GNWs can be the nucleation point for a series of investigations on both GNWs and GNW-based materials. Cai et al. demonstrated (in the paper that motivated our study on nanowiggles) the viability of synthesizing not only GNWs, but also multi-terminal GNW-junctions [4]. At the same time this is an important result by itself, it also points a possible path to be followed in the investigation of GNW-based nanostructures. This is because a multi-terminal joint is a natural system to be considered if one proposes to embed such GNW systems into more complex systems. So, studying GNWs in more complex structures like multi-terminal junctions is among the problems we intend to give attention in future studies.

APPENDIX A – Input examples for TBFOR

TBfor works with two input files. The First one contains the structure to be simulated and other parameters needed for the calculation. Below we show an example:

```
system_label
1  1  10  0.2D0   3.84D0
2
1  12   1.1   3.0
2  12   1.1   3.0
100.000    0.000    0.000
  0.000  100.000    0.000
  0.000    0.000   12.780
2
  0.000    0.000    0.000
  0.000    0.000    0.500
   20
1        0.000000000      2.459512147     -5.680000000
2        0.000000000      1.229756073     -4.970000000
2        0.000000000      3.689268220     -4.970000000
1        0.000000000      1.229756073     -3.550000000
2        0.000000000      3.689268220     -3.550000000
2        0.000000000      0.000000000     -2.840000000
1        0.000000000      2.459512147     -2.840000000
2        0.000000000      0.000000000     -1.420000000
2        0.000000000      2.459512147     -1.420000000
1        0.000000000      1.229756073     -0.710000000
1        0.000000000      2.459512147      5.680000000
2        0.000000000      1.229756073      4.970000000
2        0.000000000      3.689268220      4.970000000
1        0.000000000      1.229756073      3.550000000
2        0.000000000      3.689268220      3.550000000
2        0.000000000      0.000000000      2.840000000
1        0.000000000      2.459512147      2.840000000
2        0.000000000      0.000000000      1.420000000
2        0.000000000      2.459512147      1.420000000
1        0.000000000      1.229756073      0.710000000
```

The first line contains the label for structure. All the input files will be named with this label followed by an extension.

The second line contains the number of **k** points along the directions of the reciprocal

lattice vectors $\mathbf{K}_1$, $\mathbf{K}_2$ and $\mathbf{K}_3$, respectively. They are followed by the mixing parameter β (see Chapter 2) and the value of the on-site repulsion from the Hubbard model (see Chapter 2).

Third line contains the number n_s of species. The next n_s lines contains the species identification (integers in increasing order), the number of neighbors to be counted for atoms from this species, the minimum and the maximum distances, respectively, to the neighbors of this species.

The following three lines contains the lattice vectors.

The next line determines the number n_k of special points determining the path on the reciprocal space to plot the bands. The electronic bands will be interpolated along the lines defined by these points. The next n_k lines determine these special points, namely, the coordinates for each point written in the basis $\mathbf{K}_1$, $\mathbf{K}_2$ and $\mathbf{K}_3$.

The following line contains the number n_a of atoms and the following n_a lines have the species identification and the coordinates (x, y and z) for each atom.

The second input file has the TB parameters. If the species are numbered by 1, 2, 3, ..., we insert the information for each species in that order. For species i we insert (in this order):

- Its site energy;
- Hopping for first neighbors for the interaction of species i with species i;
- Hopping for second neighbors for the interaction of species i with species i;
- Hopping for third neighbors for the interaction of species i with species i;
- Hopping for first neighbors for the interaction of species i with species $i+1$;
- Hopping for second neighbors for the interaction of species i with species $i+1$;
- Hopping for third neighbors for the interaction of species i with species $i+1$;
- ...
- Hopping for first neighbors for the interaction of species i with species n_s;
- Hopping for second neighbors for the interaction of species i with species n_s;
- Hopping for third neighbors for the interaction of species i with species n_s;

Below is an example with 2 species:

```
 0.00D0    # Site energy for species 1
-3.20D0    # Hopping - 1st neighbors - species 1 and species 1
 0.00D0    # Hopping - 2nd neighbors - species 1 and species 1
-0.30D0    # Hopping - 3rd neighbors - species 1 and species 1
-3.20D0    # Hopping - 1st neighbors - species 1 and species 2
 0.00D0    # Hopping - 2nd neighbors - species 1 and species 2
-0.30D0    # Hopping - 3rd neighbors - species 1 and species 2
 0.00D0    # Site energy for species 2
-3.40D0    # Hopping - 1st neighbors - species 2 and species 2
 0.00D0    # Hopping - 2nd neighbors - species 2 and species 2
-0.30D0    # Hopping - 3rd neighbors - species 2 and species 2
```

APPENDIX B – Generating GNWs coordinates: utility program

In this appendix we present a simple tool to generate atomic coordinates for the four achiral GNW types. The main program unit is below:

```
PROGRAM wiggle
!!!!!!!!!!!!!!!!!!!!!!!!!!!!!!!!!!!!!!!!!!!!!!!!!!!!
! Program to generate atomic coordinates for GNWs
! Written by Eduardo Costa Girao
! in September 7, 2011.
!!!!!!!!!!!!!!!!!!!!!!!!!!!!!!!!!!!!!!!!!!!!!!!!!!!!
USE wiggle_var
USE wiggle_tasks
IMPLICIT none
! Input data
CALL ask_gnw_type
CALL ask_wp
CALL ask_lp
CALL ask_wo
CALL ask_lo
! Determining parameters
CALL initial_parameters
CALL parallel_parameters
CALL oblique_parameters
CALL mixed_parameters
! creating the parallel part
CALL create_parallel
! creating the oblique part
CALL create_oblique
!making final
CALL assembling
!Writing output
CALL writting
!Number of atoms
CALL number_of_atoms
END PROGRAM wiggle
```

The variables are declared within the following module:

```
MODULE wiggle_var
!!!!!!!!!!!!!!!!!!!!!!!!!!!!!!!!!!!!!!!!!!!!!!!!!!!!
```

```
      ! Module declaring the variables for wiggle.90
      ! Written by Eduardo Costa Girao
      ! in September 7, 2011.
      !!!!!!!!!!!!!!!!!!!!!!!!!!!!!!!!!!!!!!!!!!!!!!!!!!!!
      IMPLICIT none
      SAVE

      DOUBLE PRECISION:: yp1(100000),zp1(100000),yp2(100000),zp2(100000)
      DOUBLE PRECISION:: yo1(100000),zo1(100000),yo2(100000),zo2(100000)
      DOUBLE PRECISION:: yf(100000),zf(100000),yf2(100000),zf2(100000)
      DOUBLE PRECISION:: pi,acc,a,theta,lattice,dr
      DOUBLE PRECISION:: atmp0,btmp0,atmp1,btmp1,atmp2,btmp2
      DOUBLE PRECISION:: basis1,basis2,basis3,basis4
      DOUBLE PRECISION:: basis5,basis6,basis7,basis8
      DOUBLE PRECISION:: base1,base2,base4,base5
      DOUBLE PRECISION:: base6,base7,base8,param1
      INTEGER:: Lp,Wp,Lo,Wo,i,j,par,obl,nat,unit,nattmp,ncells,tmp,tmp2
      LOGICAL:: add

      END MODULE wiggle_var
```

And the subroutines with the specific tasks called in the main program are contained in the following module:

```
      MODULE wiggle_tasks
      !!!!!!!!!!!!!!!!!!!!!!!!!!!!!!!!!!!!!!!!!!!!!!!!!!!!
      ! Module containing the subroutines for wiggle.90
      ! Written by Eduardo Costa Girao
      ! in September 7, 2011.
      !!!!!!!!!!!!!!!!!!!!!!!!!!!!!!!!!!!!!!!!!!!!!!!!!!!!
      USE wiggle_var
      IMPLICIT none
      SAVE
!!!!!!!!!!!!!!!!!!!!!!!!!!!!!!!!!!!!!!!!!!!!!!!!!!!!!!!!!!!!!!!!!!!
      CONTAINS
!!!!!!!!!!!!!!!!!!!!!!!!!!!!!!!!!!!!!!!!!!!!!!!!!!!!!!!!!!!!!!!!!!!
        SUBROUTINE ask_gnw_type
        !!!!!!!!!!!!!!!!!!!!!!!!!!!!!!!!!!!!!!!!!!!
        ! Subroutine to determine the GNW type
        !!!!!!!!!!!!!!!!!!!!!!!!!!!!!!!!!!!!!!!!!!!
        USE wiggle_var
        IMPLICIT none

        PRINT*,'************************************************'
        PRINT*,'***************** WIGGLE PROGRAM ***************'
        PRINT*,'************************************************'
        PRINT*,'Parallel Sector:' ; PRINT*,'A->1' ; PRINT*,'Z->2'
        READ*,par
        PRINT*,'Oblique Sector:' ; PRINT*,'A->1' ; PRINT*,'Z->2'
        READ*,obl
        PRINT*,'Number of cells'
        READ*,ncells

        END SUBROUTINE ask_gnw_type
```

```
!!!!!!!!!!!!!!!!!!!!!!!!!!!!!!!!!!!!!!!!!!!!!!!!!!!!!!!!!!!!!!!!!!!!!!!
        SUBROUTINE ask_wp
        !!!!!!!!!!!!!!!!!!!!!!!!!!!!!!!!!!!!!!!!!!!!
        ! Subroutine to determine Wp
        !!!!!!!!!!!!!!!!!!!!!!!!!!!!!!!!!!!!!!!!!!!!
        USE wiggle_var
        IMPLICIT none

        PRINT*,'Parallel Width:'
        READ*,Wp

        END SUBROUTINE ask_wp
!!!!!!!!!!!!!!!!!!!!!!!!!!!!!!!!!!!!!!!!!!!!!!!!!!!!!!!!!!!!!!!!!!!!!!!
        SUBROUTINE ask_lp
        !!!!!!!!!!!!!!!!!!!!!!!!!!!!!!!!!!!!!!!!!!!!
        ! Subroutine to determine Lp
        !!!!!!!!!!!!!!!!!!!!!!!!!!!!!!!!!!!!!!!!!!!!
        USE wiggle_var
        IMPLICIT none

        PRINT*,'Parallel Length:'
        IF((par.eq.1).AND.(obl.eq.1).AND.(MOD(Lp,3).eq.0))THEN
         PRINT*,'Lp has to be >1 and can not be a multiple of 3 for AA-GNWs'
        ELSE IF((par.eq.1).AND.(obl.eq.2).AND.(MOD(Lp,3).ne.2))THEN
          PRINT*,'Lp has to be 2 plus a multiple of 3 for AZ-GNWs'
        ELSE
          PRINT*,'Lp has to be >0 for ZA- and ZZ-GNWs'
        END IF
        READ*,Lp
        IF((par.eq.1).AND.(obl.eq.1).AND.(MOD(Lp,3).eq.0))THEN
          STOP 'Lp can not be a multiple of 3 for AA-GNWs'
        END IF
        IF((par.eq.1).AND.(obl.eq.2).AND.(MOD(Lp,3).ne.2))THEN
          STOP 'Lp has to be 2 plus a multiple of 3 for AZ-GNWs'
        END IF

        END SUBROUTINE ask_lp
!!!!!!!!!!!!!!!!!!!!!!!!!!!!!!!!!!!!!!!!!!!!!!!!!!!!!!!!!!!!!!!!!!!!!!!
        SUBROUTINE ask_wo
        !!!!!!!!!!!!!!!!!!!!!!!!!!!!!!!!!!!!!!!!!!!!
        ! Subroutine to determine Wo
        !!!!!!!!!!!!!!!!!!!!!!!!!!!!!!!!!!!!!!!!!!!!
        USE wiggle_var
        IMPLICIT none

        PRINT*,'Oblique Width:'
        IF((par.eq.1).AND.(obl.eq.1))THEN
          PRINT*,'Wo has to be greater or equal to ',0.5*DFLOAT(1+Wp-Lp),'+Ymin'
          READ*,Wo
          tmp=MOD(2*Wo+Lp-Wp-1,3)
          IF(tmp.eq.1) tmp2=1
          IF(tmp.eq.2) tmp2=5
          IF(tmp.eq.0) tmp2=3
          IF((2*Wo+Lp-Wp-1).lt.tmp2)THEN
```

```
            PRINT*,'Wo has to be greater or equal to ',0.5*DFLOAT(1+Wp-Lp),'+Ymin'
            STOP
          END IF
        ELSE IF((par.eq.1).AND.(obl.eq.2))THEN
          PRINT*,'Wo has to be greater or equal to ',DFLOAT(2+3*Wp-Lp)/6.0
          READ*,Wo
          IF(Wo.lt.(DFLOAT(2+3*Wp-Lp)/6.0))THEN
            PRINT*,'Wo has to be greater or equal to ',DFLOAT(2+3*Wp-Lp)/6.0
            STOP
          END IF
        ELSE IF((par.eq.2).AND.(obl.eq.2))THEN
          PRINT*,'Wo has to be greater or equal to ',DFLOAT(7+3*Wp-3*Lp)/6.0
          READ*,Wo
          IF(Wo.lt.(DFLOAT(7+3*Wp-3*Lp)/6.0))THEN
            PRINT*,'Wo has to be greater or equal to ',DFLOAT(7+3*Wp-3*Lp)/6.0
            STOP
          END IF
        ELSE IF((par.eq.2).AND.(obl.eq.1))THEN
          PRINT*,'Wo has to be greater or equal to ',DFLOAT(1+3*Wp-Lp)/2.0
          READ*,Wo
          IF(Wo.lt.(DFLOAT(1+3*Wp-Lp)/2.0))THEN
            PRINT*,'Wo has to be greater or equal to ',DFLOAT(1+3*Wp-Lp)/2.0
            STOP
          END IF
        END IF

        END SUBROUTINE ask_wo
!!!!!!!!!!!!!!!!!!!!!!!!!!!!!!!!!!!!!!!!!!!!!!!!!!!!!!!!!!!!!!!!!!!
        SUBROUTINE ask_lo
        !!!!!!!!!!!!!!!!!!!!!!!!!!!!!!!!!!!!!!
        ! Subroutine to determine Lo
        !!!!!!!!!!!!!!!!!!!!!!!!!!!!!!!!!!!!!!
        USE wiggle_var
        IMPLICIT none

        PRINT*,'Oblique Length:'
        IF((par.eq.1).AND.(obl.eq.1))THEN
          PRINT*,'Lo has to be 3i+',3-MOD(2*Wo+2*Lp-2*Wp-1,3)
          READ*,Lo
          IF(MOD(2*Wo+Lo+2*Lp-2*Wp-1,3).ne.0)THEN
            PRINT*,'Lo has to be 3i+',3-MOD(2*Wo+2*Lp-2*Wp-1,3)
            STOP
          END IF
        ELSE
          READ*,Lo
        END IF

        IF(Lo.lt.Wp)THEN
          STOP 'Lo can not be less than Wp'
        END IF

        END SUBROUTINE ask_lo
!!!!!!!!!!!!!!!!!!!!!!!!!!!!!!!!!!!!!!!!!!!!!!!!!!!!!!!!!!!!!!!!!!!
        SUBROUTINE initial_parameters
```

```
        !!!!!!!!!!!!!!!!!!!!!!!!!!!!!!!!!!!!!!
        ! Subroutine to determine some initial
        ! parameters
        !!!!!!!!!!!!!!!!!!!!!!!!!!!!!!!!!!!!!!
        USE wiggle_var
        IMPLICIT none
        pi=DACOS(-1.0D0)
        acc=1.42
        a=acc*DSQRT(3.0D0)
        unit=100
        nat=0

        END SUBROUTINE initial_parameters
!!!!!!!!!!!!!!!!!!!!!!!!!!!!!!!!!!!!!!!!!!!!!!!!!!!!!!!!!!!!!!!!!!!
        SUBROUTINE parallel_parameters
        !!!!!!!!!!!!!!!!!!!!!!!!!!!!!!!!!!!!!!
        ! Subroutine to determine some parallel
        ! sector parameters
        !!!!!!!!!!!!!!!!!!!!!!!!!!!!!!!!!!!!!!
        USE wiggle_var
        IMPLICIT none
        IF(par.eq.1)THEN
          base1=-acc    ; base2=acc*3.0 ; base4=0.0D0     ; base5=acc*1.5D0
          base6=a*0.5D0 ; base7=-acc    ; base8=acc*0.5D0 ; param1=0.0D0
          basis7=-acc*DFLOAT(Lp)*0.5D0  ; basis8=0.0D0
        ELSE IF(par.eq.2)THEN
          base1=-a*0.5D0  ; base2=a       ; base4=acc/2.0 ; base5=a*0.5D0
          base6=acc*1.5D0 ; base7=a*0.5D0 ; base8=0.0D0   ; param1=a*0.5D0
          basis7=-a*DFLOAT(Lp+1)*0.5D0    ; basis8=-acc
        END IF

        END SUBROUTINE parallel_parameters
!!!!!!!!!!!!!!!!!!!!!!!!!!!!!!!!!!!!!!!!!!!!!!!!!!!!!!!!!!!!!!!!!!!
        SUBROUTINE oblique_parameters
        !!!!!!!!!!!!!!!!!!!!!!!!!!!!!!!!!!!!!!
        ! Subroutine to determine some oblique
        ! sector parameters
        !!!!!!!!!!!!!!!!!!!!!!!!!!!!!!!!!!!!!!
        USE wiggle_var
        IMPLICIT none
        IF(obl.eq.1)THEN
          basis1=-acc      ; basis2=acc*3.0 ; basis3=0.0D0
          basis4=acc*1.5D0 ; basis5=a*0.5D0 ; basis6=0.0D0
        ELSE IF(obl.eq.2)THEN
          basis1=-a*0.5D0 ; basis2=a         ; basis3=acc*0.5D0
          basis4=a*0.5D0  ; basis5=acc*1.5D0 ; basis6=0.0D0
        END IF

        END SUBROUTINE oblique_parameters
!!!!!!!!!!!!!!!!!!!!!!!!!!!!!!!!!!!!!!!!!!!!!!!!!!!!!!!!!!!!!!!!!!!
        SUBROUTINE mixed_parameters
        !!!!!!!!!!!!!!!!!!!!!!!!!!!!!!!!!!!!!!
        ! Subroutine to determine some mixed
        ! parameters
```

```
        !!!!!!!!!!!!!!!!!!!!!!!!!!!!!!!!!!!!!!!!
        USE wiggle_var
        IMPLICIT none
        IF(par.eq.obl)THEN
          theta=pi/3.0
          atmp1=DSQRT(3.0D0)
          atmp2=DSQRT(3.0D0)
        ELSE
          theta=pi/6.0
          atmp1=DSQRT(3.0D0)/3.0D0
          atmp2=DSQRT(3.0D0)/3.0D0
        END IF

        IF((par.eq.1).AND.(obl.eq.1))THEN
          lattice=DFLOAT(2*Wo+Lo+2*Lp-2*Wp-1)*acc
          IF(MOD(Lp,3).eq.2) basis6=acc
          btmp1=-DFLOAT(2*Wo+Lp-2)*a*0.5D0-0.1D0
          btmp2=-DFLOAT(Lp)*a*0.5D0+0.1D0
        ELSE IF((par.eq.1).AND.(obl.eq.2))THEN
          lattice=DFLOAT(6*Wo+3*Lo+2*Lp-6*Wp-1)*acc
          btmp1=-DFLOAT(6*Wo+Lp-4)*a/6.0D0-0.1D0
          btmp2=-DFLOAT(Lp)*a/6.0D0+0.1D0
        ELSE IF((par.eq.2).AND.(obl.eq.2))THEN
          lattice=DFLOAT(2*Wo+Lo+2*Lp-2*Wp)*a
          btmp1=-DFLOAT(6*Wo+3*Lp-3)*acc/2.0D0-0.1D0
          btmp2=-DFLOAT(3*Lp+1)*acc/2.0D0+0.1D0
        ELSE IF((par.eq.2).AND.(obl.eq.1))THEN
          lattice=DFLOAT(2*Wo+3*Lo+2*Lp-6*Wp-2)*a
          btmp1=-DFLOAT(2*Wo+Lp-3)*acc*0.5D0-0.1D0
          btmp2=-DFLOAT(Lp-1)*acc*0.5D0+0.1D0
        END IF

        END SUBROUTINE mixed_parameters
!!!!!!!!!!!!!!!!!!!!!!!!!!!!!!!!!!!!!!!!!!!!!!!!!!!!!!!!!!!!!!!!!!!
        SUBROUTINE create_parallel
        !!!!!!!!!!!!!!!!!!!!!!!!!!!!!!!!!!!!!!!!
        ! Subroutine to create the parallel part
        !!!!!!!!!!!!!!!!!!!!!!!!!!!!!!!!!!!!!!!!
        USE wiggle_var
        IMPLICIT none
        DO i=1,unit
          zp1(2*i-1)=base1+DFLOAT(i-unit/2)*base2
          zp1(2*i)=DFLOAT(i-unit/2)*base2
          yp1(2*i-1)=base4
          yp1(2*i)=0.0D0
        END DO
        DO i=2,Wp
          zp1((i-1)*2*unit+1:2*unit*i)=zp1(1:2*unit)+DFLOAT(MOD(i+1,2))*base5
          yp1((i-1)*2*unit+1:2*unit*i)=yp1(1:2*unit)+DFLOAT(i-1)*base6
        END DO
        IF(MOD(Lp,2).eq.0) zp1(1:2*unit*Wp)=zp1(1:2*unit*Wp)+base7
        IF(MOD(Lp,2).eq.1) zp1(1:2*unit*Wp)=zp1(1:2*unit*Wp)+base8
        zp2=zp1+DFLOAT(MOD(Lo-Wp,2))*base5
        yp2=yp1-DFLOAT(Lo-Wp)*base6
```

```
        END SUBROUTINE create_parallel
!!!!!!!!!!!!!!!!!!!!!!!!!!!!!!!!!!!!!!!!!!!!!!!!!!!!!!!!!!!!!!!!!!!!!!!
        SUBROUTINE create_oblique
        !!!!!!!!!!!!!!!!!!!!!!!!!!!!!!!!!!!!!!!!!!
        ! Subroutine to create the oblique part
        !!!!!!!!!!!!!!!!!!!!!!!!!!!!!!!!!!!!!!!!!!
        USE wiggle_var
        IMPLICIT none

        DO i=1,unit
          zo1(2*i-1)=basis1+DFLOAT(i-unit/2)*basis2
          zo1(2*i)=DFLOAT(i-unit/2)*basis2
          yo1(2*i-1)=basis3
          yo1(2*i)=0.0D0
        END DO
        DO i=2,Wo
          zo1((i-1)*2*unit+1:2*unit*i)=zo1(1:2*unit)+DFLOAT(MOD(i+1,2))*basis4
          yo1((i-1)*2*unit+1:2*unit*i)=yo1(1:2*unit)+DFLOAT(i-1)*basis5
        END DO
        zo1(1:2*unit*Wo)=zo1(1:2*unit*Wo)+basis6
        DO i=1,2*unit*Wo
          atmp0=zo1(i) ; btmp0=yo1(i)
          zo1(i)=atmp0*COS(theta)-btmp0*SIN(theta)
          yo1(i)=atmp0*SIN(theta)+btmp0*COS(theta)
        END DO
        zo1(1:2*unit*Wo)=zo1(1:2*unit*Wo)+basis7
        yo1(1:2*unit*Wo)=yo1(1:2*unit*Wo)+basis8
        zo2(1:2*unit*Wo)=-zo1(1:2*unit*Wo)
        yo2(1:2*unit*Wo)=yo1(1:2*unit*Wo)

        END SUBROUTINE create_oblique
!!!!!!!!!!!!!!!!!!!!!!!!!!!!!!!!!!!!!!!!!!!!!!!!!!!!!!!!!!!!!!!!!!!!!!!
        SUBROUTINE assembling
        !!!!!!!!!!!!!!!!!!!!!!!!!!!!!!!!!!!!!!!!!!
        ! Subroutine to assemble the GNW
        !!!!!!!!!!!!!!!!!!!!!!!!!!!!!!!!!!!!!!!!!!
        USE wiggle_var
        IMPLICIT none

        DO i=1,2*unit*Wp
          IF(((yp1(i)-atmp1*zp1(i)+btmp1).le.0).AND. &
             ((yp1(i)+atmp1*zp1(i)+btmp1).le.0).AND. &
             (zp1(i).le.lattice*0.5D0+0.1).AND. &
             (zp1(i).ge.-lattice*0.5D0+param1-0.1))THEN
            nat=nat+1
            yf(nat)=yp1(i) ; zf(nat)=zp1(i)
          END IF
        END DO
        DO i=1,2*unit*Wp
          IF((((yp2(i)-atmp2*zp2(i)+btmp2).ge.0).OR. &
              ((yp2(i)+atmp2*zp2(i)+btmp2).ge.0)).AND. &
             (zp2(i).le.lattice*0.5D0+0.1).AND. &
             (zp2(i).ge.-lattice*0.5D0+param1-0.1))THEN
```

```
            nat=nat+1
            yf(nat)=yp2(i) ; zf(nat)=zp2(i)
          END IF
        END DO
        DO i=1,2*unit*Wo
          IF((yo1(i).lt.-0.1).AND.(yo1(i).gt.MAXVAL(0.1+yp2(1:2*unit*Wp))).AND. &
             (zo1(i).le.lattice*0.5D0+0.1).AND. &
             (zo1(i).ge.-lattice*0.5D0+param1-0.1))THEN
            nat=nat+1
            yf(nat)=yo1(i) ; zf(nat)=zo1(i)
          END IF
        END DO
        DO i=1,2*unit*Wo
          IF((yo2(i).lt.-0.1).AND.(yo2(i).gt.MAXVAL(0.1+yp2(1:2*unit*Wp))).AND. &
             (zo2(i).le.lattice*0.5D0+0.1).AND. &
             (zo2(i).ge.-lattice*0.5D0+param1-0.1))THEN
            nat=nat+1
            yf(nat)=yo2(i) ; zf(nat)=zo2(i)
          END IF
        END DO
        nattmp=0
        DO i=1,nat
          add=.true.
          DO j=1,i-1
            dr=DSQRT((yf(i)-yf(j))**2+(zf(i)-zf(j))**2)
            IF(dr.lt.0.1) add=.false.
            IF(dr.lt.0.1) EXIT
          END DO
          IF(add)THEN
            nattmp=nattmp+1
            yf2(nattmp)=yf(i) ; zf2(nattmp)=zf(i)
          END IF
        END DO
        nat=nattmp
        yf(1:nat)=yf2(1:nat) ; zf(1:nat)=zf2(1:nat)

        END SUBROUTINE assembling
!!!!!!!!!!!!!!!!!!!!!!!!!!!!!!!!!!!!!!!!!!!!!!!!!!!!!!!!!!!!!!!!!!!!!!!!!!
        SUBROUTINE writting
        !!!!!!!!!!!!!!!!!!!!!!!!!!!!!!!!!!!!!!!
        ! Subroutine to write the xyz data
        !!!!!!!!!!!!!!!!!!!!!!!!!!!!!!!!!!!!!!!
        USE wiggle_var
        IMPLICIT none

        open(unit=1,file='wiggle.xyz')
        write(1,*) nat*ncells
        write(1,*)
        DO j=1,ncells
          DO i=1,nat
            write(1,*) 'C', 0.0,yf(i),zf(i)+DFLOAT(j-1)*lattice
          END DO
        END DO
        write(1,*)
```

```
        END SUBROUTINE writting
!!!!!!!!!!!!!!!!!!!!!!!!!!!!!!!!!!!!!!!!!!!!!!!!!!!!!!!!!!!!!!!!!!!!!!!
        SUBROUTINE number_of_atoms
        !!!!!!!!!!!!!!!!!!!!!!!!!!!!!!!!!!!!!!!!!!
        ! Subroutine to calculate the number
        ! of atoms in the GNW
        !!!!!!!!!!!!!!!!!!!!!!!!!!!!!!!!!!!!!!!!!!
        USE wiggle_var
        IMPLICIT none

        print*,nat
        IF((par.eq.1).AND.(obl.eq.1))THEN
          IF(((MOD(Lp,3).eq.2).AND.(MOD(Lo-Wp,3).eq.0)).OR.((MOD(Lp,3).eq.1).AND.(MOD(Lo-Wp,3).eq.2)))THEN
            nat=2*(2*Wo+Lo+2*Lp-2*Wp-1)*Lo/3-2*(2*Lp+Lo-Wp-1)*(Lo-Wp)/3
          ELSE IF((MOD(Lp,3).eq.2).AND.(MOD(Lo-Wp,3).eq.2))THEN
            nat=2*(2*Wo+Lo+2*Lp-2*Wp-1)*Lo/3-2*(2*Lp+Lo-Wp)*(Lo-Wp-1)/3-4*(Lp+1)/3
          ELSE IF((MOD(Lp,3).eq.2).AND.(MOD(Lo-Wp,3).eq.1))THEN
            nat=2*(2*Wo+Lo+2*Lp-2*Wp-1)*Lo/3-2*(2*Lp+Lo-Wp+1)*(Lo-Wp-2)/3-8*(Lp+1)/3
          ELSE IF((MOD(Lp,3).eq.1).AND.(MOD(Lo-Wp,3).eq.1))THEN
            nat=2*(2*Wo+Lo+2*Lp-2*Wp-1)*Lo/3-2*(2*Lp+Lo-Wp)*(Lo-Wp-1)/3-4*(Lp-1)/3
          ELSE IF((MOD(Lp,3).eq.1).AND.(MOD(Lo-Wp,3).eq.0))THEN
            nat=2*(2*Wo+Lo+2*Lp-2*Wp-1)*Lo/3-2*(2*Lp+Lo-Wp+1)*(Lo-Wp-2)/3-2*(2+4*(Lp-1)/3)
          END IF
        ELSE IF((par.eq.1).AND.(obl.eq.2))THEN
            nat=2*(6*Wo+3*Lo+2*Lp-6*Wp-1)*Lo/3-2*(2*Lp+3*Lo-3*Wp-1)*(Lo-Wp)/3
        ELSE IF((par.eq.2).AND.(obl.eq.2))THEN
            nat=2*(2*Wo+Lo+2*Lp-2*Wp)*Lo-2*(2*Lp+Lo-Wp)*(Lo-Wp)
        ELSE IF((par.eq.2).AND.(obl.eq.1))THEN
            nat=2*(2*Wo+3*Lo+2*Lp-6*Wp-2)*Lo-2*(2*Lp+3*Lo-3*Wp-2)*(Lo-Wp)
        END IF
        print*,nat

        END SUBROUTINE number_of_atoms
!!!!!!!!!!!!!!!!!!!!!!!!!!!!!!!!!!!!!!!!!!!!!!!!!!!!!!!!!!!!!!!!!!!!!!!
      END MODULE wiggle_tasks
```

APPENDIX C – Publications

Publications related to this thesis

- E. C. Girão, A. G. Souza Filho, V. Meunier. "Electronic transport properties of carbon nanotoroids". *Nanotechnology* **22**(7), 075701 (2011).
- E. C. Girão, A. G. Souza Filho, V. Meunier. "Electronic transmission selectivity in multiterminal graphitic nanorings". *Applied Physics Letters* **98**(11), 112111 (2011).
- E. C. Girão, L. Liang, E. Cruz-Silva, A. G. Souza Filho, V. Meunier. "Emergence of atypical properties in assembled graphene nanoribbons". *Physical Review Letters* **107**, 135501 (2011).

Other publications

- E. C. Girão, Y. Liebold-Ribeiro, J. A. Batista, E. B. Barros, S. B. Fagan, J. Mendes Filho, M. S. Dresselhaus, A. G. Souza Filho. "Functionalization of single-wall carbon nanotubes through chloroform adsorption: theory and experiment". *Physical Chemistry Chemical Physics* **12**(7), 1518 (2010).
- E. C. Girão, S. B. Fagan, I. Zanella, A. G. Souza Filho. "Nicotine adsorption on single wall carbon nanotubes". *Journal of Hazardous Materials* **184**(1-3), 678 (2010).
- M. H. Pan, E. C. Girão,X. Jia, S. Bhaviripudi, Q. Li, J. Kong, V. Meunier, M. S. Dresselhaus "Topographic and spectroscopic characterization of electronic edge states in CVD grown graphene nanoribbons". *Nano Letters*, in press (2012).

Bibliography

[1] R. Van Noorden. "The trials of new carbon". *Nature* **469**(7328), 14 (2011).

[2] W. A. Harrison. *Electronic structure and the properties of solids*. Dover Publications, Inc.: New York.

[3] A. R. Botello-Mendez, X. Declerck, M. Terrones, H. Terrones, J. C. Charlier. "One-dimensional extended lines of divacancy defects in graphene". *Nanoscale* **3**(7), 2868 (2011).

[4] J. Cai, P. Ruffieux, R. Jaafar, M. Bieri, T. Braun, S. Blankenburg, M. Muoth, A. P. Seitsonen, M. Saleh, X. Feng, K. Muellen, R. Fasel. "Atomically precise bottom-up fabrication of graphene nanoribbons". *Nature* **466**(7305), 470 (2010).

[5] H. Terrones, M. Terrones, E. Hernandez, N. Grobert, J. Charlier, P. Ajayan. "New metallic allotropes of planar and tubular carbon". *Physical Review Letters* **84**(8), 1716 (2000).

[6] B. van Wees, H. Van Houten, C. W. J. Beenakker, J. G. Williamson, L. P. Kouwenhoven, D. van der Marel, C. T. Foxon. "Quantized conductance of point contacts in a two-dimensional electron-gas". *Physical Review Letters* **60**(9), 848 (1988).

[7] E. C. Girão, A. G. Souza Filho, V. Meunier. "Electronic transport properties of carbon nanotoroids". *Nanotechnology* **22**(7), 075701 (2011).

[8] E. C. Girão, A. G. Souza Filho, V. Meunier. "Electronic transmission selectivity in multiterminal graphitic nanorings". *Applied Physics Letters* **98**(11), 112111 (2011).

[9] E. C. Girão, L. Liang, E. Cruz-Silva, A. G. Souza Filho, V. Meunier. "Emergence of atypical properties in assembled graphene nanoribbons". *Physical Review Letters* **107**, 135501 (2011).

[10] H. W. Kroto, J. R. Heath, S. C. Obrien, R. F. Curl, R. E. Smalley. "C-60 - Buckminsterfullerene". *Nature* **318**(6042), 162 (1985).

[11] R. P. Feynman. *There's Plenty of Room at the Bottom*. American Physical Society meeting at Caltech.

[12] M. S. Dresselhaus, G. Dresselhaus, P. C. Eklund. University of Pennsylvania Workshop.

[13] S. Iijima. "Helical microtubules of graphitic carbon". *Nature* **354**(6348), 56 (1991).

[14] S. Iijima, T. Ichihashi. "Single-shell carbon nanotubes of 1 nm diameter". *Nature* **363**(6430), 603 (1993).

[15] D. S. Bethune, C. H. Kiang, M. S. Devries, G. Gorman, R. Savoy, J. Vazquez, R. Beyers. "Cobalt-catalyzed growth of carbon nanotubes with single-atomic layerwalls". *Nature* **363**(6430), 605 (1993).

[16] K. Novoselov, A. Geim, S. Morozov, D. Jiang, Y. Zhang, S. Dubonos, I. Grigorieva, A. Firsov. "Electric field effect in atomically thin carbon films". *Science* **306**(5696), 666 (2004).

[17] P. R. Wallace. "The band theory of graphite". *Physical Review* **71**(9), 622 (1947).

[18] R. Saito, G. Dresselhaus, M. S. Dresselhaus. *Physical Properties of Carbon Nanotubes*. London: Imperial College Press.

[19] M. N. Ramos, K. C. Lopes, A. M. Tavares, E. Ventura, S. A. do Monte, R. C. M. U. Araújo. "Effects of wave function modifications on calculated carbonâcarbontriple bond lengths". *Journal of Molecular Structure: THEOCHEM* **758**(2-3), 253 (2006).

[20] R. J. Baierle, S. B. Fagan, R. Mota, A. J. R. da Silva, A. Fazzio. "Electronic and structural properties of silicon-doped carbon nanotubes". *Physical Review B* **64**, 085413 (2001).

[21] I. Cabria, J. W. Mintmire, C. T. White. "Metallic and semiconducting narrow carbon nanotubes". *Physical Review B* **67**, 121406 (2003).

[22] S. Das Sarma, S. Adam, E. H. Hwang, E. Rossi. "Electronic transport in two-dimensional graphene". *Reviews of Modern Physics* **83**(2), 407 (2011).

[23] V. V. Cheianov, V. I. Fal'ko. "Selective transmission of dirac electrons and ballistic magnetoresistance of n-p junctions in graphene". *Physical Review B* **74**(4) (2006).

[24] B. Huard, J. A. Sulpizio, N. Stander, K. Todd, B. Yang, D. Goldhaber-Gordon. "Transport measurements across a tunable potential barrier in graphene". *Physical Review Letters* **98**(23), 236803 (2007).

[25] F. Schwierz. "Graphene transistors". *Nature Nanotechnology* **5**(7), 487 (2010).

[26] C.-A. Palma, P. Samori. "Blueprinting macromolecular electronics". *Nature Chemistry* **3**(6), 431 (2011).

[27] F. Xia, V. Perebeinos, Y.-m. Lin, Y. Wu, P. Avouris. "The origins and limits of metal-graphene junction resistance". *Nature Nanotechnology* **6**(3), 179 (2011).

[28] K. Novoselov. "Mind the gap". *Nature Materials* **6**(10), 720 (2007).

[29] Y.-W. Son, M. L. Cohen, S. G. Louie. "Energy gaps in graphene nanoribbons". *Physical Review Letters* **97**(21), 216803 (2006).

[30] O. V. Yazyev. "Emergence of magnetism in graphene materials and nanostructures". *Reports on Progress in Physics* **73**(5), 056501 (2010).

[31] L. Pisani, J. A. Chan, B. Montanari, N. M. Harrison. "Electronic structure and magnetic properties of graphitic ribbons". *Physical Review B* **75**(6), 064418 (2007).

[32] K. Wakabayashi, M. Fujita, H. Ajiki, M. Sigrist. "Electronic and magnetic properties of nanographite ribbons". *Physical Review B* **59**(12), 8271 (1999).

[33] F. Munoz-Rojas, J. Fernandez-Rossier, J. J. Palacios. "Giant Magnetoresistance in Ultrasmall Graphene Based Devices". *Physical Review Letters* **102**(13), 136810 (2009).

[34] Y.-W. Son, M. L. Cohen, S. G. Louie. "Half-metallic graphene nanoribbons". *Nature* **444**(7117), 347 (2006).

[35] A. Saffarzadeh, R. Farghadan. "A spin-filter device based on armchair graphene nanoribbons". *Applied Physics Letters* **98**(2), 023106 (2011).

[36] Z. F. Wang, Q. W. Shi, Q. Li, X. Wang, J. G. Hou, H. Zheng, Y. Yao, J. Chen. "Z-shaped graphene nanoribbon quantum dot device". *Applied Physics Letters* **91**(5), 053109 (2007).

[37] Y. Hancock, K. Saloriutta, A. Uppstu, A. Harju, M. J. Puska. "Spin-Dependence in Asymmetric, V-Shaped-Notched Graphene Nanoribbons". *Journal of Low Temperature Physics* **153**(5-6), 393 (2008).

[38] H. Sevincli, M. Topsakal, S. Ciraci. "Superlattice structures of graphene-based armchair nanoribbons". *Physical Review B* **78**(24), 245402 (2008).

[39] M. Topsakal, H. Sevincli, S. Ciraci. "Spin confinement in the superlattices of graphene ribbons". *Applied Physics Letters* **92**(17), 173118 (2008).

[40] P. Simonis, C. Goffaux, P. Thiry, L. Biro, P. Lambin, V. Meunier. "STM study of a grain boundary in graphite". *Surface Science* **511**(1-3), 319 (2002).

[41] J. Lahiri, Y. Lin, P. Bozkurt, I. I. Oleynik, M. Batzill. "An extended defect in graphene as a metallic wire". *Nature Nanotechnology* **5**(5), 326 (2010).

[42] X. Lin, J. Ni. "Half-metallicity in graphene nanoribbons with topological line defects". *Physical Review B* **84**(7), 075461 (2011).

[43] P. M. Ajayan, B. I. Yakobson. "Graphene: Pushing the boundaries". *Nature Materials* **10**(6), 415 (2011).

[44] O. V. Yazyev, S. G. Louie. "Electronic transport in polycrystalline graphene". *Nature Materials* **9**(10), 806 (2010).

[45] J. Campos-Delgado, J. M. Romo-Herrera, X. Jia, D. A. Cullen, H. Muramatsu, Y. A. Kim, T. Hayashi, Z. Ren, D. J. Smith, Y. Okuno, T. Ohba, H. Kanoh, K. Kaneko, M. Endo, H. Terrones, M. S. Dresselhaus, M. Terrones. "Bulk production of a new form of sp2 carbon: Crystalline graphene nanoribbons". *Nano Letters* **8**(9), 2773 (2008).

[46] X. Wang, H. Dai. "Etching and narrowing of graphene from the edges". *Nature Chemistry* **2**(8), 661 (2010).

[47] R. Yang, L. Zhang, Y. Wang, Z. Shi, D. Shi, H. Gao, E. Wang, G. Zhang. "An Anisotropic Etching Effect in the Graphene Basal Plane". *Advanced Materials* **22**(36), 4014 (2010).

[48] L. Xie, L. Jiao, H. Dai. "Selective Etching of Graphene Edges by Hydrogen Plasma". *Journal of the American Chemical Society* **132**(42), 14751 (2010).

[49] D. V. Kosynkin, A. L. Higginbotham, A. Sinitskii, J. R. Lomeda, A. Dimiev, B. K. Price, J. M. Tour. "Longitudinal unzipping of carbon nanotubes to form graphene nanoribbons". *Nature* **458**(7240), 872 (2009).

[50] L. Jiao, L. Zhang, X. Wang, G. Diankov, H. Dai. "Narrow graphene nanoribbons from carbon nanotubes". *Nature* **458**(7240), 877 (2009).

[51] X. Jia, J. Campos-Delgado, M. Terrones, V. Meunier, M. S. Dresselhaus. "Graphene edges: a review of their fabrication and characterization". *Nanoscale* **3**(1), 86 (2011).

[52] V. Coluci, D. Galvao, A. Jorio. "Geometric and electronic structure of carbon nanotube networks: 'super'-carbon nanotubes". *Nanotechnology* **17**(3), 617 (2006).

[53] V. R. Coluci, S. O. Dantas, A. Jorio, D. S. Galvao. "Mechanical properties of carbon nanotube networks by molecular mechanics and impact molecular dynamics calculations". *Physical Review B* **75**(7), 075417 (2007).

[54] J. M. Romo-Herrera, M. Terrones, H. Terrones, S. Dag, V. Meunier. "Covalent 2d and 3d networks from 1d nanostructures: Designing new materials". *Nano Letters* **7**(3), 570 (2007).

[55] J. M. Romo-Herrera, M. Terrones, H. Terrones, V. Meunier. "Guiding Electrical Current in Nanotube Circuits Using Structural Defects: A Step Forward in Nanoelectronics". *ACS Nano* **2**(12), 2585 (2008).

[56] J. M. Romo-Herrera, M. Terrones, H. Terrones, V. Meunier. "Electron transport properties of ordered networks using carbon nanotubes". *Nanotechnology* **19**(31), 315704 (2008).

[57] M. Terrones, F. Banhart, N. Grobert, J.-C. Charlier, H. Terrones, P. M. Ajayan. "Molecular junctions by joining single-walled carbon nanotubes". *Physical Review Letters* **89**(7), 075505 (2002).

[58] M. Endo, H. Muramatsu, T. Hayashi, Y. Kim, G. Van Lier, J. Charlier, H. Terrones, M. Terrones, M. Dresselhaus. "Atomic nanotube welders: Boron interstitials triggering connections in double-walled carbon nanotubes". *Nano Letters* **5**(6), 1099 (2005).

[59] T. G. Pedersen, C. Flindt, J. Pedersen, N. A. Mortensen, A.-P. Jauho, K. Pedersen. "Graphene antidot lattices: Designed defects and spin qubits". *Physical Review Letters* **100**(13), 136804 (2008).

[60] A. R. Botello-Mendez, E. Cruz-Silva, J. M. Romo-Herrera, F. Lopez-Urias, M. Terrones, B. G. Sumpter, H. Terrones, J. C. Charlier, V. Meunier. "Quantum transport in graphene nanonetworks". *Nano Letters* **11**(8), 3058 (2011).

[61] R. G. Amorim, A. Fazzio, A. Antonelli, F. D. Novaes, A. J. R. da Silva. "Divacancies in graphene and carbon nanotubes". *Nano Letters* **7**(8), 2459 (2007).

[62] E. C. Girão, S. B. Fagan, I. Zanella, A. G. Souza Filho. "Nicotine adsorption on single wall carbon nanotubes". *Journal of Hazardous Materials* **184**(1-3), 678 (2010).

[63] J. A. Rodriguez-Manzo, F. Banhart. "Creation of Individual Vacancies in Carbon Nanotubes by Using an Electron Beam of 1 angstrom Diameter". *Nano Letters* **9**(6), 2285 (2009).

[64] S. Berber, A. Oshiyama. "Reconstruction of mono-vacancies in carbon nanotubes: Atomic relaxation vs. spin polarization". *Physica B-Condensed Matter* **376**, 272 (2006).

[65] S. Ihara, S. Itoh. "Helically coiled and toroidal cage forms of graphitic carbon". *Carbon* **33**(7), 931 (1995).

[66] P. Liu, Y. W. Zhang, C. Lu. "Atomistic simulations of formation and stability of carbon nanorings". *Physical Review B* **72**(11), 115408 (2005).

[67] J. Liu, H. Dai, J. Hafner, D. Colbert, R. Smalley, S. Tans, C. Dekker. "Fullerene 'crop circles'". *Nature* **385**(6619), 780 (1997).

[68] R. Martel, H. Shea, P. Avouris. "Rings of single-walled carbon nanotubes". *Nature* **398**(6725), 299 (1999).

[69] M. Ahlskog, E. Seynaeve, R. J. M. Vullers, C. V. Haesendonck, A. Fonseca, K. Hernadi, J. B. Nagy. "Ring formations from catalytically synthesized carbon nanotubes". *Chemical Physics Letters* **300**(1-2), 202 (1999).

[70] M. Huhtala, A. Kuronen, K. Kaski. "Carbon nanotube structures: molecular dynamics simulation at realistic limit". *Computer Physics Communications* **146**(1), 30 (2002).

[71] S. Zhao, S. Zhang, M. Xia, E. Zhang, X. Zuo. "Optimum diameter of small single-wall carbon tori". *Physics Letters A* **331**(3-4), 238 (2004).

[72] C. Feng, K. Liew. "Energetics and structures of carbon nanorings". *Carbon* **47**(7), 1664 (2009).

[73] V. Meunier, P. Lambin, A. A. Lucas. "Atomic and electronic structures of large and small carbon tori". *Physical Review B* **57**(23), 14886 (1998).

[74] L. Liu, G. Y. Guo, C. S. Jayanthi, S. Y. Wu. "Colossal paramagnetic moments in metallic carbon nanotori". *Physical Review Letters* **88**(21), 217206 (2002).

[75] L. Liu, C. S. Jayanthi, S. Y. Wu. "Structural and electronic properties of a carbon nanotorus: Effects of delocalized and localized deformations". *Physical Review B* **64**(3), 033412 (2001).

[76] M. Jack, M. Encinosa. "Quantum electron transport in toroidal carbon nanotubes with metallic leads". *Molecular Simulation* **34**(1), 9 (2008).

[77] Y. Chou, G. Guo, L. Liu, C. Jayanthi, S. Wu. "Electrical conductance of carbon nanotori in contact with single-wall carbon nanotubes". *Journal of Applied Physics* **96**(4), 2249 (2004).

[78] S. Tans, A. Verschueren, C. Dekker. "Room-temperature transistor based on a single carbon nanotube". *Nature* **393**(6680), 49 (1998).

[79] K. Jensen, J. Weldon, H. Garcia, A. Zettl. "Nanotube radio". *Nano Letters* **7**(11), 3508 (2007).

[80] V. Barone, O. Hod, G. E. Scuseria. "Electronic structure and stability of semiconducting graphene nanoribbons". *Nano Letters* **6**(12), 2748 (2006).

[81] M. Bieri, M.-T. Nguyen, O. Groening, J. Cai, M. Treier, K. Ait-Mansour, P. Ruffieux, C. A. Pignedoli, D. Passerone, M. Kastler, K. Muellen, R. Fasel. "Two-Dimensional Polymer Formation on Surfaces: Insight into the Roles of Precursor Mobility and Reactivity". *Journal of the American Chemical Society* **132**(46), 16669 (2010).

[82] L. Grill, M. Dyer, L. Lafferentz, M. Persson, M. V. Peters, S. Hecht. "Nano-architectures by covalent assembly of molecular building blocks". *Nature Nanotechnology* **2**(11), 687 (2007).

[83] J. Lu, P. S. E. Yeo, C. K. Gan, P. Wu, K. P. Loh. "Transforming C(60) molecules into graphene quantum dots". *Nature Nanotechnology* **6**(4), 247 (2011).

[84] L. Lafferentz, F. Ample, H. Yu, S. Hecht, C. Joachim, L. Grill. "Conductance of a Single Conjugated Polymer as a Continuous Function of Its Length". *Science* **323**(5918), 1193 (2009).

[85] M. Born, J. R. Oppenheimer. "Zur quantentheorie der molekeln". *Annalen der Physik* **84**, 457 (1927).

[86] R. M. Martin. *Electronic structure: Basic Theory and Practical Methods*. Cambridge University Press: Cambridge, UK.

[87] D. R. Hartree. "The wave mechanics of an atom with non-coulombic central fields: parts i, ii, iii". *Mathematical Proceedings of The Cambridge Philosophical Society* **24**, 89, 111, 426 (1928).

[88] V. Fock. *Zeitschrift fur Physik* **61**, 126 (1930).

[89] J. C. Slater. "The electronic structure of atoms—the hartree-fock method and correlation". *Reviews of Modern Physics* **35**, 484 (1963).

[90] P. Hohenberg, W. Kohn. "Inhomogeneous Electron Gas". *Physical Review B* **136**(3B), B864 (1964).

[91] W. Kohn, L. J. Sham. "Self-Consistent Equations Including Exchange and Correlation Effects". *Physical Review* **140**(4A), 1133 (1965).

[92] G. Kresse, J. Furthmuller. "Efficiency of ab-initio total energy calculations for metals and semiconductors using a plane-wave basis set". *Computational Materials Science* **6**(1), 15 (1996).

[93] G. Kresse, J. Furthmüller. "Efficient iterative schemes for *ab initio* total-energy calculations using a plane-wave basis set". *Physical Review B* **54**, 11169 (1996).

[94] F. Bloch. *Zeitschrift fur Physik* **52**, 555 (1928).

[95] N. W. Ashcroft, N. D. Mermin. *Solid state Physics*. Thomson Learning, Inc.

[96] H. Jones, N. F. Mott, H. W. B. Skinner. "A theory of the form of the x-ray emission bands of metals". *Physical Review* **45**, 379 (1934).

[97] J. C. Slater, G. F. Koster. "Simplified LCAO Method for the Periodic Potential Problem". *Physical Review* **94**(6), 1498 (1954).

[98] J. Hubbard. "Electron correlations in Narrow Energy bands IV Atomic Representation". *Proceedings of the Royal Society of London Series A - Mathematical and Physical Sciences* **285**(1403), 542 (1965).

[99] P. Pulay. "Convergence Acceleration of Iterative Sequences - The Case of SCF Iteration". *Chemical Physics Letters* **73**(2), 393 (1980).

[100] D. R. Bowler, M. J. Gillan. "An efficient and robust technique for achieving self consistency in electronic structure calculations". *Chemical Physics Letters* **325**(4), 473 (2000).

[101] M. Ferrier, L. Angers, A. C. H. Rowe, S. Guéron, H. Bouchiat, C. Texier, G. Montambaux, D. Mailly. "Direct measurementof the phase-coherence length in a gaas/gaalas squarenetwork". *Physical Review Letters* **93**, 246804 (2004).

[102] F. Miao, S. Wijeratne, Y. Zhang, U. C. Coskun, W. Bao, C. N. Lau. "Phase-coherent transport in graphene quantum billiards". *Science* **317**(5844), 1530 (2007).

[103] D. A. Wharam, T. J. Thornton, R. Nwebury, M. Pepper, H. Ahmed, J. E. F. Frost, D. G. Hasko, D. C. Peacock, D. A. Ritchie, G. A. C. Jones. "One-dimensional transport and the quantization of the ballistic resistance". *Journal of Physics C-Solid State Physics* **21**(8), L209 (1988).

[104] M. Di Ventra. *Electrical Transport in Nanoscale Systems*. Cambridge University Press (2008).

[105] R. Landauer. "Conductance determined by transmission - probes and quantized constriction resistance". *Journal of Physics-Condensed Matter* **1**(43), 8099 (1989).

[106] S. Datta. *Quantum Transport: Atom to Transistor*. Cambridge University Press (2005).

[107] M. P. L. Sancho, J. M. L. Sancho, J. Rubio. "Highly convergent schemes for the calculation of bulk and surface Green-Functions". *Journal of Physics F-Metal Physics* **15**(4), 851 (1985).

[108] M. P. L. Sancho, J. M. L. Sancho, J. Rubio. "Quick iterative scheme for the calculation of transfer-matrices - application to Mo(100)". *Journal of Physics F - Metal Physics* **14**(5), 1205 (1984).

[109] V. Meunier, B. G. Sumpter. "Amphoteric doping of carbon nanotubes by encapsulation of organic molecules: Electronic properties and quantum conductance". *Journal of Chemical Physics* **123**(2) (2005).

[110] M. B. Nardelli. "Electronic transport in extended systems: Application to carbon nanotubes". *Physical Review B* **60**(11), 7828 (1999).

[111] K. Kazymyrenko, X. Waintal. "Knitting algorithm for calculating Green functions in quantum systems". *Physical Review B* **77**(11), 115119 (2008).

[112] J. G. Lewis. "Algorithm-582 - The Gibbs-Poole-Stockmeyer and Gibbs-King algorithms for reordering sparse matrices". *ACM Transactions on Mathematical Software* **8**(2), 190 (1982).

[113] *http://www.netlib.org/toms/582*.

[114] *http://www.netlib.org/lapack/*.

[115] P. M. Agrawal, B. S. Sudalayandi, L. M. Raff, R. Komanduri. "A comparison of different methods of young's modulus determination for single-wall carbon nanotubes (swcnt) using molecular dynamics (md) simulations". *Computational Materials Science* **38**(2), 271 (2006).

[116] A. Jorio, M. S. Dresselhaus, G. Dresselhaus. *Carbon Nanotubes: Advanced Topics in the Synthesis, Structure, Properties and Applications*. Berlin: Springer.

[117] R. Saito, G. Dresselhaus, M. S. Dresselhaus. "Trigonal warping effect of carbon nanotubes". *Physical Review B* **61**(4), 2981 (2000).

[118] M. Milnera, J. Kürti, M. Hulman, H. Kuzmany. "Periodic resonance excitation and intertube interaction from quasicontinuous distributed helicities in single-wall carbon nanotubes". *Physical Review Letters* **84**(6), 1324 (2000).

[119] I. Laszlo. "Topological description and construction of single wall carbon nanotube junctions". *Croatica Chemica Acta* **78**(2), 217 (2005).

[120] S. Gupta, A. Saxena. "Nanocarbon materials: probing the curvature and topology effects using phonon spectra". *Journal of Raman Spectroscopy* **40**(9), 1127 (2009).

[121] H. J. Choi, J. Ihm, S. G. Louie, M. L. Cohen. "Defects, quasibound states, and quantum conductance in metallic carbon nanotubes". *Physical Review Letters* **84**(13), 2917 (2000).

[122] A. N. Andriotis, M. Menon, D. Srivastava, L. Chernozatonskii. "Transport properties of single-wall carbon nanotube y junctions". *Physical Review B* **65**(16), 165416 (2002).

[123] A. Cresti, N. Nemec, B. Biel, G. Niebler, F. Triozon, G. Cuniberti, S. Roche. "Charge Transport in Disordered Graphene-Based Low Dimensional Materials". *Nano Research* **1**(5), 361 (2008).

[124] A. D. Franklin, R. A. Sayer, T. D. Sands, T. S. Fisher, D. B. Janes. "Toward surround gates on vertical single-walled carbon nanotube devices". *Journal of Vacuum Science & Technology B* **27**(2), 821 (2009).

[125] S. Sorgenfrei, C.-y. Chiu, M. Johnston, C. Nuckolls, K. L. Shepard. "Debye screening in single-molecule carbon nanotube field-effect sensors". *Nano Letters* **11**(9), 3739 (2011).

[126] D. Gunlycke, C. T. White. "Tight-binding energy dispersions of armchair-edge graphene nanostrips". *Physical Review B* **77**, 115116 (2008).

[127] T. Jayasekera, P. K. Pillalamarri, J. W. Mintmire, V. Meunier. "Effect of phase-breaking events on electron transport in mesoscopic and nanodevices". *International Journal of Quantum Chemistry* **108**(15), 2896 (2008).